Propeller-Wing Whirl Flutter

An analytical study

V.Q. Liu Xu

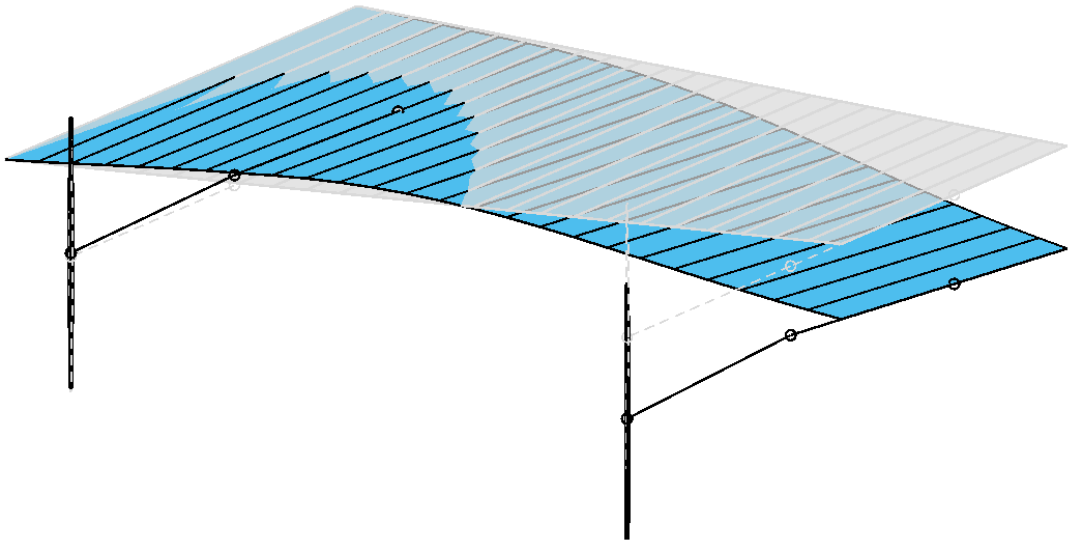

TU Delft

Propeller-Wing Whirl Flutter

An analytical study

by

V.Q. Liu Xu

to obtain the degree of Master of Science
at the Delft University of Technology,
to be defended publicly on Thursday July 2, 2020 at 01:00 PM.

Student number:	4714482	
Project duration:	May 1, 2019 – June 1, 2020	
Thesis committee:	Dr. ir. R. de Breuker,	TU Delft, supervisor
	Prof. dr. ir. L.L.M. Veldhuis,	TU Delft, supervisor
	Dr. ir. T. Sinnige,	TU Delft

This thesis is confidential and cannot be made public until July 2, 2020.

TU Delft

Acknowledgements

This report is the culmination of the Graduation project as part of the Master Program in Flight Performance and Propulsion at the Faculty of Aerospace Engineering of Delft University of Technology.

As I write this, a sentiment of excitement and happiness, but also nostalgia, overwhelms me. It has been a long journey but the experiences I have gained are invaluable and the people, irreplaceable.

I am sincerely grateful to every classmate, colleague, professor, and researcher who have helped in this graduation project by allocating some of their time to answer my questions and reply to my long emails. In particular, my supervisors, Leo Veldhuis and Roeland de Breuker, for their critical and insightful feedback.

Many thanks to all the friends that kept me company in the countless lunch breaks and coffee/tea breaks during the past year. You are the reason why I kept going to the office during the periods of greatest frustration, until it was possible.

Thank you, Giorgio, for your encouraging words and for your willingness to listen to me ramble on and on about my thesis.

To my dearest friend, Tsveta, we have made it! ;)

To my family, without whom I would not be where I am.

Vanessa
Delft, June 2020

"All models are wrong, but some are useful"

— George Box

Table of Contents

Abstract

Electrification of aviation is driving new aircraft configurations consisting in slender, lighter wings with several propellers spread across the wing span, including the wing tips. Thinner wings with high aspect ratios tend to be more flexible, and thus, more susceptible to wing flutter, a dynamic aeroelastic instability characterised by diverging oscillatory motions of the wing. As propellers are flexibly attached to the wing, another aeroelastic instability, called precession or whirl flutter, can occur. The nature of this phenomena lies in the additional forces and moments created by rotating blades as the propeller hub describes a "whirling" motion about the static thrust axis due to gyroscopic effects. These dynamic instabilities can happen independently or coupled together causing severe structural damage on the aircraft and when occurred during flight, lead to fatal accidents. Hence, it becomes essential to analyse any new propeller-driven aircraft configuration regarding wing flutter and whirl flutter.

Present research project focuses on the analysis of the aeroelastic behaviour of a flexible cantilever wing with flexibly attached tractor propeller/s. Attention is given to wingtip-mounted propeller-wings. For this purpose, three mathematical models have been derived to analyse the dynamic behaviour of an isolated propeller, a flexible cantilever wing, and a flexible cantilever wing with flexibly attached propeller/s. The isolated propeller model represent the classical propeller whirl flutter solution using Houbolt-Reed propeller aerodynamic derivatives. The wing model analyses the classical wing bending-torsion flutter and divergence; the structural model is a linear dynamic Euler-Bernoulli beam model and the aerodynamic model is represented by a combination of strip theory and two-dimensional Theodorsen's unsteady aerodynamic theory formulated in time domain using a two-finite state approximation. The propeller-wing model combines the previous two with the addition of appropriate structural and aerodynamic coupling terms. Following the validation/verification of the models, case studies have been performed on an isolated propeller, a flexible cantilever wing, a flexible cantilever wing with an inboard propeller, a flexible cantilever wing with a wingtip-mounted propeller, and a flexible cantilever wing with an inboard and a wingtip-mounted propeller. Moreover, parametric studies have been carried out on the wingtip-mounted propeller-wing model with respect to nacelle stiffness, nacelle structural damping, propeller mass, propeller pivoting length, mass moment of inertia about the axis of rotation, and propeller advance ratio. In all analyses, the propeller is a fixed-pitch propeller assumed to be operating in windmilling conditions. Propeller-wing aerodynamic interference effects have been ignored.

The aeroelastic behaviour of a wing with flexibly mounted propeller/s may be very different from that of a wing with rigidly mounted propeller/s. Reasons lie in the interaction between the additional whirl modes and the wing modes due to gyroscopic coupling. Whereas propeller and wing aerodynamics may drive the (coupled) backward whirl mode unstable, wing aerodynamics alone may drive the (coupled) forward whirl mode unstable. As the propeller is moved from an inboard position to the wing tip, there is further coupling between the propeller whirl modes and the wing modes; in turn, instabilities driven by the coupled whirl modes may dominate the aeroelastic stability of the propeller-wing model.

Parametric studies on the wingtip-mounted propeller-wing model show that: if the average nacelle stiffness is increased/decreased, having higher stiffness in pitch than in yaw is more stabilising until certain limiting conditions determined the stability of other propeller-wing modes; small changes in the nacelle structural damping barely influences the critical speed; changes in propeller mass or propeller pivoting length increase the system critical speed if the changes result in higher propeller-wing inertia parameters, except the propeller mass moment of inertia about the axis of rotation, whose effects on whirl flutter stability is destabilising; with a fixed-pitch windmilling propeller, the effects of propeller advance ratio is barely appreciable.

List of Figures

List of Tables

I

BACKGROUND

1

Introduction

Environmental concerns drive a growing interest in new aircraft configurations based on electric propulsion. This interest is also motivated by quick advances in high performance electrical machines [82]. Patterson et al. [83] remarks that in the near term, even without radical breakthroughs in electrical machines, small, general aviation aircraft can be electrically powered by means of increasing the aircraft aerodynamic efficiency and lowering the aircraft empty weight fractions. One way to achieve this is through higher aspect ratio and thinner wings with wingtip-mounted and/or distributed propellers where several tractor propellers are placed along the wing span, including the wing tips [103](see Figure 1.1). Such configurations demand special care with regards to airframe-propulsion system integration and wing structural design not only to achieve higher aerodynamic efficiency and noise reduction but also to lessen potential negative effects of propeller/s on the aircraft dynamic behaviour.

(a) NASA X-57 Maxwell [67].

(b) EcoPulse [2].

Figure 1.1: Examples of distributed propulsion aircraft.

Thinner wings with high aspect ratios tend to be more flexible. And as propellers are positioned closer to the wing tip, the flexible wing becomes more susceptible to some aeroelastic problems such as the classical wing flutter, a dynamic aeroelastic instability characterised by unstable vibrations of the wing [71]; by placing the propeller towards the wing tip, it changes the wing torsional moment of inertia and there is further interaction between the bending and torsional modes of wing vibration [102].

On the other hand, as propellers are flexibly mounted on the aircraft, another dynamic aeroelastic instability, called precession or whirl flutter, can occur. The nature of this phenomena lies in the additional forces and moments created by rotating blades as the propeller hub describes a “whirling” motion about the static thrust axis due to gyroscopic effects [86]. As in the case of classical wing flutter, whirl flutter on a propeller aircraft is not an isolated phenomenon and is also susceptible to interactions with wing elasticity, wing aerodynamics [90], and aircraft flight dynamics [38].

Both classical wing flutter and propeller whirl flutter have a critical forward velocity at which the system is neutrally stable. When the system meets a disturbance such as a gust and/or the forward velocity exceeds the critical forward velocity, in the case of classical wing flutter the wing describes a diverging oscillatory motion, and in the case of whirl flutter the propeller hub describes a diverging spiral motion. These dynamic instabilities can happen independently or coupled together causing severe structural damage on the aircraft and when occurred during flight, lead to fatal accidents [16][58]. The most notorious instances are the accidents of two Lockheed L-188C Electra airliners in 1959 and 1960 which occurred due to "failure of the port wing due to the forces coming from the undamped propeller whirl mode" and "failure of the starboard wing due to the flutter caused by the vibration of the outboard engine", respectively [16]. Because of this, it becomes essential to analyse any new propeller-driven aircraft configuration with respect to wing flutter and whirl flutter.

Nowadays, aeroelastic analysis regarding wing flutter and whirl flutter can be modelled via Finite Element Methods, Multi-Body Simulations or CFD-based simulations. Experimental work include wind tunnel tests on aeroelastic models [16], Ground Vibration Testing [18][22], and flight flutter testing [58]. The use of FEM or other software tools typically require high computational time and high level of detailed knowledge regarding the new aircraft design. Experimental tests require actual models to be built which is both time-consuming and costly. Neither are suitable to be used during the early design stages of a new aircraft configuration where usually no detailed geometric, structural, and aerodynamic knowledge is available and it is necessary to analyse multiple aircraft designs in a short amount of time. A compromise is found on quasi-analytical models which represent advanced low/high fidelity models that can potentially be used in Multidisciplinary Design Optimisation (MDO) applications [3].

The classical wing flutter has been widely studied [28] and analytical methods for its prediction are well covered in conventional aeroelasticity books such as Bisplinghoff et al. [10], Dowell [23], Fung [27] and Hodges and Pierce [36]. The phenomenon of propeller whirl flutter, although also broadly researched, is less well-known due to the shift in interest from propeller- to turbofan-powered aircraft. However, the relevance of whirl flutter has prevailed in the development of tilt-rotors.

Present graduation project focuses on the analysis of the aeroelastic behaviour of a cantilever wing with flexibly attached tractor propeller/s. The main goal to develop an analytical model that is capable of predicting wing flutter and whirl flutter characteristics. The choice of an analytical model has been made upon the interest of having a flexible tool to be used during the conceptual-preliminary design phase of propeller-driven aircraft configurations; to provide design guidelines with respect to wing/whirl flutter and to shed new insights on how wing/whirl flutter develop on wingtip-mounted-propeller and distributed-propeller wing configurations.

Within this framework, a literature study has been carried out; the main findings are summarised in Chapter 2. Following the literature study, a series of research questions have been formulated and the appropriate research work has been planned; this is presented in Chapter 3.

2

State of the Art

Current chapter presents the state of the art on propeller whirl flutter and reviews several aspects of propeller-wing systems from an aeroelastic standpoint.

Section 2.1 introduces the topic of whirl flutter. Section 2.2 explains the mechanism that drives propeller whirl flutter. Section 2.3 describes the development of propeller aerodynamics due to gyroscopic motions. Section 2.4 reviews analytical and numerical modelling methods developed to analyse propeller whirl flutter. Some notions of whirl flutter in tiltrotors are introduced in Section 2.5. Section 2.6 presents the effects of several parameters that influence propeller whirl flutter. General aspects of wing flutter are described in Section 2.7. Finally, Section 2.8 explains briefly the aerodynamic benefits of wingtip-mounted propellers, the basics of propeller-wing aerodynamic interference effects, and the effects of wingtip-mounted propellers on wing dynamics.

2.1. Introduction to Whirl Flutter

Whirl flutter is an aeroelastic dynamic instability caused by the interaction between gyroscopic effects[1] and unsteady aerodynamic forces and moments acting on elastically supported rotating propeller/rotor systems. The instability is characterized by a spiral motion described by the propeller/rotor hub which induces unstable vibrations and potential failures in the structure where the propeller/rotor-engine system is mounted. Whirl flutter can appear in propeller-driven aircraft as propeller whirl flutter, in V/STOL aircraft (i.e. tiltrotors) as proprotor whirl flutter, in wind turbines [48], and in helicopters [60].

The occurrence of whirl flutter was first recognised by Taylor and Browne in 1938 when studying methods to isolate vibrations in aircraft power plants. Several years later, Scanlan and Truman [96] investigated further this phenomenon and showed that "the whirling of a rigid propeller may materially affect wing normal mode shapes and frequencies". Whirl flutter was taken into account by some aircraft designers but such practice was later discouraged because large safety margins were usually met [85]. The real incentive to investigate whirl flutter in depth was triggered by the accidents of two Lockheed L-188C Electra airliners in 1959 and 1960, where whirl flutter and its coupling with wing flutter were recognised as the main causes of the accidents. Following the accidents, a 1/8-scale aeroelastic model of the Lockheed L-188C was tested in the NASA Langley Transonic Dynamics Tunnel; it was shown that a reduction in stiffness on the outboad engine supports would cause propeller whirl flutter to occur [1]. Figure 2.1 illustrates the model before and after a destructive flutter testing.

During the 60s and 70s, numerous analytical and experimental research aimed at understanding propeller and proprotor whirl flutter were carried out by NASA [1, 6, 7, 45, 62, 85, 88, 97]. In 1966-1967 Reed III [86, 87] presented a comprehensive state of the art on propeller-rotor whirl flutter.

[1] In this case, gyroscopic effects are caused by the upstream location of the propeller centre of gravity with respect to the propeller pivot point. The nature of gyroscopic motion is explained in more detail in Appendix A.

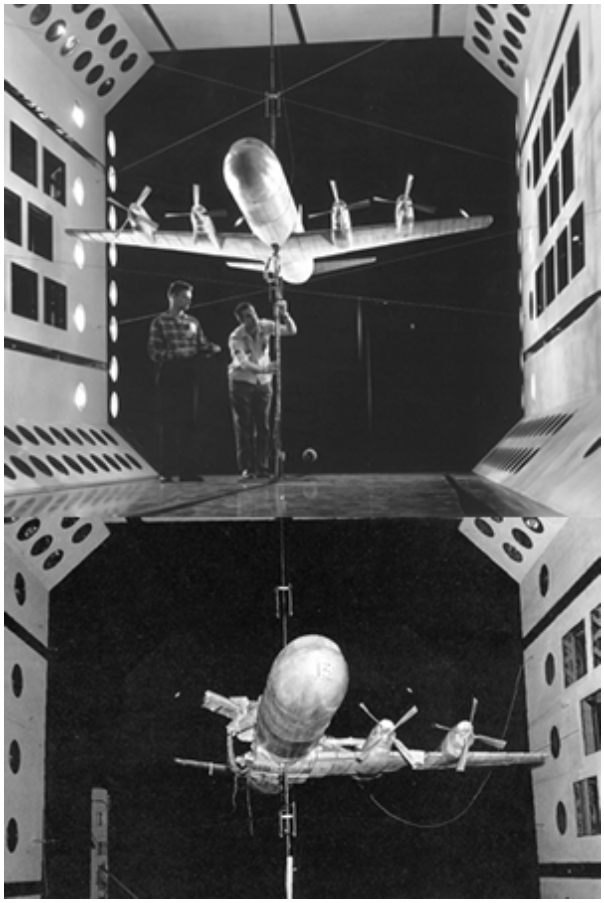

Figure 2.1: Photos of a scaled model of the Lockheed L-188C Electra being tested in the NASA Langley Transonic Dynamics Tunnel [1][24].

Despite the knowledge gained in whirl flutter and the added regulations so as to prevent the occurrence of this instability, several other fatal accidents in which whirl flutter was either the main cause or a contributing factor occurred. In 1992, a Beechcraft 1900C crashed into the ocean during a training mission. Investigations of the accidents showed that, although the aircraft had enough safety margins with respect to whirl flutter, the appearance of fatigue cracks in the engine bed structure reduced its stiffness and led to whirl flutter. In 2005, a twin-engine amphibious aircraft Grumman Turbo Mallard GF73T crashed shortly after taking off; the cause was suspected to be the propagation of wing fatigue cracks due to whirl mode vibrations. These accidents highlight the importance of considering failure modes in the analysis of wing/whirl flutter. More details regarding these accidents are given by Jiri Cecrdle in his book "Whirl flutter of turboprop aircraft structures (2015)" [16]. The book also includes a complete overview of propeller whirl flutter and some notions of whirl flutter in tilt-rotors.

Tiltrotors and helicopters feature much more complex rotor designs i.e. a swashplate or gimballed rotor systems with large, flexible blades. In consequence, the nature of proprotor whirl flutter is quite different from that of propeller whirl flutter in many aspects; these are covered in Johnson [54] and Bielawa [8], and later explained in Section 2.5.

At present, airworthiness regulations such as FAR/CS 23 and FAR/CS 25 require any turboprop powered aircraft to be certified with respect to whirl flutter [16].

2.2. Mechanism of Whirl Flutter

The mechanism of propeller whirl flutter is well explained in Reed III [86, 87], Försching [26], and Cecrdle [16]. The approach taken is the idealisation of the propeller-engine-nacelle system as a propeller with rigid blades and rigid nacelle attached to elastic mounts (Figure 4.1). The dynamic behaviour of the idealised propeller-engine-nacelle system is illustrated in Figure 2.2, Figure 2.3, and Figure 2.4.

When ignoring propeller rotation, as well as the aerodynamic and damping forces, the system has two

uncoupled natural vibration modes (i.e. pitch and yaw) each with their respective angular frequencies (see Figure 2.2).

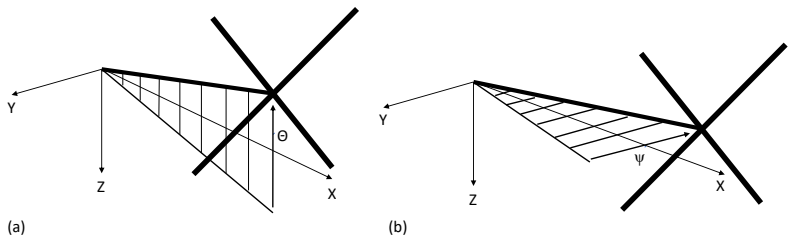

Figure 2.2: Natural vibration modes (adapted from [16][26]).

By considering propeller rotation but still ignoring the aerodynamic and damping forces, gyroscopic effects couple the natural mode shapes and cause the propeller hub to describe a whirl or precession motion around the static thrust axis. Two coupled mode shapes emerge (see Figure 2.3): a backward whirl mode and a forward whirl mode. The former has lower frequency and rotates in the opposite direction to the propeller rotation whereas the latter has higher frequency and its direction is the same as the propeller rotation. The gap between the frequencies increases as the propeller rotational speed increases.

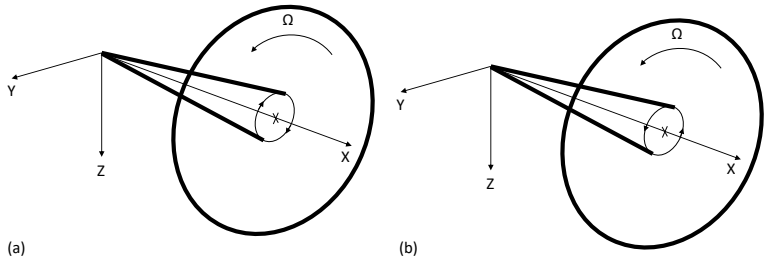

Figure 2.3: Backward (a) and forward (b) modes (adapted from [16][26]).

The system described so far is always stable. However, when taking into account the aerodynamic effects, the gyroscopic induced whirl modes change the propeller blades' angle of attack, thus, creating unsteady aerodynamic forces and moments which provide the mechanism for whirl instability. Such instability is characterized by a spiral motion of the propeller hub. If the blades are rigid, only the backward whirl mode can occur; the forward whirl mode becomes possible when the propeller blades are very flexible or have flap hinges [86].

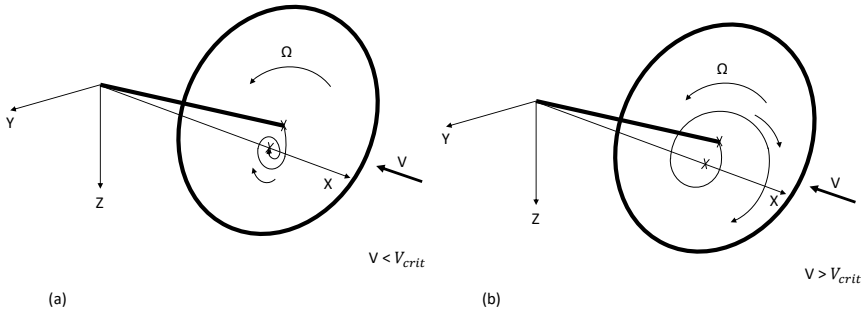

Figure 2.4: Stable (a) and unstable (b) state of gyroscopic vibrations for backward flutter mode (adapted from [16][26]).

As in classical wing flutter, there is a limit speed (flutter speed) at which there is no damping and the system is neutrally stable: if the forward speed of the system is below this flutter speed, the motion is damped

and the system is stable (Figure 2.4 (a)); if the forward speed is above this flutter speed the system becomes unstable and the spiral motion of the hub diverges (Figure 2.4 (b)). Gyroscopic divergence occurs when one of the mode frequencies is zero and the system moves in one-directional character.

2.3. Propeller Aerodynamics

The main difficulty in developing analytical methods to model whirl flutter lies in the determination of the propeller aerodynamic forces induced by gyroscopic motions. The origin of such forces can be qualitatively described using quasi-steady aerodynamic principles [87][26][16]. This is illustrated in Figure 2.5-Figure 2.7. Since the pitching and yawing motions are symmetrical, the figures only show the explanations by using a propeller pitching in the X-Z plane. Forces and moments due to yawing motions are analogous.

Figure 2.5 shows the propeller forces arising from a pitch displacement. This is equivalent to a propeller at an angle of attack θ. The blades that are going up (retreating blade) face a smaller in-plane rotational speed than the blades going down (advancing blade). Retreating blades generate less lift than advancing blades, when projected onto the rotor plane, a vertical force emerges in the negative Z-axis, $P_z(\theta)$, and a yawing motion appears about the negative Z-axis, $M_z(\theta)$. $P_z(\theta)$ increases the pithing angle and is the source of static divergence instability of the propeller; the yawing moment due to pitch $M_z(\theta)$, and its analogous, pitch moment due to yaw, $M_y(\psi)$, are the main drivers of propeller whirl flutter; they are to be balanced with aerodynamic and/or structural damping terms.

Figure 2.6 shows the propeller forces arising from a transverse linear vertical velocity $\dot{z}$. In this case, the blades that are going up are the advancing blades because $\dot{z}$ increases their in-plane rotational speed. Therefore, a vertical force emerges in the positive Z-axis, $P_z(\dot{z})$, and a yawing motion appears about the positive Z-axis, $M_z(\dot{z})$. These forces and moments oppose the propeller disc motion and damp it.

Figure 2.7 shows the propeller forces arising from the pitching angular velocity $\dot{\theta}$. The blades in the upper half of the rotor plane see smaller incoming flow speed than the blades in the lower half section. This results in a force in the positive Y-axis, $P_y(\dot{\theta})$, and a pitching moment about the positive Y-axis, $M_y(\dot{\theta})$. The lateral force $P_y(\dot{\theta})$ couples the movements around both vertical and lateral axis while the pitching moment $M_y(\dot{\theta})$ opposes the propeller disc motion, hence, damping it.

Apart from the forces and moments explained above, unsteady aerodynamics lead to additional forces and moments. Rotating blades give rise to shed vortices which cause the quasi-steady lift to be reduced in magnitude and to lag the instantaneous angle of attack by a phase angle defined by the frequency of the shed vortices [45].

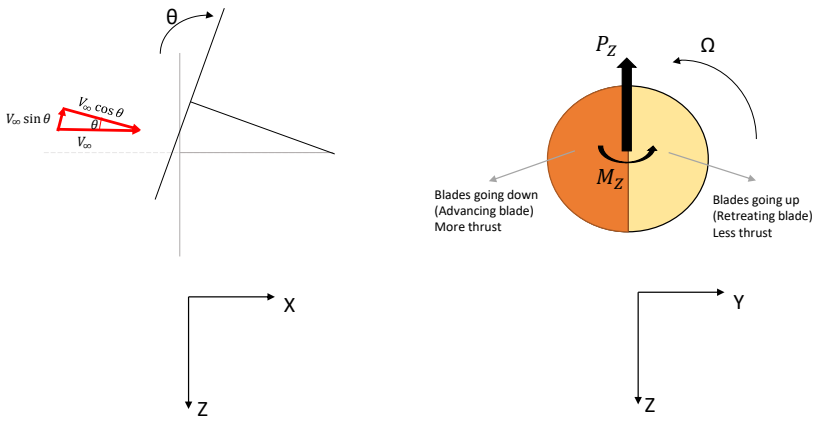

(a) Propeller pitching

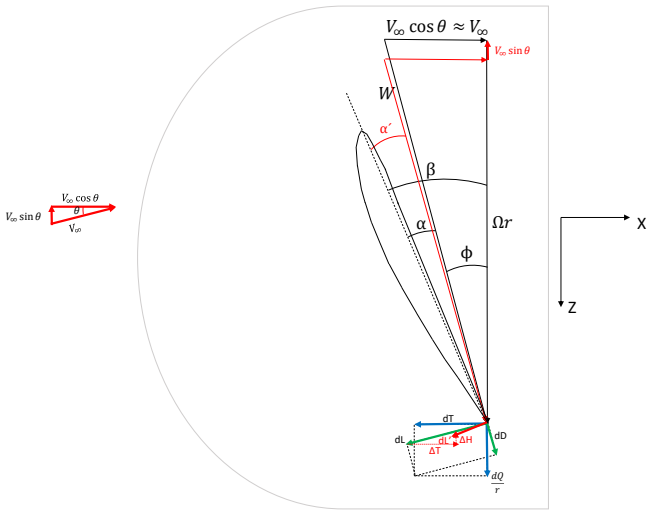

(b) Blades going up: retreating blade.

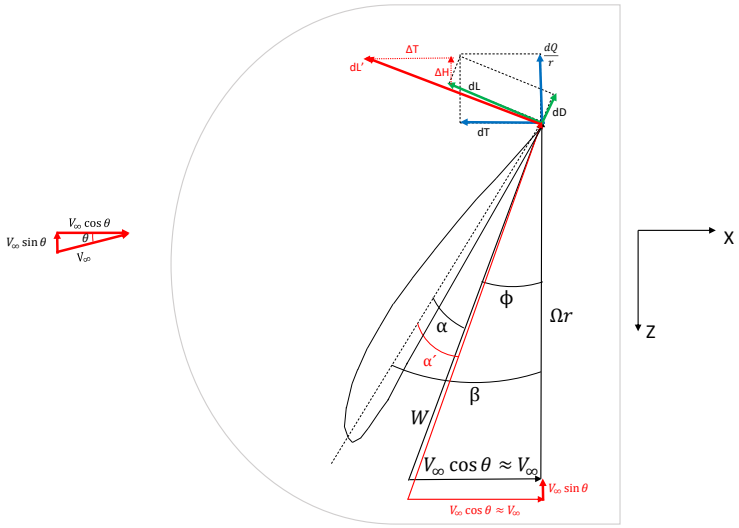

(c) Blades going down: advancing blade.

Figure 2.5: Aerodynamic forces due to pitching deflection θ (adapted from [16][26]).

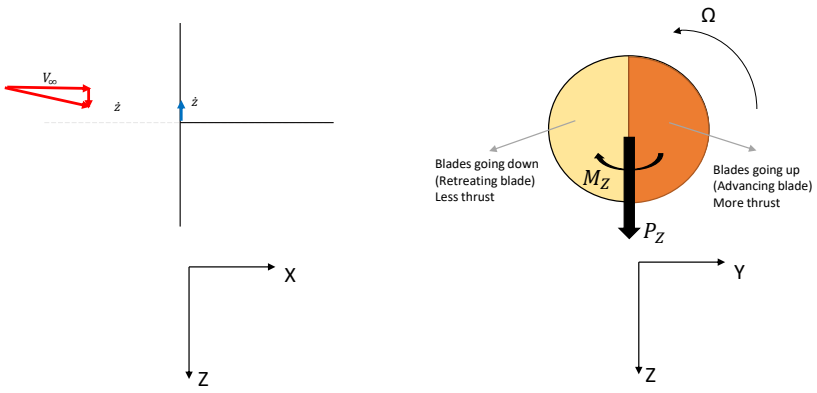

(a) Propeller with transverse linear velocity.

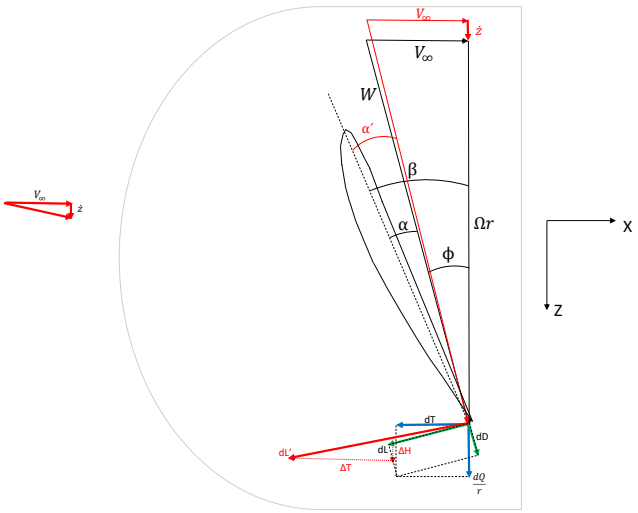

(b) Blades going up: advancing blade.

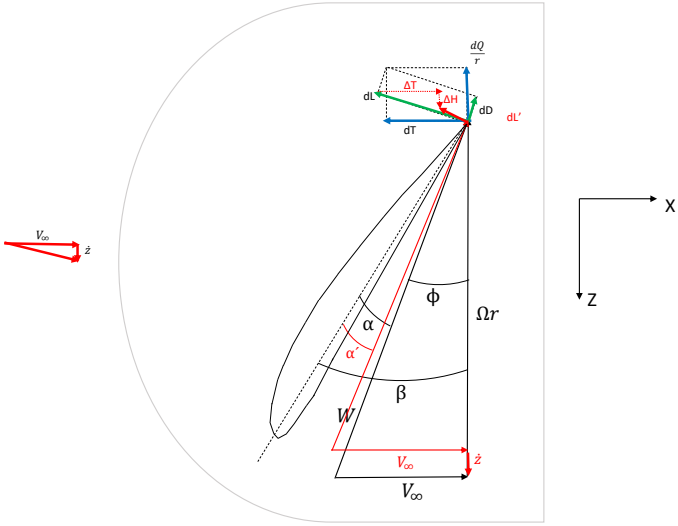

(c) Blades going down:retreating blade.

Figure 2.6: Aerodynamic forces due to a transverse linear velocity $\dot{z}$ (adapted from [16][26]).

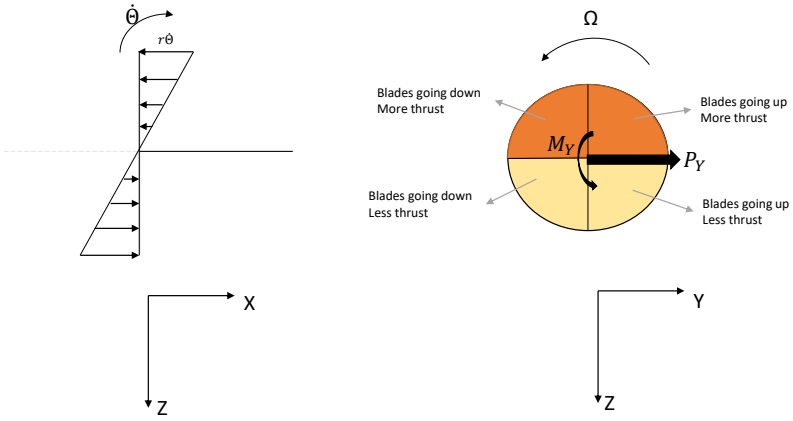

(a) Propeller pitching

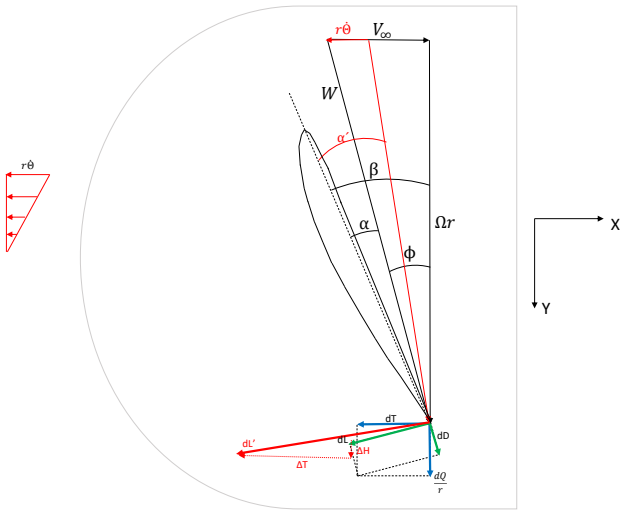

(b) Upper half section of the rotor.

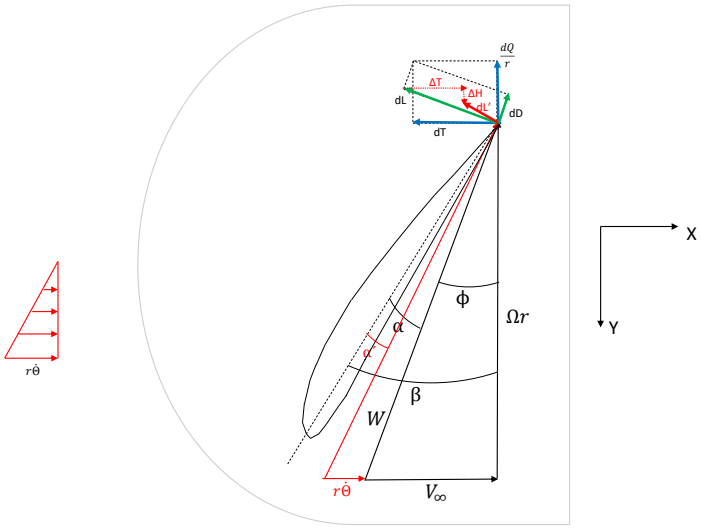

(c) Lower half section of the rotor.

Figure 2.7: Aerodynamic forces due to pitching rate $\dot{\theta}$ (adapted from [16][26]).

The case of gyroscopic induced propeller aerodynamics is analogous to that of a propeller immersed in non-homogeneous flow. When a propeller is immersed in a non-homogeneous flow, cyclically (azimuthally) varying propeller loads develop; the in-plane resultant of these loads are called 1P loads or in-plane airloads. Under certain circumstances, especially at high speed, 1P loads may represent a significant portion of the propeller thrust [79][78][30]. 1P loads can be decomposed into a vertical component and a horizontal component.

The origin of vertical 1P loads can be explained via quasi-steady aerodynamics. Consider a propeller that is at an angle of attack with respect to the incoming flow. One half of the propeller (the advancing side) sees greater angle of attack and speeds than the other half (the retreating side). In consequence, the advancing blade generates more lift and drag, and thus more thrust; when projected vertically onto the rotation plane the advancing half of the propeller gives rise to vertical forces higher in magnitude and opposite in sign than those from the retreating half. As a result, there is a net force over the entire propeller that is directing upwards. This is equivalent to what it is illustrated in Figure 2.5.

On the other hand, horizontal 1P loads have their origin in complex unsteady aerodynamic effects caused by the variations in induced velocity across the propeller disc. As the advancing half of the propeller generates more thrust, this region sheds wakes with more circulation which induces greater velocities than the retreating half. This causes the region that is closer to the wake shed by the blades in the advancing side to have larger induced velocities. As a result, blades neighbouring this region operates at a smaller angle of attack and hence, lower airloads are generated. In consequence, a net horizontal force appears in the propeller plane [79].

Methods to predict propeller aerodynamics

Whirl flutter analyses require the prediction of in-plane propeller aerodynamic forces and moments that arise due to gyroscopic motions. Traditionally, in the investigation of propeller whirl flutter, these forces are expressed in terms of aerodynamic derivatives with respect to pitch/yaw deflections and pitch/yaw deflection rates. The aerodynamic derivatives may be measured from wind tunnel tests [6] or computed analytically. Well-known analytical methods are those developed by Ribner [91, 92] and Houbolt and Reed [45]. Both methods are based on quasi-steady aerodynamics and may be supplemented by corrections for wake effects. Ribner's method is more refined than that of Houbolt and Reed's but the latter appears to give similar results and is easier to implement, therefore, it has been widely adopted in various whirl flutter studies [93][89][15].

Higher fidelity methods that account for unsteady (wake) effects directly exist, such as the Unsteady Vortex Lattice Method [109] and the Unsteady Lifting Surface Theory [35][94][95][110].

For tiltrotor whirl flutter analyses, well-known propeller aerodynamic models are found in Johnson [52] and in Kvaternik [61]. Kim et al. [59] compares Johnson's method to that of Greenberg[31]'s unsteady aerodynamic method. Similarly, Gennaretti and Greco [29] compares Theodorsen[106]'s unsteady aerodynamic method with the boundary integral equation of three-dimensional potential, unsteady flows, solved with the Boundary Element Method (BEM).

2.4. Modelling of Propeller Whirl Flutter

Propeller whirl flutter has been investigated analytically, numerically, and experimentally. Present section reviews the former two.

2.4.1. Analytical Modelling

Analytical models on propeller whirl flutter may be classified according to whether wing flexibility and blade flexibility are included.

Early analytical investigations on propeller whirl flutter excludes both wing and blade flexibility. The classical whirl flutter solution is derived under these assumptions; this is presented in Chapter 6. Related work are found in Reed III and Bland [88], Sewall [97], Houbolt and Reed [45], and Bennett and Bland [6]. Investigations show that propeller whirl flutter only occur in the backward whirl mode and the parameters that influence whirl flutter stability the most are the nacelle-engine stiffness, nacelle-engine structural damping, the propeller pivoting length, and the propeller advance ratio. The effects of these parameters are explained in Section 2.6.

Influence of blade flexibility

The inclusion of flexible blades or blades with flapping hinges into the analytical models lead to whirl flutter developing in the forward whirl mode [86][87]. Whirl flutter with flexible blades has mostly been studied with the development of tiltrotors. Johnson [52][53] presents a mathematical model to study the stability of a rotor with flexible blades in forward flight. Kvaternik [61] presents a comprehensive mathematical model to study aeroelasticity in tiltrotors. An energy balance equation is derived by Young and Lytwyn [113] to highlight the fact that whirl flutter solely occurs in the backward whirl mode if only the pylon/nacelle pitch and yaw degrees of freedom are considered.

More recently, Kunz [60] presents a unified mathematical model to analyse whirl flutter in propellers, tiltrotors and helicopters. Wing flexibility is ignored but the additional degrees of freedom introduced by tiltrotor and helicopter rotors are included. Results show that thrust has a destabilizing effect on propeller whirl flutter and helicopter rotor in forward flight but has a stabilizing effect on tiltrotors.

Influence of wing flexibility

The influence of wing flexibility on whirl flutter can be stabilizing or destabilising depending on system parameters [86, 87]. The main findings are illustrated in Figure 2.8.

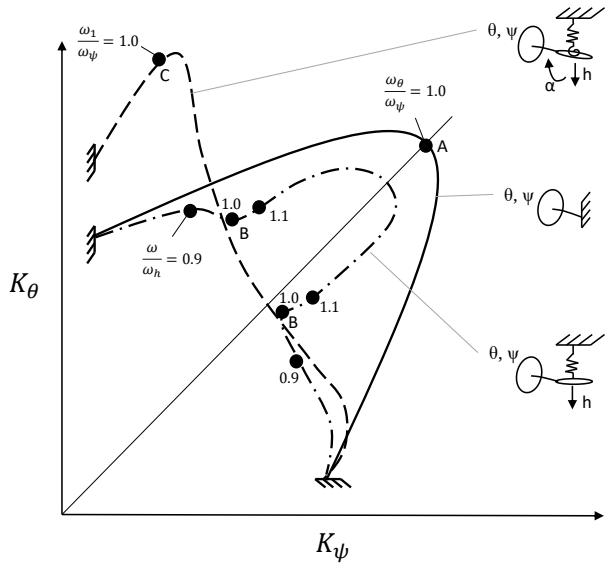

Figure 2.8: Influence of wing flexibility on whirl flutter (adapted from [86]).

Figure 2.8 shows whirl flutter boundaries of a propeller in three configurations: propeller on a rigid structure, propeller on a wing with bending motions, and propeller on a wing with bending and torsional motions.

- When the wing is assumed to be rigid, the most critical point is found on equal pitch and yaw stiffness (point A). The curve terminates in two extremes which correspond to the boundaries for static divergence.

- For the case of a propeller on a wing with bending motions or vertical translations, the influence of the wing on whirl flutter is always stabilizing and the effect is most pronounced when whirl flutter frequency (ω) coincide with the wing bending frequency (ω_h); these are the points B in Figure 2.8. It is suggested that the stabilising effects of the wing is caused by wing aerodynamic damping forces.

- Lastly, when wing bending and torsion motions are considered, the effects of the wing on whirl flutter is not always stabilising. If the wing fundamental coupled frequency (ω_1) equals the nacelle yaw frequency (ω_ψ) the effects of the wing become destabilising. A general conclusion is that when the nacelle yaw frequency is close to the wing torsion frequency the wing has a destabilizing effect.

Analytical models of a propeller with rigid blades attached to a flexible wing are presented in Bennett and Bland [7], Smith [101], and Yang et al. [111].

The propeller-wing model derived in present work (Chapter 8) is largely based on the mathematical model of Bennett and Bland [7].

Other models

Two-bladed rotors create a polar asymmetry which introduce periodic coefficients in the equations of motion. This has been treated in studies on proprotors such as Gennaretti and Greco [29] and Singh and Chopra [98].

There is limited published material concerning propellers in a pusher configuration, there is the work of Nitzsche [73, 74, 75] and Nitzsche and Rodrigues [76] who analysed the whirl-flutter problem of an advanced turboprop configuration with two pusher propellers positioned at the aircraft fuselage cone.

A non-linear version of the classical propeller whirl flutter model of Houbolt and Reed [45] is presented by Mair et al. [65].

2.4.2. Numerical Modelling

Analytical models, although very suitable for gaining physical insights, deal with limited degrees of freedom, simple geometries and many simplifying assumptions regarding propeller and wing aerodynamics. With the growing interest on tiltrotors, wingtip-mounted propellers and distributed-propeller configurations, recent studies employ more comprehensive numerical tools to account for the more complex configurations and to obtain higher fidelity solutions.

Numerical modelling of whirl flutter may be conducted with Finite Element Methods, Multibody Dynamics, and CFD/CSM codes.

Analyses carried out using Finite Element Method software rely on additional preprocessor tools to compute propeller aerodynamics, i.e. MSC/NASTRAN with PROPF-REV2 [93] or PROPFM [14][15], and ZAERO with ZUV and ZWHIRL [90][109]. PROPF-REV2 and PROPFM are based on the method developed by Houbolt and Reed [45].

Many whirl flutter studies have been carried out with Multibody Dynamic tools. The software packages used by various authors are: SIMPACK aided by PROPPY for propeller aerodynamics [90], Dymore [38–44][69], CAMRAD II [38–44][69], and Modelica [89].

2.5. Whirl Flutter on Tiltrotors

Whirl flutter on tiltrotors is characterised by the coupling of wing elastic motions with flexible proprotors [54]. Early findings on tiltrotor whirl flutter are presented in Reed and Bennett [85], Kvaternik [61], Johnson [52], and Kvaternik and Kohn [62]. Tiltrotor whirl flutter is more difficult to predict and analyse by means of simple analytical methods. From the aeroelastic point of view, the main differences between propeller whirl flutter and proprotor whirl flutter lie in the rotor design and the position and orientation of the rotor in the airframe.

Tiltrotors have complex rotor designs that usually include a swashplate, a gimbal, blade underslung, and blade preconing, amongst others. These features result in additional degrees of freedom that might couple together and lead to whirl flutter. Hence, proprotor whirl flutter and propeller whirl flutter may differ in nature.

What's more, tiltrotors have long-flexible blades which add two extra vibration modes (blade flapping and lead-lag motions) to its structural-dynamic analysis. However, when modelling turboprop propellers, the condition of rigid blades is usually assumed, as in most cases, the natural frequencies of propeller blades are much higher than the frequencies of the propeller-engine mount. Blade deformations are only considered in large propellers such as those found in military turboprop transport aircraft. Including blade flexibility adds additional degrees of freedom into the mathematical models and, in turn, more complex equations of motion. Physically, blade flexibility influences the inertial and aerodynamic characteristics of the rotor system.

Moreover, proprotors are positioned at the wing tips of tiltrotors where they experience strong aerodynamic interactions with the wing tip vortices. In addition, proprotors are usually rigidly attached to the wing via pylon, which means that the rotor follows wing deformations/rotations and face high inflow angles, especially in the transition from helicopter to forward flight regime. The rotors experience stall and complex

unsteady aerodynamic effects and the determination of aerodynamic derivatives must rely on complicated numerical simulations or experimental data.

Aircraft with wingtip-mounted propellers may seem comparable to tiltrotors. However, the propeller blades are not as flexible so the assumption of rigid blades is generally still valid. Furthermore, the wing in tiltrotors are generally thicker and shorter and thus, has higher torsional stiffness than current wings with distributed propulsion and wingtip-mounted propellers which tend to have higher aspect ratio and thinner airfoils [38].

Suffice to say that whirl flutter on tiltrotors is a much more complex phenomenon than that of propellers; because whirl flutter may come to limit the cruise speed of the tilt-rotors in airplane mode [29] it has triggered extensive investigations in this area and remains an active topic of research. Substantial literature is available and it deserves a study of its own, therefore, it will not be further explored in this report.

2.6. Parameters that influence Whirl Flutter

This section presents trend studies of parameters that influence whirl flutter stability on an isolated propeller with rigid blades. These are found in Reed III and Bland [88], Sewall [97], Houbolt and Reed [45], Kvaternik and Kohn [62], and are compiled in Reed III [86, 87], Försching [26], Cecrdle [16], and Bielawa [8].

The most influencing parameters are: nacelle stiffness in pitch and yaw (K_θ, K_ψ), pitch-yaw stiffness ratio (K_θ / K_ψ), nacelle structural damping (g_θ, g_ψ), pivot location (a), propeller rotational speed Ω, airspeed V_∞, and propeller advance ratio ($J = \frac{V_\infty}{\Omega R}$) [16]. Trend studies of these parameters are illustrated in Figure 2.9-Figure 2.16.

Influence of the propeller advance ratio on whirl flutter stability is shown in Figure 2.9. The stability boundaries correspond to a constant speed propeller. Increasing propeller advance ratio is destabilizing. The system is most prone to whirl flutter when there is the same pitch and yaw stiffness. Higher stiffness is stabilizing. For each advance ratio, there is a minimum stiffness level below which the system will diverge. If the stiffness in one direction is high enough, then the system will not experience whirl flutter even if the stiffness level in the other direction is zero. This may be explained by the gyroscopic coupling action: the system wants to go unstable in the direction of least stiffness but it is restrained from going by gyroscopic coupling with the maximum stiffness [45]. Houbolt and Reed [45] points out that structural damping changes the shape of these stiffness boundaries.

Influences of structural damping and propeller-hub-pivot-point distance are shown in Figure 2.10. Including small amounts of structural damping from nil greatly increases the calculated stable region. Moving forward the pivot location (lower values of a) causes an increase in the required stiffness ($K_\theta \sim \omega_\theta$) to avoid whirl flutter.

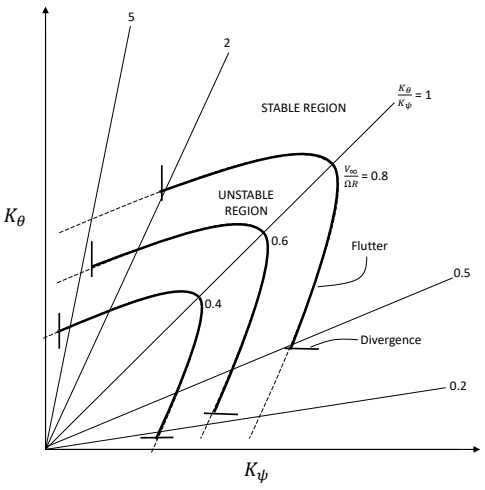

Figure 2.9: Effect of the propeller advance ratio and stiffness (adapted from [45]).

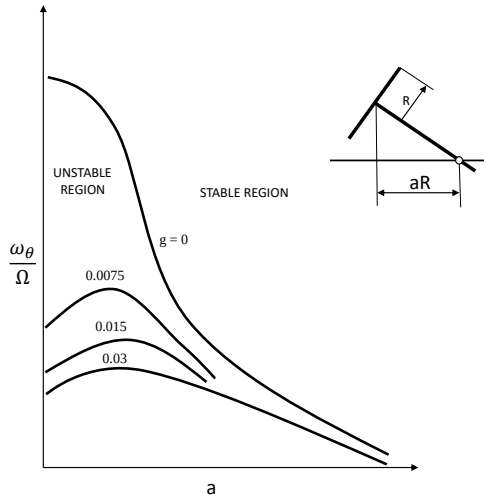

Figure 2.10: Effect of structural damping and propeller hub-pivot point distance (adapted from [45]).

Figure 2.11 shows whirl flutter stability in terms of the root-mean-square stiffness ($K_{RMS} = \sqrt{\frac{K_\theta^2 + K_\psi^2}{2}}$) and the forward velocity for various pylon pitch and yaw stiffness ratio. For small values of K_{RMS}, the influence of

stiffness asymmetry on whirl flutter stability is very small. For higher values of K_{RMS}, the influence of stiffness asymmetry is higher. Nevertheless, the assessment of whirl flutter using equal pitch and yaw stiffness is more conservative as observed in Figure 2.9.

Figure 2.12 shows the effect of pylon pitch and yaw structural damping ratio. For a symmetrical system in pylon stiffness ($\frac{K_\psi}{K_\theta} = 1$), structural damping ratio ($\frac{g_\psi}{g_\theta}$) has barely any influence on the whirl flutter stability. As the pitch-yaw stiffness becomes more unequal, more damping is needed in the direction of lower stiffness.

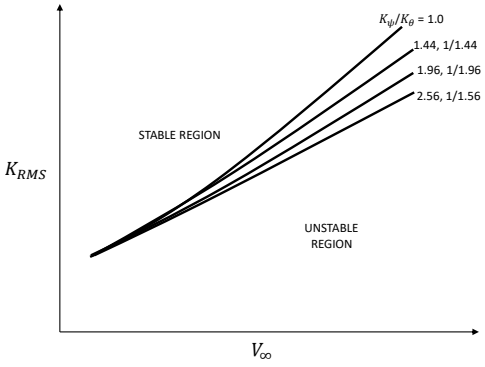

Figure 2.11: Effect of stiffness ratio for unit damping ratio (adapted from [88]).

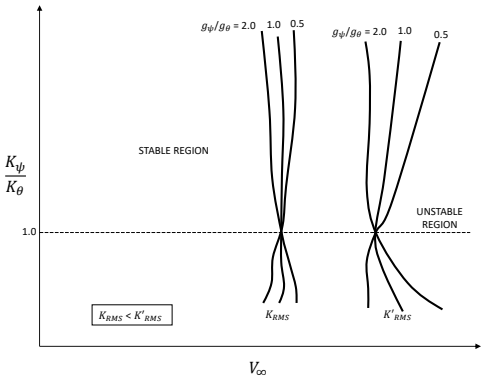

Figure 2.12: Effect of damping ratio (adapted from [88]).

Figure 2.13-Figure 2.15 illustrate examples of whirl flutter boundaries of three distinct cases: constant rotational speed, constant advance ratio, and constant pitch and yaw stiffness, respectively.

Stability boundaries with constant propeller rotational speed are shown in Figure 2.13. The lower the air velocity the lower the stiffness required to avoid flutter or divergence. At low air speeds, flutter is the limiting factor while at high air speeds, divergence becomes the limiting factor.

Figure 2.14 shows stability boundaries for a propeller with fixed blade angle — in windmilling mode, such propellers are found in most wind tunnel tests. The required stiffness is proportional to the square of the airspeed. Divergence occurs after the onset of whirl flutter.

Stability boundaries with constant pitch and yaw stiffness are shown in Figure 2.15. For high propeller revolutions, whirl flutter is the limiting factor and the flutter speed is not sensitive to the rotational speed; for lower propeller rotations, flutter speed becomes sensitive to the rotational speed; and for very low propeller revolutions, divergence becomes the limiting factor.

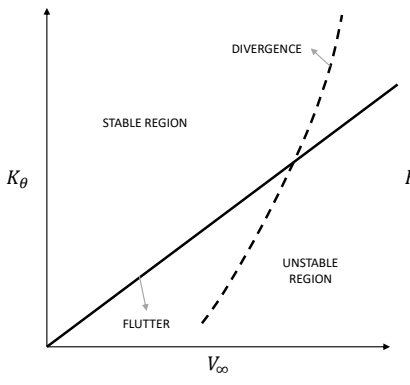

Figure 2.13: Ω = constant (adapted from [45][16]).

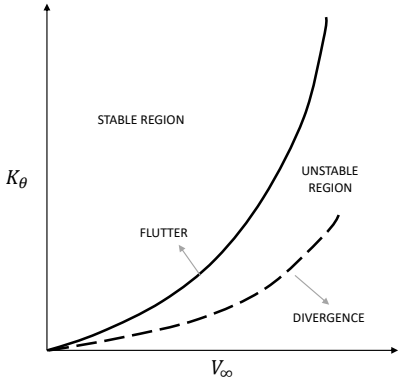

Figure 2.14: J = constant (adapted from [45][16]).

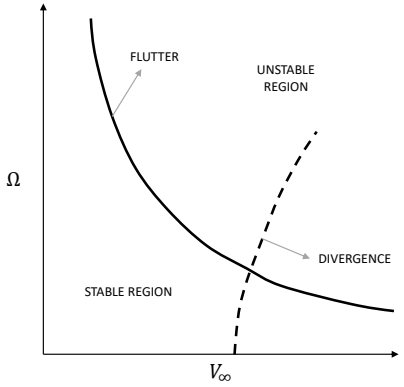

Figure 2.15: K_ψ = constant, K_θ = constant (adapted from [45][16]).

Finally, Figure 2.16 shows the effect of thrust. For high advance ratios, the stiffness required to avoid whirl flutter is very similar to that of a windmilling propeller. Hence, as first approach, it seems acceptable to analyse whirl flutter on windmilling propellers. For small advance ratios, the assumption no longer holds.

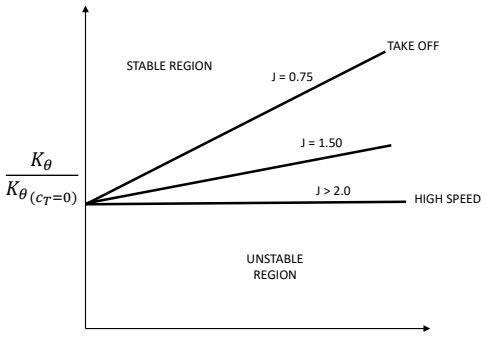

Figure 2.16: Influence of thrust coefficient (adapted from [85]).

2.7. Wing Flutter

Flutter is a dynamic instability of lifting surfaces associated with the interaction of aerodynamic, elastic, and inertial forces. It is a type of self-excited vibration characterised by oscillations with increasing amplitude; it has the potential to cause structural damage or failure. The phenomenon arises from fluid structure interactions through which energy is extracted from the air stream. Flutter speed is the minimum airspeed at which the oscillations have constant amplitude, right before they become divergent. The frequency of the oscillations at this critical speed is designated as the flutter frequency.

Most wings have much higher chordwise stiffness than spanwise stiffness. Hence, for a wing without any control surfaces, it is sufficient to define the elastic deformation of any wing cross section by the vertical displacement of the cross sectional elastic centre and the angle of rotation (torsion) about this centre. The spanwise distribution of the vertical displacements is approximately in phase, so is the spanwise torsional distribution. However, the vertical displacement is out of phase from the torsional movement and both may be out of phase from the applied aerodynamic loads. This phase difference is responsible for the wing to extract energy from the airstream and result in flutter [27]. This kind of flutter is caused by bending-torsion coupling and it is the type of flutter treated in present work (Chapter 7).

The effect structural parameters of the wing on the flutter critical speed depends on the specific combination of structural parameters. Some examples of flutter analysis show that flutter speed is more sensitive to the individual change in torsional stiffness than in bending stiffness. Increasing bending stiffness alone will initially reduce flutter speed until a minimum, when the (uncoupled) bending frequency equals the (uncoupled) torsional frequency because of mode coupling between bending and torsion; further increase in bending stiffness from this point will then, increase the flutter speed. Usually, having the inertia and elastic axes close to the line of aerodynamic centres increases the critical flutter speed as it would break the inertia and aerodynamic couplings. It is beneficial to arrange the mass and stiffness parameters so that the nodal lines of the lower free vibration modes are not close to the three-quarter chord line [9]. The critical flutter frequency usually lies between the two lowest free vibration frequencies [27].

2.8. Wingtip-mounted Propellers

Recent developments in electric propulsion have sparked a renewed interest in wingtip-mounted propellers. The use of wingtip-mounted propellers have often been relegated to the background due to aeroelastic problems and difficulties to meet one-engine-out requirements. However, scaling down the propeller and/or using distributed electric propulsion seem to resolve these issues.

2.8.1. Aerodynamic benefits of wingtip-mounted Propellers

For a finite length wing, when lift is produced the region above the wing has lower pressure than the region below the wing. Near the tip of the wing, air is forced from the region of high pressure to the region of low pressure forming a flow that curl around the wingtip which are called wingtip vortices. Such vortices have a circulatory motion and trail inboard and downwards carrying the surrounding air along with them (see Figure 2.17). The presence of these wingtip vortices induce a small downward velocity component or "downwash" near the wing. This downwash decreases the effective angle of attack which in turn decreases the total lift produced by the wing and creates additional drag known as induced drag. One interpretation of induced drag states that the wingtip vortices contain large amounts of translational and rotational kinetic energy which must be provided by extra power from the engine. If this kinetic energy is not utilized the extra

power provided by the engine is essentially lost [5].

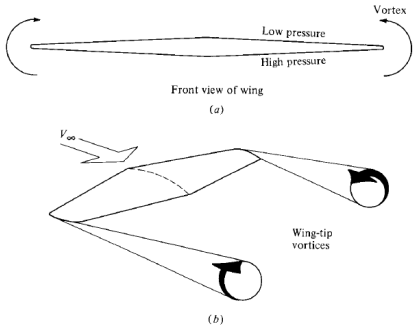

Figure 2.17: Schematic of wing-tip vortices on a finite wing [4].

The idea of placing a propeller at the wing tip is to somehow utilize the translational and rotational kinetic energy from the wingtip vortices that is otherwise lost. Snyder Jr. and Zumwalt [102] showed that placing a tractor propeller at the wingtip and turning the rotor in the opposite direction to that of the wing's trailing vortex decreases the wing drag coefficient while increasing the wing's maximum lift coefficient and effective aspect ratio. Other authors have proven that a pusher propeller experiences similar beneficial interactions such as reduction of the wing induced drag and reduction of the required engine shaft power [84][49]. Major drawbacks of a wingtip mounted propeller configuration stem from aeroelastic problems, high wing mass required by higher inertia loads, and difficulty of controlling the aircraft for one-engine-out operation [100]. Such drawbacks can be lessened and even prevented by employing smaller propellers and distributed propulsion aided by electrification of the power plant.

2.8.2. Propeller-Wing Aerodynamic Interference Effects

Propeller-wing aerodynamic interference effects are not restricted to the wing tip. Regardless of the spanwise location of the propeller, due to aerodynamic interference, an installed tractor propeller experiences *upstream effects* from the wing; whilst the wing experiences *downstream effects* from the tractor propeller. In the former, the wing changes the flow field upstream the propeller by introducing an upwash. As a result, the propeller blades perceive periodic variations in angle of attack which leads to the generation of unsteady aerodynamic loading. In the latter, the propeller yields a slipstream of increased dynamic pressure, turbulence and swirl. This increases the dynamic pressure of the air around the wing, changes the angle of attack perceived by the wing and the boundary layer properties on the wing. As a consequence, the spanwise lift distribution over the wing is modified. Figure 2.18 illustrates three spanwise lift distributions: without any propeller (prop off), with a tractor propeller rotating inboard up (prop on-inboard up), and with a tractor propeller rotating outboard up (prop on-outboard up). As it can be seen, modifications are not restricted to wing regions submerged within the propeller slipstream. With respect to the "prop off" setting, the lift is increased in the up-going blade side (W-II/W-III) and decreased in the down-going blade side (W-III/W-II) [20].

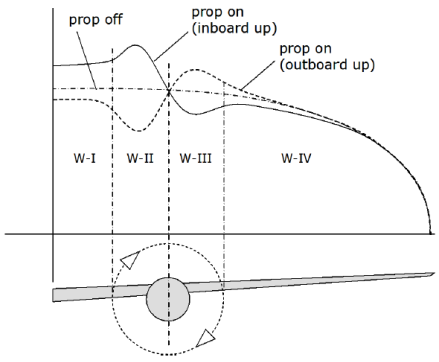

Figure 2.18: Schematic of the modified spanwise lift distribution due to propeller-wing aerodynamic interference effects [107].

Further details of propeller-wing aerodynamic interaction and the physics behind are reported by Johnson et al. [50][51][55] and more recently, by Veldhuis [107] and Sinnige [99]. Investigation on the aerodynamic interaction between distributed propellers and wings is treated in Fischer [25].

2.8.3. Effects of wingtip-mounted Propellers on Wing Dynamics

Most investigations on the aeroelastic characterization of wintip-mounted propeller-wing configurations focus on the dynamic behaviour of the wing per se, assuming rigidly attached propellers. In fact, propeller whirl flutter does not happen if the propeller with rigid blades is rigidly attached to the wing, i.e. the stiffness of the engine mount is much higher than the wing's lowest bending/torsion stiffness. In this case, interest lies mainly towards determining the effects caused by the presence of a propeller acting as an added inert mass and the effects of the propeller loads transmitted to the aircraft.

Omitting the propeller loads the presence of a tip-propeller on the wing can be regarded as an additional inert mass positioned at the wing tip. This configuration can be treated analogously to that of a wing with tip stores. Tip stores are placed on aircraft wings as tip tanks or weapons [34]. Another analogy is found on wings with tip-tanks, only that in this case, the tip-tank weight decreases as fuel is transmitted to the main fuel tank [17].

A summary of the propeller loads transmitted to aircraft are shown schematically in Figure 2.19. The loads are grouped into aerodynamic loads and inertial loads. The former is comprised of the total forces and moments acting on the propeller hub and propeller slipstream effects that modify the lift distribution over the surface behind the propeller. The latter consists of inertial forces/moments due to motions of propeller centre of gravity and gyroscopic effects due to the motion of blades around the propeller centre of gravity [105].

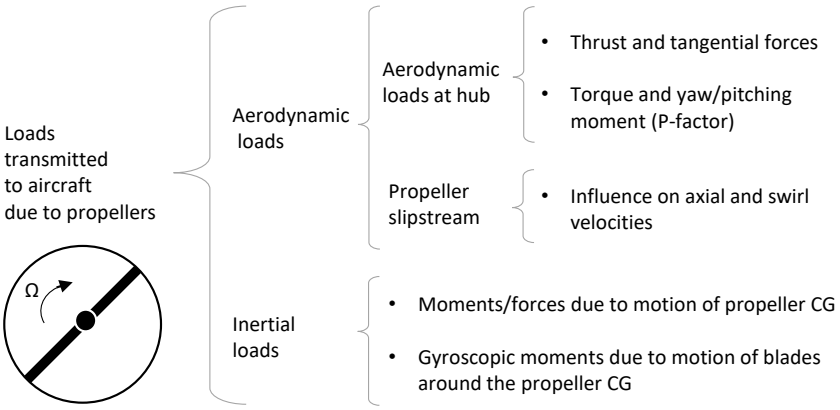

Figure 2.19: Summary of propeller loads transmitted to aircraft (adapted from [105]).

Cravana et al. [19] conducted numerical and experimental investigations of a flexible wing with distributed electric propulsion system, focusing on the effects of the spanwise location and the number of propellers on the modal frequencies of the wing. Adding propellers essentially changes the mass and loads distribution of the wing. The study demonstrates that edgewise and torsional frequencies are the most affected and there is a stronger coupling between torsional and bending modes when inertial loads are increased near wing tip.

Early studies on whirl flutter shows that thrust may be negligible, however, its influence on the dynamic behaviour of a flexible wing is of significance. The effect of thrust on high aspect ratio wings has been investigated by Hodges et al. [37] who focused mainly on the effects of thrust on bending-torsion flutter. Results suggest that thrust can have stabilising or destabilising effects on wing dynamics depending on the ratio between wing bending stiffness to torsional stiffness. Also, an increase of flutter speed of 11% has been determined when including thrust; this highlights the importance of considering thrust in the analysis of the dynamic behaviour of a flexible wing. However, due to time constraints, this is not explored in present work.

Aeroelastic characteristics of wings with rigidly attached tip-propellers have been studied analytically and numerically by Zhang et al. [114], numerically by Guruswamy [33], and experimentally by Chajec et al. [18].

2.9. Concluding Remarks

Following the literature study, it can be concluded that:

1. Recent studies on whirl flutter employ numerical methods such as Finite Element Methods, Multibody Dynamics, and CSD/CSM codes. There exist mathematical models that predict good wing/whirl flutter speeds but they are all limited to the analysis of isolated propellers (propellers on a rigid back-up structure) or a wing with propeller/s in the conventional lay out (i.e. wings with inboard propeller/s). Investigations specifically targeting wing/whirl flutter in wingtip-mounted propellers and/or distributed propellers have been carried out with Finite Element Method and Multibody Dynamics codes.

2. For the analysis of a wing with distributed propellers during the early stages of aircraft design, it is advantageous to have an analytical model that allows adding multiple propellers systematically.

3. For whirl flutter calculations in small/mid-size propellers, the assumption of rigid blades is acceptable. This is generally not the case in tiltrotor whirl flutter.

4. Several analytical methods for predicting the aerodynamics of a propeller undergoing gyroscopic motions are available. The method presented by Houbolt and Reed [45] has been widely used in propeller whirl flutter analyses. A good understanding of Houbolt and Reed's method is necessary to determine its range of applicability.

5. The influence of flexibly mounted propellers on wing flutter is inconclusive. The influence of wing flexibility on whirl flutter can be further explored. An investigation on how whirl flutter develops in a propeller-wing configuration seems necessary.

6. In practice, whirl flutter may onset with increasing airspeed, increasing propeller rotational speed, or reducing nacelle-engine stiffness. The main parameters that affect whirl flutter are nacelle-engine stiffness, nacelle-engine structural damping, propeller pivoting length, rotational speed, airspeed and advance ratio. Their influence on an isolated propeller is well studied, however, their effects on wing/whirl flutter when the propeller is attached to a flexible wing is unclear.

7. Most investigations on propeller whirl flutter have ignored propeller-wing aerodynamic interference effects. In the case of wingtip-mounted propeller-wing configurations, this assumption may be too simplistic.

8. In early studies, thrust has proved to be negligible in propeller whirl flutter analyses. However, as wings become more flexible, the influence of thrust on wing/whirl flutter may no longer be negligible and should be further explored.

Due to time constraints, present work targets the points (1)-(6). Points (7) and (8) are recommended for future work.

3

Project Definition

3.1. Research Question, Aims and Objectives

The project goal is to develop an analytical model to be used to predict the onset of wing/whirl flutter in wingtip-mounted propeller and distributed-propeller wing configurations.

The research objective is to improve the understanding of the aeroelastic behaviour of a cantilever wing with flexibly attached tractor propeller/s by predicting wing/whirl flutter behaviours using an analytical method.

Following the research objective, two main aspects are to be investigated in present thesis project: the interaction between propeller/s and a cantilever wing from an aeroelastic standpoint and the influence of general propeller-wing structural design parameters on wing/whirl flutter stability. These parameters are: nacelle stiffness, nacelle structural damping, propeller mass, propeller pivoting length, mass moment of inertia about the axis of rotation, and propeller advance ratio.

The research questions and sub-questions are:

1. What are the aeroelastic effects of propeller/s on a catilever wing?
   (a) How does propeller gyroscopic effects influence the aeroelastic behaviour of the wing?
   (b) What is the influence of propeller aerodynamics?
2. What are the effects of a cantilever flexible wing on propeller whirl flutter?
   (a) How does wing flexibility influence propeller whirl flutter?
   (b) What is the influence of wing aerodynamics?
3. What are the aeroelastic effects of placing a propeller on the wing tip?
   (a) How does the spanwise location of the propeller influence wing/whirl flutter?
   (b) What are the effects of the main propeller-wing structural design parameters on wing/whirl flutter stability?

Present research is constrained to:

- Tractor propeller/s with ≥ 3 rigid blades.
- Propeller/s operating in windmilling conditions → there is no propeller thrust.
- Propeller-wing aerodynamic interference effects are ignored.

3.2. Project Outline

Two main areas of work are defined:

- Derivation and validation/verification of a method to predict propeller aerodynamics and three aeroelastic models for the prediction of wing/whirl flutter.
- Analysis of propeller-wing configurations using the derived aeroelastic models.

Methodology

First, a method to model the aerodynamics of a propeller undergoing pitching and yawing motions is derived anew, this is the Houbolt-Reed method [45].

Subsequently, three aeroelastic models are derived:

- Isolated propeller or propeller flexibly attached to a rigid wing → classical propeller whirl flutter solution.

  The model only includes the pitch and yaw degrees of freedom of the propeller.
- Flexible cantilever wing → classical wing bending-torsion flutter and divergence.

  The structural model is a linear dynamic Euler-Bernoulli beam model and the aerodynamic model is represented by a combination of strip theory and two-dimensional Theodorsen's unsteady aerodynamic theory formulated in time domain using a two-finite state approximation.
- Propeller/s flexibly mounted on a flexible cantilever wing → whirl/wing flutter and divergence.

  It combines the previous two models.

The first two aeroelastic models are well-known models widely available in literature. The novelty in present work lies largely in the last model.

Analysis

Once the aeroelastic models have been correctly implemented, appropriate case studies and parametric studies are performed for simplified models defined from two light aircraft, namely Tecnam P2006T and NASA X-57 Maxwell.

- The case studies include three baseline models, these are: an isolated propeller, a flexible cantilever wing, and a flexible cantilever wing with an inboard propeller. Two additional propeller-wing models are analysed, these are: a flexible cantilever wing with a wingtip-mounted propeller, and a flexible cantilever wing with an inboard and a wingtip-mounted propeller.
- The parametric studies are performed on the wingtip-mounted propeller model with respect to: nacelle stiffness, nacelle structural damping, propeller mass, propeller pivoting length, mass moment of inertia about the axis of rotation, and propeller advance ratio.

Outline diagram

The outline of present report is illustrated in Figure 3.1. Chapter 1 introduces the graduation project. Chapter 2 presents the state of the art of propeller wing/whirl flutter. Propeller aerodynamics is treated in Chapter 4. The aeroelastic models are derived in Chapter 5-Chapter 8. Chapter 9-Chapter 10 explain the case study results. Chapter 11 presents the parametric studies performed on the wingtip-mounted propeller-wing model. Finally, conclusions and recommendations are given in Chapter 12.

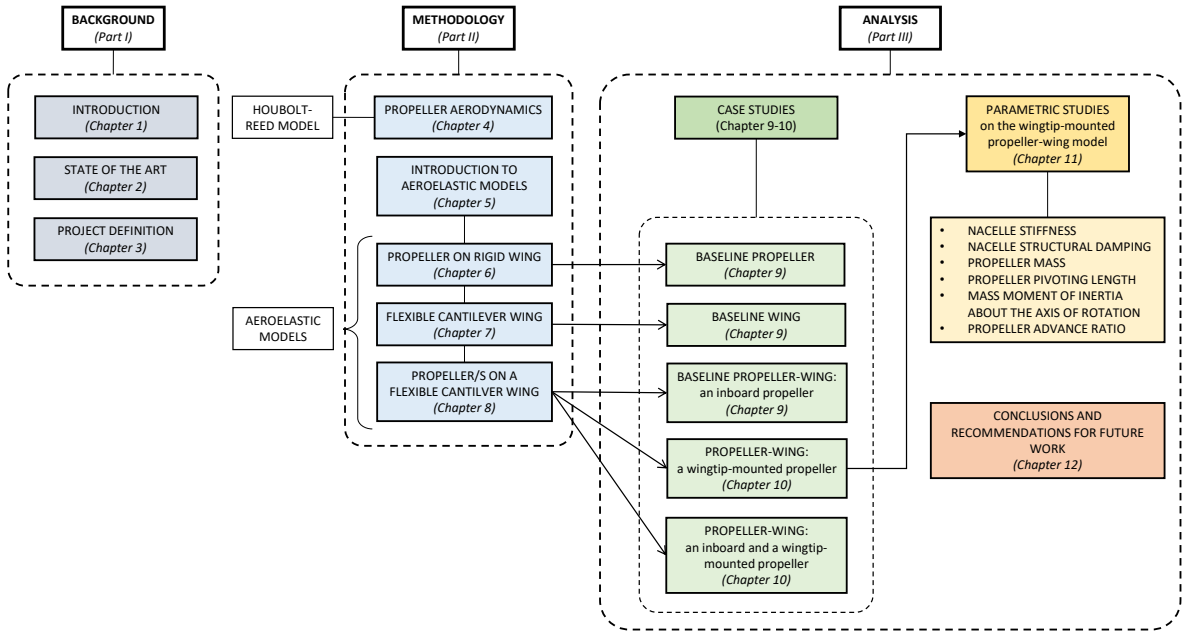

Figure 3.1: Outline of the thesis.

II

METHODOLOGY

4

Propeller Aerodynamics

A propeller under rotating and precessional motions faces non-uniform flow which create azimuthally varying aerodynamic loads. These loads result in in-plane vertical and horizontal forces and moments acting on the rotor hub. They can be expressed in terms of propeller aerodynamic derivatives.

Previous work has shown that measured propeller aerodynamic derivatives lead to adequate predictions of propeller whirl flutter boundaries [6]. The use of analytically predicted propeller aerodynamic derivatives leads to more conservative whirl flutter boundaries of similar trends but with appreciable differences in magnitude in some instances [6]. Good prediction of propeller aerodynamic derivatives is essential towards obtaining reliable whirl flutter boundaries.

Several methods have been developed in literature to analytically compute these propeller aerodynamic derivatives [91][45][109]. This chapter derives anew the method of Houbolt and Reed [45] as it has been widely used in literature for propeller whirl flutter studies; the method is also explained in Bielawa [8][Chapter 11.2.2] and in Cecrdle [16][Chapter 5.4]. A full understanding of the method is required so as to define its range of applicability. For the remaining of present report the method is designated as Houbolt-Reed's method.

Section 4.1 derives the Houbolt-Reed's method. Section 4.2 presents the validation and verification results.

4.1. Houbolt-Reed's Method

Houbolt and Reed [45] presents an analytical method to calculate the aerodynamics of a propeller in pitch and yaw by means of strip theory and quasi-steady aerodynamics. Corrections for compressibility effects, finite blade-length effects and unsteady aerodynamic effects are also presented.

In strip theory aerodynamics the wing (or blade in this case) is sub-divided into a set of small span-wise sections or strips. On each strip two-dimensional quasi-steady aerodynamics applies. The aerodynamic forces and moments acting on each strip are integrated along the wing span assuming no aerodynamic interaction between strips.

In order to take into account the aerodynamic perturbations caused by the propeller pitching and yawing motions three principal quantities are introduced. These are: the local geometric angle of attack change ($\dot{\alpha}$), the perturbation velocity in the propeller plane ($\dot{s}$), and the perturbation velocity out of the propeller plane ($\dot{w}$).

The derivation of Houbolt-Reed's method is explained as follows:

Consider a propeller with a rotor with radius R and a pivot point at a distance aR from the rotor hub as illustrated in Figure 4.1. The propeller is restricted in pitch and yaw motions at its pivot point by appropriate springs and dampers ($K_\theta, K_\psi, C_\theta, C_\psi,$). At an arbitrary instance, the propeller is pitched at an angle θ and yawed at an angle ψ. Assuming small angle deflections, the distance travelled by the propeller hub in accordance to Figure 4.2 is

$$\begin{aligned} a_1 &= e_\psi \psi \\ b_1 &= e_\theta \theta \end{aligned} \tag{4.1}$$

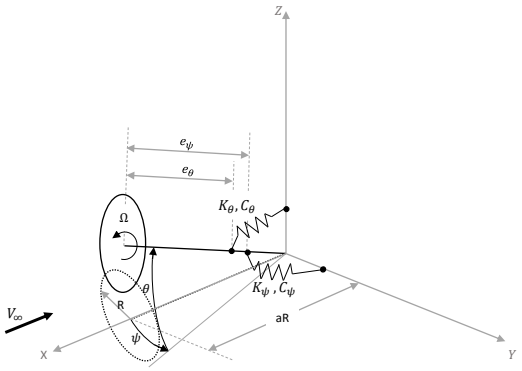

Figure 4.1: Schematic of a deflected propeller with flexible engine mounts (adapted from [8]).

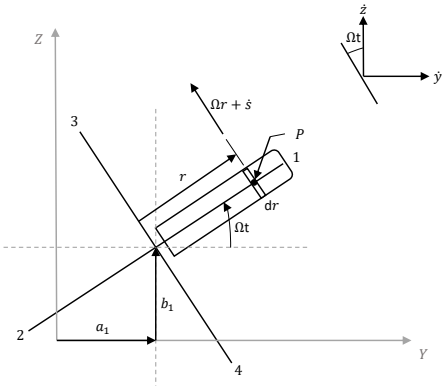

Figure 4.2: Front view geometry of deflected propeller (adapted from [8]).

where e_θ and e_ψ are the distance between the rotor hub and the elastic centres in pitch and yaw, respectively.

The coordinates of a point P at a distance r from the rotor hub in blade 1 is given by:

$$\begin{aligned} y &= a_1 + r\cos\Omega t \\ z &= b_1 + r\sin\Omega t \\ x = w &= -\psi r\cos\Omega t - \theta r\sin\Omega t \end{aligned} \tag{4.2}$$

The geometric angle of attack change due to pitch and yaw is:

$$\alpha_1 = \psi\sin\Omega t - \theta\cos\Omega t \tag{4.3}$$

The perturbation velocities are:

$$\begin{aligned} \dot{s} &= -\dot{y}\sin\Omega t + \dot{z}\cos\Omega t - \Omega r = -\dot{a}_1\cos\Omega t + \dot{b}_1\sin\Omega t \\ \dot{w} &= -\dot{\psi} r\cos\Omega t - \dot{\theta} r\sin\Omega t + \psi r\Omega\sin\Omega t - \theta r\Omega\cos\Omega t \end{aligned} \tag{4.4}$$

There is also a perturbation velocity pointing radially outwards ($\dot{r} = \dot{y}\cos\Omega t + \dot{z}\sin\Omega t$) but this component is eliminated by rotor hub reaction forces. Note that as it is defined, $\dot{s}$ and $\dot{w}$ are the velocity components of a point P in the propeller blade. The air velocity components due to perturbation are directed in the opposite direction; this is reflected in Figure 4.3.

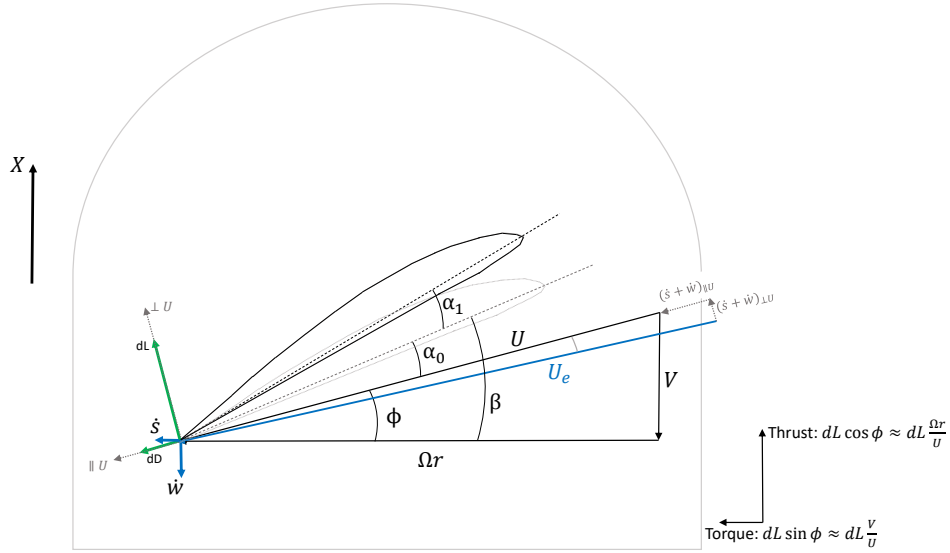

Figure 4.3: Blade section and air velocity components at point P.

The perturbation velocities, $\dot{s}$ and $\dot{w}$, have components that are in the same direction as the resultant velocity U and perpendicular to the resultant velocity U. The components that act in the direction of U have a magnitude of:

$$\dot{w}\frac{V}{U}+\dot{s}\frac{\Omega r}{U} \tag{4.5}$$

The perturbation velocities that are normal to U have a magnitude of:

$$-\dot{w}\frac{\Omega r}{U}+\dot{s}\frac{V}{U} \tag{4.6}$$

This normal component changes the effective angle of attack seen by the blade. The effective angle of attack becomes:

$$\begin{aligned}\alpha &= \alpha_0+\alpha_1+\tan^{-1}\left(-\dot{w}\frac{\Omega r}{U^2}+\dot{s}\frac{V}{U^2}\right)\approx\\ &\approx \alpha_0+\alpha_1-\dot{w}\frac{\Omega r}{U^2}+\dot{s}\frac{V}{U^2}\end{aligned} \tag{4.7}$$

where α_0 is the steady lift angle of attack expressed as the difference between the blade twist angle β and the inflow angle ϕ. Note that the term $-\dot{w}\frac{\Omega r}{U^2}+\dot{s}\frac{V}{U^2}$ is a first order approximation of the actual angle of attack change introduced by the perturbation velocities since $\sin\phi\approx\frac{V}{U}$ and $\cos\phi\approx\frac{\Omega r}{U}$ (see Figure 4.3).

The perturbation velocities also change the effective velocity sensed by the blade section. The final effective velocity becomes:

$$\begin{aligned}U_e &= \sqrt{\left(U+\dot{w}\frac{V}{U}+\dot{s}\frac{\Omega r}{U}\right)^2+\left(-\dot{w}\frac{\Omega r}{U}+\dot{s}\frac{V}{U}\right)^2}\approx\\ &\approx U+\dot{w}\frac{V}{U}+\dot{s}\frac{\Omega r}{U}\end{aligned} \tag{4.8}$$

The lift that develops on a section of blade 1 is therefore:

$$
\begin{aligned}
l &= \frac{1}{2}\rho U_e^2 ca\alpha = \\
&\approx \frac{1}{2}\rho ca\left(U + \dot{w}\frac{V}{U} + \dot{s}\frac{\Omega r}{U}\right)^2 \cdot \left(\alpha_0 + \alpha_1 - \dot{w}\frac{\Omega r}{U^2} + \dot{s}\frac{V}{U^2}\right)
\end{aligned}
\tag{4.9}
$$

where c is the section blade chord and a is the section lift-curve slope.
Ignoring the higher order terms, the lift becomes:

$$
\begin{aligned}
l &\approx \frac{1}{2}\rho ca\left(U^2 + 2\dot{w}V + 2\dot{s}\Omega r\right)\cdot\left(\alpha_0 + \alpha_1 - \dot{w}\frac{\Omega r}{U^2} + \dot{s}\frac{V}{U^2}\right) \approx \\
&\approx \frac{1}{2}\rho caU^2\left[\alpha_0 + \alpha_1 - \frac{\Omega r}{U^2}\left(1 - \frac{2V}{\Omega r}\alpha_0\right)\dot{w} + \frac{V}{U^2}\left(1 + \frac{2\Omega r}{V}\alpha_0\right)\dot{s}\right] = \\
&= \underbrace{\frac{1}{2}\rho caU^2\alpha_0}_{\text{steady-state lift}} + \underbrace{\frac{1}{2}\rho caU^2\left[\alpha_1 - \frac{\Omega r}{U^2}\left(1 - \frac{2V}{\Omega r}\alpha_0\right)\dot{w} + \frac{V}{U^2}\left(1 + \frac{2\Omega r}{V}\alpha_0\right)\dot{s}\right]}_{\text{non-steady lift}}
\end{aligned}
\tag{4.10}
$$

The non-steady lift terms also depend on the steady-state angle of attack α_0. However, $\frac{2V}{\Omega r}\alpha_0$ and $\frac{2\Omega r}{\Omega r}\alpha_0$ are generally small compared to the unit term shown in the same parenthesis. Their contribution is small and therefore, can be ignored in the computation of section lift. In fact, for a non-thrusting propeller $\alpha_0 = 0$.

Setting $\alpha_0 = 0$ means that in the absence of pitching and yawing motions, the propeller rotates at a speed Ω that forms an inflow angle ϕ with the incoming airspeed V such that $\phi = \beta$, where β is the blade angle measured from the rotor plane to the airfoil zero lift line. Therefore, aerodynamic forces are only generated when the propeller performs pitching and yawing motions, which in turn creates a geometric angle of attack α_1, an in-plane perturbation velocity $\dot{s}$, and an out-of-plane perturbation velocity $\dot{w}$. If this assumption is to be applied to every blade section, it implies that the propeller has constant pitch — that is, the blade angle β decreases towards the tip to account for the increasing rotational speed Ωr. Note that induced velocities are not considered.

Essentially, assuming $\alpha_0 = 0$ implies that only the lift generated by propeller blade motions are considered. For the remaining of the derivation, the terms multiplying the steady angle of attack α_0 will be neglected.

Substituting Equation 4.3 and Equation 4.4 in Equation 4.10, the non-steady lift that acts on a section of blade 1 is:

$$
\begin{aligned}
l_1 &= \frac{1}{2}\rho ca\left(U^2\alpha_1 - \dot{w}\Omega r + \dot{s}V\right) = \\
&= -\frac{1}{2}\rho ca\left(V^2\theta - V\dot{b}_1 - \Omega r^2\dot{\psi}\right)\cos\Omega t + \frac{1}{2}\rho ca\left(V^2\psi - V\dot{a}_1 + \Omega r^2\dot{\theta}\right)\sin\Omega t = \\
&= -f_1\cos\Omega t + f_2\sin\Omega t
\end{aligned}
\tag{4.11}
$$

The lift that develops on the other blades can be derived from Equation 4.11 by replacing:

$$
\begin{array}{llll}
\text{blade 2:} & \Omega t & \text{by} & \Omega t + \pi \\
\text{blade 3:} & \Omega t & \text{by} & \Omega t + \dfrac{\pi}{2} \\
\text{blade 4:} & \Omega t & \text{by} & \Omega t + \dfrac{3\pi}{2}
\end{array}
$$

Using trigonometric relations, it is found that:

$$
\begin{aligned}
l_2 &= -l_1 \\
l_3 &= f_1\sin\Omega t + f_2\cos\Omega t \\
l_4 &= -l_3
\end{aligned}
\tag{4.12}
$$

4.1.1. Propeller Side Forces and Moments

The section lift can be further decomposed into thrust and torque components. The lift vector is approximated to be perpendicular to the direction of U as illustrated in Figure 4.3.

The section lift in blade 1 is decomposed into the directions of thrust and torque with the following values:

$$\begin{aligned} \text{thrust:} \quad & l_1 \cos\psi \approx l_1 \frac{\Omega r}{U} \\ \text{torque:} \quad & l_1 \sin\psi \approx l_1 \frac{V}{U} \end{aligned} \tag{4.13}$$

The direction of these lift components are illustrated by blue arrows in Figure 4.4. The thrust component of the section lift is in the direction of the X-axis, it leads to the moment ΔM_1 which can be further decomposed into ΔM_Y and ΔM_Z. The torque component of the section lift can be decomposed into the side forces l_Y and l_z. The direction of these forces and moments are as indicated in Figure 4.4.

For simplicity, drag is ignored in the calculation of the present aerodynamic loads.

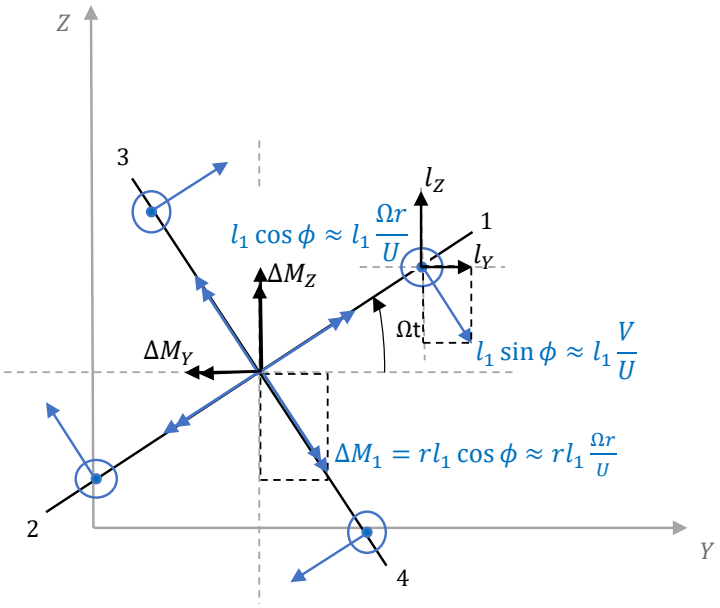

Figure 4.4: Thrust and torque components of the section lift. " ⊙ " vector that goes out of the plane of the page.

Summing the lift contributions of all four blades, the propeller side forces and moments are:

$$\begin{aligned} l_Y &= 2\frac{V}{U}(l_1 \sin\Omega t + l_3 \cos\Omega t) \\ l_Z &= 2\frac{V}{U}(-l_1 \cos\Omega t + l_3 \sin\Omega t) \\ \Delta M_Y &= -r\frac{\Omega r}{V} l_Y \\ \Delta M_Z &= r\frac{\Omega r}{V} l_Z \end{aligned} \tag{4.14}$$

Substituting Equation 4.11 and Equation 4.12 in Equation 4.14, the expressions for section side forces and moments from all four blades become:

$$
\begin{aligned}
l_Y &= 2\frac{V}{U}f_2 = a\rho c\frac{V}{U}\left(V^2\psi - V\dot{a}_1 + \Omega r^2\dot{\theta}\right)\\
l_Z &= 2\frac{V}{U}f_1 = a\rho c\frac{V}{U}\left(V^2\theta - V\dot{b}_1 - \Omega r^2\dot{\psi}\right)\\
\Delta M_Y &= -2\frac{\Omega r^2}{U}f_2 = -a\rho c\frac{\Omega r^2}{U}\left(V^2\psi - V\dot{a}_1 + \Omega r^2\dot{\theta}\right) = -\frac{\Omega r^2}{V}l_Y\\
\Delta M_Z &= 2\frac{\Omega r^2}{U}f_1 = a\rho c\frac{\Omega r^2}{U}\left(V^2\theta - V\dot{b}_1 - \Omega r^2\dot{\psi}\right) = \frac{\Omega r^2}{V}l_Z
\end{aligned}
\tag{4.15}
$$

Equation 4.15 are to be integrated from blade root radius r_0 to blade tip radius R to establish the formulas for the total aerodynamic forces and moments at the propeller hub. Assuming theoretical lift curve slope ($a = 2\pi$), these are:

$$
\begin{aligned}
L_Y &= \frac{1}{2}\rho V^2 S'\left[\left(\frac{4\Omega c_0}{V}A_1\right)\left(\psi - \frac{\dot{a}_1}{V}\right) + \left(\frac{4\Omega c_0}{V}A_2\right)\left(\frac{\dot{\theta}R}{V}\right)\right]\\
L_Z &= \frac{1}{2}\rho V^2 S'\left[\left(\frac{4\Omega c_0}{V}A_1\right)\left(\theta - \frac{\dot{b}_1}{V}\right) + \left(-\frac{4\Omega c_0}{V}A_2\right)\left(\frac{\dot{\psi}R}{V}\right)\right]\\
M_Y &= -\frac{1}{2}\rho V^2 S' R\left[\left(\frac{4\Omega c_0}{V}A_2\right)\left(\psi - \frac{\dot{a}_1}{V}\right) + \left(\frac{4\Omega c_0}{V}A_3\right)\left(\frac{\dot{\theta}R}{V}\right)\right]\\
M_Z &= \frac{1}{2}\rho V^2 S' R\left[\left(\frac{4\Omega c_0}{V}A_2\right)\left(\theta - \frac{\dot{b}_1}{V}\right) + \left(-\frac{4\Omega c_0}{V}A_3\right)\left(\frac{\dot{\psi}R}{V}\right)\right]
\end{aligned}
\tag{4.16}
$$

where $S' = \pi R^2$ is the rotor area. The factors A_i are integrals along the blade whose expressions are:

$$
\begin{aligned}
A_1 &= \int_{\eta_0}^{1}\frac{c}{c_0}\frac{\mu^2}{\sqrt{\mu^2+\eta^2}}d\eta\\
A_2 &= \int_{\eta_0}^{1}\frac{c}{c_0}\frac{\mu\eta^2}{\sqrt{\mu^2+\eta^2}}d\eta\\
A_3 &= \int_{\eta_0}^{1}\frac{c}{c_0}\frac{\eta^4}{\sqrt{\mu^2+\eta^2}}d\eta
\end{aligned}
\tag{4.17}
$$

where $\mu = \frac{J}{\pi} = \frac{V}{\Omega R}$ is the advance ratio, $\eta = \frac{r}{R}$, $\eta_0 = \frac{r_0}{R}$, and c_0 is the reference chord.

4.1.2. Compressibility and Finite-Length Blade Corrections

The method described so far makes use of incompressible flow and a theoretical lift-curve slope of 2π. Modifications to the expressions in Equation 4.17 are necessary to account for the compressibility and the induction effects of a blade with finite length. One approach often used in straight wings of finite aspect ratio is to multiply the lift-curve slope by two factors: the Grauert-Prandtl Mach number correction and the compressible-flow aspect ratio correction.

Note that a major difference between a straight wing and a propeller blade is that the wake shed by a rotating blade is helical in nature. This has further consequences which will be treated in subsection 4.1.4.

The Grauert-Prandtl Mach number correction factor is:

$$
\frac{1}{\sqrt{1-M_r^2}} \tag{4.18}
$$

The compressible-flow aspect ratio correction factor is[1]:

$$
\frac{A'}{A'+2} \qquad \text{with} \quad A' = A\sqrt{1-M_r^2} \tag{4.19}
$$

[1] The lift curve slope with downwash effects is defined by $\frac{dC_l}{d\alpha} = \frac{a_0}{1+\frac{a_0}{\pi A}}$.

Multiplying both factors yields:

$$\frac{A}{2+A\sqrt{1-M_r^2}} = \frac{A}{2+A\sqrt{1-M^2[1+\eta^2/\mu^2]}} \tag{4.20}$$

where M_r is the resultant Mach number at each blade section, A is the aspect ratio, and M is the forward-flight Mach number. The resultant Mach number M_r is defined from the blade resultant velocity $\sqrt{V^2+(\Omega r)^2}$ whereas the forward-flight Mach number M is defined from the incoming airspeed V.

The aspect ratio is defined as:

$$A = \frac{R(1-\eta_0)^2}{c_0 \int_{\eta_0}^1 \frac{c}{c_0} d\eta} \tag{4.21}$$

The expression in Equation 4.20 can be inserted under the integrals in Equation 4.17. Thus, Equation 4.17 becomes:

$$\begin{aligned}
A_1 &= \int_{\eta_0}^1 \frac{c}{c_0} \frac{\mu^2 A}{\sqrt{\mu^2+\eta^2}\left[2+A\sqrt{1-M^2\left(1+\eta^2/\mu^2\right)}\right]} d\eta \\
A_2 &= \int_{\eta_0}^1 \frac{c}{c_0} \frac{\mu\eta^2 A}{\sqrt{\mu^2+\eta^2}\left[2+A\sqrt{1-M^2\left(1+\eta^2/\mu^2\right)}\right]} d\eta \\
A_3 &= \int_{\eta_0}^1 \frac{c}{c_0} \frac{\eta^4 A}{\sqrt{\mu^2+\eta^2}\left[2+A\sqrt{1-M^2\left(1+\eta^2/\mu^2\right)}\right]} d\eta
\end{aligned} \tag{4.22}$$

These expressions assumes a theoretical lift-curve slope of 2π and include the Glauert-Prandtl Mach number correction factor and finite-length blade correction.

When the propeller operates at over speed, the propeller blade tip speed can become supersonic. As a consequence, the square-root of the Mach number correction turns negative. To avoid this problem, Rodden and Rose [93] proposes a cut-off-value of compressible lift-curve slope, $a_m = 4\pi$. If

$$M^2\left(1+\frac{\eta^2}{\mu^2}\right) > 1-\left(\frac{a_0}{a_m}\right)^2 \tag{4.23}$$

the following correction is applied:

$$M^2\left(1+\frac{\eta^2}{\mu^2}\right) = 1-\left(\frac{a_0}{a_m}\right)^2 \tag{4.24}$$

a_0 is the theoretical lift curve slope ($a_0 = 2\pi$).

4.1.3. Introducing Propeller aerodynamic Derivatives

The aerodynamic forces and moments that act on a propeller under whirling motions are traditionally expressed in terms of propeller aerodynamic derivatives with respect to a pitch angle θ, a yaw angle ψ, a pitch rate $\frac{\dot{\overline{\theta}}R}{V}$, and a yaw rate $\frac{\dot{\overline{\psi}}R}{V}$. The orientation of the rotations and the direction of the forces and moments are in line with the system defined in Figure 6.1b. The expressions for these forces and moments are:

$$\begin{aligned}
F_Z &= \frac{1}{2}\rho V^2 S'\left(C_{Z_\theta}\overline{\theta} + C_{Z_\psi}\overline{\psi} + C_{Z_q}\frac{\dot{\overline{\theta}}R}{V} + C_{Z_r}\frac{\dot{\overline{\psi}}R}{V}\right) \\
M_{Y,p} &= \rho V^2 S' R\left(C_{m_\theta}\overline{\theta} + C_{m_\psi}\overline{\psi} + C_{m_q}\frac{\dot{\overline{\theta}}R}{V} + C_{m_r}\frac{\dot{\overline{\psi}}R}{V}\right) \\
F_Y &= \frac{1}{2}\rho V^2 S'\left(C_{Y_\theta}\overline{\theta} + C_{Y_\psi}\overline{\psi} + C_{Y_q}\frac{\dot{\overline{\theta}}R}{V} + C_{Y_r}\frac{\dot{\overline{\psi}}R}{V}\right) \\
M_{Z,p} &= \rho V^2 S' R\left(C_{n_\theta}\overline{\theta} + C_{n_\psi}\overline{\psi} + C_{n_q}\frac{\dot{\overline{\theta}}R}{V} + C_{n_r}\frac{\dot{\overline{\psi}}R}{V}\right)
\end{aligned} \tag{4.25}$$

where $\overline{\theta}$ and $\overline{\psi}$ are the effective pitch and yaw angles, respectively:

$$\begin{aligned} \overline{\theta} &= \theta - \frac{e_\theta \dot{\theta}}{V} \\ \overline{\psi} &= \psi - \frac{e_\psi \dot{\psi}}{V} \end{aligned} \tag{4.26}$$

There are in total sixteen propeller aerodynamic derivatives. Because of symmetry between the pitching and yawing motions and assuming no aerodynamic interference between the wing and the propeller, the following relations are found (The reasoning is explained in Appendix B):

$$\begin{aligned} C_{Z_\psi} &= C_{Y_\theta} & C_{Z_r} &= C_{Y_q} \\ C_{m_\psi} &= -C_{n_\theta} & C_{m_r} &= -C_{n_q} \\ C_{Y_\psi} &= -C_{Z_\theta} & C_{Y_r} &= -C_{Z_q} \\ C_{n_\psi} &= C_{m_\theta} & C_{n_r} &= C_{m_q} \end{aligned} \tag{4.27}$$

Ignoring the second time derivatives of the angles θ and ψ, equating Equation 4.25 with Equation 4.16[2,3] the following results are found:

$$\begin{aligned} C_{Y\psi} &= -C_{Z\theta} = \frac{4\Omega c_0}{V} A_1 \\ C_{Yq} &= C_{Zr} = -\frac{4\Omega c_0}{V} A_2 \\ C_{m\psi} &= -C_{n\theta} = \frac{2\Omega c_0}{V} A_2 \\ C_{mq} &= C_{nr} = -\frac{2\Omega c_0}{V} A_3 \end{aligned} \tag{4.28}$$

Note that the expressions in Equation 4.16 only lead to eight propeller aerodynamic derivatives. These are: $C_{Y\psi} = -C_{Z\theta}$, $C_{Yq} = C_{Zr}$, $C_{m\psi} = -C_{n\theta}$, and $C_{mq} = C_{nr}$. The remaining of the aerodynamic derivatives that appear in Equation 4.25 represent aerodynamic loads caused by wake effects. The theoretical derivation of these terms will be explained in subsection 4.1.4.

4.1.4. Wake Effects

The expressions derived so far are based on quasi-steady aerodynamics. A rotating-precessing propeller blade has a similar behaviour to that of oscillating wings. The propeller blade develops an oscillatory lift and the oscillatory lift generates shed vortices which induce a lift lag. This lift lag consists of a change in magnitude and orientation of the lift predicted by quasi-steady theory. The problem is further complicated by several reasons: first, the propeller treated here has four blades and thus, four wakes which can cause induced effects; second, with the blades rotating the wakes are helical; and third, with the propeller rotating and precessing at different frequencies, the wake experiences two frequency components.

In this section, a greatly simplified approach is taken so as to include basic notions of wake effects. The following treatment is not exactly rigorous but it corroborates the existence of other aerodynamic terms that can not be predicted by quasi-steady aerodynamics.

Consider the lift expression given by Equation 4.11. Assuming oscillatory motions with $\theta = \theta_0 e^{i\omega t}$ and $\psi = \psi_0 e^{i\omega t}$. The motion of the propeller blades can be represented by:

[2] Comparing Figure 6.1b to the system in Figure 4.1, the orientation of the pitching motion and M_Y has the opposite direction. When establishing the equivalence between Equation 4.25 and Equation 4.16, in the expressions of Equation 4.16, θ needs to be changed by $-\theta$ and M_Y by $-M_Y$.

[3] Note that from Equation 4.1: $a_1 = e_\psi \psi$ and $b_1 = e_\theta \theta$

$$
\begin{aligned}
f_1 &= \frac{1}{2}\rho c a\left(V^2\theta - V\dot{b}_1 - \Omega r^2\dot{\psi}\right) = \\
&= \underbrace{\frac{1}{2}\rho c a\left(V^2\theta_0 - V e_\theta \theta_0 \omega i - \Omega r^2 \psi_0 \omega i\right)}_{f_{10}} e^{i\omega t} = \\
&= f_{10} e^{i\omega t} \\
f_2 &= \frac{1}{2}\rho c a\left(V^2\psi - V\dot{a}_1 + \Omega r^2\dot{\theta}\right) = \\
&= \underbrace{\frac{1}{2}\rho c a\left(V^2\psi_0 - V e_\psi \psi_0 \omega i + \Omega r^2 \theta_0 \omega i\right)}_{f_{20}} e^{i\omega t} = \\
&= f_{20} e^{i\omega t}
\end{aligned}
\tag{4.29}
$$

The lift in Equation 4.11 can be expressed as:

$$
\begin{aligned}
l_1 &= -f_{10} e^{i\omega t}\frac{e^{i\Omega t} + e^{-i\Omega t}}{2} + f_{20} e^{i\omega t}\frac{e^{i\Omega t} - e^{-i\Omega t}}{2i} = \\
&= -\frac{1}{2}(f_{10} + i f_{20}) e^{i(\Omega+\omega)t} - \frac{1}{2}(f_{10} - i f_{20}) e^{-i(\Omega-\omega)t}
\end{aligned}
\tag{4.30}
$$

This expression shows that the lift and consequently its wake, has two frequency components as previously mentioned: $\Omega+\omega$ and $\Omega-\omega$. This lift is analogous to the circulatory lift that appears in oscillating wings. To account for the wake effects or lift lag effects, the expression needs to be multiplied by the Theodorsen function $C(k) = F(k) + iG(k)$[4]:

$$
l_1' = -\frac{F_1 + iG_1}{2}\left(f_{10} + i f_{20}\right) e^{i\Omega+\omega t} - \frac{F_2 - iG_2}{2}\left(f_{10} - i f_{20}\right) e^{-i(\Omega-\omega)t}
\tag{4.32}
$$

$(F_1 + iG_1)$ and $(F_2 - iG_2)$ are to be defined by the reduced frequencies k_1 and k_2, respectively.

$$
k_1 = \frac{(\Omega+\omega)c}{2\sqrt{(\Omega r)^2 + V^2}}, \qquad k_2 = \frac{(\Omega-\omega)c}{2\sqrt{(\Omega r)^2 + V^2}}
\tag{4.33}
$$

Note the negative sign in $(F_2 - iG_2)$. $(F_1 + iG_1)$ is associated to a motion proportional to $e^{i\omega t}$ whereas $(F_2 - iG_2)$ is associated to a motion proportional to $e^{-i\omega t}$ provided that Ω is greater than ω (negative frequencies).

Reducing Equation 4.32 backwards and considering $i f_1 = \frac{\dot{f}_1}{\omega}$ and $i f_2 = \frac{\dot{f}_2}{\omega}$, the lift including lift lag effects in a section in blade 1 is given by:

$$
\begin{aligned}
l_1' = &\frac{F_1 + F_2}{2}\left(-f_1\cos\Omega t + f_2\sin\Omega t\right) + \frac{G_1 + G_2}{2}\left(f_1\sin\Omega t + f_2\cos\Omega t\right) + \\
&+ \frac{G_1 - G_2}{2\omega}\left(-\dot{f}_1\cos\Omega t + \dot{f}_2\sin\Omega t\right) - \frac{F_1 - F_2}{2\omega}\left(\dot{f}_1\sin\Omega t + \dot{f}_2\cos\Omega t\right) = \\
= &\frac{F_1 + F_2}{2} l_1 + \frac{G_1 + G_2}{2} l_3 + \frac{G_1 - G_2}{2\omega}\hat{l}_1 - \frac{F_1 - F_2}{2\omega}\hat{l}_3
\end{aligned}
\tag{4.34}
$$

where

$$
\hat{l}_1 = -\dot{f}_1\cos\Omega t + \dot{f}_2\sin\Omega t, \qquad \hat{l}_3 = \dot{f}_1\sin\Omega t + \dot{f}_2\cos\Omega t
$$

[4]The Theodorsen function, or the lift-deficiency function, $C(k)$, is defined by:

$$
C(K) = F(k) + iG(k) = \frac{H_1^{(2)}(k)}{H_1^{(2)}(k) + i H_0^{(2)}(k)}
\tag{4.31}
$$

where $H_n^{(2)}(k)$ are the nth order Hankel functions of the second kind, which are, in turn, composed of Bessel functions of the first and second kinds[8].

Analogously, similar expressions for the other blades can also be derived:

$$
\begin{aligned}
l_2' &= -\,l_1' \\
l_3' &= \frac{F_1+F_2}{2}\left(f_1\sin\Omega t + f_2\cos\Omega t\right) - \frac{G_1+G_2}{2}\left(-f_1\cos\Omega t + f_2\sin\Omega t\right) + \\
&\quad + \frac{G_1-G_2}{2\omega}\left(\dot{f}_1\sin\Omega t + \dot{f}_2\cos\Omega t\right) + \frac{F_1-F_2}{2\omega}\left(-\dot{f}_1\cos\Omega t + \dot{f}_2\sin\Omega t\right) = \\
&= \frac{F_1+F_2}{2}l_3 - \frac{G_1+G_2}{2}l_1 + \frac{G_1-G_2}{2\omega}\hat{l}_3 + \frac{F_1-F_2}{2\omega}\hat{l}_1 \\
l_4' &= -\,l_3'
\end{aligned}
\tag{4.35}
$$

The propeller side forces and moments are given as in Equation 4.14. Now including lift lag effects:

$$
\begin{aligned}
l_Y' &= \frac{F_1+F_2}{2}l_Y + \frac{G_1+G_2}{2}l_Z + \frac{G_1-G_2}{2\omega}\hat{l}_Y - \frac{F_1-F_2}{2\omega}\hat{l}_Z \\
l_Z' &= \frac{F_1+F_2}{2}l_Z - \frac{G_1+G_2}{2}l_Y + \frac{G_1-G_2}{2\omega}\hat{l}_Z + \frac{F_1-F_2}{2\omega}\hat{l}_Y \\
\Delta M_Y' &= -r\frac{\Omega r}{V}l_Y' \\
\Delta M_Z' &= r\frac{\Omega r}{V}l_Z'
\end{aligned}
\tag{4.36}
$$

Lift lag effects reduce the magnitude of the quasi-steady lift l_Y and l_Z and also turns the quasi-steady lift in the direction of rotation by an angle $\gamma = \tan^{-1}\frac{|G_1+G_2|}{F_1+F_2}$. In general, ω is small compared with Ω. Also, the first two terms in the lift expressions in Equation 4.36 include the average values of F's and G's. This indicates that the F's and G's can be approximated by using the reduced frequency $k = \frac{\Omega c}{2U}$ which means that the last two terms in the lift expressions, $\hat{l}_Y$ and $\hat{l}_Z$, can be dropped. Therefore, Equation 4.36 becomes:

$$
\begin{aligned}
l_Y' &\approx Fl_Y + Gl_Z \\
l_Z' &\approx Fl_Z - Gl_Y \\
\Delta M_Y' &\approx -r\frac{\Omega r}{V}(Fl_Y + Gl_Z) = F\Delta M_Y - G\Delta M_Z \\
\Delta M_Z' &\approx r\frac{\Omega r}{V}(Fl_Z - Gl_Y) = F\Delta M_Z + G\Delta M_Y
\end{aligned}
\tag{4.37}
$$

The total resultant aerodynamic forces and moments at the propeller hub are obtained by integrating Equation 4.37 from blade root radius r_0 to blade tip radius R:

$$
\begin{aligned}
L_Y &= \frac{1}{2}\rho V^2 S'\left\{F\left[\left(\frac{4\Omega c_0}{V}A_1\right)\left(\psi - \frac{\dot{a}_1}{V}\right) + \left(\frac{4\Omega c_0}{V}A_2\right)\left(\frac{\dot{\theta}R}{V}\right)\right] + G\left[\left(\frac{4\Omega c_0}{V}A_1\right)\left(\theta - \frac{\dot{b}_1}{V}\right) + \left(-\frac{4\Omega c_0}{V}A_2\right)\left(\frac{\dot{\psi}R}{V}\right)\right]\right\} \\
L_Z &= \frac{1}{2}\rho V^2 S'\left\{F\left[\left(\frac{4\Omega c_0}{V}A_1\right)\left(\theta - \frac{\dot{b}_1}{V}\right) + \left(-\frac{4\Omega c_0}{V}A_2\right)\left(\frac{\dot{\psi}R}{V}\right)\right] - G\left[\left(\frac{4\Omega c_0}{V}A_1\right)\left(\psi - \frac{\dot{a}_1}{V}\right) + \left(\frac{4\Omega c_0}{V}A_2\right)\left(\frac{\dot{\theta}R}{V}\right)\right]\right\} \\
M_Y &= -\frac{1}{2}\rho V^2 S' R\left\{F\left[\left(\frac{4\Omega c_0}{V}A_2\right)\left(\psi - \frac{\dot{a}_1}{V}\right) + \left(\frac{4\Omega c_0}{V}A_3\right)\left(\frac{\dot{\theta}R}{V}\right)\right] + G\left[\left(\frac{4\Omega c_0}{V}A_2\right)\left(\theta - \frac{\dot{b}_1}{V}\right) + \left(-\frac{4\Omega c_0}{V}A_3\right)\left(\frac{\dot{\psi}R}{V}\right)\right]\right\} \\
M_Z &= \frac{1}{2}\rho V^2 S' R\left\{F\left[\left(\frac{4\Omega c_0}{V}A_2\right)\left(\theta - \frac{\dot{b}_1}{V}\right) + \left(-\frac{4\Omega c_0}{V}A_3\right)\left(\frac{\dot{\psi}R}{V}\right)\right] - G\left[\left(\frac{4\Omega c_0}{V}A_2\right)\left(\psi - \frac{\dot{a}_1}{V}\right) + \left(\frac{4\Omega c_0}{V}A_3\right)\left(\frac{\dot{\theta}R}{V}\right)\right]\right\}
\end{aligned}
\tag{4.38}
$$

Ignoring the second time derivatives of the angles θ and ψ, comparing Equation 4.38 with Equation 4.25 it is possible to calculate all the propeller aerodynamic derivatives[5,6]:

$$
\begin{aligned}
C_{Y\psi} &= -C_{Z\theta} = \frac{4\Omega c_0}{V} I_1 & \qquad C_{Y\theta} &= C_{Z\psi} = -\frac{4\Omega c_0}{V} J_1 \\
C_{Yq} &= C_{Zr} = -\frac{4\Omega c_0}{V} I_2 & \qquad C_{Yr} &= -C_{Zq} = -\frac{4\Omega c_0}{V} J_2 \\
C_{m\psi} &= -C_{n\theta} = \frac{2\Omega c_0}{V} I_2 & \qquad C_{m\theta} &= C_{n\psi} = -\frac{2\Omega c_0}{V} J_2 \\
C_{mq} &= C_{nr} = -\frac{2\Omega c_0}{V} I_3 & \qquad C_{mr} &= -C_{nq} = -\frac{2\Omega c_0}{V} J_3
\end{aligned}
\tag{4.39}
$$

with the blade integrals given by:

$$
\begin{aligned}
I_1 &= \frac{\mu^2 A}{c_0} \int_{\eta_0}^{1} \frac{c(\eta) F(k)}{\sqrt{\mu^2+\eta^2}\left[2 + A\sqrt{1 - M^2\left(1+\eta^2/\mu^2\right)}\right]} d\eta \\
I_2 &= \frac{\mu A}{c_0} \int_{\eta_0}^{1} \frac{\eta^2 c(\eta) F(k)}{\sqrt{\mu^2+\eta^2}\left[2 + A\sqrt{1 - M^2\left(1+\eta^2/\mu^2\right)}\right]} d\eta \\
I_3 &= \frac{A}{c_0} \int_{\eta_0}^{1} \frac{\eta^4 c(\eta) F(k)}{\sqrt{\mu^2+\eta^2}\left[2 + A\sqrt{1 - M^2\left(1+\eta^2/\mu^2\right)}\right]} d\eta \\
J_1 &= \frac{\mu^2 A}{c_0} \int_{\eta_0}^{1} \frac{c(\eta) G(k)}{\sqrt{\mu^2+\eta^2}\left[2 + A\sqrt{1 - M^2\left(1+\eta^2/\mu^2\right)}\right]} d\eta \\
J_2 &= \frac{\mu A}{c_0} \int_{\eta_0}^{1} \frac{\eta^2 c(\eta) G(k)}{\sqrt{\mu^2+\eta^2}\left[2 + A\sqrt{1 - M^2\left(1+\eta^2/\mu^2\right)}\right]} d\eta \\
J_3 &= \frac{A}{c_0} \int_{\eta_0}^{1} \frac{\eta^4 c(\eta) G(k)}{\sqrt{\mu^2+\eta^2}\left[2 + A\sqrt{1 - M^2\left(1+\eta^2/\mu^2\right)}\right]} d\eta
\end{aligned}
\tag{4.40}
$$

These blade integrals also include compressibility and finite blade-length corrections mentioned earlier. Note that these expressions are only valid for a propeller with four blades and a incompressible lift-curve slope of $a = 2\pi$. To account for a different number of blades N_b ($N_b > 2$), Equation 4.40 is modified as:

[5] As mentioned earlier, the expressions in Equation 4.25 are in accordance to the system defined in Figure 6.1b. Comparing it to the system in Figure 4.1, the orientation of the pitching motion and M_Y has the opposite direction. When establishing the equivalence between Equation 4.25 and Equation 4.38, in the expressions of Equation 4.38, θ needs to be changed by $-\theta$ and M_Y by $-M_Y$.

[6] Note that from Equation 4.1: $a_1 = e_\psi \psi$ and $b_1 = e_\theta \theta$

$$
\begin{aligned}
I_1 &= \frac{N_b}{4}\frac{\mu^2 A}{c_0}\int_{\eta_0}^{1}\frac{c(\eta)F(k)}{\sqrt{\mu^2+\eta^2}\left[2+A\sqrt{1-M^2\left(1+\eta^2/\mu^2\right)}\right]}d\eta \\
I_2 &= \frac{N_b}{4}\frac{\mu A}{c_0}\int_{\eta_0}^{1}\frac{\eta^2 c(\eta)F(k)}{\sqrt{\mu^2+\eta^2}\left[2+A\sqrt{1-M^2\left(1+\eta^2/\mu^2\right)}\right]}d\eta \\
I_3 &= \frac{N_b}{4}\frac{A}{c_0}\int_{\eta_0}^{1}\frac{\eta^4 c(\eta)F(k)}{\sqrt{\mu^2+\eta^2}\left[2+A\sqrt{1-M^2\left(1+\eta^2/\mu^2\right)}\right]}d\eta \\
J_1 &= \frac{N_b}{4}\frac{\mu^2 A}{c_0}\int_{\eta_0}^{1}\frac{c(\eta)G(k)}{\sqrt{\mu^2+\eta^2}\left[2+A\sqrt{1-M^2\left(1+\eta^2/\mu^2\right)}\right]}d\eta \\
J_2 &= \frac{N_b}{4}\frac{\mu A}{c_0}\int_{\eta_0}^{1}\frac{\eta^2 c(\eta)G(k)}{\sqrt{\mu^2+\eta^2}\left[2+A\sqrt{1-M^2\left(1+\eta^2/\mu^2\right)}\right]}d\eta \\
J_3 &= \frac{N_b}{4}\frac{A}{c_0}\int_{\eta_0}^{1}\frac{\eta^4 c(\eta)G(k)}{\sqrt{\mu^2+\eta^2}\left[2+A\sqrt{1-M^2\left(1+\eta^2/\mu^2\right)}\right]}d\eta
\end{aligned}
\tag{4.41}
$$

To account for a different number of blades N_b ($N_b > 2$) and the real lift-curve slope distribution $a(\eta)$, Equation 4.40 is modified as:

$$
\begin{aligned}
I_1 &= \frac{N_b}{4}\frac{1}{2\pi}\frac{\mu^2}{c_0}\int_{\eta_0}^{1}\frac{a(\eta)c(\eta)F(k)}{\sqrt{\mu^2+\eta^2}}d\eta \\
I_2 &= \frac{N_b}{4}\frac{1}{2\pi}\frac{\mu}{c_0}\int_{\eta_0}^{1}\frac{a(\eta)\eta^2 c(\eta)F(k)}{\sqrt{\mu^2+\eta^2}}d\eta \\
I_3 &= \frac{N_b}{4}\frac{1}{2\pi}\frac{1}{c_0}\int_{\eta_0}^{1}\frac{a(\eta)\eta^4 c(\eta)F(k)}{\sqrt{\mu^2+\eta^2}}d\eta \\
J_1 &= \frac{N_b}{4}\frac{1}{2\pi}\frac{\mu^2}{c_0}\int_{\eta_0}^{1}\frac{a(\eta)c(\eta)G(k)}{\sqrt{\mu^2+\eta^2}}d\eta \\
J_2 &= \frac{N_b}{4}\frac{1}{2\pi}\frac{\mu}{c_0}\int_{\eta_0}^{1}\frac{a(\eta)\eta^2 c(\eta)G(k)}{\sqrt{\mu^2+\eta^2}}d\eta \\
J_3 &= \frac{N_b}{4}\frac{1}{2\pi}\frac{1}{c_0}\int_{\eta_0}^{1}\frac{a(\eta)\eta^4 c(\eta)G(k)}{\sqrt{\mu^2+\eta^2}}d\eta
\end{aligned}
\tag{4.42}
$$

It is shown in Cecrdle [15] that the use of the real lift-curve slope distributions yields conservative propeller aerodynamic derivatives (smaller absolute values) and therewith, more conservative whirl flutter predictions.

The aerodynamic derivatives $C_{mr} = -C_{nq}$ and $C_{Yr} = -C_{Zq}$ are set to zero in Rodden and Rose [93] due to their small values and lack of correlation with experimental data. However, in this report, they will be included in all analysis for completeness.

Note that $C_{Y\psi} = -C_{Z\theta}$, $C_{Yq} = C_{Zr}$, $C_{m\psi} = -C_{n\theta}$, and $C_{mq} = C_{nr}$ arise from steady aerodynamics; while $C_{Y\theta} = C_{Z\psi}$, $C_{Yr} = -C_{Zq}$, $C_{m\theta} = C_{n\psi}$, and $C_{mr} = -C_{nq}$ arise from unsteady aerodynamics. It is shown in Reed III and Bland [88] that for very large advance ratios, including the extra derivatives that arise from unsteady aerodynamics has a stabilizing effect on the propeller backward whirl mode.

Applying Theodorsen's function to the lift formula in Equation 4.30 introduces a phase lag to the steady lift. In Theodorsen's theory, a flat wake is assumed. For very large advance ratios, applying Theodorsen's function to account for wake effects is a good approximation. However, for low advance ratios, the phase lag predicted by Theodorsen's function tends to be too small. For low advance ratios, the modified version of Theodorsen's function derived by Loewy [64] seems more suitable; as instead of a flat wake it assumes a helical wake, which approximates better that of a propeller. Low advance ratios are more common in helicopters or tiltrotors operating in vertical or tilted mode. Propellers usually operate at higher advance ratios.

4.1.5. Final Expressions for Propeller Aerodynamics

In spite of the arduous derivations, implementation of the Houbolt-Reed's method is rather simple.

The complete set of aerodynamic forces and moments due to propeller pitching and yawing motions are determined by the combination of Equation 4.25, Equation 4.26, Equation 4.39, and Equation 4.41 or Equation 4.42.

Note that the inclusion of wing flexibility and aerodynamic interference effects may change the effective pitch and yaw angles defined in Equation 4.26.

$$\begin{aligned}
F_Z &= \frac{1}{2}\rho V^2 S'\left(C_{Z_\theta}\overline{\theta} + C_{Z_\psi}\overline{\psi} + C_{Z_q}\frac{\dot{\overline{\theta}}R}{V} + C_{Z_r}\frac{\dot{\overline{\psi}}R}{V}\right) \\
M_{Y,p} &= \rho V^2 S' R\left(C_{m_\theta}\overline{\theta} + C_{m_\psi}\overline{\psi} + C_{m_q}\frac{\dot{\overline{\theta}}R}{V} + C_{m_r}\frac{\dot{\overline{\psi}}R}{V}\right) \\
F_Y &= \frac{1}{2}\rho V^2 S'\left(C_{Y_\theta}\overline{\theta} + C_{Y_\psi}\overline{\psi} + C_{Y_q}\frac{\dot{\overline{\theta}}R}{V} + C_{Y_r}\frac{\dot{\overline{\psi}}R}{V}\right) \\
M_{Z,p} &= \rho V^2 S' R\left(C_{n_\theta}\overline{\theta} + C_{n_\psi}\overline{\psi} + C_{n_q}\frac{\dot{\overline{\theta}}R}{V} + C_{n_r}\frac{\dot{\overline{\psi}}R}{V}\right)
\end{aligned} \tag{4.25}$$

$$\begin{aligned}
\overline{\theta} &= \theta - \frac{e_\theta \dot{\theta}}{V} \\
\overline{\psi} &= \psi - \frac{e_\psi \dot{\psi}}{V}
\end{aligned} \tag{4.26}$$

$$\begin{aligned}
C_{Y\psi} &= -C_{Z\theta} = \frac{4\Omega c_0}{V} I_1 & C_{Y\theta} &= C_{Z\psi} = -\frac{4\Omega c_0}{V} J_1 \\
C_{Yq} &= C_{Zr} = -\frac{4\Omega c_0}{V} I_2 & C_{Yr} &= -C_{Zq} = -\frac{4\Omega c_0}{V} J_2 \\
C_{m\psi} &= -C_{n\theta} = \frac{2\Omega c_0}{V} I_2 & C_{m\theta} &= C_{n\psi} = -\frac{2\Omega c_0}{V} J_2 \\
C_{mq} &= C_{nr} = -\frac{2\Omega c_0}{V} I_3 & C_{mr} &= -C_{nq} = -\frac{2\Omega c_0}{V} J_3
\end{aligned} \tag{4.39}$$

4.1.6. Comments

Propeller aerodynamics in Houbolt-Reed's method is based on strip theory and 2D quasi steady aerodynamics. Drag forces are neglected. Compressibility and blade finite-length effects are included via correction factors. Induced velocities at the rotor disk are ignored. Wake effects are added by means of modifying the lift magnitude and lift orientation via Theodorsen function. Windmilling conditions are assumed; therefore the propeller does not generate thrust. It is also assumed that propeller blade twist distribution is lineal (constant pitch) — the inflow angle without considering the perturbed values ($\dot{\alpha_1}, \dot{s}, \dot{w}$) is constant along the blade radius.

Differences with the expressions found in literature

Comparing the propeller aerodynamic derivatives derived in this report with the expressions given in Rodden and Rose [93], there is a difference in sign in the aerodynamic derivative C_{nq} (and thus C_{mr}).

The expression derived in this report is:

$$C_{nq} = -C_{mr} = \frac{2\Omega c_0}{V} J_3$$

whereas the expression given in Rodden and Rose [93] is:

$$C_{nq} = -C_{mr} = -\frac{2\Omega c_0}{V} J_3$$

Rodden and Rose [93] set this derivative to zero for it having very small values, therefore, a qualitative comparison is not possible.

4.2. Validation and Verification

The expressions derived in Section 4.1 to predict the propeller aerodynamic derivatives are implemented in Matlab. The validation and verification of the implementation is carried out by replicating some propeller aerodynamic derivative values found in literature, namely those obtained by Bennett and Bland [6] (fixed-pitch propeller) and Rodden and Rose [93] (constant speed propeller).

Bennett and Bland [6] conducted an experimental campaign in which they measured five propeller aerodynamic derivatives from a windmilling propeller and compared their experimental results with two sets of theoretical derivatives, namely Ribner [91] and Houbolt and Reed [45]. The propeller was a 1/8-scale model of a typical turboprop aircraft propeller treated in Reed III and Bland [88]; it has four aluminium blades with a radius of 0.8438 ft and a blade semichord of 0.1823 ft at three-quarter radius, therefore, a solidity at three-quarter radius of 0.1834. The measured derivatives were: $C_{Z\theta}$, $C_{m\theta}$, $C_{Y\theta}$, $C_{m\psi}$, C_{mq}, and C_{Yq}.

As mentioned, the theoretical derivatives were calculated by employing two methods: Houbolt-Reed's method, which is explained in Section 4.1 and Ribner's method [91]. Both methods give direct expressions to calculate four propeller aerodynamic derivatives, these are: $C_{Z\theta}$, $C_{m\psi}$, C_{mq}, C_{Yq} (or their counterparts: $C_{Y\psi}$, $C_{n\theta}$, C_{nr}, C_{Zr}). Ribner's method [91] does not include expressions to calculate propeller aerodynamic derivatives that arise due to wake effects. On the other hand, as explained in Section 4.1, Houbolt-Reed's method [45] includes expressions to calculate the complete set of the propeller aerodynamic derivatives by including wake effects (Equation (4.39)) but these are not used in Bennett and Bland [6]. Instead, a slightly simpler approach is taken and explained below.

Bennett and Bland [6] only uses the expressions that do not include wake effects nor compressibility effects (M = 0) but includes the finite blade-length corrections factor (Equation (4.22) and Equation (4.28)). These expressions only allow to determine four derivatives ($C_{Z\theta}$, $C_{m\psi}$, C_{mq}, and C_{Yq}). The derivatives $C_{m\theta}$ and $C_{Y\theta}$ are obtained by using the theoretical expressions given in Reed III and Bland [88]. The method introduced in Reed III and Bland [88] is analogous to Houbolt-Reed's method and it is as follows: $C_{Z\psi}$ appears because of phase-lags of aerodynamic forces acting on the propeller. When the propeller is at a yawed position with respect to the free stream direction, the propeller blades perceive angle of attack oscillations. As a consequence, the side force due to yaw ($C_{Y\psi} = -C_{Z\theta}$) undergoes a phase lag δ and a vertical force ($C_{Z\psi} = C_{Y\theta}$) arises. The vertical force is given by:

$$C_{Z\psi} = C_{Y\psi} \tan\delta \tag{4.43}$$

where the phase lag δ can be estimated using the Theodorsen's function for oscillatory flow ($C(k) = F(k) + iG(k)$). The expression for the phase lag δ is given by:

$$\delta = \tan^{-1}\left[\frac{-G(k)}{F(k)}\right] \tag{4.44}$$

$C(k)$ is a function of the reduced frequency $k = \frac{\Omega b}{2U}$ which depends on the propeller rotational velocity Ω, the blade element chord b, and the free stream velocity U. k can be approximated by the reduced frequency of a blade element at the quarter chord section:

$$k_{0.75R} = \frac{b_{0.75R}}{2R\sqrt{\left(\frac{3}{4}\right)^2 + \left(\frac{J}{\pi}\right)^2}} \tag{4.45}$$

Analogously, $C_{m\theta} = C_{n\psi}$ is given by:

$$C_{m\theta} = C_{m\psi} \tan\delta \tag{4.46}$$

The geometrical and operational features of the propeller tested by Bennett and Bland [6] is found in [[6],Figure 4, Figure 5 and Table I]. Results obtained with present analysis is compared with those obtained by Bennett and Bland [6] in Figure 4.5. As it can be seen, present analysis calculates the exact same values for all the propeller aerodynamic derivatives as in Bennett and Bland [6] except for $C_{m\theta}$ and $C_{m\psi}$. $C_{m\theta}$ depends on $C_{m\psi}$ according to Equation (4.46). Therefore, the discrepancy lies in the values of $C_{m\psi}$. The reason for this discrepancy is unknown but present implementation predicts values which are slightly closer to the experimental data.

With Figure 4.5, present implementation of propeller aerodynamic derivatives is verified and validated for the case of including finite blade-length aspect ratio corrections, and excluding wake effects and compressibility effects (M = 0).

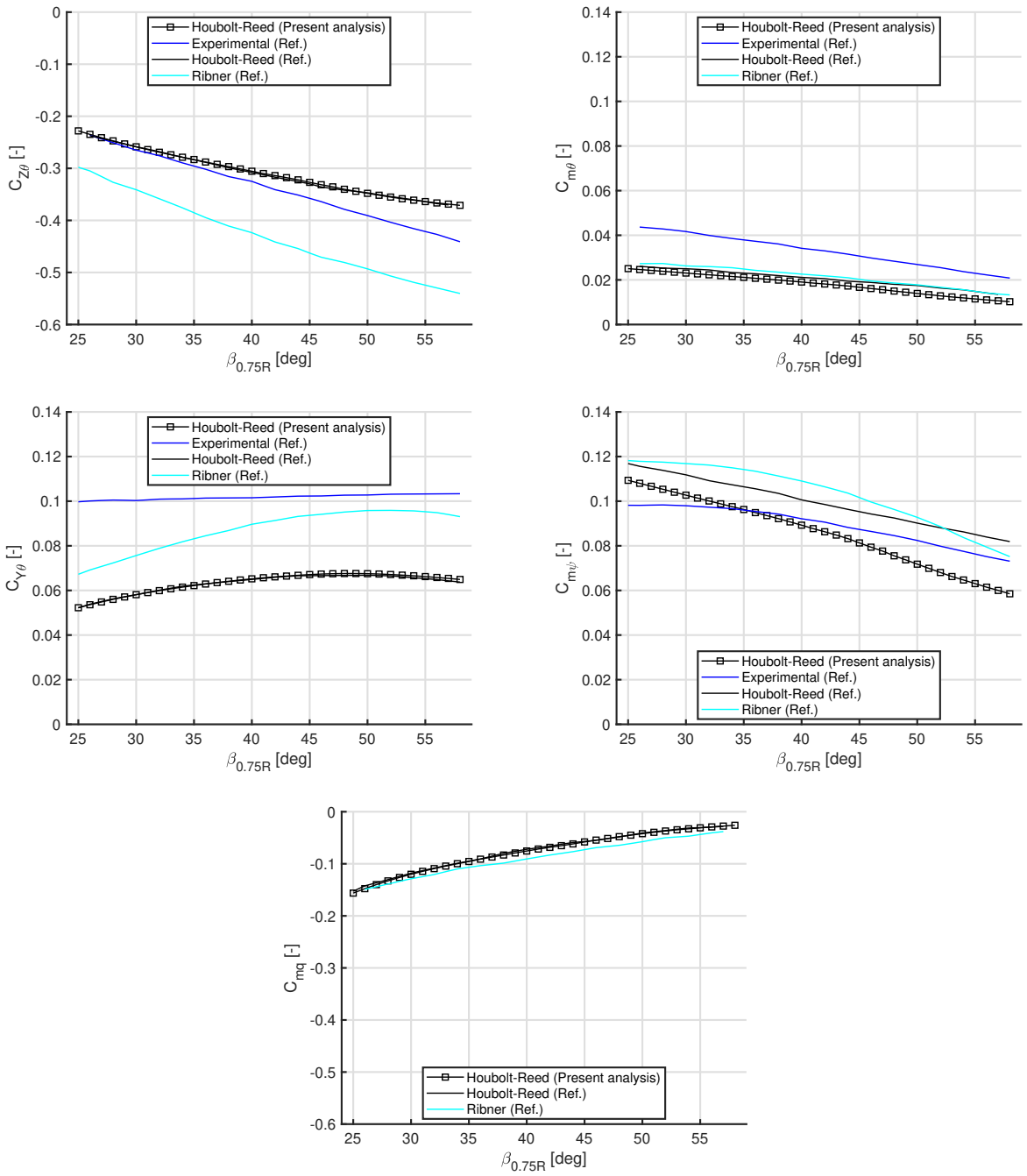

Figure 4.5: Propeller aerodynamic derivatives using Houbolt-Reed's method excluding wake effects. Comparison with data from Bennett and Bland [6].

The validation for the case of including compressibility effects with operational Mach number $M \neq 0$, finite blade-length aspect ratio correction, and wake effects (Equation (4.39) and Equation (4.41)) is conducted by comparing results from present calculations with those found in Rodden and Rose [93]. The propeller analysed by Rodden and Rose [93] is the same as the one in Bennett and Bland [6] but with twice the amount of the propeller blade chord. Also, a typical propeller rotational speed Ω of 1800 RPM and a speed of sound of 1116 ft/s are assumed in order to calculate the operational Mach number. Results are shown in Table 4.1 and the relative errors in Table 4.2. As it can be seen, the results are very approximate, minor differences can be attributed to numerical truncation and/or a different numerical scheme employed to solve the blade integrals. These findings are expected since the propeller aerodynamic expressions derived and used in Rodden and Rose [93] are exactly the same as the ones used in the present analysis, with the exception of $C_{nq} = -C_{mr}$.

Note that Table 4.1 and Table 4.2 only show five out of the eight distinct propeller aerodynamic derivatives. Validation of the other derivatives is not possible since they are not reported in Rodden and Rose [93].

$\beta_{0.75R}$	25	35	46	52	58	$\beta_{0.75R}$	25	35	46	52	58
Reference [93]						**Present Analysis**					
$C_{Z\theta}$	-0.3310	-0.4180	-0.5120	-0.5660	-0.6190	$C_{Z\theta}$	-0.328	-0.420	-0.516	-0.575	-0.622
$C_{m\theta}$	0.0400	0.0362	0.0304	0.0264	0.0221	$C_{m\theta}$	0.040	0.036	0.030	0.026	0.022
C_{mq}	-0.2160	-0.1391	-0.0833	-0.0603	-0.0422	C_{mq}	-0.219	-0.138	-0.082	-0.057	-0.042
$C_{Z\psi}$	0.0877	0.1106	0.1320	0.1408	0.1461	$C_{Z\psi}$	0.087	0.111	0.133	0.143	0.147
$C_{m\psi}$	0.1506	0.1373	0.1188	0.1067	0.0937	$C_{m\psi}$	0.152	0.138	0.119	0.105	0.094

Table 4.1: Comparison of the propeller aerodynamic derivatives with Rodden and Rose [93].

$\beta_{0.75R}$ [deg]	25	35	46	52	58
	Error [%]				
$C_{Z\theta}$	-0.93	0.50	0.88	1.55	0.54
$C_{m\theta}$	0.79	0.27	0.00	-1.42	0.13
C_{mq}	1.59	-1.08	-2.00	-4.96	-1.33
$C_{Z\psi}$	-0.94	0.69	0.86	1.23	0.66
$C_{m\psi}$	0.72	0.16	-0.15	-1.28	0.03

Table 4.2: Comparison of the propeller aerodynamic derivatives with Rodden and Rose [93].

For completeness, the values of all the aerodynamic derivatives calculated for the case of excluding compressibility effects (Mach = 0), but including finite blade-length aspect ratio correction, and wake effects (Equation (4.39) and Equation (4.41)) are shown in Figure 4.6. The propeller analysed is the one used in Bennett and Bland [6]. The results obtained by Bennett and Bland [6] are also shown. The propeller aerodynamic derivatives calculated by present analysis follow the same trend as the experimental values and in some cases, their values are fairly approximate. In all cases, present analysis predicts aerodynamic derivatives with smaller absolute values than the experimental derivatives. Therefore, present method predicts conservative propeller aerodynamic loads.

Figure 4.7 presents the influence of compressibility effects on propeller aerodynamic derivatives when the theoretical lift curve slope of 2π is assumed. Increasing the Mach number increases the absolute value of the propeller aerodynamic derivatives. For Mach values below 0.2 the change in value of the propeller aerodynamic derivatives are small. When the Mach number approximates to 1, the change in the derivatives becomes barely noticeable. This is because the propeller blade tip speed becomes supersonic and a cut-off-value of compressible lift-curve slope is applied in the correction of compressibility effects (Equation (4.24)). Including compressibility effects, present method do not calculate conservative values at high Mach numbers; further validation/verification is required.

Final comments

For a complete verification of the Houbolt-Reed's method, it is necessary to obtain experimental values of the complete set of propeller aerodynamic derivatives, especially the derivatives that have not been verified in present work. This is proposed for future work.

Furthermore, note that these derivatives have been validated for a propeller in windmilling condition.

Unless otherwise specified, present work employs propeller aerodynamic derivatives evaluated by the method of Houbolt and Reed including compressibility and aspect ratio correction factors, and wake effects.

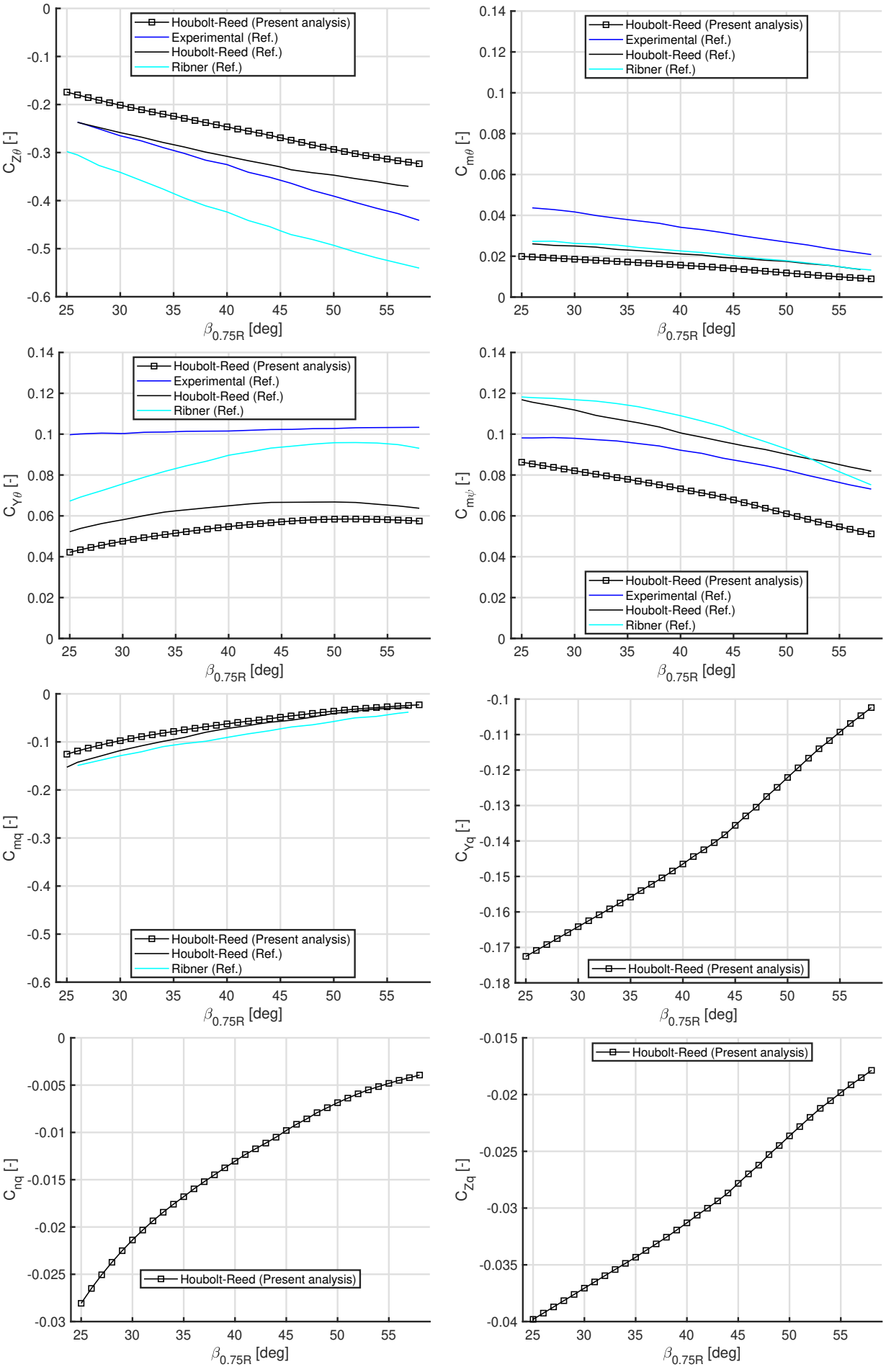

Figure 4.6: Propeller aerodynamic derivatives using Houbolt-Reed's method including wake effects. Mach = 0. Comparison with data from Bennett and Bland [6].

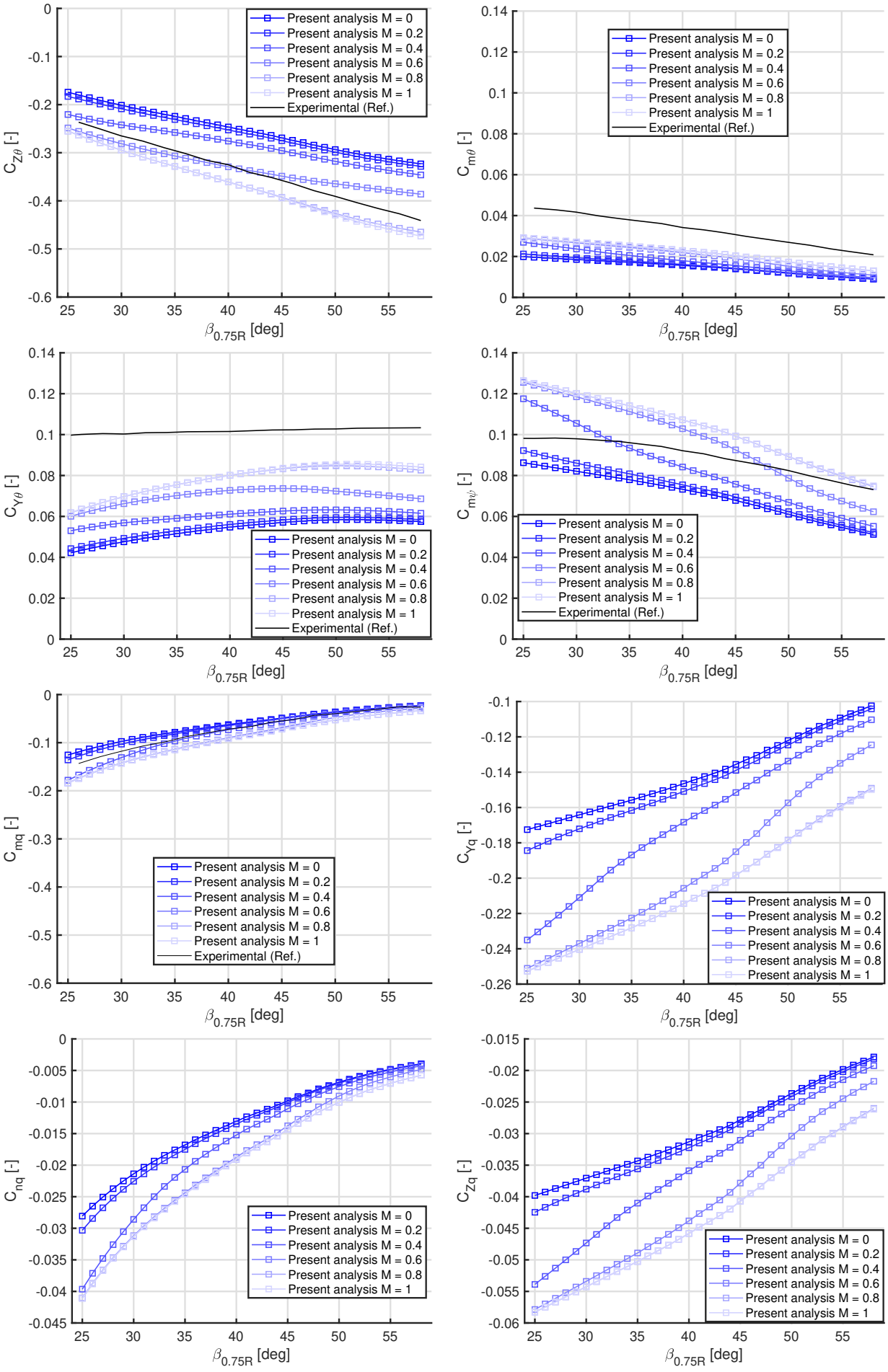

Figure 4.7: Propeller aerodynamic derivatives using Houbolt-Reed's method including wake effects. Mach changes from 0 to 1. Comparison with experimental data from Bennett and Bland [6].

5

Aeroelastic Models: Introduction

This chapter introduces the common tools that will be used in the following chapters to derive the aeroelastic models and analyse their aeroelastic behaviour.

5.1. Derivation of Equations of Motion

The equations of motion of the aeroelastic systems to be analysed in present report are to be derived via Lagrange's equations.

The Lagrange's equations are represented by:

$$\frac{d}{dt}\left(\frac{\partial T}{\partial \dot{q}_i}\right) - \frac{\partial T}{\partial q_i} + \frac{\partial U}{\partial q_i} + \frac{\partial D}{\partial \dot{q}_i} = Q_i \tag{5.1}$$

where q_i is the generalized degrees of freedom and Q_i the generalized forces in the system. T is the kinetic energy, U is the potential energy, and D is the dissipation/damping function.

The structural model determines the generalized coordinates that define the motion of the specific system under analysis. The principle of virtual work is then applied to determine the generalized forces and moments that act upon these generalized degrees of freedom. Such forces and moments are to be represented by the appropriate aerodynamic models.

The aeroelastic analyses in present work investigate the dynamic responses of a cantilever wing and propeller/s after a small deviation from an equilibrium state. Therefore, the generalized degrees of freedom are displacements from the equilibrium state.

5.2. State-Space System: the Eigenvalue Analysis

The equations of motion for the aeroelastic systems to be derived in present report has the following form

$$\mathbf{M}\ddot{\mathbf{q}} + \mathbf{C}\dot{\mathbf{q}} + \mathbf{K}\mathbf{q} = \mathbf{0} \tag{5.2}$$

where **M** is the mass matrix, **C** is the damping matrix, **K** is the stiffness matrix, and **q** is the vector of N degrees of freedom of the aeroelastic system.

Equation (5.2) is a set of second-order differential equations which can be reduced to a set of first-order differential equations by being written in a state-space form such as:

$$\begin{bmatrix} \dot{\mathbf{q}} \\ \ddot{\mathbf{q}} \end{bmatrix} = \begin{bmatrix} \mathbf{0} & \mathbf{I} \\ -\mathbf{M}^{-1}\mathbf{K} & -\mathbf{M}^{-1}\mathbf{C} \end{bmatrix} \begin{bmatrix} \mathbf{q} \\ \dot{\mathbf{q}} \end{bmatrix} \tag{5.3}$$

where **0** and **I** are zero and identity matrices, respectively.

The stability of the aeroelastic system can be analysed by obtaining the eigenvalues and eigenvectors of the state matrix **J**

$$\mathbf{J} = \begin{bmatrix} \mathbf{0} & \mathbf{I} \\ -\mathbf{M}^{-1}\mathbf{K} & -\mathbf{M}^{-1}\mathbf{C} \end{bmatrix} \tag{5.4}$$

J is a $2N \times 2N$ matrix, if all matrix elements are real numbers there will be N pairs of eigenvalues with each pair being real values or forming a complex conjugate pair. Each of these pairs have associated a distinct mode shape. The eigenvalues of **J** provide information of the frequency and damping rate of the aeroelastic system's vibrational modes, and the corresponding eigenvectors represent the mode shapes. For a given mode, the undamped natural frequency ω and damping ratio ζ are calculated from the real and imaginary parts of the eigenvalue λ [47]:

$$\begin{aligned} \omega &= \sqrt{\Re(\lambda)^2 + \Im(\lambda)^2} \\ \zeta &= -\frac{\Re(\lambda)}{\omega} \end{aligned} \tag{5.5}$$

Thus, the eigenvalues can also be expressed as

$$\lambda = -\zeta\omega \pm j\omega\sqrt{1-\zeta^2} \tag{5.6}$$

where $j = \sqrt{-1}$.

The system is unstable when the damping ratio ζ becomes negative or when the real part of the eigenvalue λ becomes positive. The undamped natural frequencies ω determine which modes are coupling to cause an instability: instability can happen when the frequencies of two different modes come close to each other.

The eigenvectors **z** of the state matrix **J** are the mode shapes of the aeroelastic system and have the following form

$$\mathbf{z}_i = \begin{bmatrix} \hat{\mathbf{x}}_i \\ \lambda_i \hat{\mathbf{x}}_i \end{bmatrix} \tag{5.7}$$

where $\hat{\mathbf{x}}_i$ are the first N elements of the eigenvector related to the i^{th} mode, these are the displacement components of the mode shapes. In this case, they are the first N elements of the eigenvectors because matrix **J** is arranged according to $\begin{bmatrix} \mathbf{q} \\ \dot{\mathbf{q}} \end{bmatrix}$.

The general solution to Equation (5.3) is given by

$$\mathbf{q} = \sum_{i=1}^{2N} c_i \hat{\mathbf{x}}_i e^{\lambda_i t} = \sum_{i=1}^{2N} c_i \hat{\mathbf{x}}_i e^{-\zeta_i \omega_i t} e^{j\omega_i \sqrt{1-\zeta_i^2} t} \tag{5.8}$$

where c_i are constants to be determined by the initial conditions. The physical time response is simply the real part of **q**.

Complex mode shapes

If the eigenvalues are complex values, the associated eigenvectors will also constitute of complex numbers. One way of visualizing these complex mode shapes is to plot them in time.

Let $\hat{\mathbf{x}}$ be the displacement components of a complex mode shape

$$\hat{\mathbf{x}} = \Re(\hat{\mathbf{x}}) + j\Im(\hat{\mathbf{x}}) \tag{5.9}$$

By definition, the physical displacement in time defined by the complex mode shape, $\mathbf{x}(t)$, is given by

$$\mathbf{x}(t) = \Re\left(\hat{\mathbf{x}} e^{-\zeta_i \omega_i t} e^{j\omega_d t}\right) \tag{5.10}$$

where ω_d is the damped natural frequency of the mode shape defined as $\omega_d = \omega\sqrt{1-\zeta^2}$ and t the time. Introducing Euler's formula

$$\begin{aligned} \mathbf{x}(t) &= e^{-\zeta_i \omega_i t} \cdot \Re\left[\left(\Re(\hat{\mathbf{x}}) + j\Im(\hat{\mathbf{x}})\right) \cdot \left(\cos\omega_d t + j\sin\omega_d t\right)\right] = \\ &= e^{-\zeta_i \omega_i t} \cdot \left[\Re(\hat{\mathbf{x}})\cos\omega_d t - \Im(\hat{\mathbf{x}})\sin\omega_d t\right] \end{aligned} \tag{5.11}$$

Note that flutter is a particular case in which the value of damping ζ becomes zero going from positive to negative. Therefore, the expression for plotting a mode shape in flutter would be:

$$\mathbf{x}(t) = \Re\left(\hat{\mathbf{x}}e^{j\omega t}\right) = \Re(\hat{\mathbf{x}})\cos\omega t - \Im(\hat{\mathbf{x}})\sin\omega t \tag{5.12}$$

5.2.1. Identifying the Instabilities

To identify the instabilities of the aeroelastic system a velocity interval is specified. The velocity starts from an initial velocity, usually zero, and is increased by ΔV. At each velocity V, the matrix **J** is determined and its eigenvalues and eigenvectors (mode shapes) are calculated.

After the calculations are made for all the velocities in the set interval, it is possible to plot V-g and V-f curves, these are inflow airspeeds versus damping ratio curves and inflow airspeeds versus frequency curves, respectively. The first velocity at which the damping ratio of a mode becomes zero is defined as the critical speed and marks the start of an instability. System instabilities (i.e. wing/whirl flutter and wing/whirl divergence) are identified by having negative damping ratios:

- Wing/whirl flutter is an instability with diverging oscillatory/spiral motions. The eigenvalues are complex numbers with a positive real part and a non-zero imaginary part. Therefore, the motion will have a non-zero natural frequency and a negative damping ratio. Flutter velocity is defined as the velocity at which the damping ratio becomes zero.

- Wing/whirl divergence is an instability with diverging static motions. The eigenvalues are real positive numbers. Therefore, the motion will have a zero or non-zero natural frequency and a damping ratio of value minus one. Zero natural frequency takes place when the imaginary part first becomes zero.

V-g and V-f diagrams can also be represented by the real part and imaginary part of the eigenvalues. In this case, V-g curves show the inflow airspeeds versus the real part of the eigenvalues and V-f curves show the inflow airspeeds versus the imaginary part of the eigenvalues. Another useful diagram is the root locus plot: the imaginary parts are plotted against the real parts. Then, the instabilities are identified by detecting the velocities at which the real part of the eigenvalues becomes positive. Null imaginary parts are peculiar to wing/whirl divergence.

5.2.2. Benignity of Flutter

There are different types of flutter behaviours depending on how damping changes with increasing airspeed (see Figure 5.1). Soft flutter is characterised by a gradual decrease in damping with increasing airspeed, whereas hard flutter occurs when this decrease is abrupt and violent. In hump mode, damping decreases to soon increase again returning to stability, this may result in much lower flutter speed [57].

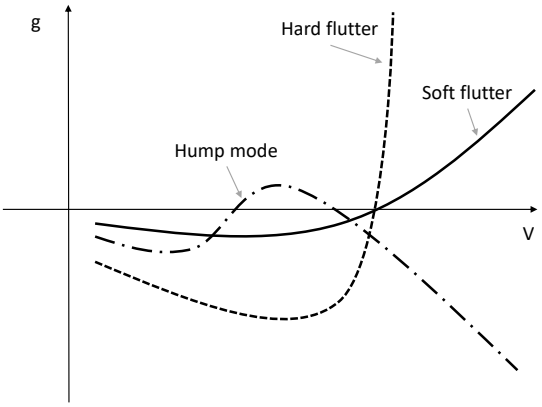

Figure 5.1: V-g diagram showing different flutter behaviours (adapted from [57]). Here, 'g' may be the real part of the eigenvalues or the negative of damping '$-\zeta$'.

Benignity of flutter is a concept that can be employed to evaluate flutter behaviours. For a chosen velocity interval around the flutter velocity (ΔV) the corresponding interval of damping ratio ($\Delta\zeta$) is determined. Benignity is defined as

$$\text{Benignity} = \left(\frac{\Delta\zeta}{\Delta V}\right)^{-1} \tag{5.13}$$

High benignity values indicate that flutter can be avoided by adding small amounts of structural damping. Low values of benignity values indicate that large amount of structural damping is required to avoid the onset of flutter.

Flutter benignity may also be gauged intuitively by looking at the V-g diagram. Small slope around the flutter velocity indicate high benignity and acute slope around the flutter velocity indicate low benignity.

5.2.3. Ordering the Mode Shapes

It can happen that at each velocity iteration, depending on the criterion used to order the eigenvalues, the order of mode shapes (eigenvectors) can switch from the previous velocity iteration. For example, if the eigenvalues are ordered in ascending order of their real part, at the velocity iteration where the real part of one mode becomes smaller than the real part of another mode, the eigenvalues switch their order in the vector and so do their corresponding mode shapes. If a switch occurs, the modes must be re-ordered. To track the mode shapes at each velocity iteration, the cross-orthogonality correlation analysis of modes before and after each iteration is performed.

The correlation analysis is performed using the Modal Assurance Criterion (MAC), which is expressed as

$$\text{MAC}(\boldsymbol{\phi_1}, \boldsymbol{\phi_2}) = \frac{\left(\boldsymbol{\phi_1}^T \cdot \boldsymbol{\phi_2}\right)^2}{\left(\boldsymbol{\phi_1}^T \cdot \boldsymbol{\phi_1}\right)\left(\boldsymbol{\phi_2}^T \cdot \boldsymbol{\phi_2}\right)} \tag{5.14}$$

where $\boldsymbol{\phi_1}$ and $\boldsymbol{\phi_2}$ are the correlated modes. If $\boldsymbol{\phi_1}$ and $\boldsymbol{\phi_2}$ are identical, MAC will have a value of one; if $\boldsymbol{\phi_1}$ and $\boldsymbol{\phi_2}$ are very different, the MAC value will be close to zero.

At each velocity iteration, the modes of current iteration is compared to the modes of the previous iteration by calculating the matrix of MAC values. The modes of current iteration are reordered accordingly so the order of modes remain the same at each velocity iteration.

6

Propeller on a Rigid Wing

This chapter deals with the dynamic behaviour of an isolated propeller under pitching and yawing motions (propeller flexibly attached to a rigid wing). The nacelle-pylon is simplified as a massless rigid rod with two elastic centres for pitch and yaw deflections. Small-angle approximation is applied to both. The propeller rotor is simplified as a rotor with $N_b > 2$ blades. There are no aerodynamic interference effects induced by the wing or adjacent structural elements. The kinetic energy of the rotating parts are ignored.

The kinematic scheme of an isolated propeller with pitching and yawing motions is visualized in Figure 6.1. The propeller pitches an angle θ about the Y_I-axis and yaws an angle ψ about the $Z-$axis. The propeller aerodynamic loads are composed of a side-force F_Y in the $Y-$axis, vertical force F_Z in the $Z-$axis and moments $M_{Y,P}$ and $M_{Z,P}$ about the $Y-$ and $Z-$axis, respectively. If the propeller is windmilling, there is no thrust force. If the propeller is not windmilling, there will be a thrust force acting on the X-axis. Thrust has very little effect on the dynamic system of an isolated propeller or a propeller on rigid wing and it is often neglected [85]. X_I, Y_I, and Z_I are the space fixed axes and X, Y, and Z are the body fixed axes that do not rotate with the propeller.

6.1. Derivation of the Equations of Motion

The system shown in Figure 6.1 is modelled into a dynamic system with two degrees of freedom. The equations of motion of such a system is formulated via Lagrange's equations.

The Lagrange's equations are represented by:

$$\frac{d}{dt}\left(\frac{\partial T}{\partial \dot{q}_i}\right) - \frac{\partial T}{\partial q_i} + \frac{\partial U}{\partial q_i} + \frac{\partial D}{\partial \dot{q}_i} = Q_i \tag{5.1}$$

where q_i is the generalized degrees of freedom and Q_i the generalized forces in the system. T is the kinetic energy, U is the potential energy, and D is the dissipation/damping function.

The generalized degrees of freedom are the pitch θ and yaw ψ angles and the generalized forces are given by the aerodynamic forces and moments acting on the pitching and yawing propeller.

The angular velocities of the system are the pitch rate $\dot{\theta}$, the yaw rate $\dot{\psi}$, and the propeller rotational speed Ω. These vectors can be grouped into the components along the X, Y, and Z axes:

$$\begin{aligned} \omega_X &= \Omega + \dot{\theta}\sin\psi \approx \Omega + \dot{\theta}\psi \\ \omega_Y &= \dot{\theta}\cos\psi \approx \dot{\theta} \\ \omega_Z &= \dot{\psi} \end{aligned} \tag{6.1}$$

The total kinetic energy of the system is:

$$\begin{aligned} T &= \frac{1}{2}I_X\omega_X^2 + \frac{1}{2}I_Y\omega_Y^2 + \frac{1}{2}I_Z\omega_Z^2 \approx \\ &\approx \frac{1}{2}I_X\left(\Omega^2 + 2\Omega\dot{\theta}\psi\right) + \frac{1}{2}I_Y\dot{\theta}^2 + \frac{1}{2}I_Z\dot{\psi}^2 \end{aligned} \tag{6.2}$$

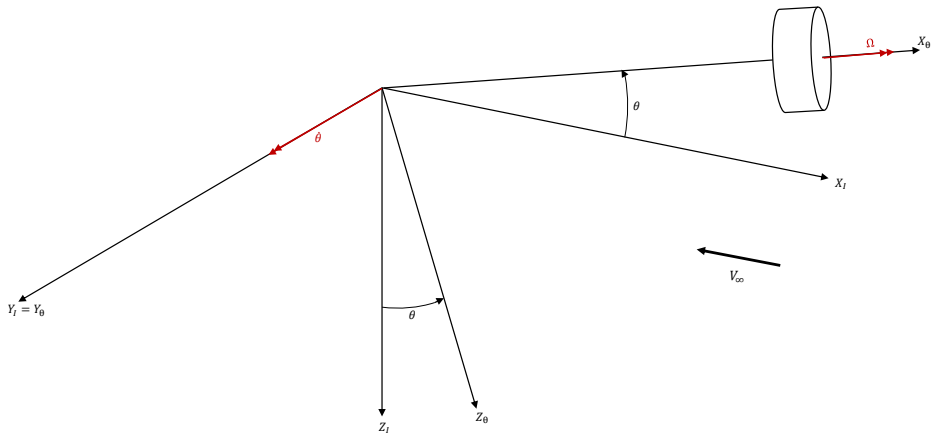

(a) θ rotation

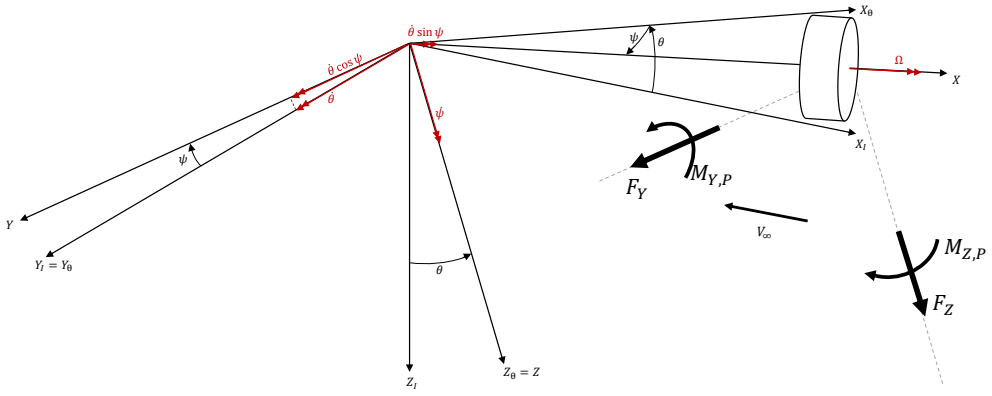

(b) ψ rotation

Figure 6.1: Kinematic scheme of the idealized propeller-engine-nacelle system (adapted from [88]).

where I_X is propeller mass moment of inertia about the axis of rotation, and I_Y and I_Z are the propeller mass moments of inertia about Y and Z axes, respectively.

The potential energy of the system is:

$$U = \frac{1}{2} K_\theta \theta^2 + \frac{1}{2} K_\psi \psi^2 \tag{6.3}$$

where K_θ stiffness of the propeller attachment in pitch and K_ψ is the stiffness of the propeller attachment in yaw.

The structural damping of the system is modelled as 'hysteretic' damping (or also known as simply 'structural damping') commonly employed in flutter analysis [1]:

$$D = \frac{1}{2} \frac{K_\theta g_\theta}{\omega} \dot{\theta}^2 + \frac{1}{2} \frac{K_\psi g_\psi}{\omega} \dot{\psi}^2 \tag{6.7}$$

where ω is damped natural pitching/yawing frequency and g_θ and g_ψ are the damping coefficients for the uncoupled pitch and yaw modes, respectively.

Applying the Lagrange's equations, the differential equations of motion are:

$$\begin{aligned}
&\underbrace{I_Y \ddot{\theta}}_{\text{Inertia}} + \underbrace{I_X \Omega \dot{\psi}}_{\text{Gyroscopic}} + \underbrace{K_\theta \theta}_{\text{Elastic}} + \underbrace{\frac{K_\theta g_\theta}{\omega} \dot{\theta}}_{\text{Structural damping}} = \underbrace{M_Y}_{\text{Aerodynamic}} \\
&\underbrace{I_Z \ddot{\psi}}_{\text{Inertia}} - \underbrace{I_X \Omega \dot{\theta}}_{\text{Gyroscopic}} + \underbrace{K_\psi \psi}_{\text{Elastic}} + \underbrace{\frac{K_\psi g_\psi}{\omega} \dot{\psi}}_{\text{Structural damping}} = \underbrace{M_Z}_{\text{Aerodynamic}}
\end{aligned} \tag{6.8}$$

where $I_X \Omega \dot{\psi}$ and $-I_X \Omega \dot{\theta}$ are the gyroscopic terms that couple pitching and yawing motions; M_Y and M_Z are the aerodynamic forces. From Equation (6.8), the nature of the various forces and moments that act on the system can be identified; the inertia, damping, and elastic components are typical of dynamic systems but the gyroscopic and aerodynamic forces are induced by the rotating propeller.

M_Y is the total pitching moment about the pitching pivot point and M_Z is the total yawing moment about the yawing pivot point. These moments are obtained from the in-plane aerodynamic forces and moments that act on the propeller hub (see Equation (4.25)). When the propeller axis is deflected in pitch or yaw with respect to the free stream, aerodynamic forces and moments are generated and are proportional to the angle

[1] There are two types of structural damping model often used in Aeroelasticity: 'Hysteretic' or (misleadingly called) structural damping and viscous damping. In structural (hysteretic) damping, the damping force is proportional to the elastic restoring force and it is in phase with the oscillation velocity. In viscous damping, the damping force is proportional to the oscillation velocity.

Let's consider the motion in pitch, θ. It is possible to establish an equivalence between structural damping and viscous damping for the same amount of damping energy dissipated. At a given oscillation amplitude and for a sinusoidal pithing motion of frequency ω:

$$g_\theta = 2\zeta_\theta \frac{\omega}{\omega_\theta} \tag{6.4}$$

$$\zeta_\theta = \frac{c_\theta}{2 I_Y \omega_\theta} \tag{6.5}$$

where ζ_θ is the viscous damping coefficient relative to critical damping, ω_θ is the undamped natural pitching frequency of a nonrotating propeller, and c_θ is the damping coefficient. If the propeller is not spinning, $\omega \approx \omega_\theta$, therefore, $g_\theta \approx 2\zeta_\theta$. If the propeller is spinning, gyroscopic effects cause the values of ω to be different from that of ω_θ, in such cases, the calculated damping forces will depend on whether the system is modelled with the 'hysteretic' type or viscous type of structural damping [70][88].

In current work, if structural or 'hysteretic' damping is to be substituted by viscous damping, assuming equal dissipated energy between both models and $\omega_\theta = \sqrt{\frac{K_\theta}{I_Y}}$, the following is applied:

$$\frac{K_\theta g_\theta}{\omega} = 2\zeta_\theta \omega_\theta I_Y \tag{6.6}$$

this is known as the viscous equivalent of the structural damping model.

$\overline{\eta} = \frac{K_\theta g_\theta}{\omega}$ is also called loss factor and $K_\theta(1 + \overline{\eta} j)$ the complex stiffness model or the Kelvin–Voigt model which is often found describing the internal damping in viscoelastic materials [47].

deflected and its rate of change (assuming small deflections). Therefore, the aerodynamic forces and moments can be expressed as function of aerodynamic derivatives with respect to the pitch and yaw deflections and their respective rate of change.

$$\begin{aligned} F_Z &= \frac{1}{2}\rho V^2 S'\left(C_{Z_\theta}\overline{\theta} + C_{Z_\psi}\overline{\psi} + C_{Z_q}\frac{\dot{\overline{\theta}}R}{V} + C_{Z_r}\frac{\dot{\overline{\psi}}R}{V}\right) \\ M_{Y,P} &= \rho V^2 S' R\left(C_{m_\theta}\overline{\theta} + C_{m_\psi}\overline{\psi} + C_{m_q}\frac{\dot{\overline{\theta}}R}{V} + C_{m_r}\frac{\dot{\overline{\psi}}R}{V}\right) \\ F_Y &= \frac{1}{2}\rho V^2 S'\left(C_{Y_\theta}\overline{\theta} + C_{Y_\psi}\overline{\psi} + C_{Y_q}\frac{\dot{\overline{\theta}}R}{V} + C_{Y_r}\frac{\dot{\overline{\psi}}R}{V}\right) \\ M_{Z,P} &= \rho V^2 S' R\left(C_{n_\theta}\overline{\theta} + C_{n_\psi}\overline{\psi} + C_{n_q}\frac{\dot{\overline{\theta}}R}{V} + C_{n_r}\frac{\dot{\overline{\psi}}R}{V}\right) \end{aligned} \tag{4.25}$$

where ρ is the air density, V the free stream velocity, S' the propeller disk area ($S' = \pi R^2$), R the propeller radius, $\overline{\theta}$ and $\overline{\psi}$ the effective pitch and yaw angles between the propeller axis and the relative wind.

$$\begin{aligned} \overline{\theta} &= \theta - \frac{e_\theta \dot{\theta}}{V} \\ \overline{\psi} &= \psi - \frac{e_\psi \dot{\psi}}{V} \end{aligned} \tag{4.26}$$

where e_θ is the pitch rotational axis to the propeller plane and e_ψ is the yaw rotational axis to the propeller plane. e_θ and e_ψ are positive.

The moments around the pivot points are:

$$\begin{aligned} M_Y &= M_{Y,P} - e_\theta F_Z \\ M_Z &= M_{Z,P} + e_\psi F_Y \end{aligned} \tag{6.9}$$

Because of symmetry between the pitching and yawing motions and assuming no aerodynamic interference between the wing and the propeller:

$$\begin{aligned} C_{Z_\psi} &= C_{Y_\theta} & C_{Z_r} &= C_{Y_q} \\ C_{m_\psi} &= -C_{n_\theta} & C_{m_r} &= -C_{n_q} \\ C_{Y_\psi} &= -C_{Z_\theta} & C_{Y_r} &= -C_{Z_q} \\ C_{n_\psi} &= C_{m_\theta} & C_{n_r} &= C_{m_q} \end{aligned} \tag{4.27}$$

Substituting Equation 4.25, Equation 4.26, Equation 4.27, and Equation 6.9 in Equation 6.8 yields the following:

$$\mathbf{M_s}\ddot{\mathbf{q}} + \mathbf{C_s}\dot{\mathbf{q}} + \mathbf{K_s}\mathbf{q} = \mathbf{M_a}\ddot{\mathbf{q}} + \mathbf{C_a}\dot{\mathbf{q}} + \mathbf{K_a}\mathbf{q} \tag{6.10}$$

where $\mathbf{q}$ is the vector of generalised coordinates, $\mathbf{M_s}$ is the propeller structural mass matrix, $\mathbf{C_s}$ is the propeller damping mass matrix, $\mathbf{K_s}$ is the propeller stiffness mass matrix, $\mathbf{M_a}$ is the propeller aerodynamic mass matrix, $\mathbf{C_a}$ is the propeller aerodynamic damping matrix, and $\mathbf{K_a}$ is the propeller aerodynamic stiffness matrix.

The generalised coordinate vector is

$$\mathbf{q} = \begin{bmatrix} \theta \\ \psi \end{bmatrix} \tag{6.11}$$

The propeller structural mass matrix is given by

$$\mathbf{M_s} = \begin{bmatrix} I_Y & 0 \\ 0 & I_Z \end{bmatrix} \tag{6.12}$$

The propeller structural damping matrix is given by

$$\mathbf{C_s} = \begin{bmatrix} \frac{K_\theta g_\theta}{\omega} & I_X\Omega \\ -I_X\Omega & \frac{K_\psi g_\psi}{\omega} \end{bmatrix} \tag{6.13}$$

The propeller structural stiffness matrix is given by

$$\mathbf{K_s} = \begin{bmatrix} K_\theta & 0 \\ 0 & K_\psi \end{bmatrix} \tag{6.14}$$

The propeller aerodynamic mass matrix is given by

$$\mathbf{M_a} = \begin{bmatrix} -k_2 C_{mq}\frac{R}{V}\frac{e_\theta}{V} + e_\theta k_1 C_{Zq}\frac{R}{V}\frac{e_\theta}{V} & -k_2 C_{mr}\frac{R}{V}\frac{e_\psi}{V} + e_\theta k_1 C_{Zr}\frac{R}{V}\frac{e_\psi}{V} \\ -k_2 C_{nq}\frac{R}{V}\frac{e_\theta}{V} - e_\psi k_1 C_{Yq}\frac{R}{V}\frac{e_\theta}{V} & -k_2 C_{nr}\frac{R}{V}\frac{e_\psi}{V} - e_\psi k_1 C_{Yr}\frac{R}{V}\frac{e_\psi}{V} \end{bmatrix} \tag{6.15}$$

The propeller aerodynamic damping matrix is given by

$$\mathbf{C_a} = \begin{bmatrix} -k_2 C_{m\theta}\frac{e_\theta}{V} + k_2 C_{mq}\frac{R}{V} + e_\theta k_1 C_{Z\theta}\frac{e_\theta}{V} - e_\theta k_1 C_{Zq}\frac{R}{V} & -k_2 C_{m\psi}\frac{e_\psi}{V} + k_2 C_{mr}\frac{R}{V} + e_\theta k_1 C_{Z\psi}\frac{e_\psi}{V} - e_\theta k_1 C_{Zr}\frac{R}{V} \\ -k_2 C_{n\theta}\frac{e_\theta}{V} + k_2 C_{nq}\frac{R}{V} - e_\psi k_1 C_{Y\theta}\frac{e_\theta}{V} + e_\psi k_1 C_{Yq}\frac{R}{V} & -k_2 C_{n\psi}\frac{e_\psi}{V} + k_2 C_{nr}\frac{R}{V} - e_\psi k_1 C_{Y\psi}\frac{e_\psi}{V} + e_\psi k_1 C_{Yr}\frac{R}{V} \end{bmatrix} \tag{6.16}$$

The propeller aerodynamic stiffness matrix is given by

$$\mathbf{K_a} = \begin{bmatrix} k_2 C_{m\theta} - e_\theta k_1 C_{Z\theta} & k_2 C_{m\psi} - e_\theta k_1 C_{Z\psi} \\ k_2 C_{n\theta} + e_\psi k_1 C_{Y\theta} & k_2 C_{n\psi} + e_\psi k_1 C_{Y\psi} \end{bmatrix} \tag{6.17}$$

where $k_1 = \frac{1}{2}\rho V^2 S'$, $k_2 = \rho V^2 S' R$, $S' = \pi R^2$ is the area swept by the propeller blades and R is the propeller radius.

In state-space form Equation (6.10) becomes:

$$\begin{bmatrix} \dot{\mathbf{q}} \\ \ddot{\mathbf{q}} \end{bmatrix} = \begin{bmatrix} \mathbf{0} & \mathbf{I} \\ -(\mathbf{M_s}-\mathbf{M_a})^{-1}(\mathbf{K_s}-\mathbf{K_a}) & -(\mathbf{M_s}-\mathbf{M_a})^{-1}(\mathbf{C_s}-\mathbf{C_a}) \end{bmatrix} \begin{bmatrix} \mathbf{q} \\ \dot{\mathbf{q}} \end{bmatrix} \tag{6.18}$$

where $\mathbf{0}$ and $\mathbf{I}$ are 2×2 zero and identity matrices, respectively.

$$\mathbf{J} = \begin{bmatrix} \mathbf{0} & \mathbf{I} \\ -(\mathbf{M_s}-\mathbf{M_a})^{-1}(\mathbf{K_s}-\mathbf{K_a}) & -(\mathbf{M_s}-\mathbf{M_a})^{-1}(\mathbf{C_s}-\mathbf{C_a}) \end{bmatrix} \tag{6.19}$$

The eigenvalue analysis as explained in Section 5.2 is performed on $\mathbf{J}$. In this system, there are two mode shapes, backward whirl mode (lower frequency) and forward whirl mode (higher frequency). The critical velocity or whirl flutter speed is the value of the inflow velocity at which the damping ratio ζ is zero. For inflow velocities below the critical value, the damping ratio ζ of the system is positive; for inflow velocities above the critical value, the damping ratio ζ is negative (see Figure 6.2).

6.2. Verification and Validation

The expressions derived in Section 6.1 to predict possible occurrence of whirl flutter are implemented in Matlab. The validation and verification of the implementation is carried out by modelling the propellers analysed in Bennett and Bland [6][2] by comparing whirl flutter velocities and whirl flutter frequencies with their measured values.

Bennett and Bland [6] conducted an experimental campaign in which they measured whirl flutter velocities and whirl flutter frequencies of an isolated windmilling propeller with four blades. Two configurations of propeller were tested. They differ in the position of their elastic centre (the pivot point of the nacelle-pylon system). The elastic centre in Configuration (A) is positioned 0.346R from the rotor plane and the elastic centre in Configuration (B) is positioned 0.691R from the rotor plane. The change in elastic axis position also changes the moment of inertia with respect to $Y-$ and $Z-$axis.

[2]This is the same work used to validate the methodology for propeller aerodynamics, Section 4.2.

Data needed to model the propeller are extracted from [[6], Table I, Table II, Figure 4, Figure 5]. Six cases are selected for configuration (A) and seven cases for configuration (B). Each of these cases differ in the propeller blade angle at three-quarter chord $\beta_{0.75R}$, the pitch and yaw undamped frequency of the system (f_θ, f_ψ), the viscous damping parameter (ζ_θ, ζ_ψ), and the air density ρ. The input data extracted from literature are presented in Table 6.1 and Table 6.2. Note that the structural damping of the system is represented by its viscous equivalent.

case ID	$\beta_{0.75R}$ [deg]	f_θ [Hz]	f_ψ [Hz]	$2\zeta_\theta$	$2\zeta_\psi$	ρ [slug/ft^3]
1	35	9.20	9.12	0.0060	0.0090	0.00211
2	35	10.96	10.96	0.0150	0.0238	0.00217
3	46	10.96	10.96	0.0150	0.0238	0.00218
4	52	10.96	10.96	0.0150	0.0238	0.00209
5	58	10.96	10.96	0.0150	0.0238	0.00209
6	58	10.71	10.28	0.0300	0.0393	0.00220

Table 6.1: Configuration (A). $e_\psi = e_\theta = 0.346R, I_Y = I_Z = 0.0634$ slug-ft^2 [6]

case ID	$\beta_{0.75R}$ [deg]	f_θ [Hz]	f_ψ [Hz]	$2\zeta_\theta$	$2\zeta_\psi$	ρ [slug/ft^3]
7	35	7.60	7.60	0.0056	0.0053	0.00227
8	46	7.60	7.60	0.0056	0.0053	0.00226
9	52	7.60	7.60	0.0056	0.0053	0.00226
10	27.5	7.64	7.68	0.0060	0.0074	0.00226
11	35	7.64	7.68	0.0060	0.0074	0.00220
12	46	7.64	7.68	0.0060	0.0074	0.00220
13	58	7.64	7.68	0.0060	0.0062	0.00220

Table 6.2: Configuration (B). $e_\psi = e_\theta = 0.691R, I_Y = I_Z = 0.0937$ slug-ft^2 [6]

An example of modal frequency and modal damping with increasing inflow velocity is illustrated in Figure 6.2. As mentioned, there are two modes that represent the system dynamics. Forward whirl mode occurs at higher frequencies than backward whirl mode. The frequency gap between these two modes increases with increasing inflow velocity. It can be seen that forward whirl mode never goes unstable, this is the case when propeller blades are rigid, which is one of the assumptions taken in the present model. Whirl flutter velocity is represented by the inflow velocity that causes the system backward whirl mode to have zero damping.

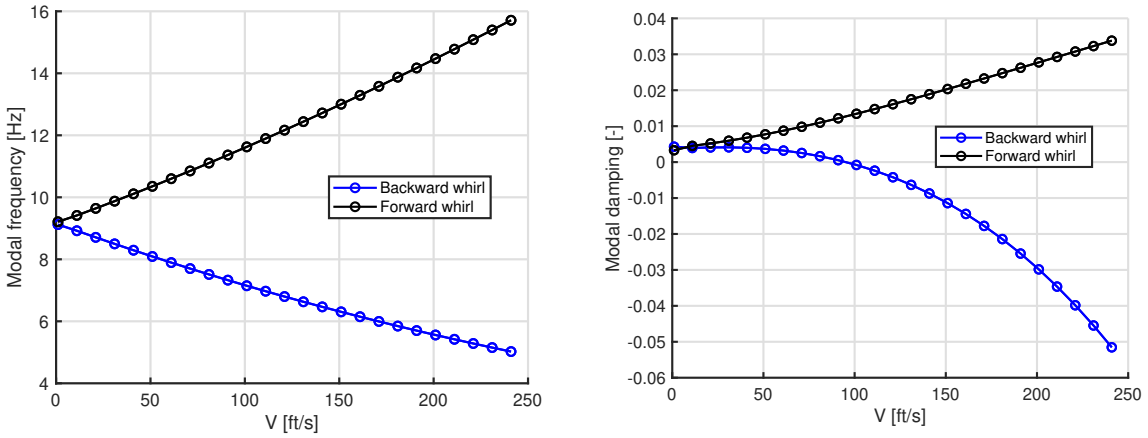

(a) Modal frequency.

(b) Modal damping.

Figure 6.2: Configuration (A) case (1). Calculated modal frequency and damping values of an isolated propeller with two degrees-of-freedom. Propeller aerodynamic derivatives from Houbolt-Reed's method are used. Whirl flutter occurs at 95 ft/s.

Whirl flutter velocities and frequencies corresponding to each of the cases described in Table 6.1 and Table 6.2 are illustrated in Figure 6.3. Apart from recording whirl flutter speeds, Bennett and Bland [6] also

measured propeller aerodynamic derivatives, i.e. $C_{Z\theta}$, $C_{m\theta}$, $C_{Y\theta}$, $C_{m\psi}$, C_{mq}, and C_{Yq}.

Experimental whirl flutter speeds and frequencies extracted from Bennett and Bland [6] (blue markers) are compared with the calculated values from present model using measured propeller aerodynamic derivatives from Bennett and Bland [6] (black markers) and the calculated values from present model using propeller aerodynamic derivatives obtained with Houbolt-Reed's method (red markers). Note that only five propeller aerodynamic derivatives were measured by Bennett and Bland [6] and thus used in the present analysis. When using Houbolt-Reed's method, all sixteen propeller aerodynamic derivatives were calculated and included in the present analysis.

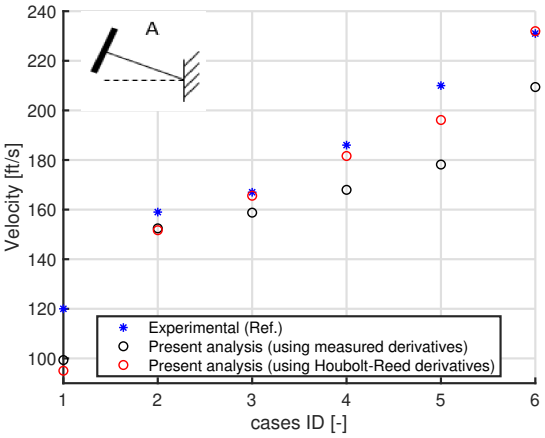

(a) Whirl flutter velocity. Configuration A.

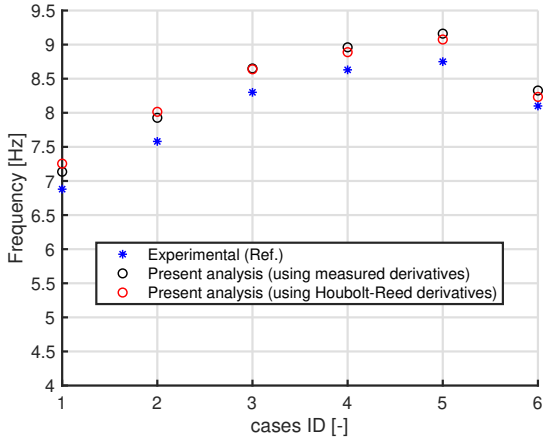

(b) Whirl flutter frequency. Configuration A.

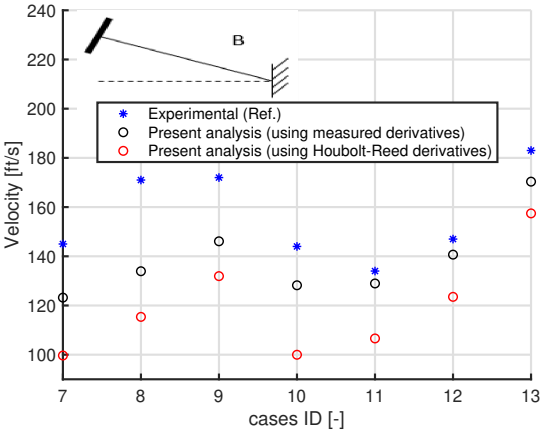

(c) Whirl flutter velocity. Configuration B.

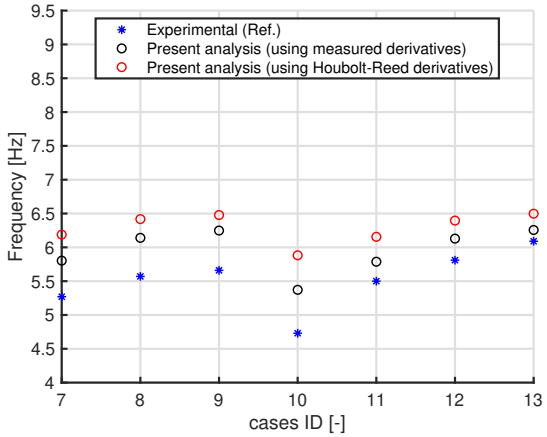

(d) Whirl flutter frequency. Configuration B.

Figure 6.3: Whirl flutter velocities and frequencies. Comparison with data from Bennett and Bland [6].

In general, analytical results are conservative. Present model predicts lower whirl flutter velocities and higher whirl flutter frequencies. In configuration (A), using calculated propeller aerodynamic derivatives can better predict flutter velocities than using measured propeller aerodynamic derivatives. In terms of frequency, the differences are small. The fact that using calculated propeller aerodynamic derivatives predicts values closer to experimental results can be attributed to the fact that all aerodynamic derivatives were included in the calculations whereas when using measured propeller aerodynamic derivatives, only five were available.

However, in configuration (B) the contrary happens. Using calculated propeller aerodynamic derivatives yields worse results in comparison with experimental data. This may be attributed to the fact that configuration (B) has the elastic axis further away from the propeller plane. The assumption of the nacelle-pylon behaving like a rigid rod is less correct; a flexible nacelle-pylon creates additional (unsteady) aerodynamic effects which are not accounted for in the present model.

In conclusion, the method presented in this section predicts satisfactorily whirl flutter velocities and frequencies of an isolated propeller with rigid blades. More accurate results can be obtained if more realistic propeller aerodynamic derivatives can be predicted.

7

Flexible Cantilever Wing

In this chapter, an aeroelastic model to characterise a flexible cantilever wing is presented. The structural model is a linear dynamic Euler beam model and the aerodynamic model employs Theodorsen strip unsteady aerodynamics formulated in time domain. Two methodologies to convert the frequency domain terms into the time domain are presented. The coupling between the structural model and the aerodynamic model is such that the aerodynamic loads are only applied on the beam nodes and the transfer to the nodal vertical displacements and nodal torsion is direct.

7.1. Wing structural Model

The wing is idealised as an unswept tapered beam. Figure 7.1 shows a cross section of the wing. The motion of the wing is defined by the vertical displacement of its elastic axis, h (positive downwards), and the rotation or twist of the airfoils about the elastic axis, α. The displacement of a point on the airfoil is defined by z_W

$$z_W(x,y,t) = h + \Big(x - ab\Big)\alpha \tag{7.1}$$

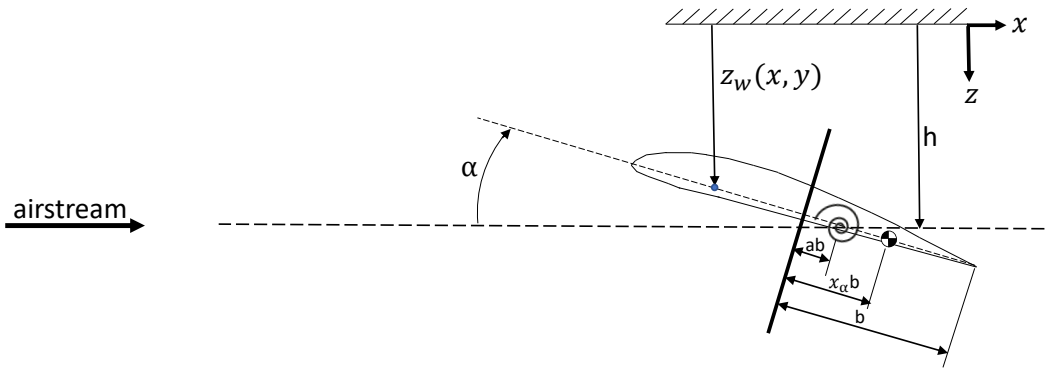

Figure 7.1: Wing cross section (adapted from [7]).

The kinetic energy of the wing is

$$T_W = \frac{1}{2}\int m_W \dot{z}_W^2 \, dy \tag{7.2}$$

where m_W is the wing mass per unit length. Substituting for z_W, this becomes

$$T_W = \frac{1}{2}\int m_W \dot{h}^2 \, dy + \frac{1}{2}\int m_W (x-ab)^2 \dot{\alpha}^2 \, dy + \int m_W (x-ab)\dot{h}\dot{\alpha} \, dy \tag{7.3}$$

The potential energy of the wing is

$$U_W = \frac{1}{2}\int GJ\Big(\frac{\partial \alpha}{\partial y}\Big)^2 dy + \frac{1}{2}\int EI\Big(\frac{\partial^2 h}{\partial y^2}\Big)^2 dy \tag{7.4}$$

where EI is the bending stiffness and GJ the torsional stiffness.

The finite element formulation (FEM) is introduced by the spacial discretization of the wing as shown in Figure 7.2. Each beam is a linear Euler Bernoulli beam which has transverse displacement, an out-of-plane bending moment, and a torsion moment. Hence, each node has three degrees of freedom: a nodal displacement h_i, a nodal bending rotation ϕ_i, and a nodal torsion α_i.

The total out-of-plane deflection of a beam element h, is defined by the nodal displacements h_i, and the nodal bending rotation[1] ϕ_i of its nodes such that

$$h = h_i N_1 + \phi_i N_2 + h_{i+1} N_3 + \phi_{i+1} N_4 = \mathbf{N}\cdot\mathbf{h}^T \tag{7.5}$$

where N_i are the Hermite shape functions to ensure C^1 continuity

$$\begin{aligned} N_1 &= \frac{1}{4}\Big(1-\xi\Big)^2\Big(2+\xi\Big) \\ N_2 &= \frac{1}{4}\Big(1+\xi\Big)^2\Big(2-\xi\Big) \\ N_3 &= \frac{l_e}{8}\Big(1-\xi\Big)^2\Big(1+\xi\Big) \\ N_4 &= \frac{l_e}{8}\Big(1+\xi\Big)^2\Big(1-\xi\Big) \end{aligned} \tag{7.6}$$

l_e is the beam length and $\xi = \frac{2y}{l_e} - 1$ is a nondimentional axial beam coordinate defined from -1 to 1.

Similarly, the torsion of the beam, α, is defined by the nodal torsion, α_i, such as

$$\alpha = \alpha_i T_1 + \alpha_{i+1} T_2 = \mathbf{T}\cdot\boldsymbol{\alpha}^T \tag{7.7}$$

where T_i are the shape functions defined as

$$\begin{aligned} T_1 &= 1 - \frac{1}{2}\Big(\xi+1\Big) \\ T_2 &= \frac{1}{2}\Big(\xi+1\Big) \end{aligned} \tag{7.8}$$

In the case of a wing discretized into only one beam element, the wing kinetic and potential energy can be expressed in terms of the nodal degrees of freedom by inserting the expressions for h and α (Equation (7.7) and Equation (7.5)) into Equation (7.3) and Equation (7.4)

$$\begin{aligned} T_W &= \frac{1}{2}\dot{\mathbf{h}}\mathbf{M_b}\dot{\mathbf{h}}^T + \frac{1}{2}\dot{\boldsymbol{\alpha}}\mathbf{M_t}\dot{\boldsymbol{\alpha}}^T + \mathbf{M_{tb}}\dot{\mathbf{h}}\dot{\boldsymbol{\alpha}} \\ U_W &= \frac{1}{2}\mathbf{h}\mathbf{K_b}\mathbf{h}^T + \frac{1}{2}\boldsymbol{\alpha}\mathbf{K_t}\boldsymbol{\alpha}^T \end{aligned} \tag{7.9}$$

where $\mathbf{M_b}$ is the bending mass matrix, $\mathbf{M_t}$ is the torsion mass matrix, $\mathbf{M_{tb}}$ is the torsion-bending mass coupling matrix, $\mathbf{K_b}$ is the bending stiffness matrix, and $\mathbf{K_t}$ is the torsion stiffness matrix.

[1] The bending rotation is defined as $\phi = \frac{\partial h(y,t)}{\partial y}$

$$
\begin{aligned}
\mathbf{M_b} &= \frac{m_W l_e}{2} \int_{-1}^{1} \mathbf{N}^T \mathbf{N} d\xi \\
\mathbf{M_t} &= \frac{\rho I_p l_e}{2} \int_{-1}^{1} \mathbf{T}^T \mathbf{T} d\xi \\
\mathbf{M_{tb}} &= \frac{m_W l_e x_\alpha b}{2} \int_{-1}^{1} \mathbf{T}^T \mathbf{N} d\xi \\
\mathbf{K_b} &= \frac{8EI}{l_e^3} \int_{-1}^{1} \frac{\partial^2 \mathbf{N}}{\partial \xi^2}^T \frac{\partial^2 \mathbf{N}}{\partial \xi^2} d\xi \\
\mathbf{K_t} &= \frac{2GJ}{l_e} \int_{-1}^{1} \frac{\partial \mathbf{N}}{\partial \xi}^T \frac{\partial \mathbf{N}}{\partial \xi} d\xi
\end{aligned}
\tag{7.10}
$$

where ρI_p is the mass polar moment of inertia per unit length of the wing, $x_\alpha b$ is the dimensional distance between the wing elastic axis to the centre of gravity, EI is the wing bending stiffness, and GJ is the wing torsional stiffness.

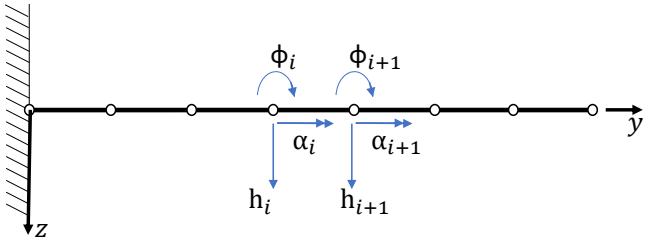

(a) Wing plan view.

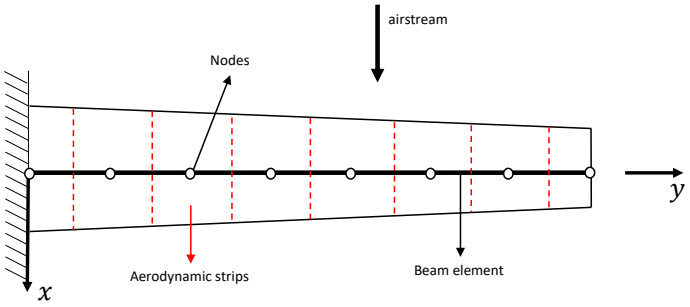

(b) Finite element representation.

Figure 7.2: Geometry of a clamped wing.

Conducting the integrals in Equation (7.10), the bending mass matrix is given by

$$
M_b = \begin{bmatrix}
\frac{13}{35} l_e m_W & \frac{11}{210} l_e^2 m_W & \frac{9}{70} l_e m_W & -\frac{13}{420} l_e^2 m_W \\
\frac{11}{210} l_e^2 m_W & \frac{1}{105} l_e^3 m_W & \frac{13}{430} l_e^2 m_W & -\frac{1}{140} l_e^3 m_W \\
\frac{9}{70} l_e m_W & \frac{13}{420} l_e^2 m_W & \frac{13}{35} l_e m_W & -\frac{11}{210} l_e^2 m_W \\
-\frac{13}{420} l_e^2 m_W & -\frac{1}{140} l_e^3 m_W & -\frac{11}{210} l_e^2 m_W & \frac{1}{105} l_e^3 m_W
\end{bmatrix}
\tag{7.11}
$$

The torsion mass matrix is given by

$$\mathbf{M_t} = \begin{bmatrix} \frac{\rho I_p l_e}{3} & \frac{\rho I_p l_e}{6} \\ \frac{\rho I_p l_e}{6} & \frac{\rho I_p l_e}{3} \end{bmatrix} \tag{7.12}$$

The torsion-bending inertial coupling mass matrix is given by

$$\mathbf{M_{tb}} = \begin{bmatrix} \frac{7}{20} m_W l_e x_\alpha b & \frac{1}{20} m_W l_e^2 x_\alpha b & \frac{3}{20} m_W l_e x_\alpha b & -\frac{1}{30} m_W l_e^2 x_\alpha b \\ \frac{3}{20} m_W l_e x_\alpha b & \frac{1}{30} m_W l_e^2 x_\alpha b & \frac{7}{20} m_W l_e x_\alpha b & -\frac{1}{20} m_W l_e^2 x_\alpha b \end{bmatrix} \tag{7.13}$$

The bending stiffness matrix is given by

$$\mathbf{K_b} = EI \begin{bmatrix} \frac{12EI}{l_e^3} & \frac{6EI}{l_e^2} & -\frac{12EI}{l_e^3} & \frac{6EI}{l_e^2} \\ \frac{6EI}{l_e^2} & \frac{4EI}{l_e} & -\frac{6EI}{l_e^2} & \frac{2EI}{l_e} \\ -\frac{12EI}{l_e^3} & -\frac{6EI}{l_e^2} & \frac{12EI}{l_e^3} & -\frac{6EI}{l_e^2} \\ \frac{6EI}{l_e^2} & \frac{2EI}{l_e} & -\frac{6EI}{l_e^2} & \frac{4EI}{l_e} \end{bmatrix} \tag{7.14}$$

The torsion stiffness matrix is given by

$$\mathbf{K_t} = \begin{bmatrix} \frac{GJ}{l_e} & -\frac{GJ}{l_e} \\ -\frac{GJ}{l_e} & \frac{GJ}{l_e} \end{bmatrix} \tag{7.15}$$

Defining a global displacement vector as

$$\mathbf{q_W} = \begin{bmatrix} h_1 & \phi_1 & \alpha_1 & h_2 & \phi_2 & \alpha_2 \end{bmatrix}^T \tag{7.16}$$

and then applying Lagrange's equations to the wing kinetic and potential energy expressions. The equations of motion of the wing may be expressed as

$$\mathbf{M_{s,g}} \ddot{\mathbf{q}}_\mathbf{W} + \mathbf{K_{s,g}} \mathbf{q_W} = \mathbf{Q_W} \tag{7.17}$$

where $\mathbf{M_{s,g}}$ is the global mass matrix obtained by assembling together the bending mass matrix, the torsion mass matrix, and the torsion-bending inertial coupling mass matrix according to the order of the degrees of freedom in the global displacement vector. Analogously, the global stiffness matrix $\mathbf{K_{s,g}}$ is assembled with the bending stiffness matrix and the torsion stiffness matrix. Note that there is no stiffness coupling between beam bending and beam torsion. $\mathbf{Q_W}$ is the global vector that represent the wing aerodynamic loads acting on the nodes of the beam model.

The wing aerodynamic loads that act on each node are

$$\mathbf{Q_W}_i = \begin{bmatrix} Q_{h,W} \\ 0 \\ Q_{\alpha,W} \end{bmatrix} \tag{7.18}$$

where $Q_{h,W}$ is the lift and $Q_{\alpha,W}$ is the aerodynamic pitching moment acting on an specific node.

The global wing aerodynamic load vector $\mathbf{Q_W}$ is

$$\mathbf{Q_W} = \begin{bmatrix} Q_{h,W_1} & 0 & Q_{\alpha,W_1} & Q_{h,W_2} & 0 & Q_{\alpha,W_2} \end{bmatrix}^T \tag{7.19}$$

where Q_{h,W_i} is the wing lift force and Q_{α,W_i} is the wing pitching moment acting on node i.

If the wing is discretized into n beam elements ($n > 1$), the global displacement vector becomes

$$\mathbf{q_W} = \begin{bmatrix} h_1 & \phi_1 & \alpha_1 & h_2 & \phi_2 & \alpha_2 & \dots & h_{n+1} & \phi_{n+1} & \alpha_{n+1} \end{bmatrix}^T \tag{7.20}$$

Equation (7.17) still applies with the difference that the global mass matrix $\mathbf{M_{s,g}}$ and the global stiffness matrix $\mathbf{K_{s,g}}$ are now composed of the mass and stiffness matrices of all the beams and are assembled by standard FEM approaches (see Appendix C).

Similarly, the global wing aerodynamic load vector $\mathbf{Q_W}$ becomes

$$\mathbf{Q_W} = \begin{bmatrix} Q_{h,W_1} & 0 & Q_{\alpha,W_1} & Q_{h,W_2} & 0 & Q_{\alpha,W_2} & \dots & Q_{h,W_{n+1}} & 0 & Q_{\alpha,W_{n+1}} \end{bmatrix}^T \tag{7.21}$$

7.1.1. Wing Damping

If damping characteristics of the wing are known, Equation (7.17) may be modified to account for wing damping by including a damping matrix $\mathbf{C_{s,g}}$.

Internal structural damping is generally modelled with a Rayleigh damping model. Rayleigh damping is a viscous damping in which the damping matrix is a linear combination of the structural mass matrix and the structural stiffness matrix

$$\mathbf{C_{s,g}} = \mu \mathbf{M_{s,g}} + \lambda \mathbf{K_{s,g}} \tag{7.22}$$

where μ and λ are real scalars with 1/s and s units respectively and are to be obtained from either predictions or measurements of the damping level of the structure of the wing.

Including the damping matrix, the equations of motion of the wing becomes

$$\mathbf{M_{s,g}}\ddot{\mathbf{q}}_\mathbf{W} + \mathbf{C_{s,g}}\dot{\mathbf{q}}_\mathbf{W} + \mathbf{K_{s,g}}\mathbf{q_W} = \mathbf{Q_W} \tag{7.23}$$

7.2. Wing aerodynamic Model

Wing aerodynamics are approximated by the strip theory approach: the wing is divided into several sections and the aerodynamic loads on each section are calculated as if the section belonged to a infinite wing. This means that the loads on each section may be calculated by assuming each section to be a two dimensional airfoil. The total lift and moment acting on the wing will be the addition of the loads acting on each section from the wing root to the wing tip, assuming no aerodynamic interference effects between strips.

There are several aerodynamic theories available to evaluate the aerodynamic loads that act on a two dimensional airfoil. The choice of any specific aerodynamic model relies on the degree of fidelity of the load predictions and the numerical method that one wants to use to solve their final equations. Present work will use the unsteady aerodynamic theory developed by Theodorsen [106]. Theodorsen's theory determines the unsteady aerodynamic force and moment acting on a thin airfoil in harmonic motion in a two-dimensional incompressible fluid. Because Theodorsen's expressions are given in the hybrid time-frequency domain, frequency dependent terms are converted into the time domain employing Wagner's indicial function approximation [108]. Two methodologies are presented and are hereby designated as Wagner's method and Leishman-Nguyen's method.

7.2.1. Theodorsen's Theory

Theodorsen's theory models the unsteady lift on a two-dimensional flat-plate airfoil with simple harmonic motions. Ideal, attached flow conditions are assumed and the effect of wake history is modelled by a planar wake (the wake moves with freestream) that changes the induced circulation around the airfoil. The section lift force and section pitching moment about the elastic axis is given by Theodorsen as

$$L = \underbrace{\pi\rho b^2\left(\ddot{h} + V\dot{\alpha} - ba\ddot{\alpha}\right)}_{\text{non-circulatory lift}} + \underbrace{2\pi\rho V b C(k)\, w}_{\text{circulatory lift}} \tag{7.24}$$

$$M = \underbrace{\pi\rho b^2\left[ab\ddot{h} - Vb\left(\frac{1}{2} - a\right)\dot{\alpha} - b^2\left(\frac{1}{8} + a^2\right)\ddot{\alpha}\right]}_{\text{non-circulatory moment}} + \underbrace{2\pi\rho V b^2\left(a + \frac{1}{2}\right)C(k)\, w}_{\text{circulatory moment}} \tag{7.25}$$

where V is the airstream velocity, ρ is the air density, b is the airfoil semichord, h is vertical displacement of the airfoil elastic axis, α is the airfoil rotation about the elastic axis, a is the location of the elastic axis as fraction of the semichord, and w is the total aerodynamic downwash at the three-quarter chord position in the airfoil defined as

$$w = \dot{h} + V\alpha + b\left(\frac{1}{2} - a\right)\dot{\alpha} \tag{7.26}$$

The function $C(k)$, called the lift-deficiency function or Theodorsen function, represents the effect of the unsteadiness introduced by the wake history. k is the reduced frequency $k = \frac{\omega b}{V}$ where ω is the frequency of motion of the flat plate airfoil. $C(k)$ is defined by Equation (4.31) in Section 4.1.4.

The non-circulatory lift and non-circulatory moment are results of added mass effects, whilst the circulatory lift and circulatory moment include the wake history effects. The circulatory moment is the circulatory lift times $b\left(a + \frac{1}{2}\right)$, which is the distance between the airfoil's three-quarter chord to the elastic axis.

Because the generalised coordinate h is positive downward and the lift given by Theodorsen's expression is positive upward

$$\begin{aligned} Q_{h,W} &= -L \\ Q_{\alpha,W} &= M \end{aligned} \tag{7.27}$$

Substituting Equation (7.24) and Equation (7.25) in Equation (7.18) and later in Equation (7.17) completes the equations of motion that model the dynamics of the flexible wing. However, because of the introduction of the Theodorsen function the final equations are a set of aeroelastic equations in time and frequency domain. There are several methods for solving them [21], current work aims to solve them in the pure time domain. Therefore, it is necessary to transform the frequency-dependent components, i.e. circulatory lift and circulatory moment, into their time-dependent counterparts. For this, two methodologies are described in present work: Wagner's method and Leishman-Nguyen's method.

7.2.2. Wagner's Method

Wagner's theory models the unsteady lift on a two-dimensional flat-plate airfoil with arbitrary pithing motions. Under ideal attached flow assumptions, Wagner introduces a function called Wagner function, $\Phi(t)$, which allows to compute analytically the change in circulatory lift in response to a step in angle of attack. Then, the arbitrary motion response can be determined by convolution with this indicial response. Wagner function is related to Theodorsen function in that they constitute a Fourier Transform pair. This allows to establish an equivalence between Theodorsen's circulatory lift expression with that of Wagner's. This relation can be expressed as[2]

$$C(k)\, w = \Phi(0)\, w(t) - \int_0^t \frac{d\Phi(t - t_0)}{d\, t_0}\, w(t_0)\, d\, t_0 \tag{7.28}$$

Jones [56] introduced a two-pole exponential approximation to the Wagner function, i.e.,

$$\Phi(t) = 1 - \Psi_1 e^{-\epsilon_1 \frac{V}{b} t} - \Psi_2 e^{-\epsilon_2 \frac{V}{b} t} \tag{7.29}$$

where $\Psi_1 = 0.165$, $\Psi_2 = 0.335$, $\epsilon_1 = 0.0455$, and $\epsilon_2 = 0.3$.

Substituting Equation (7.28) and Equation (7.29) in Equation (7.24) and Equation (7.25) transforms the hybrid time and frequency domain equations into pure time domain. The integrals from the Wagner's lift expression can be eliminated by introducing aerodynamic states which in turn allows to rewrite the final equations as Ordinary Differential Equations and be solved in the state-space form.

The aerodynamic states are defined as

$$\begin{aligned} w_1(t) &= \int_0^t e^{-\epsilon_1 \frac{V(t-t_0)}{b}}\, h(t_0)\, d\, t_0 \\ w_2(t) &= \int_0^t e^{-\epsilon_2 \frac{V(t-t_0)}{b}}\, h(t_0)\, d\, t_0 \\ w_3(t) &= \int_0^t e^{-\epsilon_1 \frac{V(t-t_0)}{b}}\, \alpha(t_0)\, d\, t_0 \\ w_4(t) &= \int_0^t e^{-\epsilon_2 \frac{V(t-t_0)}{b}}\, \alpha(t_0)\, d\, t_0 \end{aligned} \tag{7.30}$$

[2] This equivalence is obtained by combining the indicial response method with the superposition principle via DuHamel integral. The full derivation of the Wagner's method can be found in Dimitriadis [21][Appendix A.2].

Substituting Equation (7.26) and Equation (7.29) in Equation (7.28) and performing integration by parts shows that

$$\begin{aligned} C(k)\,w = \Phi(0)\,w(t) - \int_0^t \frac{d\Phi(t-t_0)}{dt_0}\,w(t_0)\,dt_0 = \Phi(0)\,w(t) - \left(h(0) + b\left(\frac{1}{2}-a\right)\alpha(0)\right)\dot{\Phi}(t) \\ + \left(h(t) + b\left(\frac{1}{2}-a\right)\alpha(t)\right)\dot{\Phi}(0) \\ - \Psi_1\left(\frac{\epsilon_1 V}{b}\right)^2 w_1(t) - \Psi_2\left(\frac{\epsilon_2 V}{b}\right)^2 w_2(t) \\ + \Psi_1\frac{\epsilon_1 V^2}{b}\left(1-\epsilon_1\left(\frac{1}{2}-a\right)\right)w_3(t) \\ + \Psi_2\frac{\epsilon_2 V^2}{b}\left(1-\epsilon_2\left(\frac{1}{2}-a\right)\right)w_4(t) \end{aligned} \tag{7.31}$$

where $\Phi(0) = 1-\Psi_1-\Psi_2$, $\dot{\Phi}(t) = \Psi_1\epsilon_1\frac{V}{b}e^{\epsilon_1\frac{V}{b}t} + \Psi_2\epsilon_2\frac{V}{b}e^{\epsilon_2\frac{V}{b}t}$, and $\dot{\Phi}(0) = \Psi_1\epsilon_1\frac{V}{b} + \Psi_2\epsilon_2\frac{V}{b}$.

Equation (7.31) can be substituted into the Theodorsen's lift and moment expressions in Equation (7.24) and Equation (7.25). There will be two equations of motion with six unknowns, namely h, α, w_1, w_2, w_3, and w_4. Four additional equations can be obtained from the aerodynamic states by applying Leibniz's rule for integrals with variable limits. Leibniz's rule states that [21]

$$\frac{d}{dt}\int_{a(t)}^{b(t)} f(t_0,t)\,dt_0 = \frac{db(t_0)}{dt}f(b(t),t) - \frac{da(t)}{dt}f(a(t),t) + \int_{a(t)}^{b(t)}\frac{\partial f(t_0,t)}{\partial t}\,dt_0 \tag{7.32}$$

where $a(t)$ and $b(t)$ are continuous and differentiable functions of t and $f(t_0,t)$ is a continuous and differentiable function of both t_0 and t. Applying this rule to the first expression in Equation (7.30) by setting $a(t)=0$, $b(t)=t$ and $f(t_0,t) = e^{-\epsilon_1\frac{V(t-t_0)}{b}}h(t_0)$ gives

$$\dot{w}_1(t) = h(t) - \frac{\epsilon_1 V}{b}\int_0^t e^{-\epsilon_1\frac{U(t-t_0)}{b}}h(t_0)\,dt_0 = h(t) - \frac{\epsilon_1 V}{b}w_1(t) \tag{7.33}$$

Applying the same to all the aerodynamic states in Equation (7.30) gives four new equations

$$\begin{aligned} \dot{w}_1(t) &= h(t) - \frac{\epsilon_1 V}{b}w_1(t) \\ \dot{w}_2(t) &= h(t) - \frac{\epsilon_2 V}{b}w_2(t) \\ \dot{w}_3(t) &= \alpha(t) - \frac{\epsilon_1 V}{b}w_3(t) \\ \dot{w}_4(t) &= \alpha(t) - \frac{\epsilon_2 V}{b}w_4(t) \end{aligned} \tag{7.34}$$

Wing aerodynamics in matrix form - Wagner

The set of equations composed by Theodorsen's formulas (Equation (7.24) and Equation (7.25)), Wagner's expression for lift (Equation (7.31)), and Leibniz's expression for the aerodynamic states (Equation (7.34)) allows to calculate two dimensional airfoil aerodynamics in a closed-form manner. The aerodynamic loads may be expressed in matrix form as

$$\begin{aligned} \begin{bmatrix} Q_{h,W} \\ Q_{\alpha,W} \end{bmatrix} = \begin{bmatrix} -L \\ M \end{bmatrix} = \mathbf{M_{aW}}\begin{bmatrix} \ddot{h} \\ \ddot{\alpha} \end{bmatrix} + \mathbf{C_{aW}}\begin{bmatrix} \dot{h} \\ \dot{\alpha} \end{bmatrix} + \mathbf{K_{aW}}\begin{bmatrix} h \\ \alpha \end{bmatrix} + \mathbf{W_0 w} + \mathbf{g}\dot{\phi}(t) \\ \dot{\mathbf{w}} = \mathbf{W_1}\begin{bmatrix} h \\ \alpha \end{bmatrix} + \mathbf{W_2 w} \end{aligned} \tag{7.35}$$

where $\mathbf{M_{aW}}$ is the airfoil aerodynamic mass matrix, $\mathbf{C_{aW}}$ is the airfoil aerodynamic damping matrix, $\mathbf{K_{aW}}$ is the airfoil aerodynamic stiffness matrix, $\mathbf{W_0}$ is the airfoil aerodynamic states influence matrix, $\mathbf{g}$ is the initial condition excitation vector, $\mathbf{W_1}$ and $\mathbf{W_2}$ are the aerodynamic states equation matrices, and $\mathbf{w}$ is the vector of aerodynamic states.

$$\mathbf{w} = \begin{bmatrix} w_1 \\ w_2 \\ w_3 \\ w_4 \end{bmatrix} \tag{7.36}$$

The wing aerodynamic mass matrix is given by

$$\mathbf{M_{aW}} = \begin{bmatrix} -\pi\rho b^2 & \pi\rho b^3 a \\ \pi\rho b^3 a & -\pi\rho b^4\left(\frac{1}{8}+a^2\right) \end{bmatrix} \tag{7.37}$$

The wing aerodynamic damping matrix is given by

$$\mathbf{C_{aW}} = \begin{bmatrix} -2\pi\rho bV\Phi(0) & -\pi\rho b^2 V - 2\pi\rho b^2 V\left(\frac{1}{2}-a\right)\Phi(0) \\ 2\pi\rho bV\Phi(0)b\left(a+\frac{1}{2}\right) & -\pi\rho b^3 V\left(\frac{1}{2}-a\right) + 2\pi\rho b^2 V\left(\frac{1}{2}-a\right)\Phi(0)b\left(a+\frac{1}{2}\right) \end{bmatrix} \tag{7.38}$$

The wing aerodynamic stiffness matrix is given by

$$\mathbf{K_{aW}} = \begin{bmatrix} -2\pi\rho bV\dot{\Phi}(0) & -2\pi\rho bV^2\Phi(0) - 2\pi\rho b^2 V\left(\frac{1}{2}-a\right)\dot{\Phi}(0) \\ 2\pi\rho bV\dot{\Phi}(0)b\left(a+\frac{1}{2}\right) & 2\pi\rho bV^2\Phi(0)b\left(a+\frac{1}{2}\right) + 2\pi\rho b^2 V\left(\frac{1}{2}-a\right)\dot{\Phi}(0)b\left(a+\frac{1}{2}\right) \end{bmatrix} \tag{7.39}$$

The wing aerodynamic state influence matrix is given by $\mathbf{W_0} = 2\pi\rho bV\mathbf{W_0'}$, where $\mathbf{W_0'}$ is

$$\mathbf{W_0'} = \begin{bmatrix} \Psi_1\left(\epsilon_1\frac{V}{b}\right)^2 & \Psi_2\left(\epsilon_2\frac{V}{b}\right)^2 & -\Psi_1\epsilon_1\frac{V^2}{b}\left(1-\epsilon_1\left(\frac{1}{2}-a\right)\right) & -\Psi_2\epsilon_2\frac{V^2}{b}\left(1-\epsilon_2\left(\frac{1}{2}-a\right)\right) \\ -\Psi_1\left(\epsilon_1\frac{V}{b}\right)^2 b\left(a+\frac{1}{2}\right) & -\Psi_2\left(\epsilon_2\frac{V}{b}\right)^2 b\left(a+\frac{1}{2}\right) & \Psi_1\epsilon_1\frac{V^2}{b}\left(1-\epsilon_1\left(\frac{1}{2}-a\right)\right)b\left(a+\frac{1}{2}\right) & \Psi_2\epsilon_2\frac{V^2}{b}\left(1-\epsilon_2\left(\frac{1}{2}-a\right)\right)b\left(a+\frac{1}{2}\right) \end{bmatrix} \tag{7.40}$$

The initial condition excitation vector is given by

$$\mathbf{g} = 2\pi\rho bV\left[h(0) + b\left(\frac{1}{2}-a\right)\alpha(0)\right]\begin{bmatrix} 1 \\ -b\left(a+\frac{1}{2}\right) \end{bmatrix} \tag{7.41}$$

Finally, the aerodynamic state equation matrices are given by

$$\mathbf{W_1} = \begin{bmatrix} 1 & 0 \\ 1 & 0 \\ 0 & 1 \\ 0 & 1 \end{bmatrix} \tag{7.42}$$

$$\mathbf{W_2} = \begin{bmatrix} -\frac{\epsilon_1 V}{b} & 0 & 0 & 0 \\ 0 & -\frac{\epsilon_2 V}{b} & 0 & 0 \\ 0 & 0 & -\frac{\epsilon_1 V}{b} & 0 \\ 0 & 0 & 0 & -\frac{\epsilon_2 V}{b} \end{bmatrix} \tag{7.43}$$

The matrices $\mathbf{M_{aW}}$, $\mathbf{C_{aW}}$, $\mathbf{K_{aW}}$, $\mathbf{W_0}$, $\mathbf{g_g}$, $\mathbf{W_1}$, and $\mathbf{W_2}$ need to be introduced into Equation (7.21) to assemble the final global matrices by standard FEM approaches (see Appendix C). The global version of these matrices will be named $\mathbf{M_{a,g}}$, $\mathbf{C_{a,g}}$, $\mathbf{K_{a,g}}$, $\mathbf{W_{0,g}}$, $\mathbf{g_g}$, $\mathbf{W_{1,g}}$, and $\mathbf{W_{2,g}}$, respectively.

Analogously, the global vector of the aerodynamic states becomes:

$$\mathbf{w_g} = \begin{bmatrix} w_1^{(1)} & w_2^{(1)} & w_3^{(1)} & w_4^{(1)} & \dots & w_1^{(n+1)} & w_2^{(n+1)} & w_3^{(n+1)} & w_4^{(n+1)} \end{bmatrix}^T \tag{7.44}$$

7.2.3. Leishman and Nguyen's Method

Wagner's theory introduces four aerodynamic states. In the finite element beam model, this means that there will be four additional eigenvalues and modeshapes per beam node associated with these aerodynamic states. If the number of beam elements are large, the calculations and the later analysis become lengthier and more cumbersome. Leishman and Nguyen [63] introduced another state-space representation of unsteady lift and pitching moment in which only two additional aerodynamic states. Their method is also based on Theodorsen function and Jone's two-pole exponential approximation to the Wagner function.

The Theodorsen's circulatory lift expression may be expressed as

$$C(k)\alpha_{3/4} = \begin{bmatrix} \Big(\Psi_1 + \Psi_2\Big)\epsilon_1\epsilon_2\Big(\frac{V}{b}\Big)^2 & \Big(\Psi_1\epsilon_1 + \Psi_2\epsilon_2\Big)\Big(\frac{V}{b}\Big) \end{bmatrix} \begin{bmatrix} w_1 \\ w_2 \end{bmatrix} + \frac{1}{2}\alpha_{3/4} \tag{7.45}$$

where $\alpha_{3/4} = \frac{w}{V}$ is the angle of attack at the airfoil three quarter chord:

$$\alpha_{3/4} = \frac{\dot{h}}{V} + \alpha + b\Big(\frac{1}{2} - a\Big)\frac{\dot{\alpha}}{V} \tag{7.46}$$

The two additional equations required are

$$\begin{bmatrix} \dot{w}_1 \\ \dot{w}_2 \end{bmatrix} = \begin{bmatrix} 0 & 1 \\ -\epsilon_1\epsilon_2\Big(\frac{V}{b}\Big)^2 & -(\epsilon_1+\epsilon_2)\Big(\frac{V}{b}\Big) \end{bmatrix} \begin{bmatrix} w_1 \\ w_2 \end{bmatrix} + \begin{bmatrix} 0 \\ 1 \end{bmatrix} \alpha_{3/4} \tag{7.47}$$

Wing aerodynamics in matrix form - Leishman and Nguyen

The set of equations composed by Theodorsen's formulas (Equation (7.24) and Equation (7.25)), Leishman and Nguyen's for lift (Equation (7.45)), and the additional aerodynamic states equations (Equation (7.47)) allows to calculate two dimensional airfoil aerodynamics in a closed-form manner by introducing two aerodynamic lag states. The aerodynamic loads may be expressed in matrix form as

$$\begin{gathered} \begin{bmatrix} Q_{h,W} \\ Q_{\alpha,W} \end{bmatrix} = \begin{bmatrix} -L \\ M \end{bmatrix} = \mathbf{M_{aW}} \begin{bmatrix} \ddot{h} \\ \ddot{\alpha} \end{bmatrix} + \mathbf{C_{aW}} \begin{bmatrix} \dot{h} \\ \dot{\alpha} \end{bmatrix} + \mathbf{K_{aW}} \begin{bmatrix} h \\ \alpha \end{bmatrix} + \mathbf{W_0 w} \\ \dot{\mathbf{w}} = \mathbf{W_1 w} + \mathbf{W_2} \begin{bmatrix} \dot{h} \\ \dot{\alpha} \end{bmatrix} + \mathbf{W_3} \begin{bmatrix} h \\ \alpha \end{bmatrix} \end{gathered} \tag{7.48}$$

where $\mathbf{M_{aW}}$ is the airfoil aerodynamic mass matrix, $\mathbf{C_{aW}}$ is the airfoil aerodynamic damping matrix, $\mathbf{K_{aW}}$ is the airfoil aerodynamic stiffness matrix, $\mathbf{W_0}$ is the airfoil aerodynamic state influence matrix, $\mathbf{W_1}$, $\mathbf{W_2}$, and $\mathbf{W_3}$ are the aerodynamic state equation matrices, and $\mathbf{w}$ is the vector of aerodynamic states.

$$\mathbf{w} = \begin{bmatrix} w_1 \\ w_2 \end{bmatrix} \tag{7.49}$$

The wing aerodynamic mass matrix is given by[3]

$$\mathbf{M_{aW}} = \begin{bmatrix} -\pi\rho b^2 & \pi\rho b^3 a \\ \pi\rho b^3 a & -\pi\rho b^4\Big(\frac{1}{8} + a^2\Big) \end{bmatrix} \tag{7.50}$$

The wing aerodynamic damping matrix is given by

[3] Note that this matrix is exactly the same as that of Equation (7.37). This is because the terms of the matrix come from the non-circulatory terms of the Theodorsen's lift expression.

$$\mathbf{C_{aW}} = \begin{bmatrix} -\pi\rho bV & -\pi\rho b^2 V - \pi\rho b^2 V\left(\frac{1}{2}-a\right) \\ \pi\rho bVb\left(a+\frac{1}{2}\right) & -\pi\rho b^3 V\left(\frac{1}{2}-a\right) + \pi\rho b^2 V\left(\frac{1}{2}-a\right)b\left(a+\frac{1}{2}\right) \end{bmatrix} \tag{7.51}$$

The wing aerodynamic stiffness matrix is given by

$$\mathbf{K_{aW}} = \begin{bmatrix} 0 & -\pi\rho bV^2 \\ 0 & \pi\rho V^2 b^2\left(a+\frac{1}{2}\right) \end{bmatrix} \tag{7.52}$$

The wing aerodynamic state influence matrix is given by $\mathbf{W_0} = 2\pi\rho bV^2\mathbf{W_0'}$, where $\mathbf{W_0'}$ is

$$\mathbf{W_0'} = \begin{bmatrix} -\left(\Psi_1+\Psi_2\right)\epsilon_1\epsilon_2\left(\frac{V}{b}\right)^2 & -\left(\Psi_1\epsilon_1+\Psi_2\epsilon_2\right)\left(\frac{V}{b}\right) \\ \left(\Psi_1+\Psi_2\right)\epsilon_1\epsilon_2\left(\frac{V}{b}\right)^2 b\left(a+\frac{1}{2}\right) & \left(\Psi_1\epsilon_1+\Psi_2\epsilon_2\right)\left(\frac{V}{b}\right)b\left(a+\frac{1}{2}\right) \end{bmatrix} \tag{7.53}$$

Finally, the aerodynamic state equation matrices are given by

$$\mathbf{W_1} = \begin{bmatrix} 0 & 1 \\ -\epsilon_1\epsilon_2\left(\frac{V}{b}\right)^2 & -(\epsilon_1+\epsilon_2)\left(\frac{V}{b}\right) \end{bmatrix} \tag{7.54}$$

$$\mathbf{W_2} = \begin{bmatrix} 0 & 0 \\ \frac{1}{V} & \frac{b}{V}\left(\frac{1}{2}-a\right) \end{bmatrix} \tag{7.55}$$

$$\mathbf{W_3} = \begin{bmatrix} 0 & 0 \\ 0 & 1 \end{bmatrix} \tag{7.56}$$

The matrices $\mathbf{M_{aW}}$, $\mathbf{C_{aW}}$, $\mathbf{K_{aW}}$, $\mathbf{W_0}$, $\mathbf{W_1}$, $\mathbf{W_2}$, and $\mathbf{W_3}$ need to be introduced into Equation (7.21) to assemble the final global matrices by standard FEM approaches (see Appendix D). The global version of these matrices will be named $\mathbf{M_{a,g}}$, $\mathbf{C_{a,g}}$, $\mathbf{K_{a,g}}$, $\mathbf{W_{0,g}}$, $\mathbf{W_{1,g}}$, $\mathbf{W_{2,g}}$, and $\mathbf{W_{3,g}}$, respectively.

Analogously, the global vector of the aerodynamic states becomes:

$$\mathbf{w_g} = \begin{bmatrix} w_1^{(1)} & w_2^{(1)} & \dots & w_1^{(n+1)} & w_2^{(n+1)} \end{bmatrix}^T \tag{7.57}$$

7.3. Aeroelastic Equations of the Cantilever Wing

The equations of motion that describe the aeroelastic behaviour of a flexible cantilever wing are Equation (7.23).

$$\mathbf{M_{s,g}}\ddot{\mathbf{q}}_\mathbf{W} + \mathbf{C_{s,g}}\dot{\mathbf{q}}_\mathbf{W} + \mathbf{K_{s,g}}\mathbf{q_W} = \mathbf{Q_W} \tag{7.23}$$

The global wing aerodynamic load vector $\mathbf{Q_W}$ may be obtained either by the aerodynamic matrices defined via Wagner's method or by those defined via Leishman and Nguyen's method. Results are equivalent since they are essentially different implementations of the same principle.

Employing Leishan and Nguyen's method, for example, Equation (7.23) becomes:

$$\begin{aligned} \mathbf{M_{s,g}}\ddot{\mathbf{q}}_\mathbf{W} + \mathbf{C_{s,g}}\dot{\mathbf{q}}_\mathbf{W} + \mathbf{K_{s,g}}\mathbf{q_W} &= \mathbf{M_{a,g}}\ddot{\mathbf{q}}_\mathbf{W} + \mathbf{C_{a,g}}\dot{\mathbf{q}}_\mathbf{W} + \mathbf{K_{a,g}}\mathbf{q_W} + \mathbf{W_{0,g}}\mathbf{w_g} \\ \dot{\mathbf{w}}_\mathbf{g} &= \mathbf{W_{1,g}}\mathbf{w} + \mathbf{W_{2,g}}\dot{\mathbf{q}}_\mathbf{W} + \mathbf{W_{3,g}}\mathbf{q_W} \end{aligned} \tag{7.58}$$

Equation (7.58) can be rearranged into a state-space form (see Section 5.1):

$$\begin{bmatrix} \dot{\mathbf{q}}_\mathbf{W} \\ \ddot{\mathbf{q}}_\mathbf{W} \\ \dot{\mathbf{w}}_\mathbf{g} \end{bmatrix} = \begin{bmatrix} \mathbf{0} & \mathbf{I} & \mathbf{0} \\ -\left(\mathbf{M_{s,g}}-\mathbf{M_{a,g}}\right)^{-1}\left(\mathbf{K_{s,g}}-\mathbf{K_{a,g}}\right) & -\left(\mathbf{M_{s,g}}-\mathbf{M_{a,g}}\right)^{-1}\left(\mathbf{C_{s,g}}-\mathbf{C_{a,g}}\right) & \left(\mathbf{M_{s,g}}-\mathbf{M_{a,g}}\right)^{-1}\mathbf{W_{0_g}} \\ \mathbf{W_{3,g}} & \mathbf{W_{2_g}} & \mathbf{W_{1_g}} \end{bmatrix} \begin{bmatrix} \mathbf{q}_\mathbf{W} \\ \dot{\mathbf{q}}_\mathbf{W} \\ \mathbf{w_g} \end{bmatrix} \tag{7.59}$$

where **0** and **I** are zero and identity matrices, respectively.

The degrees of freedom at wing root are always null because the wing is cantilevered at its root. Therefore, the state matrix must be reduced, meaning that the rows and columns corresponding to the fixed degrees of freedom must be eliminated. The eigenvalues and the eigenvectors are calculated from the reduced state matrix. From the eigenvalues, one can extract the undamped natural frequencies and the damping ratios; the mode shapes are the eigenvectors themselves. V-g and V-f diagrams may be plotted to analyse the instabilities.

7.4. Verification and Validation

The validation and verification of the wing aeroelastic model is carried out by analysing the wing structural model and the wing aeroelastic behaviour.

The structural model is verified by comparing the free vibration modes with their analytical results; whereas the wing aeroelastic behaviour is analysed by comparing flutter and divergence speeds with data available in literature. For this purpose, the wing analysed in Patil et al. [81] is modelled using present methodology. The wing description is tabulated in Table 7.1.

Parameter	**Value**	**Units**
Half span	16	m
Chord	1	m
Mass per unit length	0.75	kg/m
Polar mass moment of inertia (50% chord)	0.1	kg·m
Spanwise elastic axis	50% chord	[-]
Centre of gravity	50% chord	[-]
Bending rigidity (EI)	2×10^4	N·m^2
Torsional rigidity (GJ)	1×10^4	N·m^2
Flight condition		
Altitude	20	km
Density of air	0.0889	kg/m^3

Table 7.1: Wing model data [81]

7.4.1. Wing free Vibration Modes

Wing free vibration modes from the finite element beam model are compared with analytical solutions from uniform beam bending dynamics and uniform beam torsional dynamics. The analytical expressions are extracted from Hodges and Pierce [36].

The analytical formulas for the first three wing bending frequencies are

$$\omega_{b_1} = 1.8751^2\sqrt{\frac{EI}{ml^4}} \qquad \omega_{b_2} = 4.69409^2\sqrt{\frac{EI}{ml^4}} \qquad \omega_{b_3} = 7.85476^2\sqrt{\frac{EI}{ml^4}} \tag{7.60}$$

where m is the beam mass per unit length, l is the beam length, and EI is the beam bending rigidity.

The analytical formulas for the corresponding bending mode shapes ϕ_i are given by

$$\begin{aligned}
\phi_{b_1}(x) &= \cosh\left(\frac{1.8751}{l}x\right) - \cos\left(\frac{1.8751}{l}x\right) - 0.734096\left[\sinh\left(\frac{1.8751}{l}x\right) - \sin\left(\frac{1.8751}{l}x\right)\right] \\
\phi_{b_2}(x) &= \cosh\left(\frac{4.69409}{l}x\right) - \cos\left(\frac{4.69409}{l}x\right) - 1.01847\left[\sinh\left(\frac{4.69409}{l}x\right) - \sin\left(\frac{4.69409}{l}x\right)\right] \\
\phi_{b_3}(x) &= \cosh\left(\frac{7.85476}{l}x\right) - \cos\left(\frac{7.85476}{l}x\right) - 0.999224\left[\sinh\left(\frac{7.85476}{l}x\right) - \sin\left(\frac{7.85476}{l}x\right)\right]
\end{aligned} \tag{7.61}$$

where x is the distance along the beam length.

The analytical formula for the first torsion frequency ω_t is given by

$$\omega_t = \frac{\pi}{2L}\sqrt{\frac{GJ}{\rho I_p}} \tag{7.62}$$

where GJ is the beam torsional rigidity and ρI_p is the beam mass polar moment of inertia.
The analytical formula for the first torsion mode shape ϕ_t is given by

$$\phi_t(x) = \sin\left(\frac{\pi}{2l}x\right) \tag{7.63}$$

A comparison of the wing natural frequencies obtained from the finite element beam model and the analytical expressions are shown in Table 7.2.

Mode	**Present analysis**	**Exact**	**Error** [%]
First flatwise bending	2.2431	2.2428	+0.01
Second flatwise bending	14.102	14.056	+0.33
Third flatwise bending	39.846	39.356	+1.25
First torsion	31.401	31.046	+1.15

Table 7.2: Comparison of wing natural frequencies (rad/s). Present analysis used 3 beam elements.

Figure 7.3a shows the convergence of the natural frequencies with increasing number of elements and comparison with the analytical values (blue line). Figure 7.3b shows the comparison between mode shapes from the finite element beam model and the mode shapes from the analytical expressions (blue line).

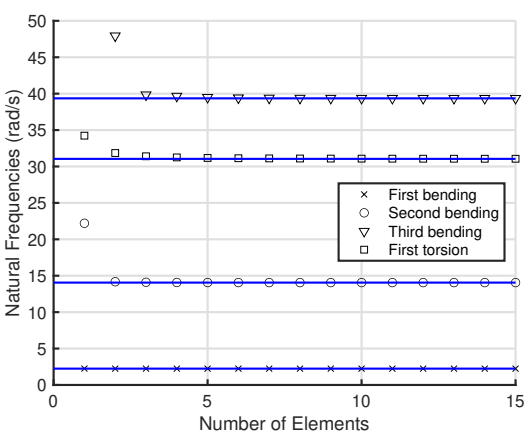

(a) Variation of natural frequencies with number of elements.

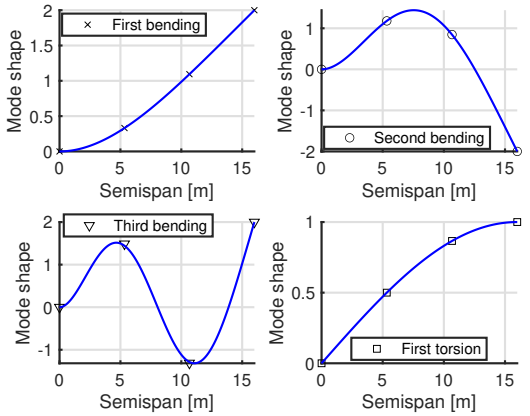

(b) Mode shapes comparison. Finite element beam model contains three beam elements.

Figure 7.3: Wing beam free vibration frequencies and modes. Blue lines indicate analytical solutions.

In general almost identical results are obtained by using only three beam elements. Note the slightly slower convergence for higher bending frequencies.

The structural model derived from Euler-Bernoulli beam elements is correctly implemented.

7.4.2. Aeroelastic Analysis

The aeroelastic behaviour of the wing is obtained by solving Equation (7.59). Verification is carried out by comparing flutter speed, flutter frequency and divergence speed.

Figure 7.4 shows the results of the eigenvalue analysis of Equation (7.59). The system goes unstable when the damping ratio becomes negative or when the real part of the eigenvalues becomes positive.

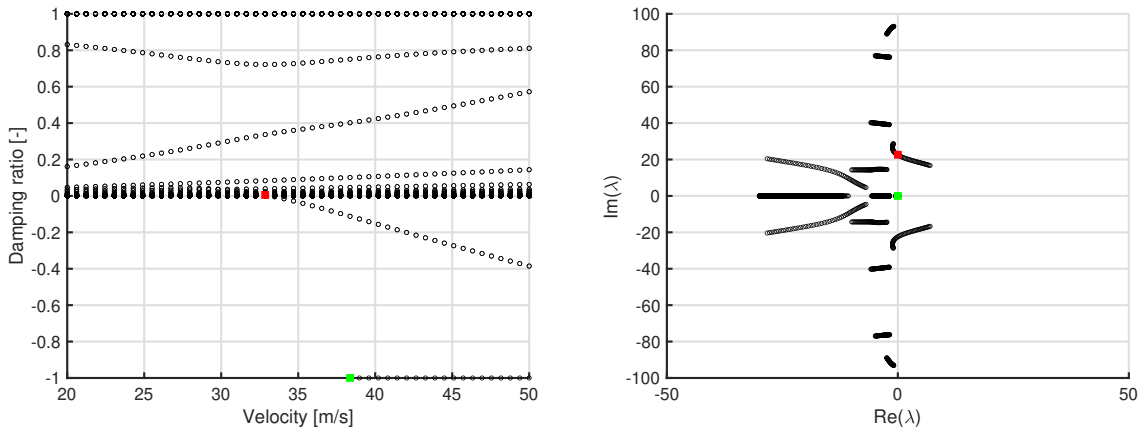

(a) Damping ratio vs. Velocity.

(b) Root loci plot.

Figure 7.4: Damping plots and eigenvalue plots. Red markers indicate flutter and green markers indicate divergence.

Figure 7.5 shows the convergence of the aeroelastic results with the number of beam elements.

Table 7.3 compares the aeroelastic results with those extracted from Patil et al. [81]. Patil et al. [81] uses the theory of Patil [80] which employs the Rayleigh-Ritz method with uncoupled beam mode shapes and Theodorsen's two-dimensional thin-airfoil theory for unsteady aerodynamics. Comparisons show almost identical results with the present analyses yielding slightly higher flutter speed, flutter frequency, and divergence speed.

Note that the aeroelastic results from present analysis also depend on the increase in velocity ΔV within the velocity interval used to determine the onset of flutter and divergence, smaller increase in velocities may lead to closer values to the "real" calculated instability speeds; this comes at a computational cost.

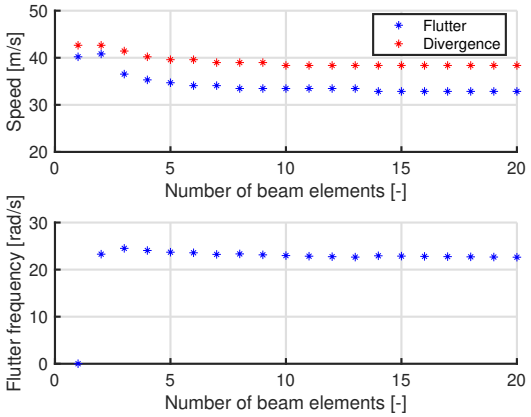

Figure 7.5: Convergence of flutter speed, flutter frequency, and divergence speed with the number of beam elements.

Parameter	**Present analysis**	**Analysis of Ref.[81] using the theory of Patil [80]**	**Difference [%]**
Flutter speed [m/s]	32.86	32.51	+1.1
Flutter frequency [rad/s]	22.64	22.37	+1.2
Divergence speed [m/s]	38.37	37.15	+3.3

Table 7.3: Comparison of flutter and divergence speeds with results from Patil et al. [81]. Present analysis uses 20 beam elements.

7.5. Modified Strip Analysis: Wing of finite Span

One of the main assumptions in the wing aerodynamic model explained in Section 7.2 is that the wing is divided into several sections and the aerodynamic loads on each section are calculated as if the section belonged to a infinite wing. This assumption is valid for high aspect ratio wings where each aerodynamic section can be treated as a two dimensional airfoil. However, in reality, air is a compressible fluid and as explained in Section 2.8.1, wings have finite span and therefore, three dimensional aerodynamic effects such as wingtip vortices take place; this leads to induced downwash effects which in turn decrease the total lift produced by the wing and change the lift distribution over the wing. Subsequently, flutter and divergence speeds can be altered.

Yates Jr. [112] addresses finite span, taper, sweep, and compressibility effects by modelling wing unsteady aerodynamics with the modified strip analysis method; aeroelastic analysis is carried out in the frequency domain using Rayleigh type analysis with uncoupled vibration modes (coupled vibration modes may also be used). In this method, spanwise distributions of steady flow section lift-curve slope and local aerodynamic centre for the undeformed wing are used. These steady aerodynamic parameters may be obtained from any suitable aerodynamic theory or experiment; Bland and Yates Jr. [11] suggests to use the one that yields the most accurate steady-state load distributions over the undeformed wing.

Essentially, the method developed in Yates Jr. [112] consists in modifying Theodorsen's lift and pitching moment expressions (Equation (7.24) and Equation (7.25)) to include variable lift-curve slope and variable aerodynamic center: the value 2π for section lift curve slope is replaced by the variable C_{l_α}, the quarter-chord aerodynamic-center position ($a_c = -\frac{1}{2}$) is replaced by the variable a_c, and the distance from the elastic axis to the point of application of the downwash condition $b\left(\frac{1}{2} - a\right)$ is replaced by $b\left(\frac{C_{l_\alpha}}{2\pi} + a_c - a\right)$.

Including these modifications, the expressions for section lift L and section pitching moment M have the following form

$$L = \underbrace{\pi\rho b^2\left(\ddot{h} + V\dot{\alpha} - ba\ddot{\alpha}\right)}_{\text{non-circulatory lift}} + \underbrace{C_{l_\alpha}\rho V b C(k)\, w}_{\text{circulatory lift}} \tag{7.64}$$

$$M = \underbrace{\pi\rho b^2\left[ab\ddot{h} - Vb\left(\frac{C_{l_\alpha}}{2\pi} + a_c - a\right)\dot{\alpha} - b^2\left(\frac{1}{8} + a^2\right)\ddot{\alpha}\right]}_{\text{non-circulatory moment}} + \underbrace{C_{l_\alpha}\rho V b^2\left(a - a_c\right)C(k)\, w}_{\text{circulatory moment}} \tag{7.65}$$

$$w = \dot{h} + V\alpha + b\left(\frac{C_{l_\alpha}}{2\pi} + a_c - a\right)\dot{\alpha} \tag{7.66}$$

7.5.1. Inclusion into the aeroelastic Equations of a Cantilever Wing

Equation (7.64), Equation (7.65), and Equation (7.66) are to be transformed into the time domain. This can be realised by employing either Wagner's method or Leishman-Nguyen's method.

Wagner's method in matrix form

Using Wagner's method, the aerodynamic loads may be expressed in matrix form as

$$\begin{aligned}\begin{bmatrix} Q_{h,W} \\ Q_{\alpha,W}\end{bmatrix} = \begin{bmatrix} -L \\ M\end{bmatrix} &= \mathbf{M_{aW}}\begin{bmatrix}\ddot{h} \\ \ddot{\alpha}\end{bmatrix} + \mathbf{C_{aW}}\begin{bmatrix}\dot{h} \\ \dot{\alpha}\end{bmatrix} + \mathbf{K_{aW}}\begin{bmatrix} h \\ \alpha\end{bmatrix} + \mathbf{W_0 w} + \mathbf{g}\dot{\phi}(t) \\ \dot{\mathbf{w}} &= \mathbf{W_1}\begin{bmatrix} h \\ \alpha\end{bmatrix} + \mathbf{W_2 w}\end{aligned} \tag{7.35}$$

The wing aerodynamic mass matrix is given by

$$\mathbf{M_{aW}} = \begin{bmatrix} -\pi\rho b^2 & \pi\rho b^3 a \\ \pi\rho b^3 a & -\pi\rho b^4\left(\frac{1}{8} + a^2\right)\end{bmatrix} \tag{7.67}$$

The wing aerodynamic damping matrix is given by

$$\mathbf{C_{aW}} = \begin{bmatrix} -C_{l_\alpha}\rho bV\Phi(0) & -\pi\rho b^2 V - C_{l_\alpha}\rho b^2 V\left(\frac{C_{l_\alpha}}{2\pi} + a_c - a\right)\Phi(0) \\ C_{l_\alpha}\rho bV\Phi(0)b\left(a-a_c\right) & -\pi\rho b^3 V\left(\frac{C_{l_\alpha}}{2\pi} + a_c - a\right) + C_{l_\alpha}\rho b^2 V\left(\frac{C_{l_\alpha}}{2\pi} + a_c - a\right)\Phi(0)b\left(a-a_c\right) \end{bmatrix} \tag{7.68}$$

The wing aerodynamic stiffness matrix is given by

$$\mathbf{K_{aW}} = \begin{bmatrix} -C_{l_\alpha}\rho bV\dot{\Phi}(0) & -C_{l_\alpha}\rho bV^2\Phi(0) - C_{l_\alpha}\rho b^2 V\left(\frac{C_{l_\alpha}}{2\pi} + a_c - a\right)\dot{\Phi}(0) \\ C_{l_\alpha}\rho bV\dot{\Phi}(0)b\left(a-a_c\right) & C_{l_\alpha}\rho bV^2\Phi(0)b\left(a-a_c\right) + C_{l_\alpha}\rho b^2 V\left(\frac{C_{l_\alpha}}{2\pi} + a_c - a\right)\dot{\Phi}(0)b\left(a-a_c\right) \end{bmatrix} \tag{7.69}$$

The wing aerodynamic state influence matrix is given by $\mathbf{W_0} = C_{l_\alpha}\rho bV\mathbf{W_0'}$, where $\mathbf{W_0'}$ is

$$\mathbf{W_0'} = \begin{bmatrix} \Psi_1\left(\epsilon_1\frac{V}{b}\right)^2 & \Psi_2\left(\epsilon_2\frac{V}{b}\right)^2 & -\Psi_1\epsilon_1\frac{V^2}{b}\left(1-\epsilon_1\left(\frac{C_{l_\alpha}}{2\pi} + a_c - a\right)\right) & -\Psi_2\epsilon_2\frac{V^2}{b}\left(1-\epsilon_2\left(\frac{C_{l_\alpha}}{2\pi} + a_c - a\right)\right) \\ -\Psi_1\left(\epsilon_1\frac{V}{b}\right)^2 b\left(a-a_c\right) & -\Psi_2\left(\epsilon_2\frac{V}{b}\right)^2 b\left(a-a_c\right) & \Psi_1\epsilon_1\frac{V^2}{b}\left(1-\epsilon_1\left(\frac{C_{l_\alpha}}{2\pi} + a_c - a\right)\right)b\left(a-a_c\right) & \Psi_2\epsilon_2\frac{V^2}{b}\left(1-\epsilon_2\left(\frac{C_{l_\alpha}}{2\pi} + a_c - a\right)\right)b\left(a-a_c\right) \end{bmatrix} \tag{7.70}$$

The initial condition excitation vector is given by

$$\mathbf{g} = C_{l_\alpha}\rho bV\left[h(0) + b\left(\frac{C_{l_\alpha}}{2\pi} + a_c - a\right)\alpha(0)\right]\begin{bmatrix} 1 \\ -b\left(a-a_c\right) \end{bmatrix} \tag{7.71}$$

Finally, the aerodynamic state equation matrices are given by

$$\mathbf{W_1} = \begin{bmatrix} 1 & 0 \\ 1 & 0 \\ 0 & 1 \\ 0 & 1 \end{bmatrix} \tag{7.72}$$

$$\mathbf{W_2} = \begin{bmatrix} -\frac{\epsilon_1 V}{b} & 0 & 0 & 0 \\ 0 & -\frac{\epsilon_2 V}{b} & 0 & 0 \\ 0 & 0 & -\frac{\epsilon_1 V}{b} & 0 \\ 0 & 0 & 0 & -\frac{\epsilon_2 V}{b} \end{bmatrix} \tag{7.73}$$

Leishman-Nguyen's method in matrix form

Using Leishman-Nguyen's method, the aerodynamic loads may be expressed in matrix form as

$$\begin{bmatrix} Q_{h,W} \\ Q_{\alpha,W} \end{bmatrix} = \begin{bmatrix} -L \\ M \end{bmatrix} = \mathbf{M_{aW}}\begin{bmatrix} \ddot{h} \\ \ddot{\alpha} \end{bmatrix} + \mathbf{C_{aW}}\begin{bmatrix} \dot{h} \\ \dot{\alpha} \end{bmatrix} + \mathbf{K_{aW}}\begin{bmatrix} h \\ \alpha \end{bmatrix} + \mathbf{W_0 w}$$
$$\dot{\mathbf{w}} = \mathbf{W_1 w} + \mathbf{W_2}\begin{bmatrix} \dot{h} \\ \dot{\alpha} \end{bmatrix} + \mathbf{W_3}\begin{bmatrix} h \\ \alpha \end{bmatrix} \tag{7.48}$$

The wing aerodynamic mass matrix is given by

$$\mathbf{M_{aW}} = \begin{bmatrix} -\pi\rho b^2 & \pi\rho b^3 a \\ \pi\rho b^3 a & -\pi\rho b^4\left(\frac{1}{8} + a^2\right) \end{bmatrix} \tag{7.74}$$

The wing aerodynamic damping matrix is given by

$$\mathbf{C_{aW}} = \begin{bmatrix} -C_{l_\alpha}\frac{\rho}{2}bV & -\pi\rho b^2 V - C_{l_\alpha}\frac{\rho}{2}b^2 V\left(\frac{C_{l_\alpha}}{2\pi} + a_c - a\right) \\ C_{l_\alpha}\frac{\rho}{2}bVb\left(a-a_c\right) & -\pi\rho b^3 V\left(\frac{C_{l_\alpha}}{2\pi} + a_c - a\right) + C_{l_\alpha}\frac{\rho}{2}b^2 V\left(\frac{C_{l_\alpha}}{2\pi} + a_c - a\right)b\left(a-a_c\right) \end{bmatrix} \tag{7.75}$$

The wing aerodynamic stiffness matrix is given by

$$\mathbf{K_{aW}} = \begin{bmatrix} 0 & -C_{l_\alpha}\frac{\rho}{2}bV^2 \\ 0 & C_{l_\alpha}\frac{\rho}{2}V^2 b^2\left(a-a_c\right) \end{bmatrix} \tag{7.76}$$

The wing aerodynamic state influence matrix is given by $\mathbf{W_0} = C_{l_\alpha}\rho bV^2\mathbf{W_0'}$, where $\mathbf{W_0'}$ is

$$\mathbf{W_0'} = \begin{bmatrix} -\left(\Psi_1+\Psi_2\right)\epsilon_1\epsilon_2\left(\frac{V}{b}\right)^2 & -\left(\Psi_1\epsilon_1+\Psi_2\epsilon_2\right)\left(\frac{V}{b}\right) \\ \left(\Psi_1+\Psi_2\right)\epsilon_1\epsilon_2\left(\frac{V}{b}\right)^2 b\left(a-a_c\right) & \left(\Psi_1\epsilon_1+\Psi_2\epsilon_2\right)\left(\frac{V}{b}\right)b\left(a-a_c\right) \end{bmatrix} \tag{7.77}$$

Finally, the aerodynamic state equation matrices are given by

$$\mathbf{W_1} = \begin{bmatrix} 0 & 1 \\ -\epsilon_1\epsilon_2\left(\frac{V}{b}\right)^2 & -(\epsilon_1+\epsilon_2)\left(\frac{V}{b}\right) \end{bmatrix} \tag{7.78}$$

$$\mathbf{W_2} = \begin{bmatrix} 0 & 0 \\ \frac{1}{V} & \frac{b}{V}\left(\frac{C_{l_\alpha}}{2\pi} + a_c - a\right) \end{bmatrix} \tag{7.79}$$

$$\mathbf{W_3} = \begin{bmatrix} 0 & 0 \\ 0 & 1 \end{bmatrix} \tag{7.80}$$

Verification and Validation

The method presented in this section is verified and validated in Yates Jr. [112] in the frequency domain.

To see the impact of changing the lift curve slope distribution, the wing analysed in Patil et al. [81] is again analysed in present analyses to calculate flutter and divergence speeds with an elliptical lift curve slope distribution C_{l_α}. The elliptical lift curve slope distribution is calculated from

$$C_{l_\alpha} = 2\pi\sqrt{1-x^2} \tag{7.81}$$

where x is the non-dimensional spanwise distance from wing root.

Aeroelastic results are shown in Table 7.4. As expected, using an elliptical lift curve slope distribution, lift decreases towards the wing tip, hence, flutter and divergence speeds are increased. It is recommended to use the most accurate steady-state lift distribution over the undeformed wing for more reliable results.

Parameter	**Present analysis with elliptical C_{l_α}**	**Analysis of Ref.[81] using the theory of Patil [80]**	**Difference** [%]
Flutter speed [m/s]	37.14	32.51	+14.3
Flutter frequency [rad/s]	24.46	22.37	+9.3
Divergence speed [m/s]	47.55	37.15	+28.0

Table 7.4: Comparison of flutter and divergence speeds with results from Patil et al. [81]. Present analysis uses 20 beam elements and an elliptical lift curve slope distribution.

This method will be implemented for the validation and verification of the propeller-wing system treated in Chapter 8.

As explained in Section 2.8.2, propeller slipstream effects change the steady lift distribution over the wing, in turn, wing aeroelastic behaviour is modified. The method presented in this section allows to perform an aeroelastic analysis of the wing including the lift distribution change caused by propeller slipstream effects. This is proposed to be further addressed in future work.

8

Propeller on a Flexible Cantilever Wing

Chapter 6 modelled the case of a propeller flexibly mounted on a rigid wing whereas Chapter 7 modelled a cantilever flexible wing without any propeller. Both models were built to analyse the aeroelastic behaviour of a propeller and a wing separately. In practice, wing flexibility can induce changes in the whirl flutter behaviour. Conversely, interactions with a propeller can also induce changes in the dynamic behaviour of a flexible wing. In order to arrive at better whirl flutter and wing flutter predictions it is desirable to model the flexible wing and the propeller together so the dynamic coupling of both systems can be introduced.

This chapter deals with the analysis of the dynamic behaviour of a propeller attached to a cantilever flexible wing. The analytical model is devised following that of Bennett and Bland [7] with the main difference that the model in Bennett and Bland [7] uses uncoupled vibration modes as generalized coordinates whereas present model will use the nodal degrees of freedom of the system as generalized coordinates. The cantilever flexible wing is represented by an Euler-Bernoulli beam model as described in Chapter 7. The inclusion of a rotating propeller into the wing adds extra mass and inertia terms into the wing structural model due to propeller mass and gyroscopic effects. The aerodynamic influence of the propeller on the wing is accounted for by adding propeller aerodynamic loads as nodal forces and moments that act on the nodal degrees of freedom of the wing. On the other hand, the motion of the propeller pivot point due to wing flexibility also adds additional inertial and gyroscopic terms into the propeller structural model. What's more, the motion of the pivot point changes the effective pitch and yaw angles encountered by the propeller blades, thus, modifying propeller aerodynamics. Aerodynamic interference effects are ignored.

Figure 8.1 illustrates the geometry of a cantilever wing with a propeller and Figure 8.2 shows the kinematic scheme of such a model.

8.1. Derivation of the Equations of Motion

The wing is discretized into several beam elements and the propeller is attached to the wing through a nodal point. Structural and aerodynamic interactions between the propeller and the wing can be analysed by observing the wing section (beam node) on which the propeller is attached (Figure 8.1a). The structural model of such a configuration can be obtained by applying Lagrange's equations (Equation (5.1)) to a propeller with a moving pivot point. In the present model, the propeller pitches and yaws around the pivot point whilst the pivot point moves according to the bending and twisting of the wing nodal point to which the propeller is attached.

The problem can be treated by considering only propeller pitch θ, propeller yaw ψ, propeller-wing nodal displacement h_P, and propeller-wing nodal twist α_P.

The formulation of the equations of motion of the system begins with the kinetic energy, the potential energy and the dissipation function prior applying Lagrange's equations.

Kinetic energy

The kinetic energy can be separated into two parts: the contribution of the flexibly mounted non-rotating propeller engine system T_P and the energy of the rotating propeller T_Ω which includes the kinetic energy of

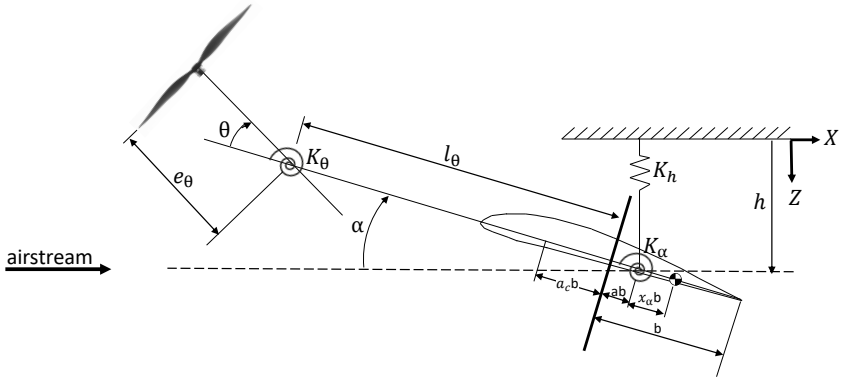

(a) Section view of the airfoil with the propeller

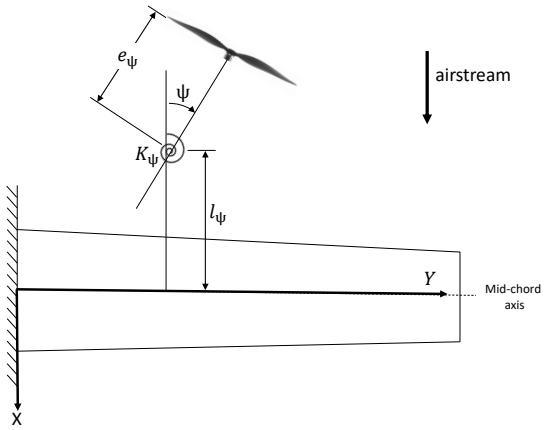

(b) Plan view

Figure 8.1: Analytical model a propeller on cantilevered flexible wing (adapted from [7]). The variables $e_\theta, e_\psi, e_\alpha, l_\theta, l_\psi, a, a_c$,and x_a are positive rearward.

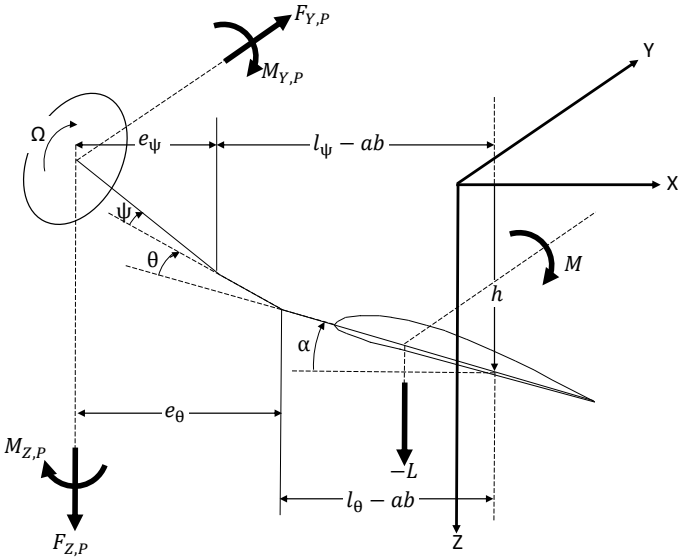

Figure 8.2: Forces and moments acting on a propeller-flexible wing (adapted from [7]). The variables $e_\theta, e_\psi, e_\alpha, l_\theta, l_\psi, a, a_c$,and x_a are positive rearward.

the gyroscopic precession.

$$T = T_P + T_\Omega \tag{8.1}$$

The kinetic energy of the non-rotating propeller engine system is given by

$$T_P = \frac{1}{2}\int m_P(x)\left(\dot{z}_P^2 + \dot{y}_P^2\right)dx \tag{8.2}$$

where m_P is the mass per unit length of the propeller engine system and

$$\begin{aligned} z_P(x,t) &= h_P + (x - a_P b_P)\alpha_P + (x - l_\theta)\theta \\ y_P(x,t) &= -(x - l_\psi)\psi \end{aligned} \tag{8.3}$$

This kinetic energy is integrated over the axial length of the propeller engine system.
Substituting Equation (8.3) into Equation (8.2) results in [1]

$$T_P = \frac{1}{2}M_P\dot{h}_P^2 + \frac{1}{2}I_{\alpha,P}\dot{\alpha}_P^2 + \frac{1}{2}I_{\theta,P}\dot{\theta}^2 + S_{\alpha,P}\dot{h}_P\dot{\alpha}_P + S_{\theta,P}\dot{h}_P\dot{\theta} + I_{\theta\alpha,P}\dot{\alpha}_P\dot{\theta} + \frac{1}{2}I_{\psi,P}\dot{\psi}^2 \tag{8.4}$$

where

$$\begin{aligned} M_P &= \int m_P(x)dx \\ S_{\alpha,P} &= \int m_P(x)[(x - l_\theta) + (l_\theta - a_P b_P)]dx = S_{\theta,P} + (l_\theta - a_P b_P)M_P \\ I_{\alpha,P} &= \int m_P(x)(x - a_P b_P)^2 dx = I_{\theta,P} + (l_\theta - a_P b_P)^2 M_P + 2(l_\theta - a_P b_P)S_{\theta,P} \end{aligned} \tag{8.5}$$

with

$$\begin{aligned} S_{\theta,P} &= \int m_P(x)(x - l_\theta)dx \\ I_{\theta,P} &= \int m_P(x)(x - l_\theta)^2 dx \\ I_{\psi,P} &= \int m_P(x)(x - l_\psi)^2 dx \\ I_{\theta\alpha,P} &= \int m_P(x)(x - a_P b_P)(x - l_\theta)dx = I_{\theta,P} + (l_\theta - a_P b_P)S_{\theta,P} \end{aligned} \tag{8.6}$$

The mass of the propeller is assumed to be distributed along the rotor rotational axis and the integrations are to be taken over the pivoting system.

The propeller angular velocity in the X-axis is $\omega_X = \Omega + \left(\dot{\theta} + \dot{\alpha}_P\right)\sin\psi \approx \Omega + \left(\dot{\theta} + \dot{\alpha}_P\right)\psi$. Therefore the kinetic energy of the rotating propeller is given by

$$T_\Omega = \frac{1}{2}I_\Omega\omega_X^2 \approx \frac{1}{2}I_\Omega\left[\Omega^2 + 2\Omega\left(\dot{\theta} + \dot{\alpha}_P\right)\psi\right] = \frac{1}{2}I_\Omega\Omega^2 + I_\Omega\Omega\dot{\theta}\psi + I_\Omega\Omega\dot{\alpha}_P\psi \tag{8.7}$$

The expression for the total kinetic energy is

$$\begin{aligned} T = &\frac{1}{2}M_P\dot{h}_P^2 + \frac{1}{2}I_{\alpha,P}\dot{\alpha}_P^2 + S_{\alpha,P}\dot{h}_P\dot{\alpha}_P + \frac{1}{2}I_{\theta,P}\dot{\theta}^2 + S_{\theta,P}\dot{h}_P\dot{\theta} \\ &+ I_{\theta\alpha,P}\dot{\alpha}_P\dot{\theta} + \frac{1}{2}I_{\psi,P}\dot{\psi}^2 + \frac{1}{2}I_\Omega\Omega^2 + I_\Omega\Omega\dot{\theta}\psi + I_\Omega\Omega\dot{\alpha}_P\psi \end{aligned} \tag{8.8}$$

[1] Note that $I_{\theta,P} = I_Y$ and $I_{\psi,P} = I_Z$, from Chapter 6.

Potential energy

The potential energy of the propeller due to flexible engine mounts is

$$U_P = \frac{1}{2}K_\theta\theta^2 + \frac{1}{2}K_\psi\psi^2 \tag{8.9}$$

where the stiffness terms K_i may be expressed in terms of uncoupled frequencies and inertia ($\omega_\theta = \sqrt{\frac{K_\theta}{I_{\theta,P}}}$ and $\omega_\psi = \sqrt{\frac{K_\psi}{I_{\psi,P}}}$)

$$U_P = \frac{1}{2}I_{\theta,P}\omega_\theta^2\theta^2 + \frac{1}{2}I_{\psi,P}\omega_\psi^2\psi^2 \tag{8.10}$$

Dissipation energy

The dissipation function can be expressed in terms of the hysteretic type of structural damping. In this case, the dissipative force is proportional to displacement.

$$D = \frac{1}{2}\frac{K_\theta g_\theta}{\omega}\dot{\theta}^2 + \frac{1}{2}\frac{K_\psi g_\psi}{\omega}\dot{\psi}^2 \tag{8.11}$$

where ω is the frequency of vibration of the system and g_i are the structural damping coefficients.
Expressing the stiffness terms K_i may be expressed in terms of uncoupled frequencies and mass/inertia

$$D = \frac{1}{2}I_{\theta,P}\omega_\theta^2\frac{g_\theta}{\omega}\dot{\theta}^2 + \frac{1}{2}I_{\psi,P}\omega_\psi^2\frac{g_\psi}{\omega}\dot{\psi}^2 \tag{8.12}$$

Equations of motion

Applying Lagrange's equations, the final equations of motion of the system are

$$\begin{aligned}
I_{\theta,P}\ddot{\theta} + K_\theta\theta + \frac{K_\theta g_\theta}{\omega}\dot{\theta} + I_\Omega\Omega\dot{\psi} + S_{\theta,P}\ddot{h}_P + I_{\theta\alpha,P}\ddot{\alpha}_P &= Q_\theta \\
-I_\Omega\Omega\dot{\theta} + I_{\psi,P}\ddot{\psi} + K_\psi\psi + \frac{K_\psi g_\psi}{\omega}\dot{\psi} - I_\Omega\Omega\dot{\alpha}_P &= Q_\psi \\
\cdots + S_{\theta,P}\ddot{\theta} + M_P\ddot{h}_P + S_{\alpha,P}\ddot{\alpha}_P &= Q_{h,W} + Q_{h,P} \\
\cdots + I_{\theta\alpha,P}\ddot{\theta} + I_\Omega\Omega\dot{\psi} + S_{\alpha,P}\ddot{h}_P + I_{\alpha,P}\ddot{\alpha}_P &= Q_{\alpha,W} + Q_{\alpha,P}
\end{aligned} \tag{8.13}$$

The "..." represent the terms that originate from wing kinetic energy and wing potential energy when deriving with respect to the propeller-wing nodal degrees of freedom (h_P, α_P). These terms are already given in the wing beam model explained in Chapter 7. Q_θ and Q_ψ are the propeller aerodynamic loads that act on the propeller, $Q_{h,P}$ and $Q_{\alpha,P}$ are the propeller aerodynamic loads that act on the propeller-wing node, and $Q_{h,W}$ and $Q_{\alpha,W}$ are the wing aerodynamic loads that act on the propeller-wing node; they are obtained from Theodorsen's theory as explained in Section 7.2.

Comparing the first two equations in Equation (8.13) with the equations of motion of the propeller on a rigid wing (Equation (6.8)), one can observe that the influence of wing flexibility on the propeller is represented by a static unbalance term ($S_{\theta,P}\ddot{h}_P$), a inertial term ($I_{\theta\alpha,P}\ddot{\alpha}_P$), and a gyroscopic term ($-I_\Omega\Omega\dot{\alpha}_P$). The gyroscopic effects that couple propeller pitching and yawing motions are represented by the terms $I_\Omega\Omega\dot{\theta}$ and $-I_\Omega\Omega\dot{\psi}$, this influence is enhanced by the twisting motions of the wing through $-I_\Omega\Omega\dot{\alpha}_P$.

The last two equations in Equation (8.13) represent the extra terms that need to be added to the wing beam model due to the influence of the propeller. The influence of the propeller on the wing is represented by a mass term ($M_P\ddot{h}_P$), static unbalance terms ($S_{\theta,P}\ddot{\theta}$, $S_{\alpha,P}\ddot{\alpha}_P$, $S_{\alpha,P}\ddot{h}_P$), inertial terms ($I_{\theta\alpha,P}\ddot{\theta}$ and $I_{\alpha,P}\ddot{\alpha}_P$), and a gyroscopic term ($I_\Omega\Omega\dot{\psi}$). Due to gyroscopic effects, propeller yawing motions may influence wing pitching motions.

8.1.1. Structural Model in Matrix Form

Propeller

The first two equations in Equation (8.13) may be expressed in matrix form as

$$\mathbf{A_s}\ddot{\mathbf{q}}_\mathbf{P} + \mathbf{B_s}\ddot{\mathbf{q}}_\mathbf{WP} + \mathbf{C_s}\dot{\mathbf{q}}_\mathbf{P} + \mathbf{D_s}\dot{\mathbf{q}}_\mathbf{WP} + \mathbf{E_s}\mathbf{q_P} = \begin{bmatrix} Q_\theta \\ Q_\psi \end{bmatrix} \tag{8.14}$$

where $\mathbf{A_s}$ and $\mathbf{B_s}$ are the structural mass matrices, $\mathbf{C_s}$ and $\mathbf{D_s}$ are the structural damping matrices, $\mathbf{E_s}$ is the structural stiffness matrices, Q_θ and Q_ψ are the propeller aerodynamic loads that act on the propeller, $\mathbf{q_P} = \begin{bmatrix} \theta \\ \psi \end{bmatrix}$ are the propeller pitch and yaw, and $\mathbf{q_{WP}} = \begin{bmatrix} h_P \\ \alpha_P \end{bmatrix}$ are the wing nodal displacement and nodal twist at the section where the propeller is positioned.

The structural mass matrices are given by

$$\mathbf{A_s} = \begin{bmatrix} I_{\theta,P} & 0 \\ 0 & I_{\psi,P} \end{bmatrix} \tag{8.15}$$

$$\mathbf{B_s} = \begin{bmatrix} S_{\theta,P} & I_{\theta\alpha,P} \\ 0 & 0 \end{bmatrix} \tag{8.16}$$

The structural damping matrices are given by

$$\mathbf{C_s} = \begin{bmatrix} \frac{K_\theta g_\theta}{\omega} & I_\Omega \Omega \\ -I_\Omega \Omega & \frac{K_\psi g_\psi}{\omega} \end{bmatrix} \tag{8.17}$$

$$\mathbf{D_s} = \begin{bmatrix} 0 & 0 \\ 0 & -I_\Omega \Omega \end{bmatrix} \tag{8.18}$$

The structural stiffness matrices are given by

$$\mathbf{E_s} = \begin{bmatrix} K_\theta & 0 \\ 0 & K_\psi \end{bmatrix} \tag{8.19}$$

Wing

The terms that appear in the last two equations in Equation (8.13) can also be arranged in matrix form as

$$\cdots + \mathbf{F_s}\ddot{\mathbf{q}}_\mathbf{P} + \mathbf{G_s}\ddot{\mathbf{q}}_\mathbf{WP} + \mathbf{H_s}\dot{\mathbf{q}}_\mathbf{P} = \begin{bmatrix} Q_{h,W} + Q_{h,P} \\ Q_{\alpha,W} + Q_{\alpha,P} \end{bmatrix} \tag{8.20}$$

where

$$\mathbf{F_s} = \begin{bmatrix} S_{\theta,P} & 0 \\ I_{\theta\alpha,P} & 0 \end{bmatrix} \tag{8.21}$$

$$\mathbf{G_s} = \begin{bmatrix} M_P & S_{\alpha,P} \\ S_{\alpha,P} & I_{\alpha,P} \end{bmatrix} \tag{8.22}$$

$$\mathbf{H_s} = \begin{bmatrix} 0 & 0 \\ 0 & I_\Omega \Omega \end{bmatrix} \tag{8.23}$$

8.2. Propeller Aerodynamics

The propeller aerodynamic loads that appear in Equation (8.13) are to be defined from the virtual work principle. The virtual work done by a propeller with moving pivot point is given by

$$\delta W = Q_{\theta,P}\delta\theta + Q_{\psi,P}\delta\psi + Q_{h,P}\delta h_P + Q_{\alpha,P}\delta\alpha_P \tag{8.24}$$

where $Q_{\theta,P}$, $Q_{\psi,P}$, $Q_{h,P}$, and $Q_{\alpha,P}$ are derived from propeller aerodynamics.

$Q_{\theta,P}$ and $Q_{\psi,P}$ are the propeller aerodynamic moments about the pivot points. $Q_{h,P}$, and $Q_{\alpha,P}$ are the propeller aerodynamic loads acting on the propeller-wing nodal degrees of freedom.

8.2.1. Propeller aerodynamic Loads on the Propeller

The propeller aerodynamic moments about the pivot point are[2]

$$\begin{aligned} Q_{\theta,P} &= M_{Y,P} + e_\theta F_{Z,P} \\ Q_{\psi,P} &= M_{Z,P} - e_\psi F_{Y,P} \end{aligned} \tag{8.25}$$

where $F_{Y,P}, M_{Y,P}, F_{Z,P}$, and $M_{Z,P}$ are the propeller aerodynamic forces and moments generated by the propeller as defined in Chapter 6 by Equation (4.25)

$$\begin{aligned} F_Z &= \frac{1}{2}\rho V^2 S'\left(C_{Z_\theta}\overline{\theta} + C_{Z_\psi}\overline{\psi} + C_{Z_q}\frac{\dot{\overline{\theta}}R}{V} + C_{Z_r}\frac{\dot{\overline{\psi}}R}{V}\right) \\ M_{Y,p} &= \rho V^2 S' R\left(C_{m_\theta}\overline{\theta} + C_{m_\psi}\overline{\psi} + C_{m_q}\frac{\dot{\overline{\theta}}R}{V} + C_{m_r}\frac{\dot{\overline{\psi}}R}{V}\right) \\ F_Y &= \frac{1}{2}\rho V^2 S'\left(C_{Y_\theta}\overline{\theta} + C_{Y_\psi}\overline{\psi} + C_{Y_q}\frac{\dot{\overline{\theta}}R}{V} + C_{Y_r}\frac{\dot{\overline{\psi}}R}{V}\right) \\ M_{Z,p} &= \rho V^2 S' R\left(C_{n_\theta}\overline{\theta} + C_{n_\psi}\overline{\psi} + C_{n_q}\frac{\dot{\overline{\theta}}R}{V} + C_{n_r}\frac{\dot{\overline{\psi}}R}{V}\right) \end{aligned} \tag{4.25}$$

With the difference that now, the influence of the flexible wing will change the propeller effective pitch and yaw angles

$$\begin{aligned} \overline{\theta} &= \theta + \alpha_P + \frac{e_\theta}{V}\dot{\theta} + \frac{e_\alpha}{V}\dot{\alpha}_P + \frac{1}{V}\dot{h}_P \\ \overline{\psi} &= \psi + \frac{e_\psi}{V}\dot{\psi} \end{aligned} \tag{8.26}$$

where h_P and α_P are the wing nodal displacement and wing nodal twist at the section where the propeller is positioned.

In matrix form

Combining the expressions in Equation (8.25), Equation (4.25), and Equation (8.26) the complete set of propeller aerodynamic forces and moments may be expressed in matrix form as

$$\begin{bmatrix} Q_{\theta,P} \\ Q_{\psi,P} \end{bmatrix} = \mathbf{A_a}\ddot{\mathbf{q}}_\mathbf{P} + \mathbf{B_a}\ddot{\mathbf{q}}_\mathbf{WP} + \mathbf{C_a}\dot{\mathbf{q}}_\mathbf{P} + \mathbf{D_a}\dot{\mathbf{q}}_\mathbf{WP} + \mathbf{E_a}\mathbf{q}_\mathbf{P} + \mathbf{F_a}\mathbf{q}_\mathbf{WP} \tag{8.27}$$

where $\mathbf{A_a}$ and $\mathbf{B_a}$ are the aerodynamic mass matrices, $\mathbf{C_a}$ and $\mathbf{D_a}$ are the aerodynamic damping matrices, $\mathbf{E_a}$ and $\mathbf{F_a}$ are the aerodynamic stiffness matrices, $\mathbf{q_P} = \begin{bmatrix} \theta \\ \psi \end{bmatrix}$ are the propeller pitch and yaw, and $\mathbf{q_{WP}} = \begin{bmatrix} h_P \\ \alpha_P \end{bmatrix}$ are the wing nodal displacement and nodal twist at the section where the propeller is positioned.

The propeller aerodynamic mass matrices are given by

[2] Again, note that e_θ and e_ψ are negative in this model, hence the change in sign with respect to Equation (6.9).

$$\mathbf{A_a} = \begin{bmatrix} k_2 C_{mq} \frac{R}{V} \frac{e_\theta}{V} + e_\theta k_1 C_{Zq} \frac{R}{V} \frac{e_\theta}{V} & k_2 C_{mr} \frac{R}{V} \frac{e_\psi}{V} + e_\theta k_1 C_{Zr} \frac{R}{V} \frac{e_\psi}{V} \\ k_2 C_{nq} \frac{R}{V} \frac{e_\theta}{V} - e_\psi k_1 C_{Yq} \frac{R}{V} \frac{e_\theta}{V} & k_2 C_{nr} \frac{R}{V} \frac{e_\psi}{V} - e_\psi k_1 C_{Yr} \frac{R}{V} \frac{e_\psi}{V} \end{bmatrix} \tag{8.28}$$

$$\mathbf{B_a} = \begin{bmatrix} k_2 C_{mq} \frac{R}{V} \frac{1}{V} + e_\theta k_1 C_{Zq} \frac{R}{V} \frac{1}{V} & k_2 C_{mq} \frac{R}{V} \frac{e_\alpha}{V} + e_\theta k_1 C_{Zq} \frac{R}{V} \frac{e_\alpha}{V} \\ k_2 C_{nq} \frac{R}{V} \frac{1}{V} - e_\psi k_1 C_{Yq} \frac{R}{V} \frac{1}{V} & k_2 C_{nq} \frac{R}{V} \frac{e_\alpha}{V} - e_\psi k_1 C_{Yq} \frac{R}{V} \frac{e_\alpha}{V} \end{bmatrix} \tag{8.29}$$

The propeller aerodynamic damping matrices are given by

$$\mathbf{C_a} = \begin{bmatrix} k_2 C_{m\theta} \frac{e_\theta}{V} + k_2 C_{mq} \frac{R}{V} + e_\theta k_1 C_{Z\theta} \frac{e_\theta}{V} + e_\theta k_1 C_{Zq} \frac{R}{V} & k_2 C_{m\psi} \frac{e_\psi}{V} + k_2 C_{mr} \frac{R}{V} + e_\theta k_1 C_{Z\psi} \frac{e_\psi}{V} + e_\theta k_1 C_{Zr} \frac{R}{V} \\ k_2 C_{n\theta} \frac{e_\theta}{V} + k_2 C_{nq} \frac{R}{V} - e_\psi k_1 C_{Y\theta} \frac{e_\theta}{V} - e_\psi k_1 C_{Yq} \frac{R}{V} & k_2 C_{n\psi} \frac{e_\psi}{V} + k_2 C_{nr} \frac{R}{V} - e_\psi k_1 C_{Y\psi} \frac{e_\psi}{V} - e_\psi k_1 C_{Yr} \frac{R}{V} \end{bmatrix} \tag{8.30}$$

$$\mathbf{D_a} = \begin{bmatrix} k_2 C_{m\theta} \frac{1}{V} + e_\theta k_1 C_{Z\theta} \frac{1}{V} & k_2 C_{m\theta} \frac{e_\alpha}{V} + k_2 C_{mq} \frac{R}{V} + e_\theta k_1 C_{Z\theta} \frac{e_\alpha}{V} + e_\theta k_1 C_{Zq} \frac{R}{V} \\ k_2 C_{n\theta} \frac{1}{V} - e_\psi k_1 C_{Y\theta} \frac{1}{V} & k_2 C_{n\theta} \frac{e_\alpha}{V} + k_2 C_{nq} \frac{R}{V} - e_\psi k_1 C_{Y\theta} \frac{e_\alpha}{V} - e_\psi k_1 C_{Yq} \frac{R}{V} \end{bmatrix} \tag{8.31}$$

The propeller aerodynamic stiffness matrices are given by

$$\mathbf{E_a} = \begin{bmatrix} k_2 C_{m\theta} + e_\theta k_1 C_{Z\theta} & k_2 C_{m\psi} + e_\theta k_1 C_{Z\psi} \\ k_2 C_{n\theta} - e_\psi k_1 C_{Y\theta} & k_2 C_{n\psi} - e_\psi k_1 C_{Y\psi} \end{bmatrix} \tag{8.32}$$

$$\mathbf{F_a} = \begin{bmatrix} 0 & k_2 C_{m\theta} + e_\theta k_1 C_{Z\theta} \\ 0 & k_2 C_{n\theta} - e_\psi k_1 C_{Y\theta} \end{bmatrix} \tag{8.33}$$

where $k_1 = \frac{1}{2}\rho V^2 S'$, $k_2 = \rho V^2 S' R$, $S' = \pi R^2$ is the area swept by the propeller blades and R is the propeller radius.

8.2.2. Propeller aerodynamic Loads on the Wing

The propeller aerodynamic loads that act on the propeller-wing nodal degrees of freedom contribute to the wing nodal lift force and wing nodal pitching moment (see Figure 8.2). These are the propeller vertical force $F_{Z,P}$ and the propeller pitching moment $M_{Y,P}$ as defined in Chapter 6 by Equation (4.25). Therefore, the propeller nodal loads are

$$\begin{aligned} Q_{h,P} &= F_{Z,P} \\ Q_{\alpha,P} &= M_{Y,P} + e_\alpha F_{Z,P} \end{aligned} \tag{8.34}$$

where

$$e_\alpha = e_\theta + l_\theta - a_P b_P \tag{8.35}$$

According to Figure 8.2, e_α, e_θ and l_θ are negative whilst $a_P b_P$ is positive. Hence the negative sign.

$F_{Z,P}$ and $M_{Y,P}$ are evaluated using the propeller effective pitch and yaw angles as defined earlier in Equation (8.26)

$$\begin{aligned} \overline{\theta} &= \theta + \alpha_P + \frac{e_\theta}{V}\dot{\theta} + \frac{e_\alpha}{V}\dot{\alpha}_P + \frac{1}{V}\dot{h}_P \\ \overline{\psi} &= \psi + \frac{e_\psi}{V}\dot{\psi} \end{aligned} \tag{8.26}$$

In matrix form

Equation (8.34) may be expressed in the following matrix form

$$\begin{bmatrix} Q_{h,P} \\ Q_{\alpha,P} \end{bmatrix} = \mathbf{P_1}\ddot{\mathbf{q}}_\mathbf{P} + \mathbf{P_2}\ddot{\mathbf{q}}_\mathbf{WP} + \mathbf{P_3}\dot{\mathbf{q}}_\mathbf{P} + \mathbf{P_4}\dot{\mathbf{q}}_\mathbf{WP} + \mathbf{P_5}\mathbf{q}_\mathbf{P} + \mathbf{P_6}\mathbf{q}_\mathbf{WP} \tag{8.36}$$

where $\mathbf{q_P} = \begin{bmatrix} \theta \\ \psi \end{bmatrix}$ are the propeller pitch and yaw, and $\mathbf{q_{WP}} = \begin{bmatrix} h_P \\ \alpha_P \end{bmatrix}$ are the wing nodal displacement and nodal twist at the section where the propeller is positioned. The matrices $\mathbf{P_1}$, $\mathbf{P_2}$, $\mathbf{P_3}$, $\mathbf{P_4}$, $\mathbf{P_5}$, and $\mathbf{P_6}$ are the aerodynamic influence matrices of the propeller on the wing and have the following expressions:

$$\mathbf{P_1} = \begin{bmatrix} k_1 C_{Zq} \frac{R}{V} \frac{e_\theta}{V} & k_1 C_{Zr} \frac{R}{V} \frac{e_\psi}{V} \\ k_2 C_{mq} \frac{R}{V} \frac{e_\theta}{V} + e_\alpha k_1 C_{Zq} \frac{R}{V} \frac{e_\theta}{V} & k_2 C_{mr} \frac{R}{V} \frac{e_\psi}{V} + e_\alpha k_1 C_{Zr} \frac{R}{V} \frac{e_\psi}{V} \end{bmatrix} \tag{8.37}$$

$$\mathbf{P_2} = \begin{bmatrix} k_1 C_{Zq} \frac{R}{V} \frac{1}{V} & k_1 C_{Zq} \frac{R}{V} \frac{e_\alpha}{V} \\ k_2 C_{mq} \frac{R}{V} \frac{1}{V} + e_\alpha k_1 C_{Zq} \frac{R}{V} \frac{1}{V} & k_2 C_{mq} \frac{R}{V} \frac{e_\alpha}{V} + e_\alpha k_1 C_{Zq} \frac{R}{V} \frac{e_\alpha}{V} \end{bmatrix} \tag{8.38}$$

$$\mathbf{P_3} = \begin{bmatrix} k_1 C_{Z\theta} \frac{e_\theta}{V} + k_1 C_{Zq} \frac{R}{V} & k_1 C_{Z\psi} \frac{e_\psi}{V} + k_1 C_{Zr} \frac{R}{V} \\ k_2 C_{m\theta} \frac{e_\theta}{V} + k_2 C_{mq} \frac{R}{V} + e_\alpha k_1 C_{Z\theta} \frac{e_\theta}{V} + e_\alpha k_1 C_{Zq} \frac{R}{V} & k_2 C_{m\psi} \frac{e_\psi}{V} + k_2 C_{mr} \frac{R}{V} + e_\alpha k_1 C_{Z\psi} \frac{e_\psi}{V} + e_\alpha k_1 C_{Zr} \frac{R}{V} \end{bmatrix} \tag{8.39}$$

$$\mathbf{P_4} = \begin{bmatrix} k_1 C_{Z\theta} \frac{1}{V} & k_1 C_{Z\theta} \frac{e_\alpha}{V} + k_1 C_{Zq} \frac{R}{V} \\ k_2 C_{m\theta} \frac{1}{V} + e_\alpha k_1 C_{Z\theta} \frac{1}{V} & k_2 C_{m\theta} \frac{e_\alpha}{V} + k_2 C_{mq} \frac{R}{V} + e_\alpha k_1 C_{Z\theta} \frac{e_\alpha}{V} + e_\alpha k_1 C_{Zq} \frac{R}{V} \end{bmatrix} \tag{8.40}$$

$$\mathbf{P_5} = \begin{bmatrix} k_1 C_{Z\theta} & k_1 C_{Z\psi} \\ k_2 C_{m\theta} + e_\alpha k_1 C_{Z\theta} & k_2 C_{m\psi} + e_\alpha k_1 C_{Z\psi} \end{bmatrix} \tag{8.41}$$

$$\mathbf{P_6} = \begin{bmatrix} 0 & k_1 C_{Z\theta} \\ 0 & k_2 C_{m\theta} + e_\alpha k_1 C_{Z\theta} \end{bmatrix} \tag{8.42}$$

where $k_1 = \frac{1}{2}\rho V^2 S'$, $k_2 = \rho V^2 S' R$, $S' = \pi R^2$ is the area swept by the propeller blades and R is the propeller radius.

Inclusion into the wing beam model

The expressions for $Q_{h,P}$ and $Q_{\alpha,P}$ are to be assembled into a global vector $\mathbf{Q_P}$ and be included into the equations of motion of the wing beam model (Equation (7.17)). Essentially, $\mathbf{Q_P}$ is the global vector that represent the propeller aerodynamic loads acting on the propeller-wing nodal point.

For the nodes where there is a propeller positioned, the propeller aerodynamic loads that act on these nodes are

$$\mathbf{Q_P}^{(i)} = \begin{bmatrix} Q_{h,P} \\ 0 \\ Q_{\alpha,P} \end{bmatrix} \tag{8.43}$$

For the nodes where there is no propeller positioned, $\mathbf{Q_P}^{(i)}$ becomes a 3-by-1 null vector. Therefore the global propeller aerodynamic load vector $\mathbf{Q_P}$ is

$$\mathbf{Q_P} = \begin{bmatrix} \mathbf{Q_P}^{(1)^T} & \mathbf{Q_P}^{(2)^T} & \dots & \mathbf{Q_P}^{(n+1)^T} \end{bmatrix}^T \tag{8.44}$$

8.3. Aeroelastic Equations of the Propeller-flexible-Wing System

8.3.1. Propeller

Combining the expressions in Equation (8.14) and Equation (8.27) the complete equations of motion of a propeller on flexible wing can be formulated in matrix form as follows

$$\left(\mathbf{A_s}-\mathbf{A_a}\right)\ddot{\mathbf{q}}_\mathbf{P}+\left(\mathbf{B_s}-\mathbf{B_a}\right)\ddot{\mathbf{q}}_\mathbf{WP}+\left(\mathbf{C_s}-\mathbf{C_a}\right)\dot{\mathbf{q}}_\mathbf{P}+\left(\mathbf{D_s}-\mathbf{D_a}\right)\dot{\mathbf{q}}_\mathbf{WP}+\left(\mathbf{E_s}-\mathbf{E_a}\right)\mathbf{q_P}+\left(-\mathbf{F_a}\right)\mathbf{q_{WP}}=\mathbf{0} \tag{8.45}$$

8.3.2. Wing

The equations of motion of the wing beam model including the influence of the propeller is obtained by combining Equation (7.23), Equation (8.20), Equation (8.27), and Equation (8.36)

$$\mathbf{M_{s,g}}\ddot{\mathbf{q}}_\mathbf{W}+\mathbf{C_{s,g}}\dot{\mathbf{q}}_\mathbf{W}+\mathbf{K_{s,g}}\mathbf{q_W}+\mathbf{F_s}\ddot{\mathbf{q}}_\mathbf{P}+\mathbf{G_s}\ddot{\mathbf{q}}_\mathbf{WP}+\mathbf{H_s}\dot{\mathbf{q}}_\mathbf{P}=\mathbf{Q_W}+\mathbf{Q_P} \tag{8.46}$$

8.3.3. Propeller - Wing

Equation (8.45) and Equation (8.46) define the aeroelastic behaviour of a propeller-flexible-wing system and need to be solved simultaneously. Present work reorganizes them into state space form and solves them using eigenvalue analysis. An example using two beam elements to model the wing is formulated in Appendix C and Appendix D. Note that the propeller must be attached to a wing nodal point.

Although only one propeller was employed to explain the methodology, the inclusion of two or more propellers is also possible. In this case there will be two more equations (Equation (8.45)) and two more unknowns (θ and ψ) per extra propeller installed onto the wing — this is explained in Appendix D.

8.4. Verification and Validation

Verification and validation of the methodology presented in this chapter is carried out by modelling the propeller-wing system analysed in Bennett and Bland [7]. Bennett and Bland [7] conducted an experimental and analytical investigation of propeller whirl flutter of a cantilever flexible wing with a fixed-pitch windmilling propeller. A sketch of this system is shown in Figure 8.3. It consists of a single propeller mounted with spring-restrained gimbals to a flexible wing in a conventional layout: the propeller is positioned between the wing root and the wing tip.

Bennett and Bland [7] tested the propeller in four different configurations. In present analysis, Configuration (A) and Configuration (C) will be analysed; Configuration (A) is the same propeller configuration tested in Bennett and Bland [6], also named as Configuration (A). Therefore, it is the same propeller already analysed in Section 4.2 to verify the propeller aerodynamic model and in Section 6.2 to verify the propeller-on-rigid-wing model. Configuration (C) differs from Configuration (A) in its mass parameters, namely, pitch mass moment of inertia $I_{\theta,P}$, yaw mass moment of inertia $I_{\psi,P}$, and pitch mass unbalance $S_{\theta,P}$.

The wing consists of an aluminium spar for stiffness and balsa pods for airfoil contour, see Figure 8.4. It has an aspect ratio of 6.97 and a taper ratio of 0.430. The elastic axis coincides with the wing spar centre line and it is swept forward 4.9°, however, the pods are formed as streamwise strips.

Data needed to model the propeller-wing system are extracted from [[7], Table I, Table II, Table III, Figure 2, Figure 4-Figure 7, Figure 9]. Model test data of the selected propeller configurations are shown in Table 8.1 and Table 8.2.

In the analyses of Bennett and Bland [7], five propeller aerodynamic derivatives were used, i.e. $C_{Z\theta}$, $C_{m\theta}$, $C_{Y\theta}$, $C_{m\psi}$, and C_{mq}. The first four are measured values extracted from Bennett and Bland [6] and the last one is calculated using Ribner's method [91]. Present analysis will calculate flutter speeds by using these five propeller aerodynamic derivatives and compare the results with those obtained by employing the full set of propeller aerodynamic derivatives computed with Houbolt-Reed's method.

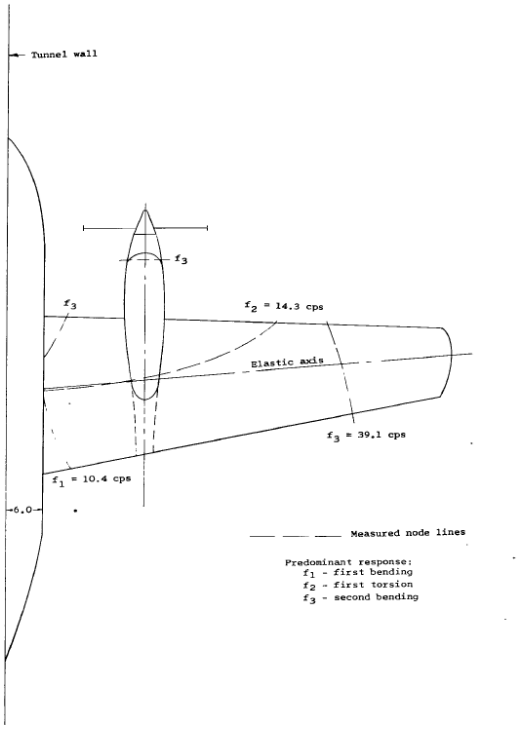

Figure 8.3: Sketch of the layout of the propeller-wing model [7].

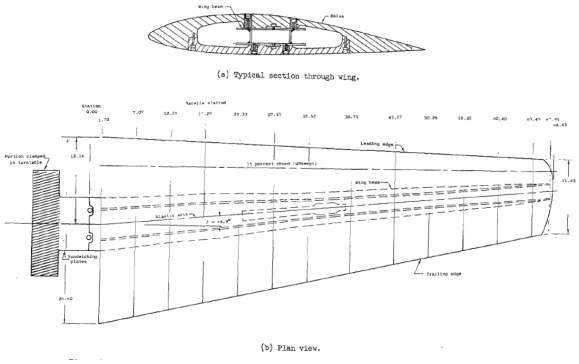

Figure 8.4: Schematic of the wing [7].

$\beta_{0.75R}$ [deg]	f_θ [Hz]	f_ψ [Hz]	$2\varsigma_\theta$	$2\varsigma_\psi$	ρ [slug/ft^3]	e_θ or e_ψ [-]
35	11.6	11.7	0.029	0.0324	0.00231	-0.31781
46	11.6	11.7	0.029	0.0324	0.00230	-0.32446
52	11.6	11.7	0.029	0.0324	0.00228	-0.32758
58	11.6	11.7	0.029	0.0324	0.00233	-0.33031

Table 8.1: Propeller Configuration (A): M_P = 0.2388 slug, $I_{\theta,P} = I_{\psi,P}$ = 0.0634 slug-ft^2, I_Ω = 0.00858 slug-ft^2, and $S_{\theta,P}$ = 0.03801 slug-ft [7].

$\beta_{0.75R}$ [deg]	f_θ [Hz]	f_ψ [Hz]	$2\varsigma_\theta$	$2\varsigma_\psi$	ρ [slug/ft^3]	e_θ or e_ψ [-]
25	19.4	20	0.0289	0.0266	0.00233	-0.31092
30	19.4	20	0.0289	0.0266	0.00233	-0.31437
35	19.4	20	0.0289	0.0266	0.00233	-0.31781
46	19.4	20	0.0289	0.0266	0.00233	-0.32446
52	19.4	20	0.0289	0.0266	0.00233	-0.32758

Table 8.2: Propeller Configuration (C): $M_P = 0.1379$ slug, $I_{\theta,P} = I_{\psi,P} = 0.01772$ slug-ft^2, $I_\Omega = 0.00858$ slug-ft^2, and $S_{\theta,P} = -0.02849$ slug-ft [7].

Verification and validation are conducted via a free vibration analysis to check the structural model and an aeroelastic analysis to check propeller and wing aerodynamics and the structural-aerodynamic coupling.

8.4.1. Free Vibration Analysis

Table 8.3 presents the first three natural frequencies of the bare spar with pods (wing without propeller-engine). The modes are coupled by wing static unbalance. Present analysis yields very approximate frequency values to those obtained from measurements and from a Rayleigh-Ritz type analysis conducted in Bennett and Bland [7].

Mode	**Present analysis**	**Measured Ref.[7]**	**Rayleigh-Ritz analysis Ref.[7]**
First bending	10.9	10.6	11.2
Second bending	42.2	39	43.1
First torsion	52.7	47	53.4

Table 8.3: Coupled natural frequencies (in Hz) of the wing spar with pods. Propeller-engine omitted.

Table 8.4 presents propeller pitch and propeller yaw natural frequencies. Exact frequency values are obtained since pitch stiffness K_θ and yaw stiffness K_θ are defined from measured uncoupled pitch and yaw frequencies and by definition, $\omega_\theta = \sqrt{\frac{K_\theta}{I_{\theta,P}}}$ and $\omega_\psi = \sqrt{\frac{K_\psi}{I_{\psi,P}}}$.

Mode	**Present analysis**	**Measured Ref.[7]**
Propeller pitch	9.21	9.21
Propeller yaw	9.34	9.34

Table 8.4: Uncoupled natural frequencies (in Hz) of the propeller.

When the propeller-engine is installed onto the wing, it increases the nodal mass and the nodal inertia at the spanwise location where the propeller is positioned. The added nodal mass is the propeller-engine mass M_P and the added nodal inertia is the mass moment of inertia of the propeller-engine about the wing elastic axis $I_{\alpha,P}$ (see Equation (8.5)). $I_{\alpha,P}$ depends on the distance between wing midchord and the propeller pivot point, l_θ, the higher this distance, the higher the value of $I_{\alpha,P}$; the distance l_θ is not specified in Bennett and Bland [7] so its value is guessed from Figure 8.3. Two values of l_θ are tested: $l_\theta = -2.2b_P$ and $l_\theta = -2.7b_P$. The change in wing mass and, especially, in wing inertia lowers the frequency of the first torsion mode and changes its mode shape. Figure 8.5 shows the first two uncoupled mode shapes, namely, the first bending mode and the first torsion mode of the wing with propeller installed. Blue line indicate the same uncoupled mode shapes calculated in Bennett and Bland [7]. With $l_\theta = -2.2b_P$, first torsion mode shape approximates better to the calculated mode shape found in Bennett and Bland [7]. First bending mode shape is not altered by the change in l_θ.

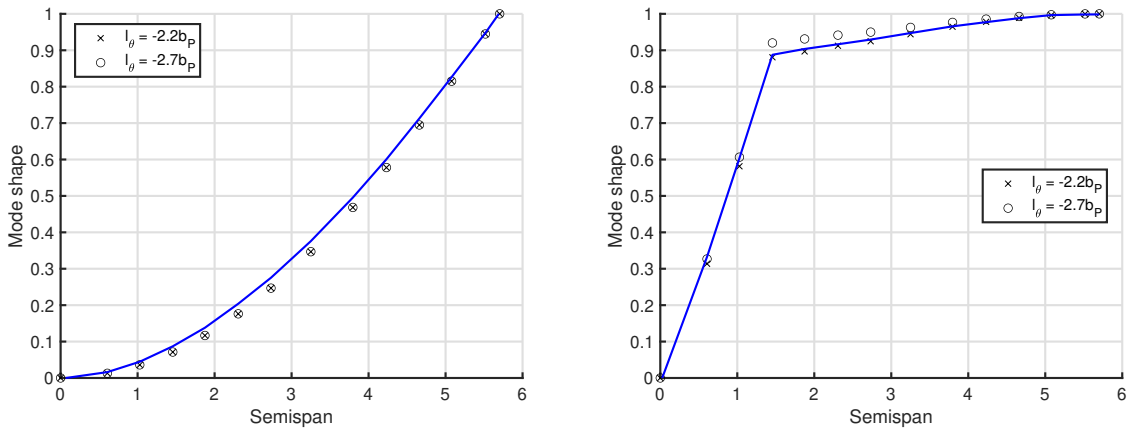

(a) First bending.

(b) First torsion.

Figure 8.5: Comparison of uncoupled mode shapes of the wing with propeller installed. Blue lines indicate calculated mode shapes from Bennett and Bland [7].

Table 8.5 presents the coupled frequencies of the entire propeller-wing model. The propeller is not rotating. The wing modes are coupled by static unbalance and the propeller pitch mode. There is good agreement in all mode shapes except for the first torsion and second bending modes. With $l_\theta = -2.2b_P$ present analysis approximate to the calculated values from reference [7] and with $l_\theta = -2.7b_P$ present analysis approximate better to the measured values from reference [7].

Mode	**Present analysis** $l_\theta = -2.2b_P$	**Present analysis** $l_\theta = -2.7b_P$	**Measured Ref.[7]**	**Rayleigh-Ritz analysis Ref.[7]**
Propeller pitch (Backward whirl)	9.3	9.2	9.3	9.2
Propeller yaw (Forward whirl)	9.3	9.3	9.3	9.3
First bending	10.8	10.8	10.4	10.1
First torsion	17.3	14.4	14.3	17.4
Second bending	42.9	42.7	39.1	–

Table 8.5: Coupled natural frequencies (in Hz) of the wing spar with pods and propeller-engine installed. The propeller is not rotating.

When the propeller rotates, gyroscopic effects change the frequency of the free vibration modes. Figure 8.6 and Figure 8.7 show the influence of propeller rotational speed on the natural frequencies of vibration in two cases, when the propeller frequency (pitch and yaw) has a value of $f_\theta = f_\psi = 11.65$ Hz and $f_\theta = f_\psi = 9.27$ Hz, respectively. Figures correspond to the propeller in Configuration (A). The main discrepancies with the results from Rayleigh-Ritz analysis are found in wing frequencies. As expected, with $l_\theta = -2.2b_P$ present analysis predicts higher first bending frequencies; whilst with $l_\theta = -2.7b_P$ present analysis predicts higher first bending frequencies and much lower first torsional frequencies. This can be due to the Rayleigh-Ritz analysis in Bennett and Bland [7] using only two uncoupled mode shapes.

The frequencies of propeller modes change with propeller rotational speed: the frequency of the backward whirl mode decreases while the frequency of the forward whirl mode increases. When the frequency of a propeller mode comes close to the frequency of a wing mode, they do not cross, instead, they split following an asymptote. Therefore, the way in which gyroscopic effects influence wing vibration modes depends on the value of propeller frequencies relative to the value of wing frequencies, both evaluated at zero propeller rotational speed.

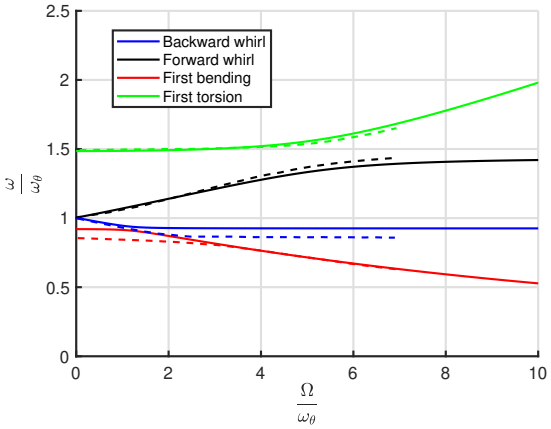

(a) Propeller pitch frequency $f_\theta = 11.65$ Hz ($f_\theta = f_\psi$).

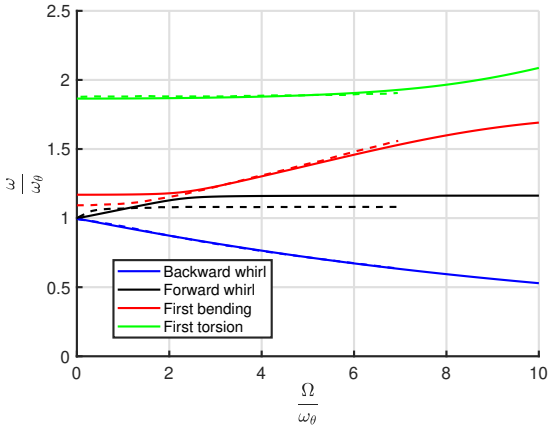

(b) Propeller pitch frequency $f_\theta = 9.27$ Hz ($f_\theta = f_\psi$).

Figure 8.6: Configuration (A): The effect of propeller rotational speed on natural frequencies of vibration with $l_\theta = -2.2b_P$. Dashed lines indicate calculated results from Bennett and Bland [7] using Rayleigh-Ritz type analysis.

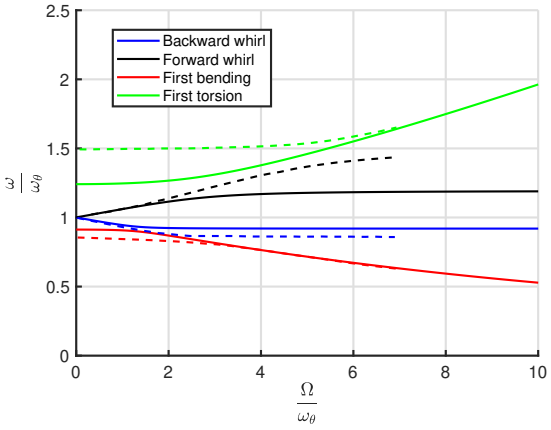

(a) Propeller pitch frequency $f_\theta = 11.65$ Hz.

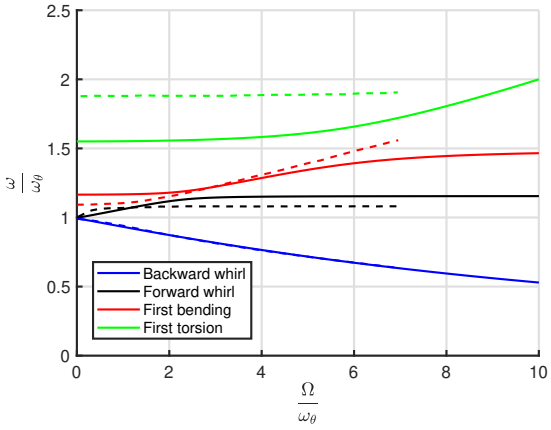

(b) Propeller pitch frequency $f_\theta = 9.27$ Hz.

Figure 8.7: Configuration (A): The effect of propeller rotational speed on natural frequencies of vibration with $l_\theta = -2.7b_P$. Dashed lines indicate calculated results from Bennett and Bland [7] using Rayleigh-Ritz type analysis.

To sum up, installing a propeller on the wing changes the natural frequencies of vibration of the wing due to change in wing mass and wing inertia, but also due to gyroscopic effects. The influence of these gyroscopic effects depend upon the parameters of the propeller-wing system, i.e. the distribution of natural frequencies of vibration of the coupled propeller-wing system.

In general, present structural model is in good agreement with verification and validation data. Confidence in the results of present analysis can be increased if the exact value of l_θ is known.

8.4.2. Aeroelastic Analysis

In this section verification and validation of the aeroelastic results are presented.

The parameters to be compared with measured and calculated data extracted from reference are propeller whirl flutter speed and propeller whirl flutter frequency.

Bennett and Bland [7] do not present quantitative results of their analysis of wing aeroelastic characteristics. Nevertheless, aeroelastic analysis of the propeller-wing system using present model are presented and described for completeness. The values of wing flutter speed, wing flutter frequency, and wing divergence speed from the complete propeller-wing model is compared with those from the flexible cantilever wing without any propellers.

Whirl flutter

Whirl flutter speeds and whirl flutter frequencies are calculated for the propeller in Configuration (A) and in Configuration (C) without wing flexibility and with wing flexibility effects.

In all cases, measured whirl flutter data extracted from reference include wing flexibility.

Without wing flexibility

Figure 8.8 and Figure 8.9 present whirl flutter speeds and whirl flutter frequencies of propeller in Configuration (A) and in Configuration (C), respectively. In each case, present analysis calculated whirl flutter speeds and whirl flutter frequencies employing (1) measured propeller aerodynamic derivatives extracted from Bennett and Bland [7], (2) calculated propeller aerodynamic derivatives using Houbolt-Reed's method with compressibility effects ($M \neq 0$), and (3) calculated propeller aerodynamic derivatives using Houbolt-Reed's method without compressibility effects ($M = 0$). Note that the experimental data presented include wing flexibility effects.

In Configuration (A) (Figure 8.8), calculated whirl flutter speeds and whirl flutter frequencies are very close to their measured counterparts. Using the calculated propeller aerodynamic derivatives from Houbolt-Reed's method, whirl flutter speeds follow the measured trend more closely .

In Configuration (C) (Figure 8.9), calculated whirl flutter speeds and whirl flutter frequencies are more conservative than their measured counterparts: whirl flutter speeds are underpredicted and whirl flutter frequencies are overpredicted. Using the measured propeller aerodynamic derivatives from Bennett and Bland [7], whirl flutter speeds and whirl flutter frequencies are slightly closer to the measured values. Discrepancies with measured data are bigger at higher propeller blade angles at three-quarter propeller radius. It seems that propeller in Configuration (C) is more affected by wing flexibility.

As expected, in both configurations, compressibility effects barely affect the whirl flutter results. This is because for Mach numbers below 0.3 the values of the propeller aerodynamic derivatives calculated using Houbolt-Reed's method hardly change (see Figure 4.7).

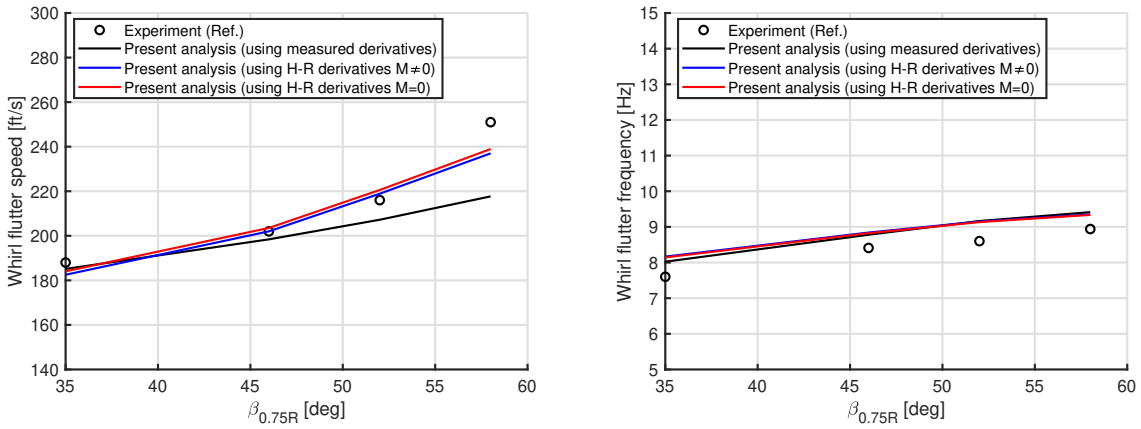

(a) Whirl flutter speed.

(b) Whirl flutter frequency.

Figure 8.8: Configuration (A): Comparison of whirl flutter speeds and whirl flutter frequencies with measured data from Bennett and Bland [7].

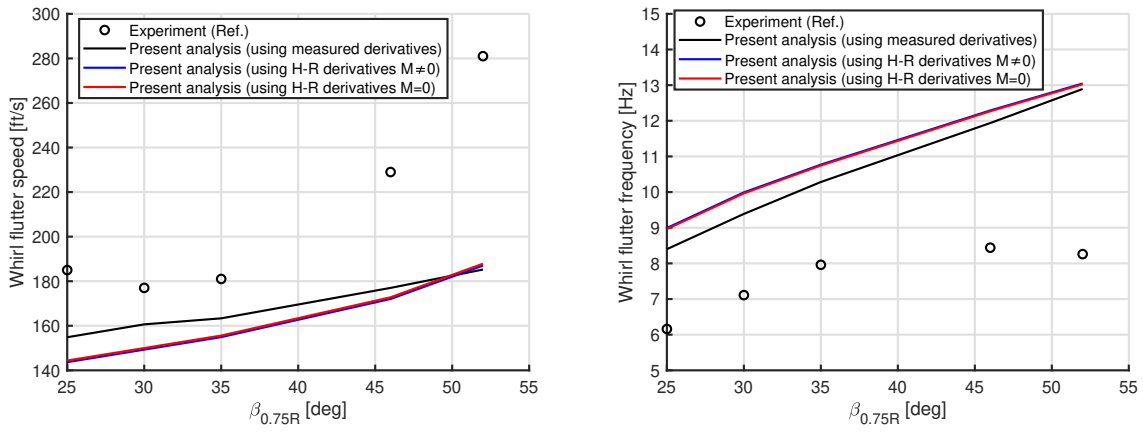

(a) Whirl flutter speed.

(b) Whirl flutter frequency.

Figure 8.9: Configuration (C): Comparison of whirl flutter speeds and whirl flutter frequencies with measured data from Bennett and Bland [7].

With wing flexibility

In this section, whirl flutter speeds and whirl flutter frequencies are calculated including wing flexibility. Figure 8.10 and Figure 8.12[3]compare whirl flutter results calculated using measured propeller aerodynamic derivatives extracted from Bennett and Bland [7], and Figure 8.11 and Figure 8.13 compare whirl flutter results calculated using propeller aerodynamic derivatives obtained from Houbolt-Reed's method without compressibility effects ($M = 0$). There is slightly better agreement with measured data in Configuration (A) when using propeller aerodynamic derivatives calculated from Houbolt-Reed's method; whereas in Configuration (C) slightly better agreement is found when using the measured propeller aerodynamic derivatives.

As the distance between wing midchord and the propeller pivot point l_θ is unknown, two different values are tested: $l_\theta = -2.2b_P$ and $l_\theta = -2.7b_P$. In general, calculated whirl flutter results are more approximate to measured whirl flutter results when $l_\theta = -2.7b_P$. This is corroborated by the fact that with $l_\theta = -2.7b_P$, calculated coupled natural frequencies are closer to their measured values (see Table 8.5).

In Configuration (A) (Figure 8.10 and Figure 8.11), calculated whirl flutter results with and without wing flexibility are almost aligned, it seems that whirl flutter results are barely influenced by wing flexibility; in Configuration (C) (Figure 8.12 and Figure 8.13), calculated whirl flutter results agree better with measured data when wing flexibility is included. Bennett and Bland [7] also calculated whirl flutter speeds and whirl flutter frequencies including wing flexibility (represented by the red line in the figures). Their approach is based on a Rayleigh-Ritz type of analysis using only the first two wing uncoupled modes (first torsional and first bending modes) and a structural damping of $g_h = g_\alpha = 0.005$ was assumed. In general, calculated results from Bennett and Bland [7] seem to obtain better agreement with measured data but results from present analysis, which do not include any type of wing damping, are not far-off.

[3]In the figures, whirl flutter speed V_f and whirl flutter frequency ω_f are non-dimensioned with the average frequency $\overline{\omega}$ and the propeller radius R. $\overline{\omega}$ is the average frequency of the uncoupled modes of propeller pitch and yaw expressed in rad/s $\left(\overline{\omega} = \frac{\omega_\theta + \omega_\psi}{2}\right)$. The propeller radius is $R = 0.8438$ ft.

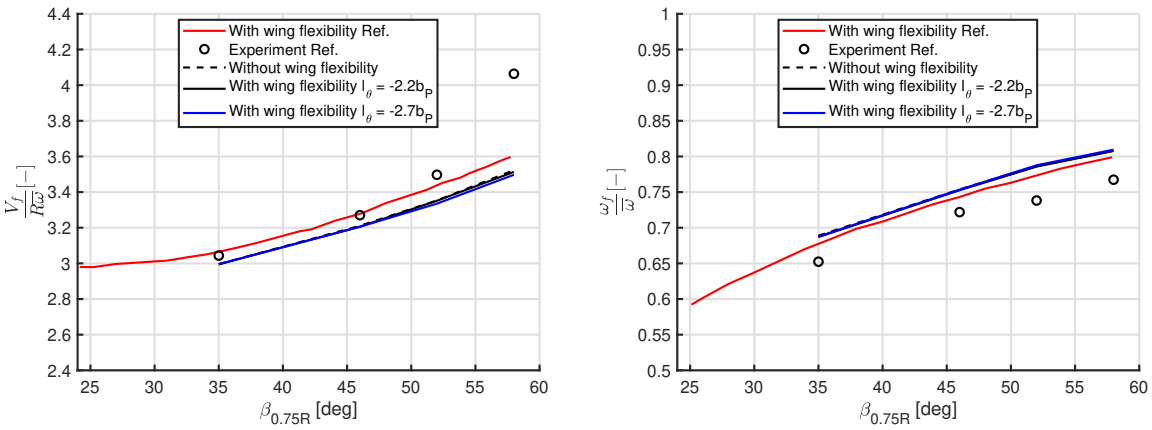

(a) Whirl flutter velocity

(b) Whirl flutter frequency.

Figure 8.10: Configuration (A): Comparison of whirl flutter velocity and whirl flutter frequency. With measured propeller aerodynamic derivatives from Bennett and Bland [7]. Without wing structural damping.

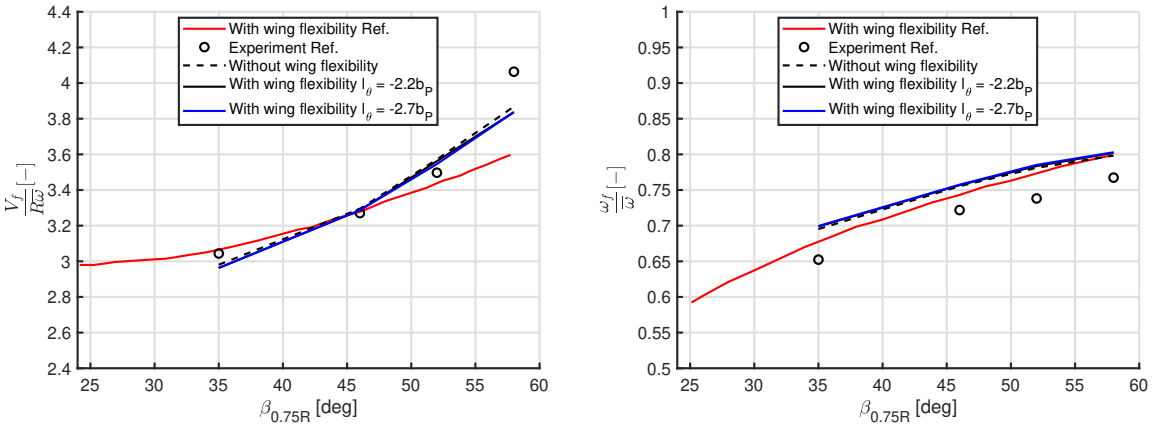

(a) Whirl flutter velocity

(b) Whirl flutter frequency.

Figure 8.11: Configuration (A): Comparison of whirl flutter velocity and whirl flutter frequency. With Houbolt-Reed propeller aerodynamic derivatives. Without wing structural damping.

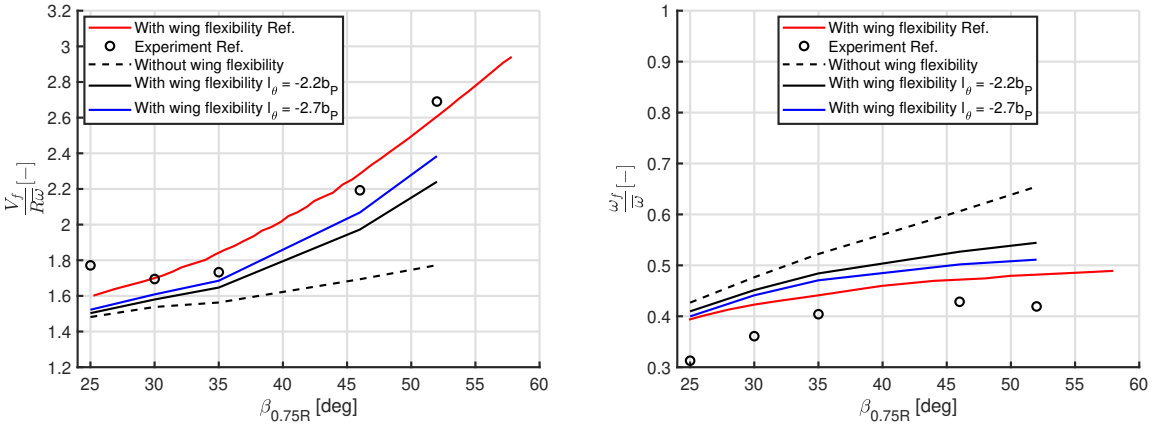

(a) Whirl flutter velocity

(b) Whirl flutter frequency.

Figure 8.12: Configuration (C): Comparison of whirl flutter velocity and whirl flutter frequency. With measured propeller aerodynamic derivatives from Bennett and Bland [7]. Without wing structural damping.

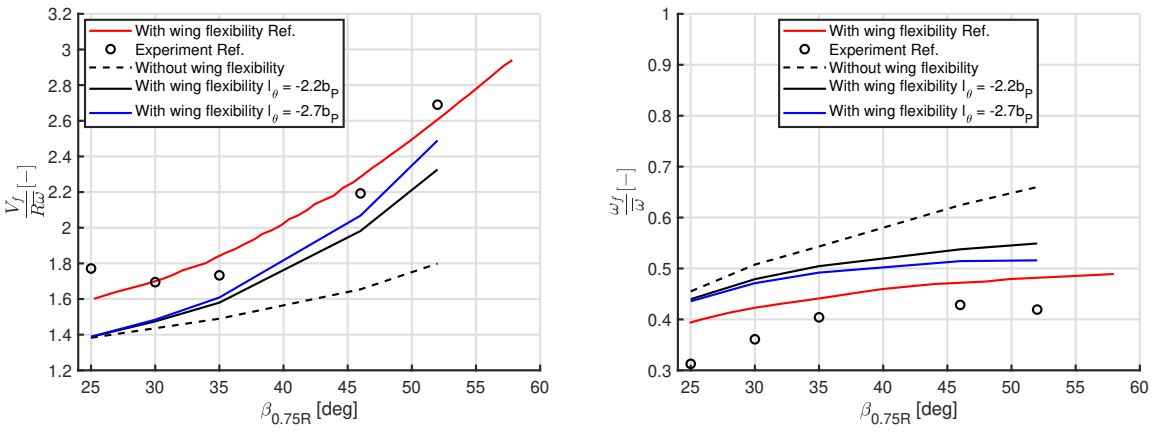

(a) Whirl flutter velocity

(b) Whirl flutter frequency.

Figure 8.13: Configuration (C): Comparison of whirl flutter velocity and whirl flutter frequency. With Houbolt-Reed propeller aerodynamic derivatives. Without wing structural damping.

To check the influence of wing structural damping in the present model, a Rayleigh damping model is used in which the constants of proportionality are $\mu = \lambda = 0.001$. Figure 8.14 - Figure 8.17 are the exact same graphs as Figure 8.10 - Figure 8.13 but including wing structural damping. As it can be seen, whirl flutter characteristics of the propeller in Configuration (A) (Figure 8.14 and Figure 8.15) have barely changed whereas whirl flutter characteristics of the propeller in Configuration (C) (Figure 8.16 and Figure 8.17) see better agreement between calculated results from present model and measurements.

It is also worth mentioning that for very high or very low values of $\beta_{0.75R}$ calculated results do not match well with measurements, this can be due to the fact that at very high or very low values of $\beta_{0.75R}$ three dimensional effects such as flow separation can occur at the propeller blades which in turn affect propeller aerodynamics.

Overall, neglecting wing structural damping, computed results in present analysis are conservative with respect to experimental data.

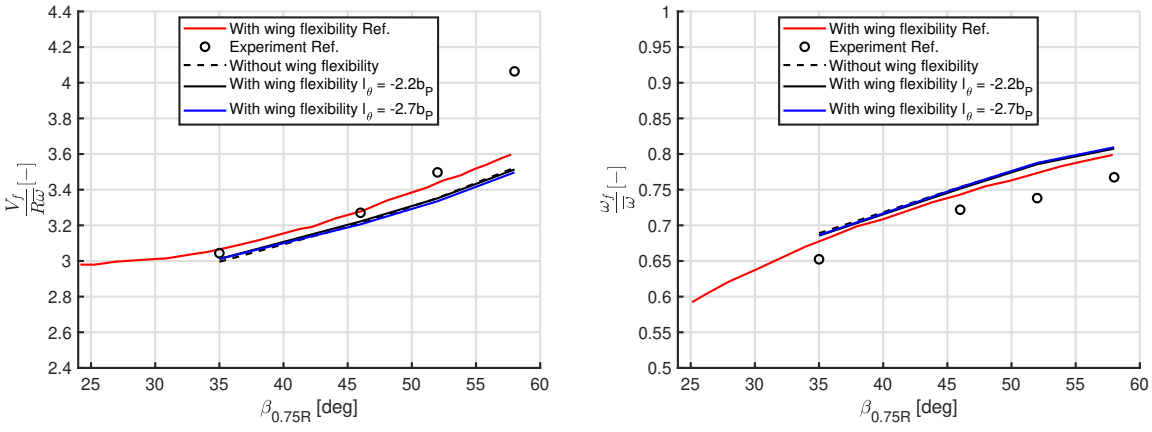

(a) Whirl flutter velocity

(b) Whirl flutter frequency.

Figure 8.14: Configuration (A): Comparison of whirl flutter velocity and whirl flutter frequency. With measured propeller aerodynamic derivatives from Bennett and Bland [7]. With wing structural damping using Rayleigh damping model: $\mu = \lambda = 0.001$.

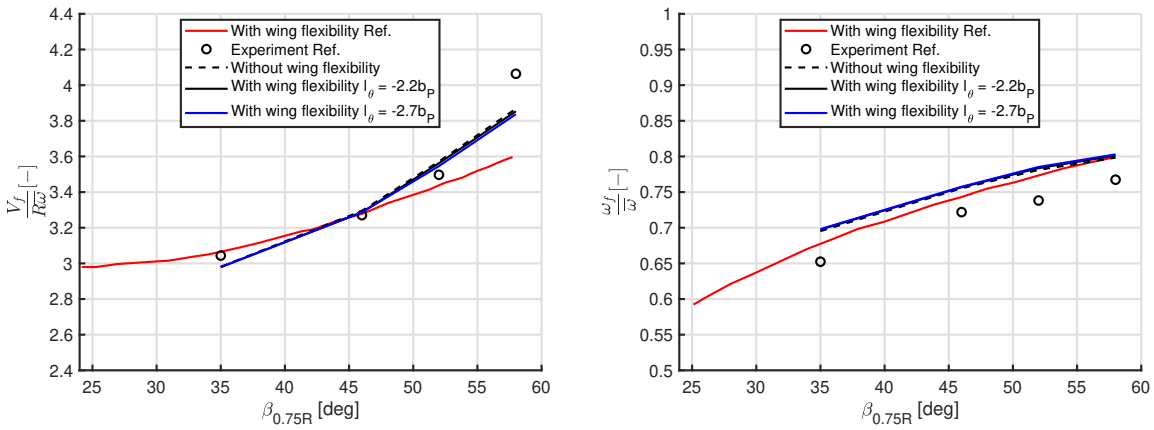

(a) Whirl flutter velocity

(b) Whirl flutter frequency.

Figure 8.15: Configuration (A): Comparison of whirl flutter velocity and whirl flutter frequency. With Houbolt-Reed propeller aerodynamic derivatives. With wing structural damping using Rayleigh damping model: $\mu = \lambda = 0.001$.

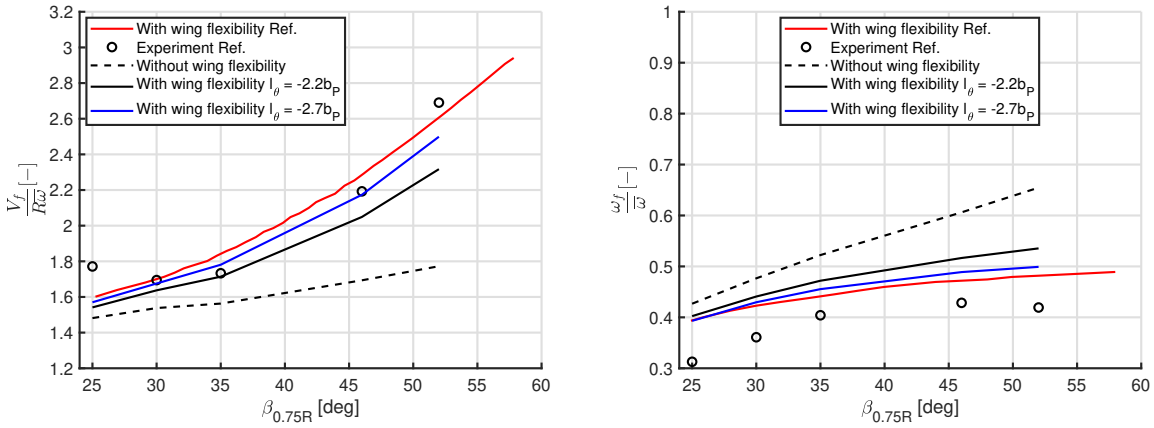

(a) Whirl flutter velocity

(b) Whirl flutter frequency.

Figure 8.16: Configuration (C): Comparison of whirl flutter velocity and whirl flutter frequency. With measured propeller aerodynamic derivatives from Bennett and Bland [7]. With wing structural damping using Rayleigh damping model: $\mu = \lambda = 0.001$.

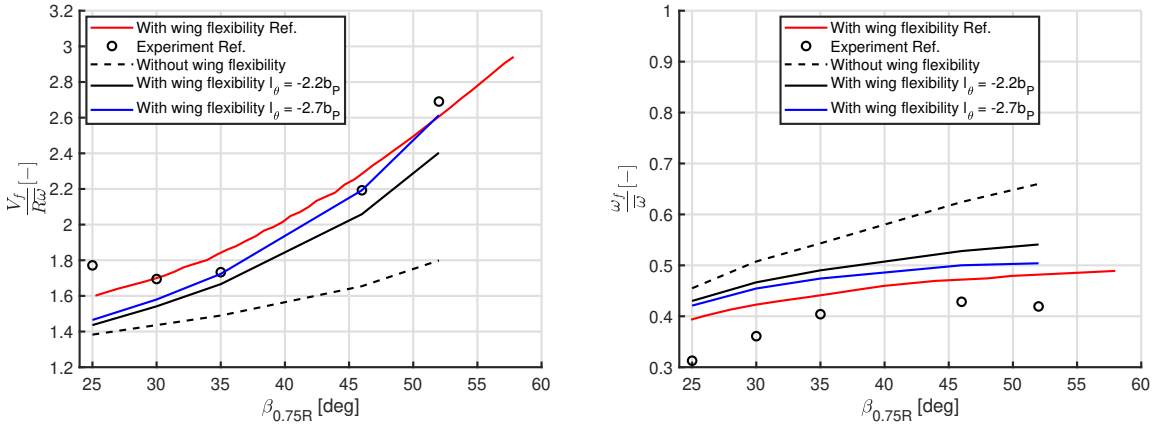

(a) Whirl flutter velocity

(b) Whirl flutter frequency.

Figure 8.17: Configuration (C): Comparison of whirl flutter velocity and whirl flutter frequency. With Houbolt-Reed propeller aerodynamic derivatives. With wing structural damping using Rayleigh damping model: $\mu = \lambda = 0.001$.

Wing flutter

Bennett and Bland [7] performed a wing flutter analysis using Rayleigh-Ritz method with the first torsional and bending modes of the wing. The propeller-engine mounting in pitch and yaw were assumed to be completely rigid. Analysis indicated no occurrence of wing flutter with or without propeller aerodynamics in the range of velocities considered in the study (below 300 ft/s). However, no specific quantitative value of the wing flutter speed is presented in Bennett and Bland [7].

Since the aeroelastic model of a flexible wing without flexibly mounted propellers (therefore neither propeller aerodynamics) was already verified in Chapter 7, the wing flutter speed obtained from this aeroelastic model may serve as a reference for the aeroelastic analysis of the flexible wing with a flexibly mounted propeller (with propeller aerodynamics).

Table 8.6 presents the wing flutter speed, wing flutter frequency, and wing divergence speed of the wing spar (with no propeller installed). Indeed, wing flutter occurs beyond 300 ft/s. The addition of propeller-engine mass, inertia, and static unbalance (wing spar with pods and propeller) increases wing flutter speed and wing flutter frequency. The increase in flutter speed is slightly higher with the propeller in Configuration (C) than with the propeller in Configuration (A). Divergence speed is not changed with Configuration (A) and it is slightly decreased in Configuration (C). These results are in line with the findings in Wang and Chen [109] and Rodden and Rose [93] where the wing with a propeller installed has higher flutter speed and lower divergence speed with respect to the wing without any propeller installed. In both configurations, higher flutter speeds are obtained with $l_\theta = -2.2 b_P$.

Parameters	**Wing spar**	**Wing spar with pods Config. A**		**Wing spar with pods Config. C**	
		$l_\theta = -2.2 b_P$	$l_\theta = -2.7 b_P$	$l_\theta = -2.2 b_P$	$l_\theta = -2.7 b_P$
Flutter speed [ft/s]	548.0	617.0	611.0	626.0	616.0
Flutter frequency [Hz]	27.0	32.3	31.9	32.7	32.3
Divergence speed [ft/s]	583.0	583.0	583.0	580.0	580.0

Table 8.6: Flutter speed, flutter frequency, and divergence speed of the wing spar and wing spar with pods and a non-rotating propeller. The propeller is rigid, therefore, there is no coupling with the propeller pitch and yaw degrees of freedom and gyroscopic effects are not included.

Table 8.7 and Table 8.8 present wing flutter speeds V_f, wing flutter frequencies f_f, and wing divergence speeds V_d of the wing with a rotating propeller installed in Configuration (A) and in Configuration (C), respectively. In both configurations, coupling the wing with a rotating propeller slightly decreases wing flutter speed and wing divergence speed with respect to their analogous cases with a non-rotating propeller.

With the propeller windmilling, higher propeller blade angle at three-quarter propeller radius ($\beta_{0.75R}$) can be translated into lower propeller rotational speeds. In both configurations, flutter speeds and divergence speeds decrease very slightly with increasing $\beta_{0.75R}$ (decreasing propeller rotational speeds).

Gyroscopic effects increase those modes whose frequencies are higher than the propeller yaw mode (forward whirl) frequency and decrease those modes whose frequencies are lower than the propeller pitch mode (backward whirl) frequency [93]. In both propeller-wing configurations, flutter occurs in a mode whose frequency is above the whirl modes, therefore gyroscopic effects increase wing flutter frequency. Although in this case, only for a very small amount.

	$l_\theta = -2.2 b_P$			$l_\theta = -2.7 b_P$		
$\beta_{0.75R}$ **[deg]**	V_f **[ft/s]**	f_f **[Hz]**	V_d **[ft/s]**	V_f **[ft/s]**	f_f **[Hz]**	V_d **[ft/s]**
35	615.0	30.9	578.0	611.0	31.3	577.0
46	613.0	33.3	577.0	607.0	33.0	576.0
52	612.0	33.4	576.0	607.0	33.0	575.0
58	612.0	33.2	576.0	607.0	33.0	574.0

Table 8.7: Configuration (A): Flutter speed, flutter frequency, and divergence speed of the wing with rotating flexible propeller. There is coupling with the propeller pitch and yaw degrees of freedom and gyroscopic effects are included. With propeller aerodynamic derivatives from Houbolt-Reed's method.

	$l_\theta = -2.2b_P$			$l_\theta = -2.7b_P$		
$\beta_{0.75R}$ [deg]	V_f [ft/s]	f_f [Hz]	V_d [ft/s]	V_f [ft/s]	f_f [Hz]	V_d [ft/s]
25	626.0	34.1	577.0	613.0	33.6	576.0
30	626.0	33.9	576.0	613.0	33.5	575.0
35	625.0	33.9	575.0	613.0	33.5	574.0
46	623.0	33.7	574.0	612.0	33.2	572.0
52	621.0	33.4	573.0	610.0	33.1	571.0

Table 8.8: Configuration (C): Flutter speed, flutter frequency, and divergence speed of the wing with rotating flexible propeller. There is coupling with the propeller pitch and yaw degrees of freedom and gyroscopic effects are included. With propeller aerodynamic derivatives from Houbolt-Reed's method.

Comments on validation and verification

Whirl flutter predictions using the method derived in this chapter have been well validated and verified. The set of only five propeller aerodynamic derivatives obtained from measurements seem to be able to capture whirl flutter characteristics rather well. However, in the absence of these measurements, Houbolt-Reed's method produce reasonable estimates of the propeller aerodynamic derivatives and the resulting whirl flutter characteristics match well with experimental data.

Wing flutter predictions have been analysed; qualitative trends are in line with findings in literature. A qualitative validation/verification is still required. This has not been possible due to lack of literature data; further validation against numerical/higher fidelity models is recommended. Nevertheless, the good agreement found in the free vibration analyses reassures the validity of present method.

III

ANALYSIS

9

Case Studies: Baseline Models

Following the validation/verification of the aeroelastic models, Part III apply them into case studies and parametric studies. Results from case studies are presented in Chapter 9 and Chapter 10 and results from parametric studies are presented in Chapter 11.

In Chapter 9, three baseline models are described, these are a baseline wing, a baseline propeller, and a baseline propeller-wing model with conventional layout — the propeller is attached to the inboard part of the wing. Aeroelastic analyses of each of these models are performed and explained following the methodology described in Part II.

The structural and geometric characteristics of the baseline models are estimated based on the light aircraft Tecnam P2006T [72] and the experimental aircraft NASA X-57 Maxwell [68][46][38]. Both aircraft are illustrated in Figure 9.1 and Figure 9.2, respectively[1].

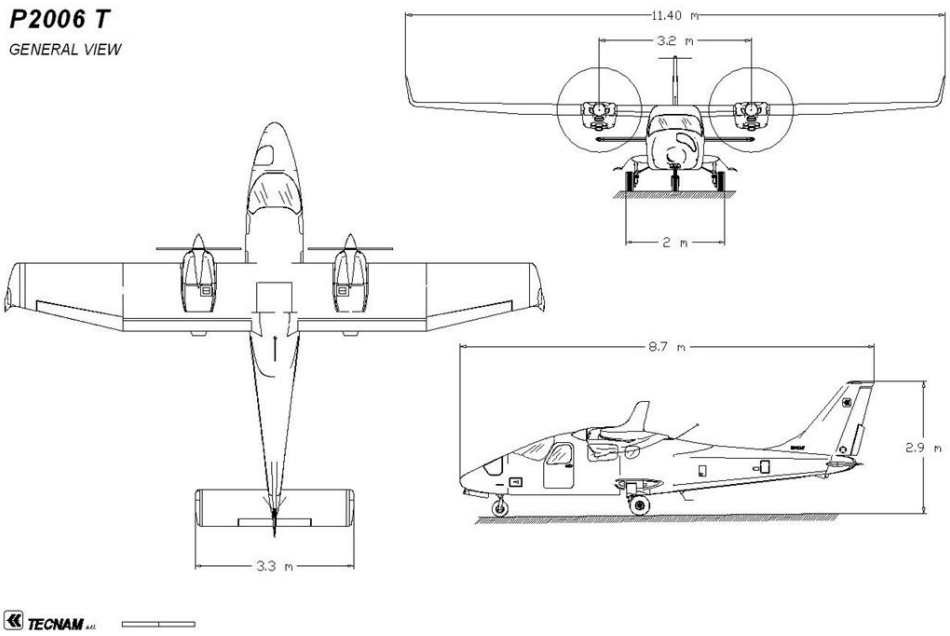

Figure 9.1: Three view drawing of Tecnam P2006T Aircraft [72].

[1] NASA X-57 Maxwell is an experimental aircraft derived from Tecnam P2006T, which is a conventional four-seater light aircraft. The main difference between the two is that X-57 Maxwell features a thinner, higher aspect ratio wing with Distributed Electric Propulsion (DEP) to increase its high-speed cruise efficiency. The wing contains a total of fourteen electrically driven tractor propellers mounted in front of the wing's leading edge: two large wingtip-mounted propellers and twelve small inboard propellers. The wingtip mounted propellers are used during all flight phases whereas the smaller inboard propellers are only used for lift augmentation for take-off and landing; in fact, when the inboard propellers are no longer needed, their blades are folded back so as to reduce drag [68][46][38].

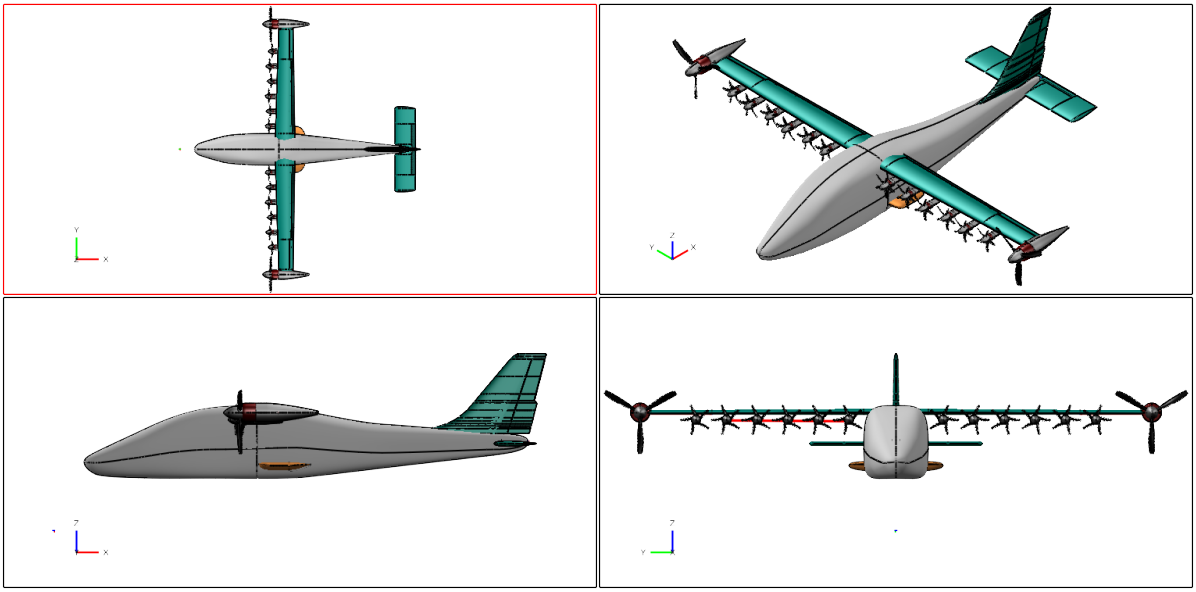

Figure 9.2: Multiple view of X-57 Maxwell. Generated with OpenVSP [77].

9.1. Baseline Wing Description and Analysis

The baseline wing (Figure 9.3) is based on the wing from Tecnam P2006T aircraft [72]. It consists of a tapered wing with constant mass and stiffness characteristics along the span. It has no sweep, twist, dihedral or control surfaces. The main parameters are tabulated in Table 9.1. The wing has an aspect ratio of ≈ 11 and a taper ratio of 0.64. The wing mid-chord axis coincides with the elastic axis and the centre of gravity distribution.

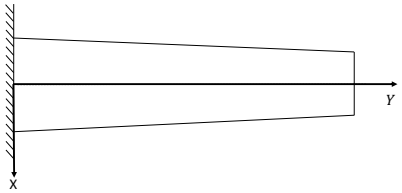

Figure 9.3: Baseline wing: simple schematic, top view. Relative dimensions are approximate.

Parameter	Value	Units
Aircraft weight	1200	kg
Cruise speed	150 (77)	knots (m/s)
Altitude	8000 (2438.4)	ft (m)
Density of air	0.962870	kg/m^3

(a) Flight condition.

Parameter	Value	Units
Wing span	11.4	m
Root chord	1.25	m
Tip chord	0.8	m
Thickness-to-chord	15%	[-]
Mass per unit length	25	kg/m
Radius of gyration (about CG)	25% chord	[-]
Spanwise elastic axis (from LE)	50% chord	[-]
Centre of gravity (from LE)	50% chord	[-]
Bending rigidity (EI)	7×10^5	N·m^2
Torsional rigidity (GJ)	2×10^5	N·m^2
Aerodynamic centre a_c (from LE)	25% chord	[-]
Lift curve slope C_{l_α}	2π	[-]

(b) Wing parameters.

Table 9.1: Definition of baseline wing.

Aeroelastic analysis of the baseline wing is carried out using the methodology presented in Chapter 7. The structural wing model has 20 beam elements, the natural frequencies of the wing are tabulated in Table 9.2a. Flutter and divergence speeds are shown in Table 9.2b and the velocity-damping-frequency (V-g-f) plots are

shown in Figure 9.4. Both flutter and divergence speeds are much higher than the proposed cruise speed (77 m/s). Flutter mode is a torsion mode that goes unstable due to interaction between the first torsion mode and the first bending mode. Divergence is caused by an aerodynamic lag state going unstable due to interaction with the first bending mode. Flutter and divergence mode shapes are shown in Figure 9.5 and Figure 9.6.

Mode	Frequency [Hz]
First bending	2.88
First torsion	16.68
Second bending	18.06
Second torsion	46.59
Third bending	50.57

(a) Natural frequencies

Parameter	Value	Units
Flutter speed	152	[m/s]
Flutter frequency	8.08	[Hz]
Divergence speed	154	[m/s]

(b) Aeroelastic results.

Table 9.2: Analysis of baseline wing.

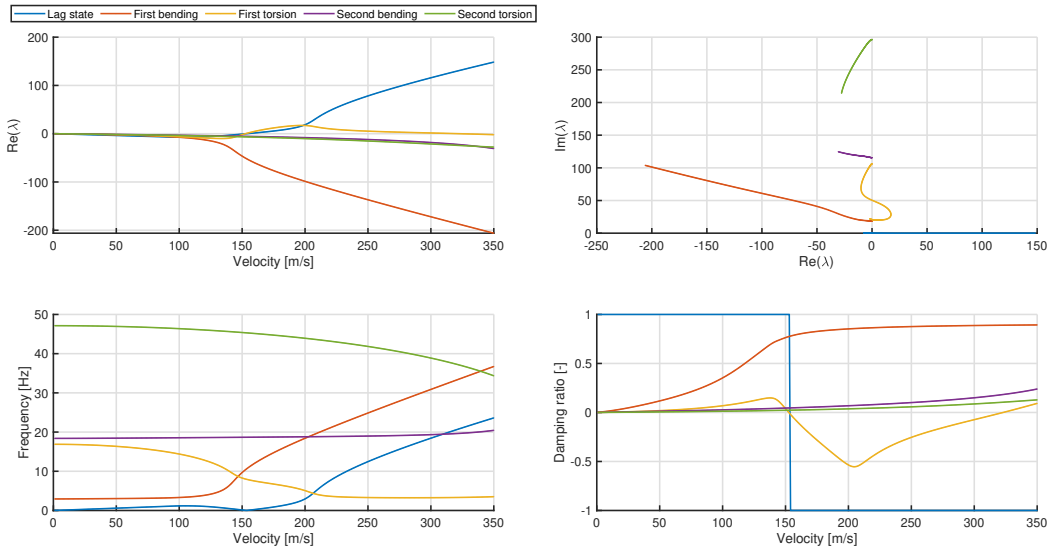

Figure 9.4: Baseline wing: V-g-f plots.

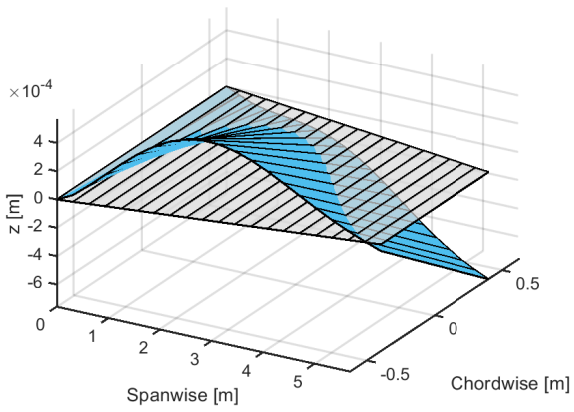

Figure 9.5: Baseline wing: flutter mode shape at time = 0 s.

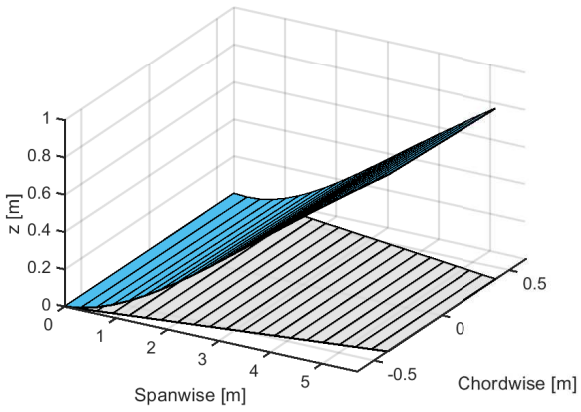

Figure 9.6: Baseline wing: divergence mode shape.

9.2. Baseline Propeller Description and Analysis

The baseline propeller is based on the wingtip-mounted propeller (cruise propeller) from NASA X-57 Maxwell [68][46][38]. It consists of a tractor propeller mounted on the wing's leading edge. The propeller is composed of a spinner, three blades, a motor, and a nacelle (Figure 9.7). For simplicity, the following assumptions are taken:

(a) The propeller is positioned at 1.6 m distance from wing root. The wing chord at this position is 1.13 m.

(b) The mass of blades-spinner is treated as a concentrated mass located at the centre of rotor plane, 0.6 m in front of the wing leading edge (-1.16 m from wing mid-chord axis).

(c) The motor-nacelle is treated as a concentrated mass located at 0.3 m in front of the wing leading edge (-0.86 m from wing mid-chord axis).

(d) The pivot points in pitch and yaw are both located on the wing mid-chord axis.

(e) The blades have constant chord and linear varying twist (constant pitch propeller).

(f) Whirl flutter is analysed with propeller in windmilling conditions.

(g) The propeller is a fixed-pitch propeller. The relation between the advance ratio and the geometric collective pitch angle $\beta_{0.75R}$ for the propeller windmilling is given by:

$$J = \tan(\beta_{0.75R} - 3°)\pi \tag{9.1}$$

where -3° is the zero lift angle of attack of the airfoil at the three-quarter-radius station.

(h) The propeller mass moment of inertia about the axis of rotation I_Ω may be estimated by idealizing the blades as thin rods with a uniform cross-sectional area [32]. Hence, a simple formula to estimate I_Ω is:

$$I_\Omega = \frac{M_r \cdot R^2}{3} \tag{9.2}$$

where M_r is the rotor mass and R the rotor radius.

(i) The propeller-wing inertia parameters ($I_{\theta,P}$, $I_{\psi,P}$, $S_{\theta,P}$, $I_{\alpha,P}$, $S_{\alpha,P}$, and $I_{\theta\alpha,P}$) are to be calculated according to Equation (8.5) and Equation (8.6). These parameters are function of the pivoting mass and its inertia, hence, they depend on the location of the pivot axes and the mass distribution of the pivoting structure.

The second condition of assumption (e) and assumption (f) are necessary to employ Houbolt-Reed's method to compute the propeller aerodynamic derivatives.

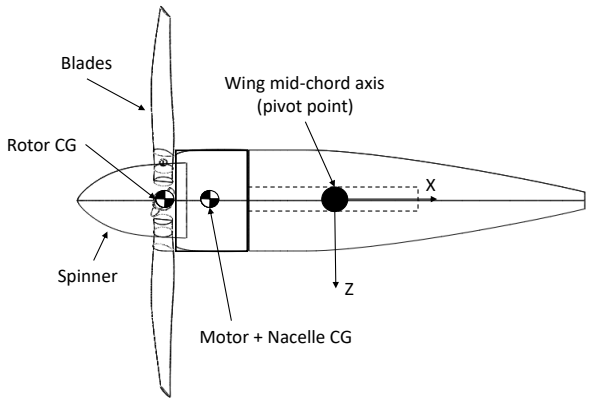

Figure 9.7: Baseline propeller: side view. Generated with OpenVSP [77].

The main parameters defining the baseline propeller are tabulated in Table 9.3 and Table 9.4.

Parameter	Value	Units
Number of blades	3	[-]
Rotor diameter	5 (1.524)	ft (m)
Hub diameter	0.824 (0.25)	ft (m)
Motor diameter	14 (0.3556)	in (m)
Blade chord	0.308 (0.094)	ft (m)
Cruise RPM	2250	rev/min
Airfoil	MH117	[-]
Geometric collective pitch angle, $\beta_{0.75R}$	35	[°]
Advance ratio, J	1.96	[-]

Table 9.3: General propeller parameters.

Parameter	Value	Units
Rotor mass	8	kg
Motor-nacelle mass	35	kg
Position of rotor CG	−1.16	m
Position of motor CG	−0.86	m
Pitch axis = yaw axis		
$l_\theta = l_\psi$	0	m
$e_\theta = e_\psi$	−1.16	m
Pitch stiffness, f_θ	7	[Hz]
Yaw stiffness, f_ψ	7	[Hz]
Pitch damping, g_θ	0.005	[-]
Yaw damping, g_ψ	0.005	[-]

Parameter	Value	Units
I_Ω	1.55	kg·m^2
$I_{\theta,P}$	36.65	kg·m^2
$I_{\psi,P}$	36.65	kg·m^2
$S_{\theta,P}$	-39.38	kg·m
$I_{\theta\alpha,P}$	36.65	kg·m^2
$I_{\alpha,P}$	36.65	kg·m^2
$S_{\alpha,P}$	-39.38	kg·m

Table 9.4: Structural parameters. Distances are measured from wing mid-chord, positive rearward.

Whirl flutter analysis of the baseline propeller on a rigid wing is carried out by employing the methodology presented in Chapter 6. Results are shown as V-g-f plots in Figure 9.8. The motion of the propeller is defined by two mode shapes, a backward whirl mode and a forward whirl mode; the former has lower frequencies than the latter. With the assumption of rigid blades and rigid wings, forward whirl mode never goes unstable, in fact, in this case, it becomes more stable with increasing airspeeds. Whirl flutter only occurs in the backward whirl mode. Note the high benignity in this flutter mode; it means that the instability has a "soft" behaviour, hence, it can be avoided by adding small amounts of structural damping. This is in accordance with findings in literature, which state that whirl flutter is rather sensitive to structural damping.

Another peculiarity is that the gap between the frequencies of forward whirl mode and backward whirl mode is widened with increasing incoming airspeed, until a certain airspeed. This has to do with the assumption of fixed-pitch propeller operating in windmilling conditions: given a fixed collective pitch angle, the advance ratio is constant, therefore, higher incoming airspeeds lead to higher propeller rotational speeds. As the propeller rotational speed increases, the forward whirl mode frequency increases and the backward whirl mode frequency decreases. This behaviour stems from the difference in sign of the gyroscopic term in Equation (6.8). For much higher airspeeds, the forward whirl mode frequency is limited by propeller aerodynamics.

Whirl flutter speed is much higher than the proposed cruise speed (77 m/s).

Parameter	Value	Units
Whirl flutter speed	221.0	[m/s]
Whirl flutter frequency	5.0	Hz
Rotational speed at flutter	4433	RPM

Table 9.5: Baseline propeller: aeroelastic results

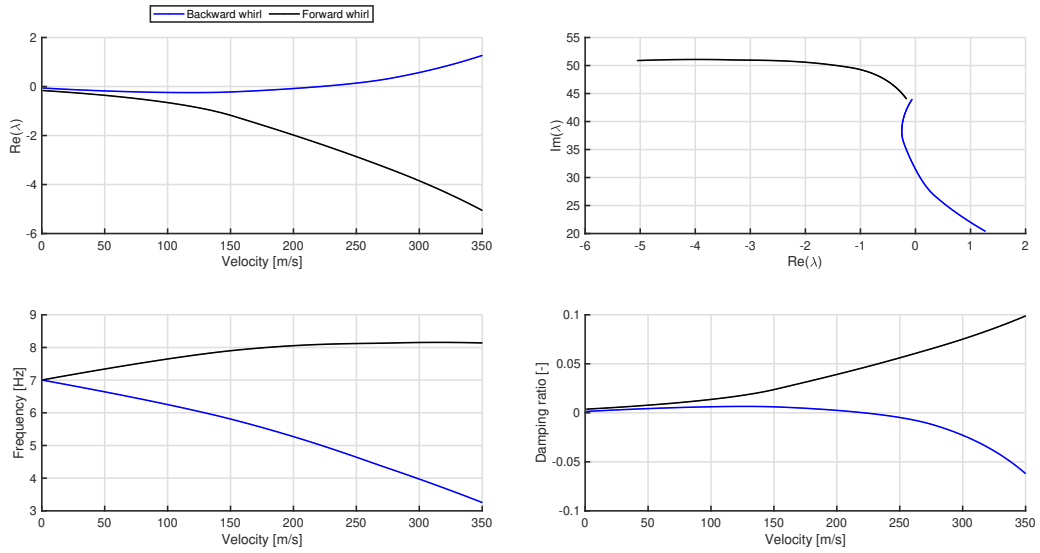

Figure 9.8: Baseline propeller (fixed-pitch propeller): V-g-f plots.

Whirl flutter mode shapes

Figure 9.9 shows the backward whirl flutter mode shape. The mode shape reflects the relative amplitude and phase lag between pitching and yawing motions. It can be observed that ψ and $\dot{\theta}$ are in phase with each other, and θ and $\dot{\psi}$ are out of phase 180°; these are conditions for a clockwise rotation if ψ is plotted in the Y-axis and θ in the X-axis. This indicates that the mode that goes unstable is indeed a backward whirl mode since the blade rotation is counter-clockwise (see Figure 6.1). Pitch θ and yaw ψ have a phase lag of 90° because of symmetry in pitch-yaw characteristics, hence, the circular path in Figure 9.9b.

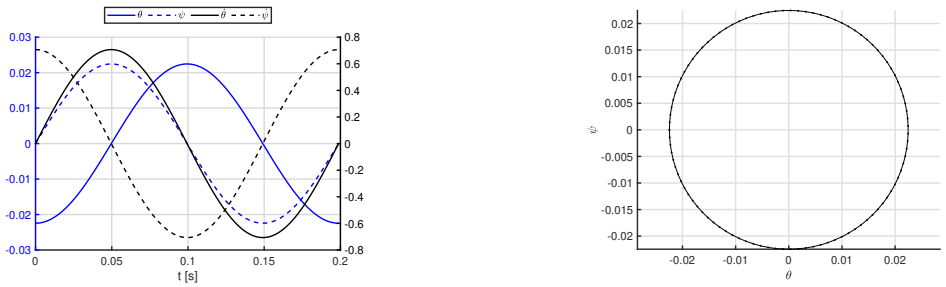

(a) Pitch and yaw displacements and their rates.

(b) Pitch and yaw displacements.

Figure 9.9: Baseline propeller with symmetric pitch-yaw characteristics ($f_\theta = 7$ Hz and $f_\psi = 7$ Hz): whirl flutter mode shape.

If pitch-yaw characteristics are no longer symmetric, such as unequal pitch and yaw stiffness or unequal pitch and yaw pivot points, the path described by the pitch-yaw displacements will become an ellipse, this means that θ and ψ will have a phase lag different than 90°. Figure 9.10 shows the backward whirl flutter mode shape of the baseline propeller modified to have unequal pitch-yaw stiffness, it can be observed that the path described by θ-ψ motions is an ellipse. The orientation of the whirl is indicated by the pitch-yaw rates; due to the applied asymmetry in pitch-yaw stiffness, ψ and $\dot{\theta}$ are slightly out of phase.

Note that the unsymmetrical propeller has a whirl flutter speed of 242 m/s which is higher than the whirl flutter speed of the symmetrical propeller in spite of having less stiffness in the yaw direction. This result matches the findings in literature which state that isolated propellers with rigid blades are more prone to whirl flutter when they have equal pylon-nacelle-stiffness [45].

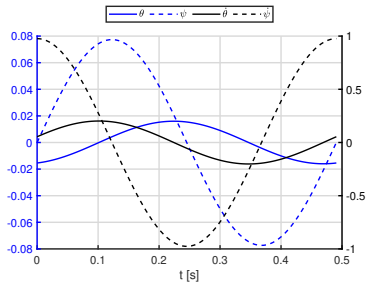

(a) Pitch and yaw displacements and their rates.

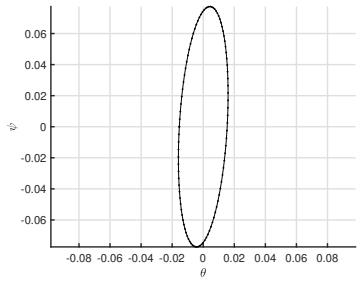

(b) Pitch and yaw displacements.

Figure 9.10: Baseline propeller with unequal pitch-yaw stiffness ($f_\theta = 7$ Hz and $f_\psi = 4$ Hz): whirl flutter mode shape.

Time simulations

It is also possible to illustrate the behaviour of propeller whirl flutter by solving the aeroelastic equations of the propeller in time domain (Equation (6.18)). Present analysis employs MATLAB ode45 function. Figure 9.11 shows variations of pitch and yaw deflections in time given an initial pitch deflection of 1°. When the disturbance is introduced at an incoming airspeed smaller than the whirl flutter speed (V = 77 m/s), the motion caused by the disturbance is damped and the propeller returns to a stable position. When the disturbance is introduced close to the whirl flutter speed (V = 222 m/s), the propeller attains a neutral motion, it does not go stable nor does it go unstable. When the disturbance is introduced at airspeeds higher than the whirl flutter speed (V = 250 m/s), the propeller follows a spiral diverging motion. In all three cases, the motion develops in the backward whirl mode: the motion occurs in the clockwise direction while the blade rotation is in the counter-clockwise direction (see Figure 6.1). Forward whirl mode is also excited by the initial disturbance, this is evidenced by the sharp corners illustrated in Figure 9.11. As the forward whirl mode is under much higher damping than the backward whirl mode, the former is quickly damped out at the beginning of the transient response. This matches the findings published in Reed III and Bland [88] and Houbolt and Reed [45]. Analogous results are illustrated in Figure 9.12 for the unsymmetrical propeller. Here, the elliptical pattern is visible.

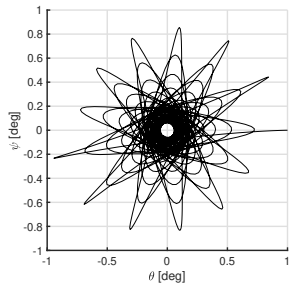

(a) Stable: V = 77 m/s

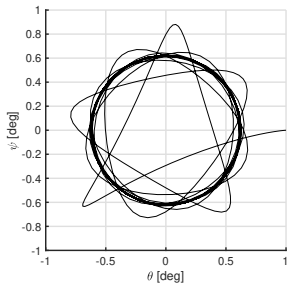

(b) Neutral: V = 222 m/s

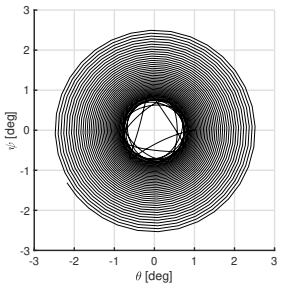

(c) Unstable: V = 250 m/s

Figure 9.11: Baseline propeller with symmetric pitch-yaw characteristics ($f_\theta = 7$ Hz and $f_\psi = 7$ Hz): time simulations run for 10 s with an initial pitch deflection of 1°.

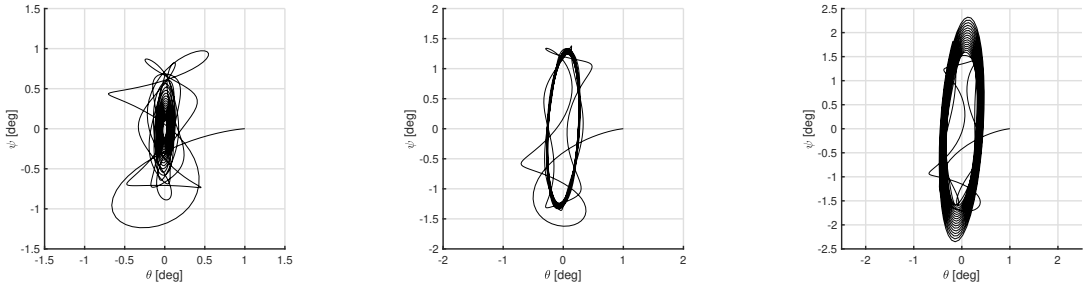

(a) Stable: V = 200 m/s (b) Neutral: V = 242 m/s (c) Unstable: V = 250 m/s

Figure 9.12: Baseline propeller with unequal pitch-yaw stiffness (f_θ = 7 Hz and f_ψ = 4 Hz): time simulations run for 10 s with an initial pitch deflection of 1°.

Another method for windmilling: Constant-speed propellers

As mentioned, the baseline propeller is assumed to be windmilling in fixed-pitch — the advance ratio remains constant and the propeller rotational speed is increased with increasing incoming airspeed. Another type of propeller is that of constant speed propeller. In this case, the propeller rotational speed remains constant and the collective blade pitch is increased with increasing airspeed so as to maintain the propeller in windmilling conditions. This leads to very different whirl flutter behaviours.

Figure 9.13 shows the V-g-f plots of the baseline propeller with such configuration. Note that only the propeller rotational speed is set to a constant value of 2250 RPM (cruise RPM) and the advance ratio is allowed to be varied, all the other parameters defining the baseline propeller remain unchanged. Three aspects are observed: first, the backward whirl mode starts from being unstable at very low airspeeds, this is due to the fact that at very low airspeeds, very small advance ratio is present which leads to some propeller aerodynamic derivatives having very high values. In practice, this can be avoided by simply not setting the advance ratio to windmilling conditions at small incoming airspeeds. Second, the backward whirl mode encounters whirl flutter at a much higher airspeed than in the case of fixed-pitch propeller[2], about 427 m/s. Third, the frequency of both backward and forward whirl modes decrease with increasing airspeed, and then, increase again after whirl flutter onset; in this case, aerodynamic effects decrease or increase the stiffness of both whirl modes together. Again, flutter also only occurs in the backward whirl mode. In this case, the flutter mode has very low benignity and but becomes divergent soon after flutter onset.

Apart from the instability at small incoming airspeeds, the constant-speed propeller is less prompt to whirl flutter than the fixed-pitch propeller. Note that the analyses are conducted in windmilling conditions, generalisation to thrusting propellers is questionable. For the remaining of the report, present analysis will restrict whirl flutter studies to the case of fixed-pitch propellers[3] as for distributed electric propulsion aircraft, it seems likely that fixed-pitch propellers will be employed — such propellers have simpler mechanism which reduces weight and favours maintainability [12]. Analysis of constant-speed propellers and general whirl flutter studies in thrusting conditions is proposed for future work.

[2] At this high airspeed, the flow is supersonic. The calculations obtained in this case have very little physical sense as compressibility effects are not considered in any of the models treated in present work, apart from the compressibility effect correction factor in Houbolt-Reed's method. The only realistic interpretation is that whirl flutter occurs at a very high airspeed.

For the remaining analyses shown in present report, flutter speeds close to or above the speed of sound are only to be considered for trend characterization.

[3] Additional results of propeller-wing models using a constant speed propeller are reported in Appendix E.

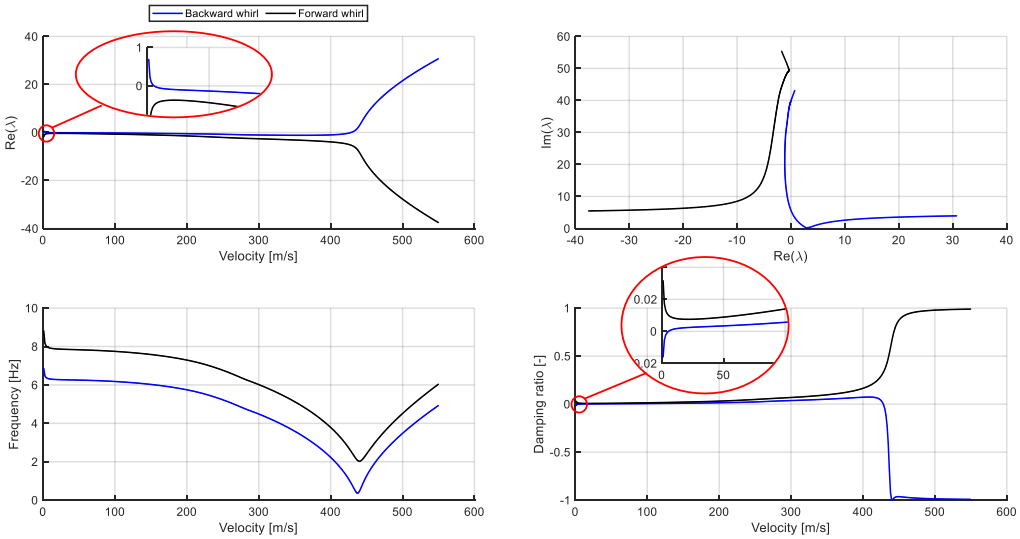

Figure 9.13: Baseline propeller (constant speed propeller): V-g-f plots.

9.3. Baseline Propeller-Wing Description and Analysis

The baseline propeller-wing model is defined by combining the baseline wing and baseline propeller described in Section 9.1 and Section 9.2, respectively. The plan view is illustrated in Figure 9.14.

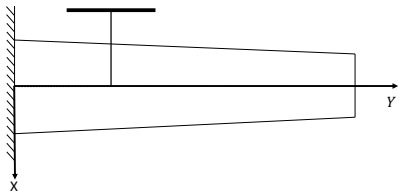

Figure 9.14: Baseline propeller-wing simple schematic, top view. Relative dimensions are approximate.

Wing flutter and whirl flutter analysis of the baseline propeller-wing model is carried out employing the methodology presented in Chapter 8. The structural wing model has 25 beam elements and the propeller is positioned on node number 8th (1.6 m from wing root). Results are presented in this section.

Ignoring aerodynamic interference effects, the interaction between a flexible wing and a flexible mounted propeller can be summarised as follows:

- The influence of installing a propeller on the wing is threefold: first, the added propeller mass changes the wing mass and inertial properties; second, a rotating propeller induces gyroscopic effects that change the wing natural vibration frequencies; and third, propeller aerodynamic forces and moments are additional sources of excitation loads on the flexible wing.

- The propeller is attached to the flexible wing through a pivot point. As the wing undergoes heaving and pitching motions, it carries the propeller with it. Consequently, the propeller experiences additional inertial and gyroscopic effects. Furthermore, the blades perceive modified effective pitch and yaw angles — this alters the propeller aerodynamic forces and moments.

9.3.1. Wing with a non-rotating Propeller rigidly attached

First, let's analyse the case of adding a non-rotating baseline propeller to the baseline wing. The propeller mounts are assumed to be rigid, hence, the added propeller may be treated as an additional inert mass that changes the mass and inertial distributions of the wing. Table 9.6 shows the frequency distribution of a wing with such configuration.

The added propeller mass couples the wing bending and torsional modes due to the rotor and motor CG being in front of the wing's leading edge. Because of the additional static unbalance, the frequency of the wing torsional modes is reduced by half, approximately; the frequency of the wing bending modes is reduced

slightly. This is reflected in the wing flutter speed and flutter frequency which are decreased to 142 m/s and 6.30 Hz, as the flutter mode of the clean wing is a torsional mode; divergence speed is barely changed, as divergence is caused by the coupling of the lowest wing bending mode and an aerodynamic lag state, and their frequencies are barely affected by the added propeller mass. The V-g-f plots in Figure 9.15 show that the flutter mode that goes unstable is still the wing torsional mode (here, second wing mode). At much higher speeds, the second wing bending mode (here, third wing mode) also goes unstable due to interaction with an aerodynamic lag state.

Mode	Frequency (with propeller)	Frequency (clean wing)	Units
First wing mode	2.85	2.88	[Hz]
Second wing mode	8.19	16.68	[Hz]
Third wing mode	17.84	18.06	[Hz]
Fourth wing mode	26.23	46.59	[Hz]
Fifth wing mode	49.98	50.57	[Hz]

Table 9.6: Baseline wing with a non-rotating baseline propeller, rigidly mounted: natural frequencies

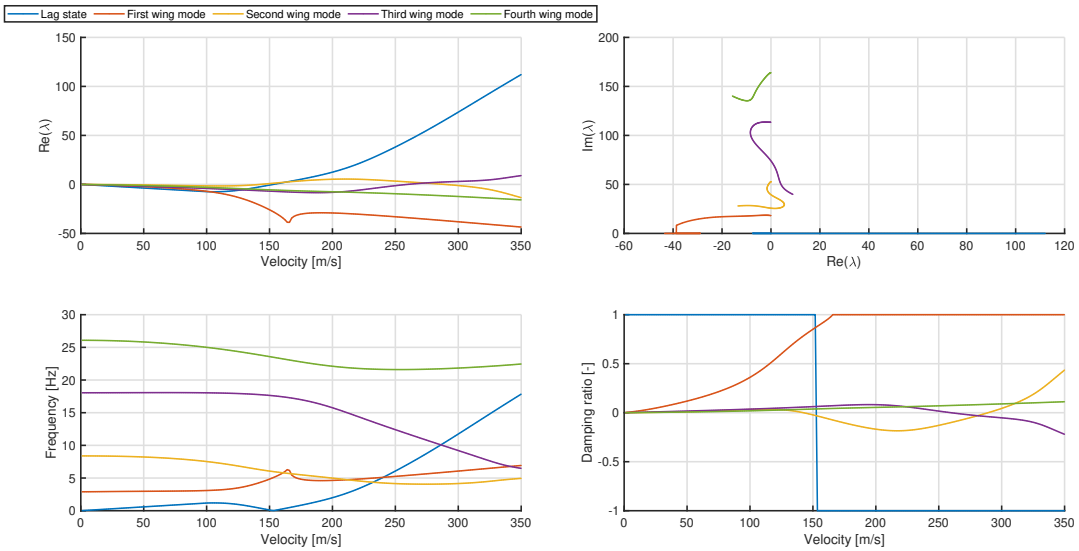

Figure 9.15: Baseline wing with a non-rotating baseline propeller, rigidly mounted: V-g-f plots.

Parameter	With one propeller	Clean wing	Units
Flutter speed	142	152	[m/s]
Flutter frequency	6.30	8.08	[Hz]
Divergence speed	153	154	[m/s]

Table 9.7: Baseline wing with a non-rotating baseline propeller, rigidly mounted: aeroelastic results.

9.3.2. Wing with a rotating Propeller flexibly attached

Now, assume that the propeller is flexibly mounted on the wing and let the propeller rotate.

On the one hand, the natural modes of the flexible mounts, i.e. pitch and yaw, will couple with wing bending and torsional modes. In consequence, the natural vibrations of the wing and the propeller are modified. The value of these frequencies are tabulated in Table 9.8. The propeller pitch mode is reduced due to structural coupling with wing torsion. Since there is no in-plane motions of the wing, the propeller yaw

mode remains unchanged. Adding a flexibly mounted propeller with pitching and yawing motions appears to increase the natural frequencies of the clean wing for a small amount, with the exception of the first wing mode. However, comparing the natural frequencies with those of the equivalent wing with a rigidly mounted non-rotating propeller, it can be seen that the frequency of the second wing mode is approximately doubled because of the introduction of flexible mounts; the frequency of all the other wing modes is also increased.

The propeller-wing structural coupling is reflected in the coupling terms in Equation (8.13).

Mode	**Frequency (flexible mounts)**	**Frequency (clean wing and isolated propeller)**	**Frequency (rigid mounts and non-rotating)**	**Units**
First wing mode	2.85	2.88	2.85	[Hz]
Propeller pitch mode	5.48	7	-	[Hz]
Propeller yaw mode	7	7	-	[Hz]
Second wing mode	17.75	16.68	8.19	[Hz]
Third wing mode	19.48	18.06	17.84	[Hz]
Fourth wing mode	49.25	46.59	26.23	[Hz]
Fifth wing mode	51.37	50.57	49.98	[Hz]

Table 9.8: Baseline wing with a rotating propeller, flexibly mounted: natural frequencies with $\Omega = 0$ RPM (First column).

On the other hand, a rotating propeller gives rise to gyroscopic effects. Propeller rotational speed Ω influences the propeller structural damping matrices and the propeller-wing coupling structural matrices (see Section 8.1.1); in essence, gyroscopic effects are introduced to the wing because of the existence of flexible mounts. Figure 9.16 shows the effects of increasing propeller rotational speed on propeller-wing natural frequencies. As observed earlier, the forward whirl mode frequency increases and the backward whirl mode decreases with increasing propeller rotational speed. The natural frequencies of the wing are also changed so as to avoid crossing with propeller natural frequencies. This interaction is weaker the more spaced the propeller-wing natural frequency distribution is.

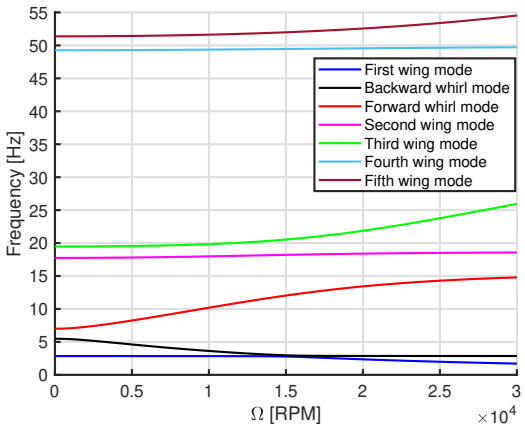

Figure 9.16: Influence of gyroscopic effects on propeller-wing natural frequencies.

Aeroelastic results of the baseline propeller-wing model with a flexibly mounted propeller are tabulated in Table 9.9. Figure 9.17 shows the V-g-f plots in which only wing aerodynamics are included in the propeller-wing aeroelastic equations, and Figure 9.18 shows the V-g-f plots in which both wing and propeller aerodynamics are included. The wing flutter speed, caused by the second wing mode going unstable, is increased with respect to the equivalent wing with a non-rotating propeller, this is because propeller-wing coupling has risen the frequency of the second wing mode; wing divergence speed remains almost unchanged.

Including or excluding propeller aerodynamics does not modify wing flutter or wing divergence speeds and their frequencies are barely changed. This suggests that in this particular model, propeller aerodynamics has little effect on the propeller-wing aeroelastic behaviour.

A very peculiar aspect is that while the backward whirl mode is stabilized, whirl flutter occurs in the forward whirl mode in form of a hump flutter. Forward whirl flutter arises from the interaction between the forward whirl mode and the second wing mode (see the V-f plots in Figure 9.17 and Figure 9.18). This instability has very little negative damping, which suggests that it would be damped with small amounts of structural damping. Including propeller aerodynamics appears to dampen both propeller whirl modes.

Figure 9.19 presents the V-g-f plots without wing aerodynamics but with propeller aerodynamics. In this case, backward whirl flutter becomes the critical mode at 213 m/s at a frequency of 4.19 Hz. The first wing mode is also driven unstable due to interaction with the backward whirl mode at 285 m/s with 2.83 Hz. Backward whirl flutter speed of the propeller-wing model is lower than that of the isolated propeller (221 m/s). However, neither of these two modes go unstable when wing aerodynamics is included in the calculations. Wing aerodynamics stabilises the backward whirl mode.

The fact that forward whirl flutter still appears even without propeller aerodynamics indicates that the instability is caused by propeller-wing structural coupling and wing aerodynamics. It has generally been assumed in literature that forward whirl flutter does not take place in propellers with rigid blades; this conclusion stems from studies of propellers on rigid wings. Results from present analysis show that forward whirl flutter may still occur to propeller with rigid blades due to interaction with wing modes and wing aerodynamics. In this example, forward whirl flutter is not a pure whirl flutter, instead, it is a combination of wing flutter and whirl flutter and it is driven unstable by wing aerodynamics.

Instability type	**Without propeller aerodynamics**	**With propeller aerodynamics**	**Units**
Wing flutter speed	173	174	[m/s]
Wing flutter frequency	9.69	9.48	[Hz]
Wing divergence speed	**152**	**152**	[m/s]
Propeller whirl flutter speed (forward whirl mode)	167	181	[m/s]
Propeller whirl flutter frequency (forward whirl mode)	7.40	7.17	[Hz]

Table 9.9: Baseline wing with a rotating baseline propeller, flexibly mounted: aeroelastic results.

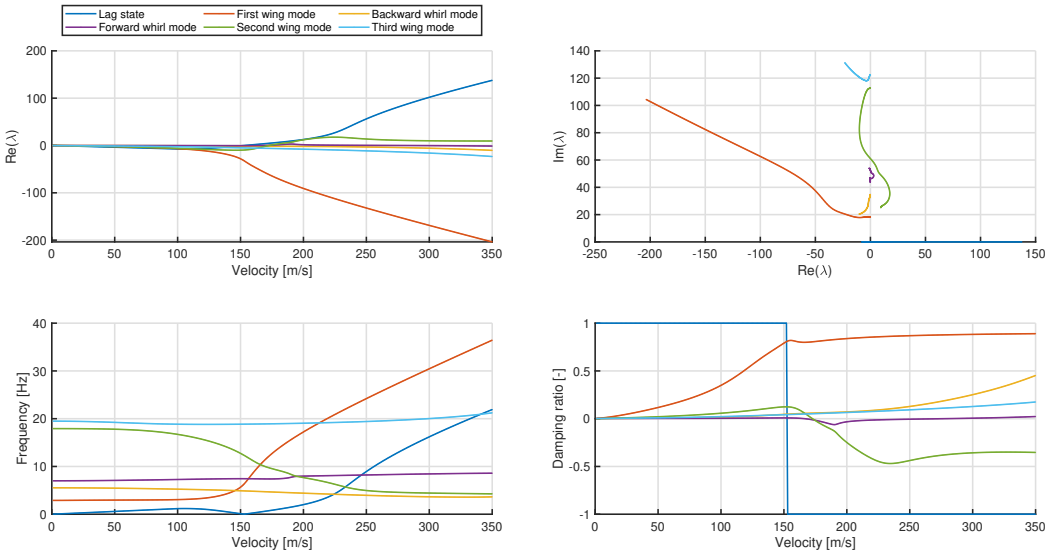

Figure 9.17: Baseline propeller-wing with wing aerodynamics and without propeller aerodynamics: V-g-f plots.

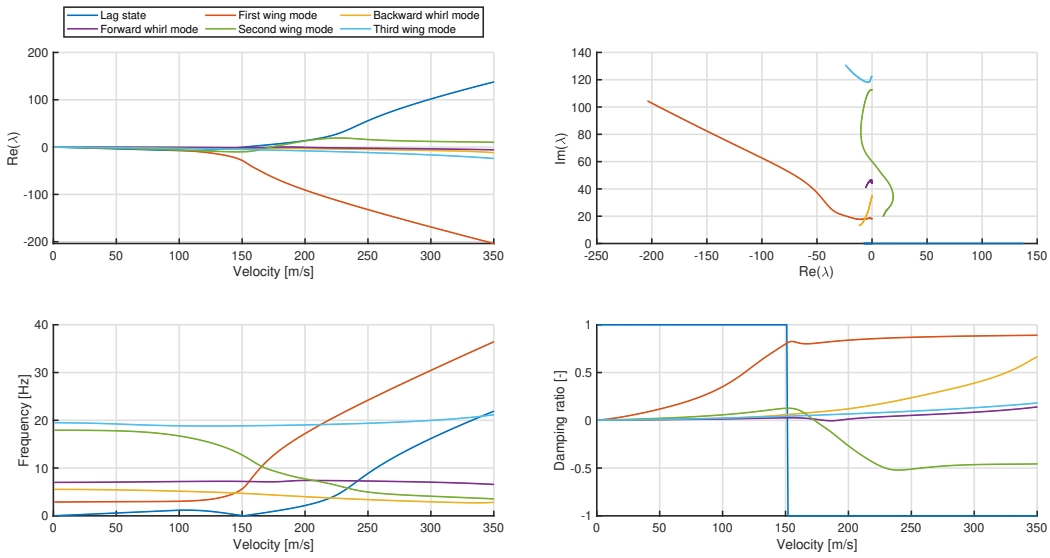

Figure 9.18: Baseline propeller-wing with wing aerodynamics and propeller aerodynamics: V-g-f plots.

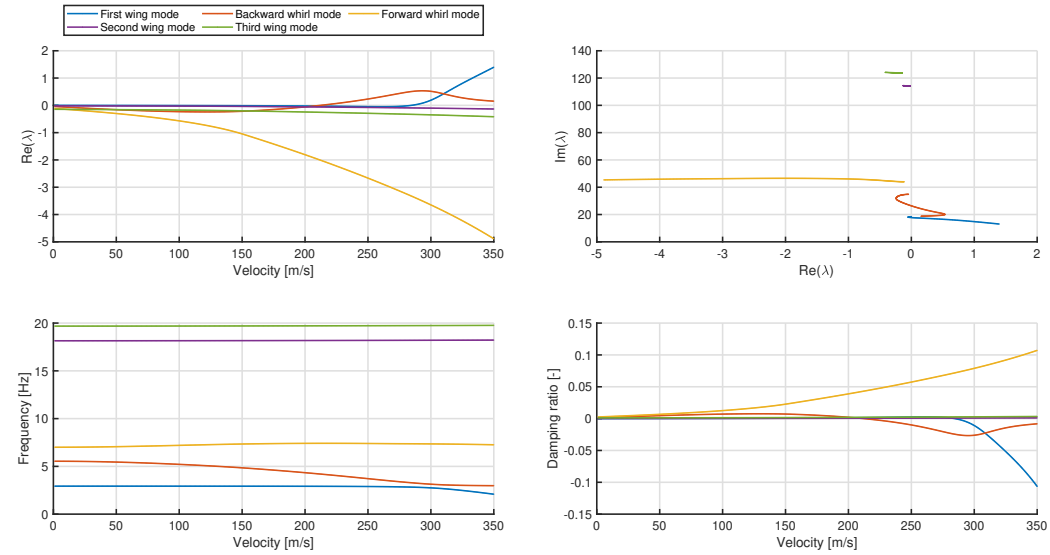

Figure 9.19: Baseline propeller-wing without wing aerodynamics but with propeller aerodynamics: V-g-f plots.

Strictly speaking, due to structural coupling between the degrees of freedom of the wing and the propeller, the modes of the propeller-wing model are coupled modes. In theory, they should be named first coupled propeller-wing mode (first wing mode), second coupled propeller-wing mode (backward whirl mode), third coupled propeller-wing mode (forward whirl mode), etc. However, for explanatory purposes, it has been decided by the author to name them as n^{th} wing modes and backward/forward whirl modes; this will be the nomenclature for the remaining of the report.

Figure 9.20 and Figure 9.21 illustrate the wing flutter and whirl flutter mode shapes, respectively. The corresponding propeller pitch and yaw deflections are also shown. The wing flutter mode is a coupled first bending-first torsion mode; the forward whirl flutter mode also carries a coupled first bending-first torsion mode. In both cases, due to propeller-wing coupling, θ and ψ no longer have a 90° phase lag, hence, the elliptical shape in the pitch-yaw deflection plots, despite having a symmetrical propeller.

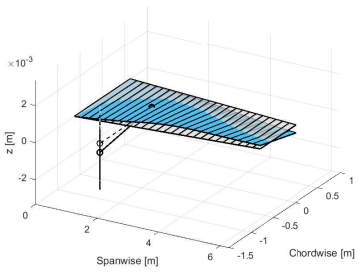

(a) Mode in 3D at time = 0 s.

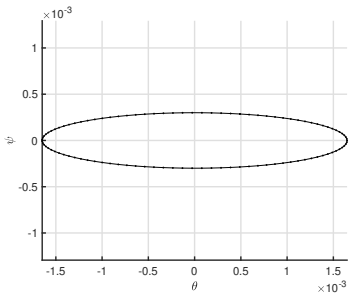

(b) Propeller pitch and yaw deflections.

Figure 9.20: Baseline propeller-wing: wing flutter mode shape.

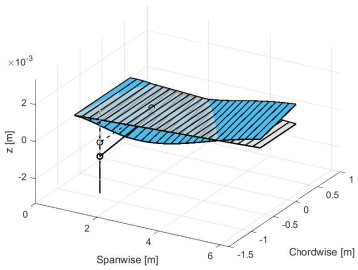

(a) Mode in 3D at time = 0 s.

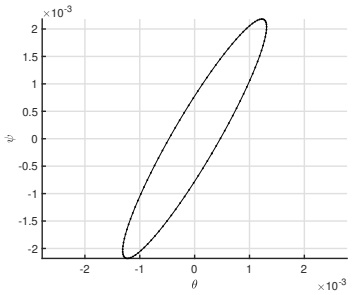

(b) Propeller pitch and yaw deflections.

Figure 9.21: Baseline propeller-wing: whirl flutter mode shape.

10

Case Studies: Other Propeller-Wing Models

Following the aeroelastic analyses of the propeller-wing model in Chapter 9, it is interesting to see the influence of the spanwise location of a propeller on the wing in terms of aeroelastic interactions. For this purpose, the baseline propeller-wing model is modified such that the propeller is moved to the wing tip.

On the other hand, it is also interesting to investigate the aeroelastic interaction of a flexible wing with multiple propellers. For this purpose, the baseline propeller-wing model is modified such that an additional propeller of the same characteristics is positioned on the wing tip.

For both models, aeroelastic analyses analogous to those performed in Chapter 9 are repeated and compared employing the methodology explained in Chapter 8 and supplemented by Appendix D.

10.1. Wing with a wingtip-mounted Propeller

In this section, aeroelastic analysis of a wingtip-mounted propeller-wing model is presented. The plan view of the model is illustrated in Figure 10.1.

It is well-known that wingtip-mounted propellers are under the influence of wing tip vortices and it is expected that this interference would influence the overall propeller-wing aeroelastic behaviour. However, the methodology presented in present work ignores the aerodynamic interference effects. Higher fidelity analysis to include propeller-wing aerodynamic interference effects is recommended and proposed for future work.

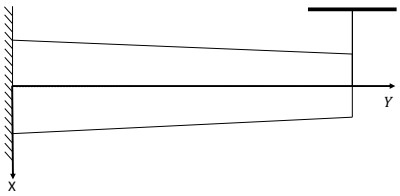

Figure 10.1: Wingtip-mounted propeller-wing simple schematic, top view. Relative dimensions are approximate.

10.1.1. Wing with a non-rotating Propeller rigidly attached

Let's consider a non-rotating baseline propeller attached to the baseline wing. The propeller mounts are assumed to be rigid, hence, the added propeller may be treated as an additional inert mass that changes the mass and inertial distributions of the wing. Table 10.1 shows the frequency distribution of the baseline wing with the baseline propeller mounted on the wing tip.

Adding the non-rotating propeller at the wing tip reduces the natural frequencies of the wing, specially the first bending and torsional modes. Figure 10.2 shows the V-g-f plots from the aeroelastic analysis. In contrast to the clean wing configuration and the baseline propeller-wing model, wing flutter occurs at higher airspeeds; the flutter mode consists of the second wing mode going unstable due to interactions with the third wing mode. Divergence does not occur in the velocity interval analysed (0-350 m/s).

Mode	Frequency (with propeller)	Frequency (clean wing)	Units
First wing mode	1.85	2.88	[Hz]
Second wing mode	6.79	16.68	[Hz]
Third wing mode	17.75	18.06	[Hz]
Fourth wing mode	32.13	46.59	[Hz]
Fifth wing mode	49.74	50.57	[Hz]

Table 10.1: Wing with a wingtip-mounted non-rotating propeller, rigidly mounted: natural frequencies

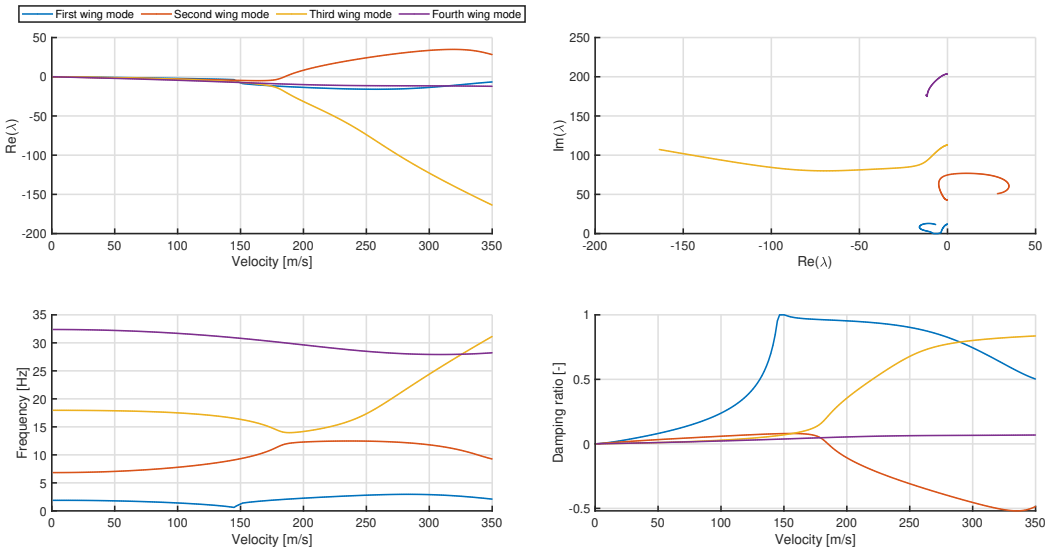

Figure 10.2: Wing with a wingtip-mounted non-rotating propeller, rigidly mounted: V-g-f plots.

Parameter	With one propeller	Clean wing	Units
Flutter speed	185	152	[m/s]
Flutter frequency	10.90	8.08	[Hz]
Divergence speed	-	154	[m/s]

Table 10.2: Wing with a wingtip-mounted non-rotating propeller, rigidly mounted: aeroelastic results.

10.1.2. Wing with a rotating Propeller flexibly attached

Table 10.3 presents the distribution of natural frequencies of the wing with a flexibly mounted propeller on the wing tip. Again, including flexible mounts has more than doubled the frequency of the second wing mode with respect to the equivalent model with rigid mounts.

Figure 10.3 shows the effects of increasing propeller rotational speed on the propeller-wing natural frequencies. The frequencies of the first wing mode and the backward whirl mode are reduced. Increasing propeller rotational speed increases the frequencies of the forward whirl mode and those wing modes whose frequencies are above the forward whirl mode, whereas the frequencies of the backward whirl mode and those wing modes below the backward whirl mode (the first wing mode) are decreased. Therefore, gyroscopic effects change the propeller whirl modes, and in turn, the natural frequencies of the wing are varied due to interaction with the whirl modes to avoid crossing.

Mode	Frequency (flexible mounts)	Frequency (clean wing and isolated propeller)	Frequency (rigid mounts and non-rotating)	Units
First wing mode	1.81	2.88	1.85	[Hz]
Backward mode	5.95	7	-	[Hz]
Forward mode	7	7	-	[Hz]
Second wing mode	17.74	16.68	6.79	[Hz]
Third wing mode	24.89	18.06	17.75	[Hz]
Fourth wing mode	49.36	46.59	32.13	[Hz]
Fifth wing mode	52.19	50.57	49.74	[Hz]

Table 10.3: Wing with a wingtip-mounted rotating propeller, flexibly mounted: natural frequencies with $\Omega = 0$ RPM (first column).

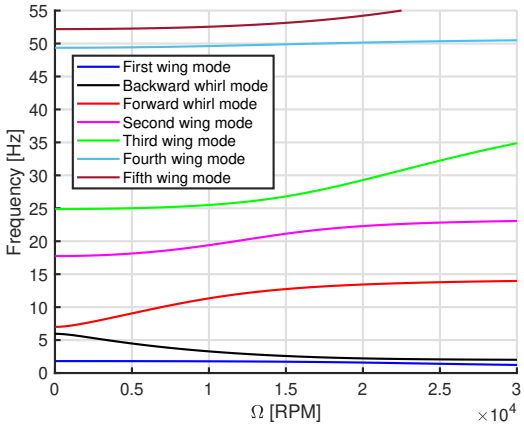

Figure 10.3: Influence of gyroscopic effects on propeller-wing natural frequencies (Wingtip-mounted configuration).

Table 10.4 presents the aeroelastic results. Figure 10.4 shows the V-g-f plots in which only wing aerodynamics are included in the propeller-wing aeroelastic equations, and Figure 10.5 shows the V-g-f plots in which both wing and propeller aerodynamics are included. In the velocity interval examined (0-350 m/s), there is no onset of wing flutter/divergence as such — the frequency of the second wing mode has been increased with respect to the equivalent model with rigid mounts. However, two modes become unstable: a forward whirl flutter mode and a backward whirl flutter mode. The first mode to go unstable is the forward whirl mode due to interaction with the second wing mode. Backward whirl mode becomes unstable due to interaction with the first wing mode.

Both forward and backward flutter modes are present when propeller aerodynamics are not included in the calculations, this suggests that they go unstable due to propeller-wing structural coupling and wing aerodynamics. Again, in this case, forward/backward whirl flutter do not represent pure whirl flutter. Instead, they are a combination of wing flutter and whirl flutter. Including propeller aerodynamics in the analysis, forward whirl mode is slightly stabilised and backward whirl mode is strongly stabilised, thus, the effect of propeller aerodynamics on both instabilities is stabilising.

At very high incoming airspeeds, forward whirl mode diverges. This is not predicted when propeller aerodynamics are not included, which indicates that this divergent behaviour is driven by propeller aerodynamics.

Figure 10.6 illustrates the V-g-f plots without wing aerodynamics but with propeller aerodynamics. It can be observed that whirl flutter occurs only in the backward whirl mode at 126 m/s with a frequency of 5.19 Hz. This indicates that backward whirl mode is also excited by propeller aerodynamics and it is stabilised by wing aerodynamics, although, not entirely eliminated. Forward whirl mode is only driven by wing aerodynamics.

Note the higher benignity in the backward whirl mode instability in all three cases.

Instability type	**Without propeller aerodynamics**	**With propeller aerodynamics**	**Units**
Propeller whirl flutter speed (forward whirl mode)	**160**	**163**	[m/s]
Propeller whirl flutter frequency (forward whirl mode)	**11.44**	**11.50**	[Hz]
Propeller divergence speed (forward whirl mode)	-	326	[m/s]
Propeller whirl flutter speed (backward whirl mode)	197	302	[m/s]
Propeller whirl flutter frequency (backward whirl mode)	6.73	6.54	[Hz]

Table 10.4: Wing with a wingtip-mounted rotating propeller, flexibly mounted: aeroelastic results.

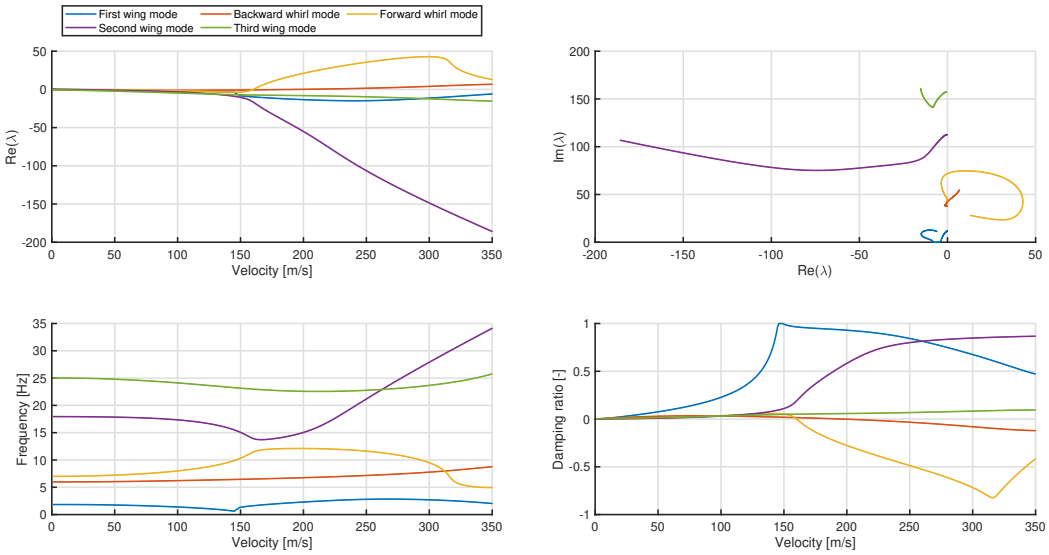

Figure 10.4: Wingtip-mounted propeller-wing with wing aerodynamics and without propeller aerodynamics: V-g-f plots.

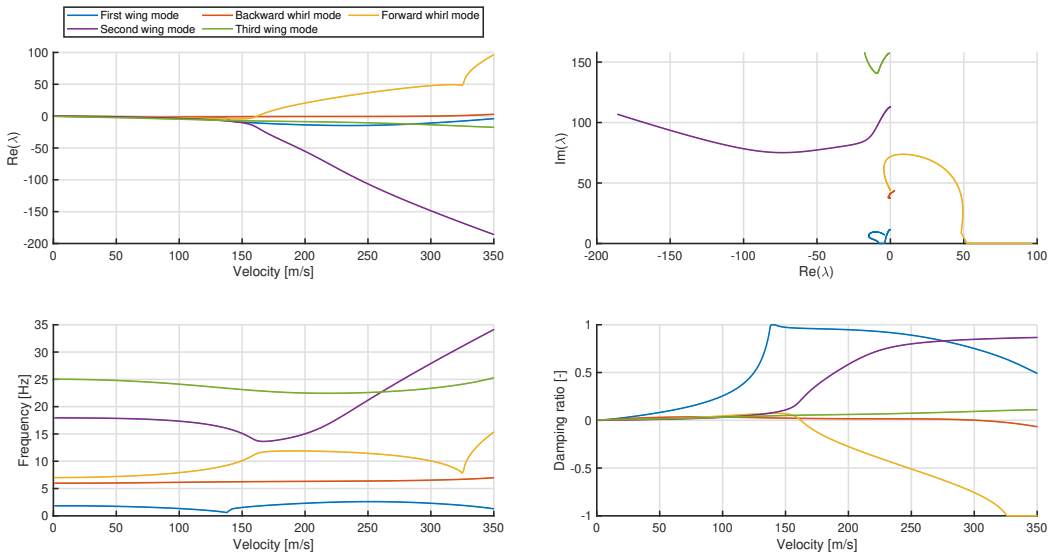

Figure 10.5: Wingtip-mounted propeller-wing with wing aerodynamics and propeller aerodynamics: V-g-f plots.

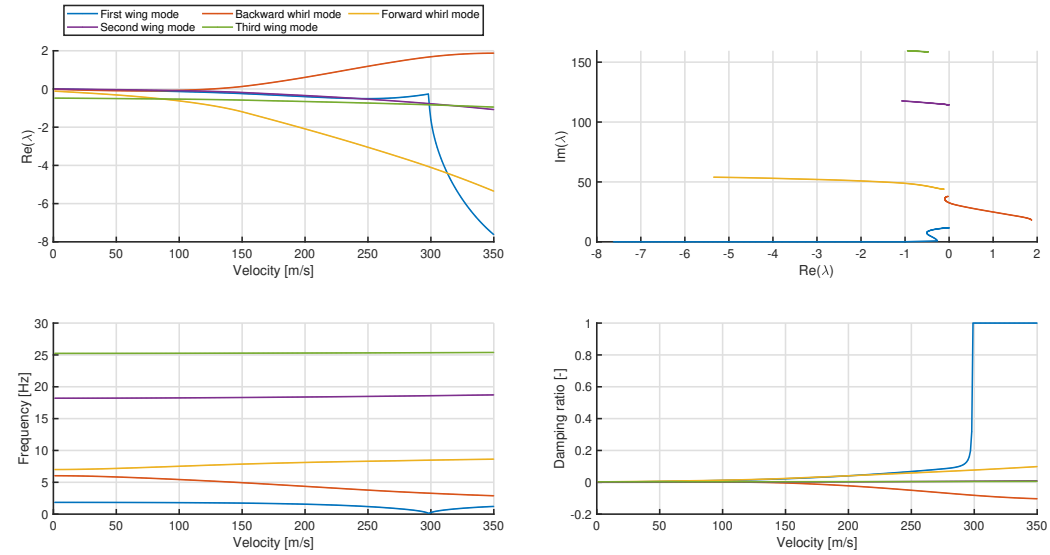

Figure 10.6: Wingtip-mounted propeller-wing without wing aerodynamics but with propeller aerodynamics: V-g-f plots.

Figure 10.7 and Figure 10.8 illustrate the forward whirl flutter and backward whirl flutter mode shapes, respectively. In both mode shapes, the wing carries second wing bending motions due to higher bending-torsion coupling caused by moving the propeller to the wing tip. Again, note the elliptical shape of the pitch-yaw deflections due to propeller-wing coupling.

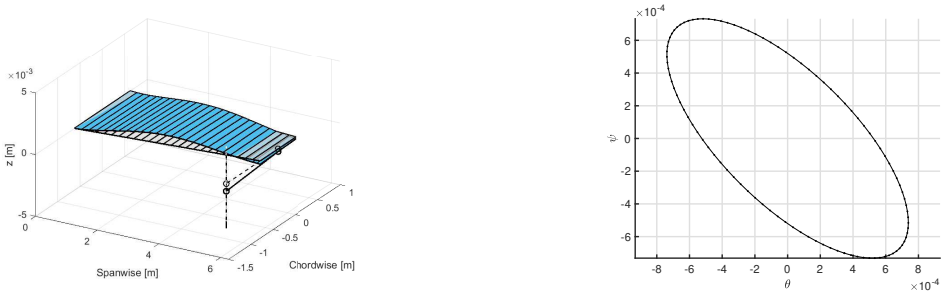

(a) Mode in 3D at time = 0 s.

(b) Propeller pitch and yaw deflections.

Figure 10.7: Wingtip-mounted propeller-wing: forward whirl flutter mode shape.

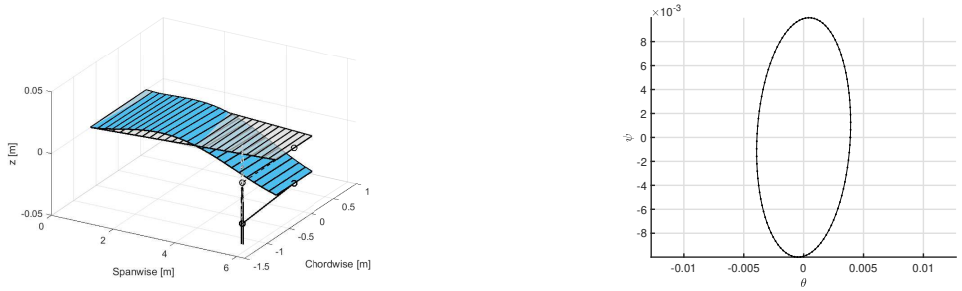

(a) Mode in 3D at time = 0 s.

(b) Propeller pitch and yaw deflections.

Figure 10.8: Wingtip-mounted propeller-wing: backward whirl flutter mode shape.

10.2. Wing with two Propellers

In this section, aeroelastic analysis of the baseline wing with two propellers is presented: one is positioned at 1.60 m from wing root and the other one is positioned at the wing tip. The propellers have the same characteristics as the baseline propeller and the clean wing is the baseline wing. This configuration is a superposition of the previous two propeller-wing models. The plan view of the configuration is illustrated in Figure 10.1.

Aeroelastic analysis is performed as in previous sections.

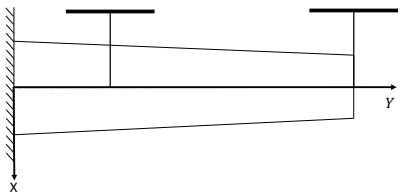

Figure 10.9: Two-propeller-wing simple schematic, top view. Relative dimensions are approximate.

10.2.1. Wing with a non-rotating Propeller rigidly attached

If both propeller mounts are assumed to be rigid, the added propellers may be treated as additional inert masses that change the mass and inertial distributions of the wing. Table 10.5 shows the frequency distribution.

In this case, adding the non-rotating propellers reduces the natural frequencies of the wing, specially the lower modes. Figure 10.10 shows the V-g-f plots from the aeroelastic analysis. In contrast to the clean wing and wingtip-mounted propeller-wing configuration, wing flutter occurs at much higher airspeeds; the flutter mode consists of the fourth wing mode which interacts with the second wing mode and then goes unstable. Divergence does not occur in the velocity interval analysed. Note that the second wing mode interacts with the third wing mode and the third wing mode is destabilised (at $V \approx 175$ m/s), however, it does not go unstable and with higher incoming airspeeds it is highly stabilised.

Mode	Frequency (with two propellers)	Frequency (clean wing)	Units
First wing mode	1.84	2.88	[Hz]
Second wing mode	6.48	16.68	[Hz]
Third wing mode	9.67	18.06	[Hz]
Fourth wing mode	20.85	46.59	[Hz]
Fifth wing mode	41.62	50.57	[Hz]

Table 10.5: Wing with two non-rotating propeller, rigidly mounted: natural frequencies

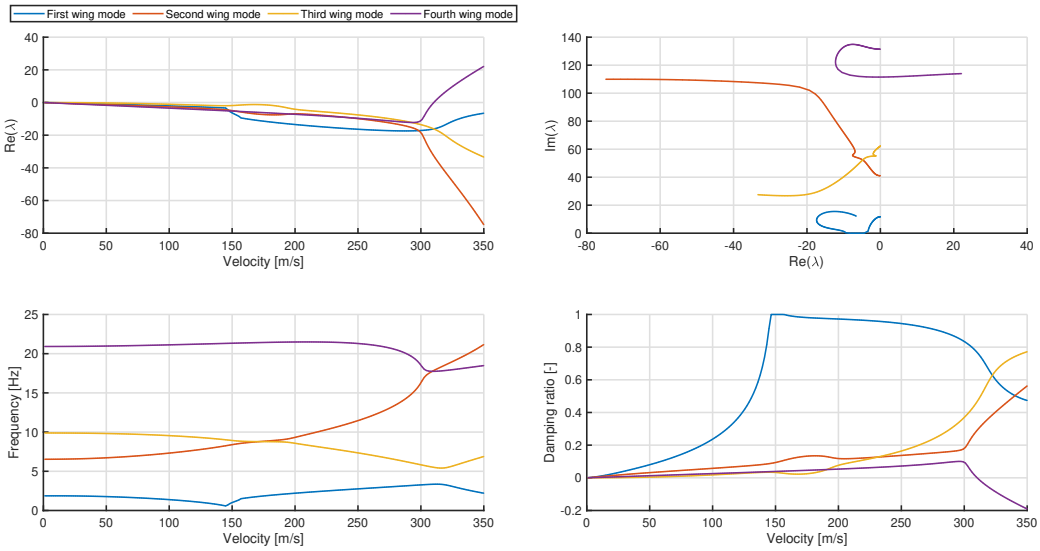

Figure 10.10: Wing with two non-rotating propeller, rigidly mounted: V-g-f plots.

Parameter	With two propellers	Clean wing	Units
Flutter speed	311	152	[m/s]
Flutter frequency	17.75	8.08	[Hz]
Divergence speed	-	154	[m/s]

Table 10.6: Wing with two non-rotating propeller, rigidly mounted: aeroelastic results.

10.2.2. Wing with a rotating Propeller flexibly attached

Table 10.7 presents the distribution of natural frequencies of the wing with flexibly mounted propellers. Considering flexible mounts has risen the natural frequencies of the wing with respect to the equivalent model with rigid mounts.

Figure 10.11 shows the effects of increasing propeller rotational speed on propeller-wing natural frequencies. Both propellers have the same rotational speed. Increasing propeller rotational speed increases the frequencies of the forward whirl modes and decreases the frequencies of the backward whirl modes. The frequencies of the whirl modes interact with each other and with those from the wing modes to avoid crossing, therefore, wing natural frequencies also change with varying propeller rotational speed.

Mode	Frequency (flexible mounts)	Frequency (clean wing and isolated propeller)	Frequency (rigid mounts and non-rotating)	Units
First wing mode	1.80	2.88	1.84	[Hz]
First backward mode	5.39	7	-	[Hz]
Second backward mode	6.21	7	-	[Hz]
First forward mode	7	7	-	[Hz]
Second forward mode	7	7	-	[Hz]
Second wing mode	18.64	16.68	6.48	[Hz]
Third wing mode	26.71	18.06	9.67	[Hz]
Fourth wing mode	50.59	46.59	20.85	[Hz]
Fifth wing mode	54.12	50.57	41.62	[Hz]

Table 10.7: Wing with two rotating propeller, flexibly mounted: natural frequencies with $\Omega = 0$ RPM (first columns).

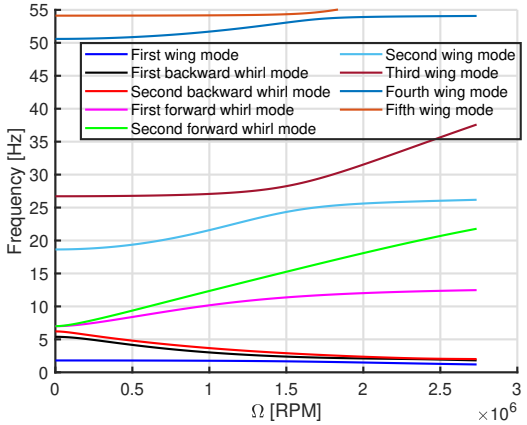

Figure 10.11: Influence of gyroscopic effects on propeller-wing natural frequencies (two-propeller-wing model).

Table 10.8 presents the aeroelastic results. Figure 10.12 shows the V-g-f plots in which only wing aerodynamics are included in the propeller-wing aeroelastic equations, and Figure 10.13 shows the V-g-f plots in which both wing and propeller aerodynamics are included. In the velocity interval examined (0-350 m/s), there is no onset of wing flutter/divergence as such. However, two instabilities appear: forward whirl flutter and backward whirl flutter. Forward whirl flutter arises from the interaction between the second forward whirl mode and the second wing mode, the mode that goes unstable is the second forward whirl mode. Backward whirl flutter arises from the second backward whirl mode due to interaction with the first backward whirl mode and the first wing mode. It appears that the second forward and second backward whirl modes are mostly related to the wingtip-mounted (outboard) propeller as the forward whirl and backward whirl modes go unstable in a similar fashion as in the wingtip-mounted propeller model.

Including propeller aerodynamics in the analysis, forward whirl flutter is destabilized for a very small amount and backward whirl flutter is stabilised. As in the case of wingtip-mounted propeller-wing model, these two instabilities are still present when propeller aerodynamics are excluded. This suggests that the onset of whirl flutter stems from the propeller-wing structural coupling and wing aerodynamics. The whirl flutter modes are not pure whirl modes, rather, they are a combination of wing flutter and whirl flutter.

Figure 10.14 presents the V-g-f plots without wing aerodynamics but with propeller aerodynamics. Without wing aerodynamics, only the backward whirl modes go unstable. The critical speed is determined by the first backward whirl mode at 199 m/s with a frequency of 4.17 Hz, followed by the second backward whirl mode at 220 m/s with a frequency of 4.56 Hz. Wing aerodynamics fully stabilises the first backward whirl mode and stabilises — increases the flutter speed of — the second backward whirl mode. Forward whirl modes do not go unstable when wing aerodynamics is excluded. Therefore, backward whirl flutter is driven by both wing and propeller aerodynamics and wing aerodynamics whereas the forward whirl flutter is only driven by wing aerodynamics.

In comparison with the wingtip-mounted propeller-wing configuration, the addition of an inboard propeller has increased the forward whirl flutter speed (the critical speed) and decreased the backward whirl flutter speed. On the other hand, in comparison with the baseline propeller-wing model in which the propeller is positioned inboard, the wing modes of the two-propeller-wing model no longer go unstable nor does the first forward whirl mode. Therefore, it appears that in present model, the critical state is determined by the outboard (wingtip-mounted) propeller.

Instability type	**Without propeller aerodynamics**	**With propeller aerodynamics**	**Units**
Propeller whirl flutter speed (second forward whirl mode)	**185**	**184**	[m/s]
Propeller whirl flutter frequency (second forward whirl mode)	**12.90**	**12.62**	[Hz]
Propeller whirl flutter speed (second backward whirl mode)	231	251	[m/s]
Propeller whirl flutter frequency (second backward whirl mode)	6.81	6.28	[Hz]

Table 10.8: Wing with two rotating propeller, flexibly mounted: aeroelastic results.

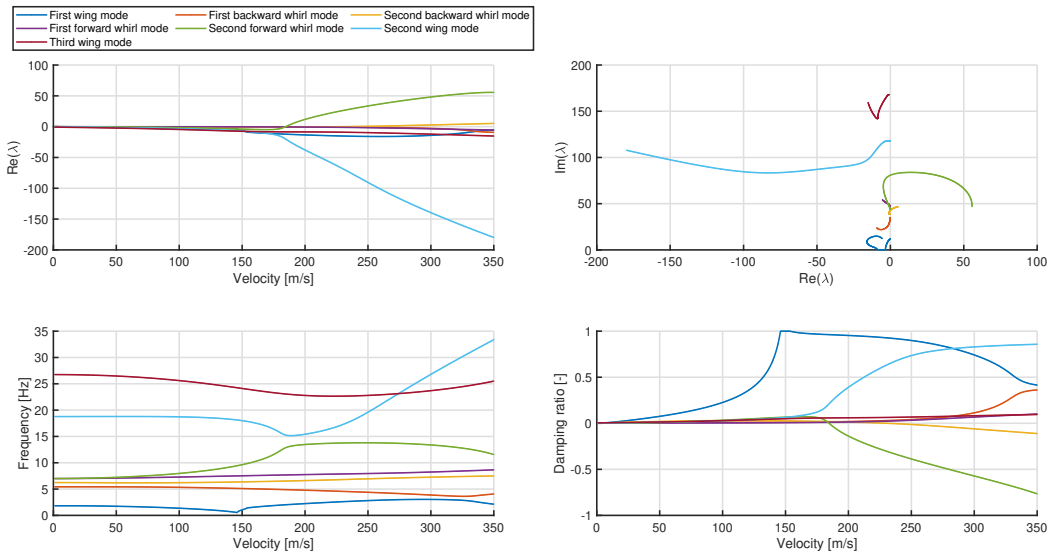

Figure 10.12: Two-propeller-wing with wing aerodynamics and without propeller aerodynamics: V-g-f plots.

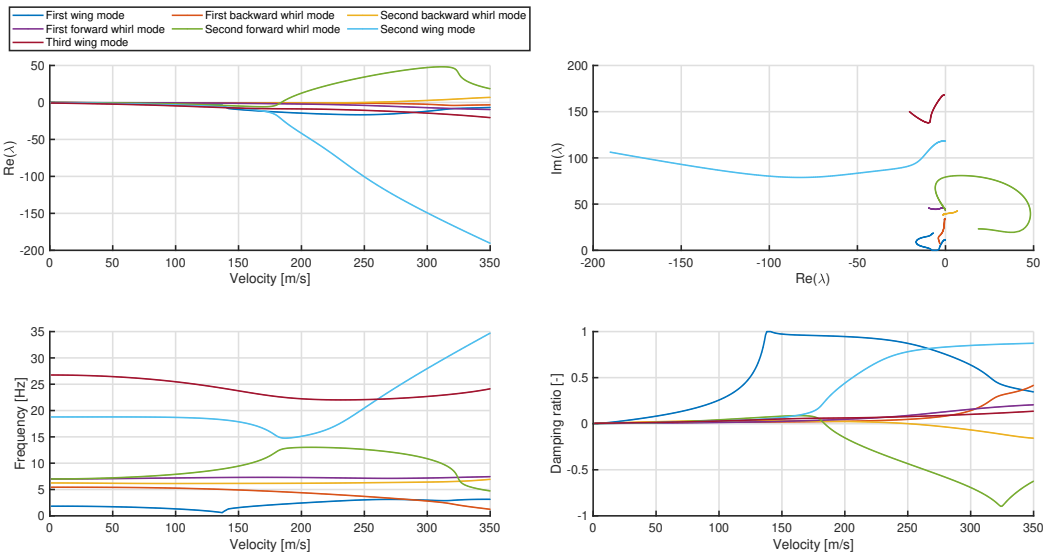

Figure 10.13: Two-propeller-wing with wing aerodynamics and propeller aerodynamics: V-g-f plots.

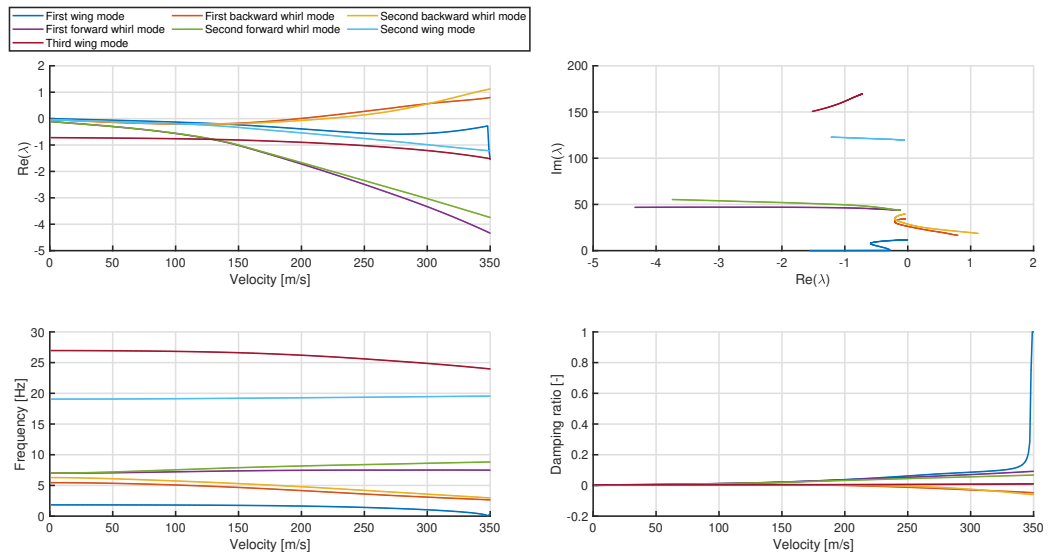

Figure 10.14: Two-propeller-wing without wing aerodynamics but with propeller aerodynamics: V-g-f plots.

Figure 10.15 and Figure 10.16 illustrate the forward whirl flutter and backward whirl flutter mode shapes, respectively. The corresponding propeller pitch and yaw deflections are also shown, in both cases, θ and ψ are out of phase due to propeller-wing coupling.

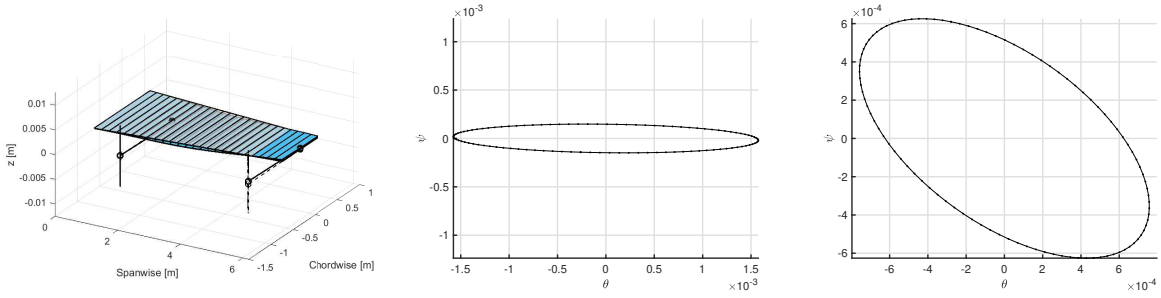

(a) Mode in 3D at time = 0 s. (b) Inboard propeller: pitch and yaw deflections. (c) Outboard propeller: pitch and yaw deflections.

Figure 10.15: Two-propeller-wing model: forward whirl flutter mode shape.

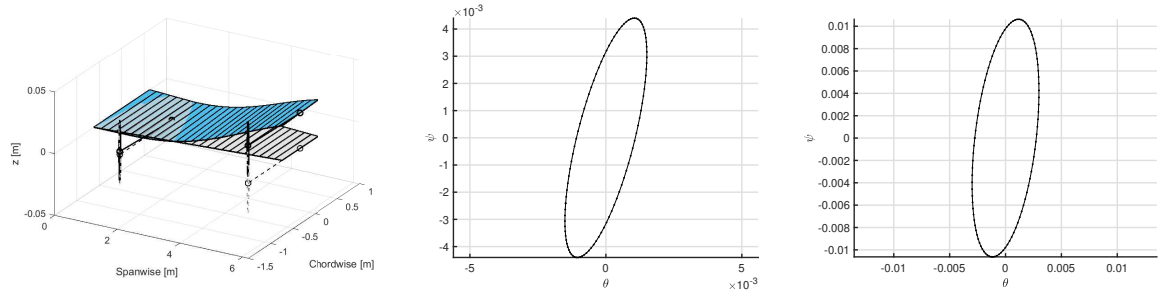

(a) Mode in 3D at time = 0 s. (b) Inboard propeller: pitch and yaw deflections. (c) Outboard propeller: pitch and yaw deflections.

Figure 10.16: Two-propeller-wing model: backward whirl flutter mode shape.

10.3. Summary

Table 10.9 summarises the critical instability that drives each model unstable. The critical instability is the instability that onsets at the lowest airspeed. Note that all the critical speeds are much above the proposed cruise speed of 77 m/s.

Let's first consider the cases of non-rotating propeller/s and rigid mounts. In the baseline propeller-wing configuration, adding an inboard propeller as an inert mass with inertia and static unbalance has reduced the critical speed with respect to the baseline wing. However, moving the propeller to the wing tip increases the critical speed, and the increase is even more pronounced when an additional propeller of equal characteristics is added to the wing tip.

Let's now consider the cases of rotating propeller/s and flexible mounts. In the baseline propeller-wing model, wing flutter is increased with respect to the baseline wing. However, divergence speed remains almost unchanged and becomes the critical speed. In the wingtip-mounted propeller-wing model, moving the propeller to the wing tip eliminates wing flutter and wing divergence in the range of speed analysed (0-350 m/s). Nevertheless, the propeller whirl modes become unstable with the forward whirl mode leading to a critical speed; compared to the baseline (isolated) propeller, backward whirl mode is greatly stabilised, but the forward whirl mode, which is always stable in the isolated propeller case, goes unstable at much lower airspeeds than the backward whirl flutter. In the two-propeller-wing model, similar trends are observed as the whirl modes of the wingtip-mounted propeller dominate the aeroelastic stability of the two-propeller-wing; however, the critical speed is higher.

In all the propeller-wing models with flexible mounts, the wing modes that flutter in the rigid mount models (second wing mode and fourth wing mode) are stabilised because including flexible mounts has risen the frequency of these wing modes, thus, making them less susceptible to flutter. However, with the exception of the baseline propeller-wing model, including rotating propellers and flexible mounts leads to lower critical speeds than their counterparts with rigid mounts and non-rotating propellers. This is because the propeller whirl modes couple with the wing modes, and the resulting coupled mode become the critical mode. Such results underline that propeller whirl modes are not to be ignored in the aeroelastic analysis of propeller-wing systems.

In the baseline propeller-wing model, backward whirl mode is fully stabilised by wing aerodynamics. In the wingtip-mounted propeller and two-propeller wing models, however, the backward whirl mode (second

backward whirl mode) is stabilised, although it still goes unstable at higher air speeds. The backward whirl mode is driven unstable by propeller and wing aerodynamics. In all three propeller-wing models, forward whirl mode (second forward whirl mode) is driven unstable by wing aerodynamics alone.

With the specific combination of structural and aerodynamic parameters employed to define the propeller-wing models in present analyses, the aeroelastic stability of the propeller-wing systems appears to be more dependent on the whirl modes of the wingtip-mounted propeller. This motivates further investigation regarding the effects of several parameters that might affect whirl flutter on the wingtip-mounted propeller-wing configuration (Chapter 11).

Model	**Instability type**	**Mode shape**	**Speed [m/s]**	**Frequency [Hz]**
Baseline wing	Wing flutter	First torsion (second wing mode)	152	8.08
Baseline propeller	Whirl flutter	Backward whirl	221	5.0
With non-rotating propeller/s and rigid mounts				
Baseline propeller-wing	Wing flutter	Second wing mode	142	6.30
Wingtip-mounted propeller-wing	Wing flutter	Second wing mode	185	10.90
Two-propeller-wing	Wing flutter	Fourth wing mode	311	17.75
With rotating propeller/s and flexible mounts				
Baseline propeller-wing	Wing divergence	Lag state	152	0
Wingtip-mounted propeller-wing	Whirl flutter	Forward whirl	163	11.50
Two-propeller-wing	Whirl flutter	Second forward whirl mode	184	12.62

Table 10.9: Critical instabilities of all the models.

11

Parametric Studies on the wingtip-mounted Propeller-Wing Model

In present chapter, the effects of various structural parameters on the aeroelastic behaviour of the wingtip-mounted propeller-wing model will be explored and compared to the isolated propeller case. The parameters are: nacelle stiffness, nacelle structural damping, propeller mass, propeller pivoting length, the propeller mass moment of inertia about the axis of rotation, and propeller advance ratio.

11.1. Nacelle Stiffness

Propeller nacelle stiffness in pitch and yaw are directly related to the natural frequencies of the propeller in pitch and yaw modes, and in turn, the backward whirl and forward whirl mode frequencies. Higher stiffness values lead to higher natural frequencies. The reduction of nacelle stiffness may be triggered by the development of fatigue cracks or other types of structural failures. To study the influence of nacelle stiffness on the wingtip-mounted propeller-wing model, the following cases are analysed:

1. The natural frequency in pitch is set constant to $f_\theta = 7$ Hz. Then, the natural frequency in yaw is modified from $f_\psi = 1$ Hz to $f_\psi = 12$ Hz.

2. The natural frequency in yaw is set constant to $f_\psi = 7$ Hz. Then, the natural frequency in pitch is modified from $f_\theta = 1$ Hz to $f_\theta = 12$ Hz.

3. The natural frequency in pitch is set equal to the natural frequency in yaw. Then, both natural frequencies are modified together from $f_\theta = f_\psi = 1$ Hz to $f_\theta = f_\psi = 12$ Hz.

For each of the above cases, the aeroelastic equations for the wingtip-mounted propeller-wing are solved to obtain the critical speed, that is the speed at which the first instability occurs and the system becomes unstable. The same calculations are also computed for the propeller on rigid wing (isolated propeller) for comparison. Figure 11.1 and Figure 11.2 plots the critical speeds against the average natural frequencies $\frac{f_\theta + f_\psi}{2}$.

Figure 11.1a shows the critical speeds for the isolated propeller. The isolated propeller has symmetrical characteristics, this means that changing the stiffness in yaw has the same effects as changing the stiffness in pitch; this is why the dashed blue line coincides with the dashed black line. (1)-(2) In the asymmetrical stiffness cases $f_\theta \neq f_\psi$, for very small values of pitch/yaw natural frequencies, the propeller diverges in the backward whirl mode; the smaller the stiffness, the sooner the propeller becomes unstable. As the pitch/yaw stiffness is further increased the critical speed becomes smaller, this is because the system is approaching symmetrical stiffness; for an isolated propeller, equal stiffness in pitch and yaw yields the most critical state. As the pitch/yaw stiffness increases again, so does the critical speed and the propeller becomes more stable. (3) In the symmetrical stiffness case $f_\theta = f_\psi$, the critical speed grows monotonically with the nacelle stiffness. Note that divergence occurs only if one of the stiffness becomes too small. With exception of the annotated markers, the critical speeds in this model are caused by the backward whirl mode going unstable.

Figure 11.1b shows the critical speeds for the wingtip-mounted propeller-wing. In this case, despite having a propeller with symmetrical characteristics, changing the stiffness in yaw has different effects than changing the stiffness in pitch due to propeller-wing coupling. It was mentioned in Section 10.1.2 that the pitch/yaw natural frequencies are between the lowest two wing mode natural frequencies; the system goes unstable due to coupling of the propeller whirl modes with these two wing modes. In fact, with the exception of the annotated markers, the markers represent critical speeds of the system due to the forward whirl mode going unstable. (1) Changing the stiffness in yaw while maintaining the stiffness in pitch constant barely changes the critical speed, this is because the propeller is mainly coupled with the wing in pitch. With very low stiffness in yaw, the backward whirl mode acquires very low frequencies and thus, diverges; with higher stiffness in yaw, the instability is driven by the forward whirl mode; as the stiffness in yaw increases further, the backward whirl mode acquires higher frequencies and couples with the forward whirl mode causing the latter to go unstable slightly sooner. (2) Analogously, with very small values of stiffness in pitch, the interaction between the whirl modes and the wing modes is such that drives the second wing mode to flutter. As the stiffness in pitch is increased, the forward whirl mode becomes again the mode that drives the system unstable and the critical speed is initially decreased (due to the change in critical mode shape) and then increased with increasing stiffness in pitch. (3) Finally, with very small values of equal stiffness in pitch and yaw, the system flutters in the backward whirl mode at a very low airspeed. As the stiffness in pitch and yaw are increased the forward whirl mode becomes again the mode that drives the system unstable and the critical speed first decreases, and then increases as the stiffness in pitch and yaw increase.

It appears that if the average nacelle stiffness is increased, having higher stiffness in pitch than in yaw is more stabilizing. If the average nacelle stiffness is decreased, having higher stiffness in pitch than in yaw is also more stabilizing but until certain limiting conditions determined by other propeller-wing modes going unstable.

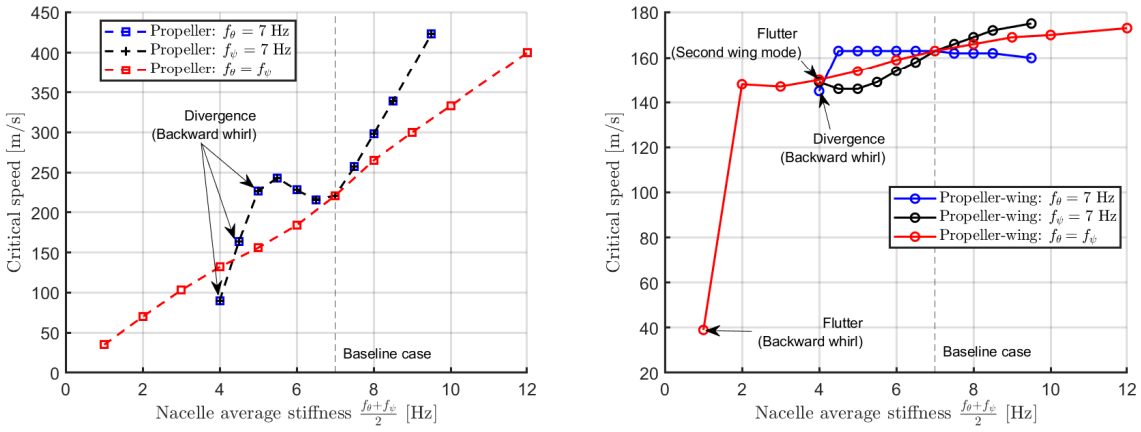

(a) Propeller on rigid wing model.

(b) Wingtip-mounted propeller-wing model.

Figure 11.1: Comparison of critical speeds: effects of asymmetric pitch-yaw stiffness.

Figure 11.2 shows the same plots of Figure 11.1 but regrouped into three different graphs to illustrate the influence of wing flexibility. Each graph represents the critical speeds obtained by modifying nacelle stiffness in yaw, nacelle stiffness in pitch, and equal nacelle stiffness in pitch and yaw, respectively. In each graph, results from the propeller on rigid wing are compared to those from the wingtip-mounted propeller on flexible wing.

In this model, the influence of wing flexibility is generally destabilizing, except for very small average stiffness values. Note that the critical instability is the forward whirl mode and not the backward whirl mode (unless otherwise indicated in the plots). The effects of varying nacelle stiffness are not very stark; this is because the critical instability of the wingtip-mounted propeller-wing model is caused by the forward whirl mode, whose instability is more dependent on wing aerodynamics.

Note that all critical speeds are much above the proposed cruise speed of 77 m/s. A dangerous situation is when the nacelle stiffness in pitch and yaw drop equally to natural frequencies ≈1 Hz or below. In this case, backward whirl flutter emerges.

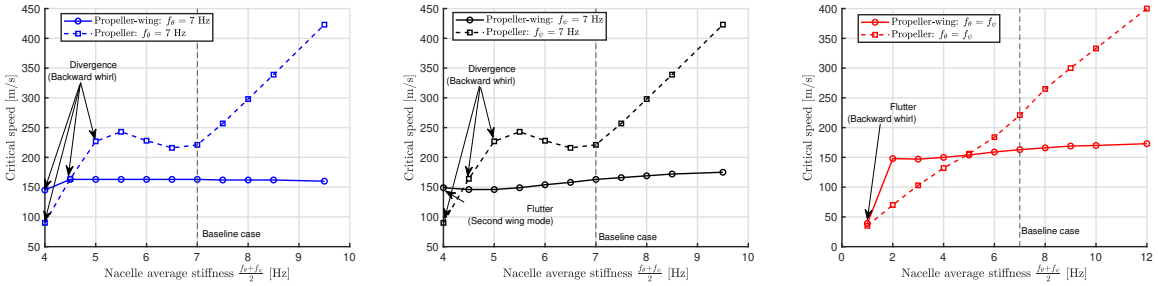

(a) Modifying nacelle yaw stiffness.

(b) Modifying nacelle pitch stiffness.

(c) Modifying equal nacelle pitch-yaw stiffness.

Figure 11.2: Effects of nacelle stiffness. Comparison of critical speeds: influence of wing flexibility.

A particular case is when the nacelle is so stiff in pitch and yaw that the frequency of forward and backward whirl modes becomes much higher than the frequency of the wing modes that go unstable. Figure 11.3 shows the V-g-f plots of the wingtip-mounted propeller-wing with a nacelle stiffness changed to $f_\theta = f_\psi = 50$ Hz, ceteris paribus. The plots are very similar to those shown in Figure 10.2, which illustrate the V-g-f plots of the same wing but with a wingtip-mounted non-rotating propeller, rigidly attached. The main difference is found in the additional forward and backward whirl modes introduced by flexible mounts. As the whirl mode frequencies are much higher, there is very little interaction between the whirl modes and the lowest two wing modes. Hence, the mode that goes unstable is the second wing mode, which is the same wing mode that goes unstable when the propeller is non-rotating and rigidly mounted, as shown in Section 10.1.1. The critical (flutter) speed is 188 m/s and the corresponding flutter frequency is 11.79 Hz. These values are very close to the values of the wing with a nonrotating, rigidly mounted propeller (compare with Table 10.2). Moreover, with such high nacelle stiffness, the propeller does not experience whirl flutter, not even in the isolated case, for the range of velocity of 0-350 m/s.

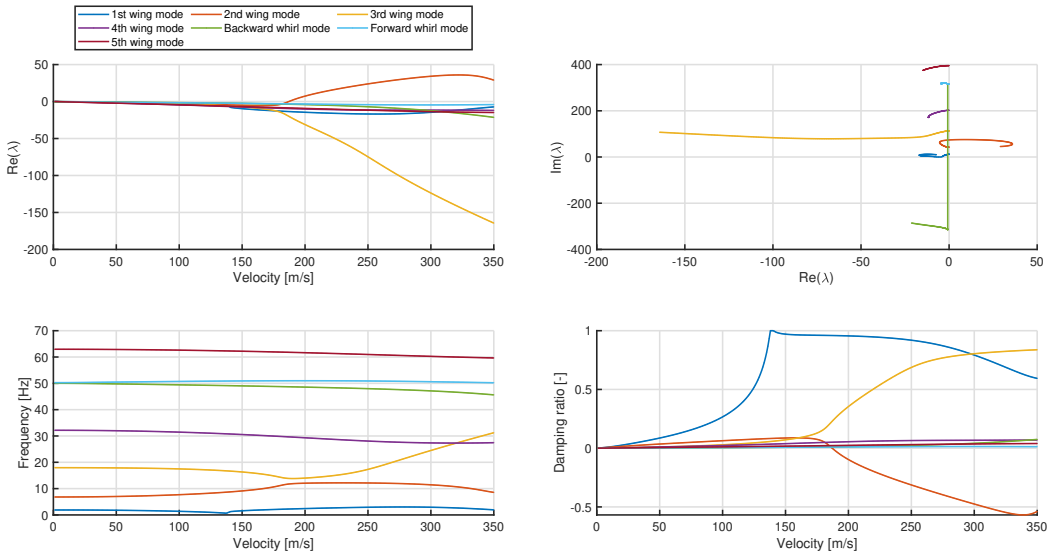

Figure 11.3: Wingtip-mounted propeller-wing with $f_\theta = f_\psi = 50$ Hz: V-g-f plots.

11.2. Nacelle structural Damping

It is underscored in literature that nacelle structural damping strongly affects whirl flutter characteristics of the isolated propeller, especially at small damping values [45]. To investigate the effects of nacelle structural damping on the wingtip-mounted propeller-wing model, parametric sweeps have been performed:

1. The structural damping in pitch is set constant to $\zeta_\theta = 0.005$. Then, the structural damping in yaw is modified from $\zeta_\psi = 0$ to $\zeta_\psi = 1$.

2. The structural damping in yaw is set constant to $\zeta_\psi = 0.005$. Then, the structural damping in pitch is modified from $\zeta_\theta = 0$ to $\zeta_\theta = 1$.

3. The structural damping in pitch is set equal to the structural damping in yaw. Then, both structural damping values are modified together from $\zeta_\theta = \zeta_\psi = 0$ to $\zeta_\theta = \zeta_\psi = 1$.

Figure 11.4 and Figure 11.5 plot the critical speeds against the average structural damping values $\frac{\zeta_\theta+\zeta_\psi}{2}$. In each figure, the upper plot illustrates the results of the parametric sweep of structural damping values between 0 and 1; the lower plot is a closer look of the upper plot for smaller structural damping values.

Note that in the isolated propeller model (propeller on rigid wing), all critical speeds are driven by the backward whirl mode. In the wingtip-mounted propeller-wing model, with the exception of the annotated markers, all the critical speeds are driven by the forward whirl mode.

Figure 11.4a shows the critical speeds for the isolated propeller. Since the propeller is symmetrical, changing structural damping in yaw has the same effect as changing structural damping in pitch. When the nacelle has little structural damping, adding small amounts of it greatly increases the critical speed. Increasing structural damping in pitch/yaw independently or both equally leads to very similar critical speed gains; this is because of symmetrical nacelle stiffness in pitch and yaw. Reed III and Bland [88] shows that as the pitch-yaw stiffness becomes more unequal, more damping is needed in the direction of lower stiffness. The case of unequal pitch-yaw stiffness with varying structural damping is not investigated in present analysis.

Figure 11.4b shows the critical speeds for the wingtip-mounted propeller wing. For small amounts of damping, there is no change in the critical speeds. For very large amounts of structural damping values, increasing structural damping in the pitch direction is the most stabilizing; the addition of wing flexibility reduces the stiffness in the pitch direction, therefore, adding structural damping in this direction has more significant effects on the flutter speed. Increasing structural damping in the yaw direction mainly stabilises the forward whirl mode; hence, as forward whirl mode is stabilized, backward whirl mode becomes unstable.

Figure 11.5 reorganises the plots shown in Figure 11.4 to compare the effects of structural damping on the isolated propeller to the effects of structural damping on the wingtip-mounted propeller-wing. Adding structural damping in the propeller-wing model is not as effective as adding structural damping to the isolated propeller. This is because the critical speeds in the propeller-wing model are mainly driven by propeller-wing coupling and wing aerodynamics.

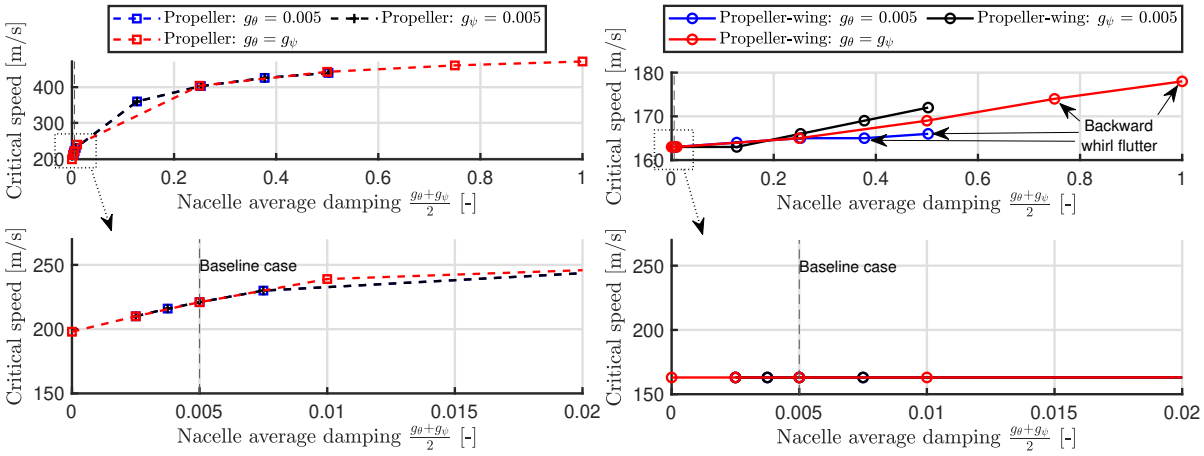

(a) Propeller on rigid wing model.

(b) Wingtip-mounted propeller-wing model.

Figure 11.4: Comparison of critical speeds: effects of asymmetric pitch-yaw structural damping.

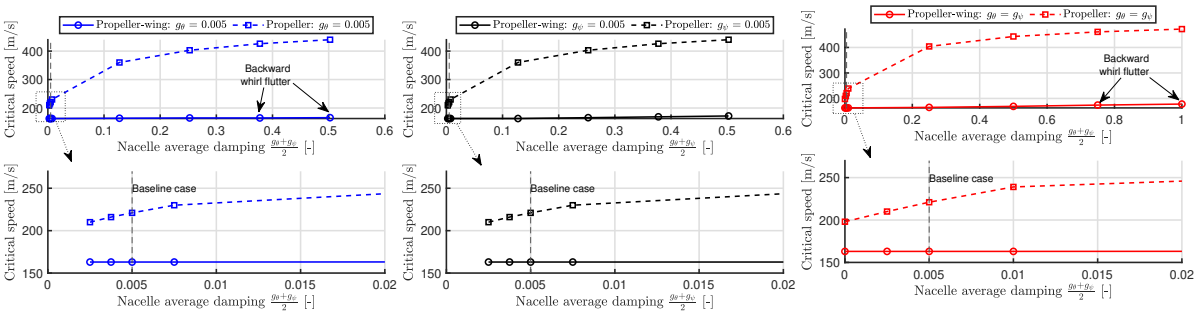

(a) Modifying nacelle yaw structural damping.

(b) Modifying nacelle pitch structural damping.

(c) Modifying equal nacelle pitch-yaw structural damping.

Figure 11.5: Effects of nacelle structural damping. Comparison of critical speeds: influence of wing flexibility.

11.3. Propeller Mass

As illustrated in Figure 9.7, the propeller mass has been simplified into two concentrated masses: a rotor mass (blades and spinner) of 8 kg and a motor-nacelle mass of 35 kg (Table 9.4). These are relatively small values that are often difficult to meet in practice, especially the motor-nacelle mass, since additional hardware will also need to be installed inside the nacelle. For this purpose, the motor-nacelle mass will be varied to investigate its effects on the aeroelastic behaviour of the wingtip-mounted propeller-wing. The effects of varying rotor mass is discussed in Section 11.5.

Increasing the motor-nacelle mass also increases the propeller-wing inertia parameters (i.e. $I_{\theta,P}$, $I_{\psi,P}$, $S_{\theta,P}$, $I_{\alpha,P}$, $S_{\alpha,P}$, and $I_{\theta\alpha,P}$). The mass moment of inertia about the axis of rotation I_Ω remains constant since I_Ω only depends on the rotor mass and the rotor radius in our simplification (Equation (9.2)). Note that in this section, only the motor-nacelle mass is varied; it is supposed that its CG location remains the same.

Figure 11.6 shows the critical speed against motor mass for the wingtip-mounted propeller-wing with flexible mounts and with rigid mounts, and the isolated propeller. Increasing the motor mass increases the mass moment of inertia of the propeller about the pitch/yaw axis. As a result, in the isolated propeller case, the system is stabilised; the instability is driven by the backward whirl mode. In the case of propeller-wing with flexible mounts, the instability is of the forward whirl type which is caused mainly by propeller-wing coupling and wing aerodynamics. The stabilising effects introduced by higher inertia parameters are not as substantial as in the isolated propeller case. Finally, in the case of propeller-wing with rigid mounts, whirl modes are non-existent; the system flutters due to the second wing mode going unstable, increasing the wing tip mass lowers the critical speed. On the other hand, if the wing tip mass is lowered by half, the wing diverges.

Note that the propeller-wing with flexible mounts yields the lowest critical speeds, with the exception of the wing divergence case.

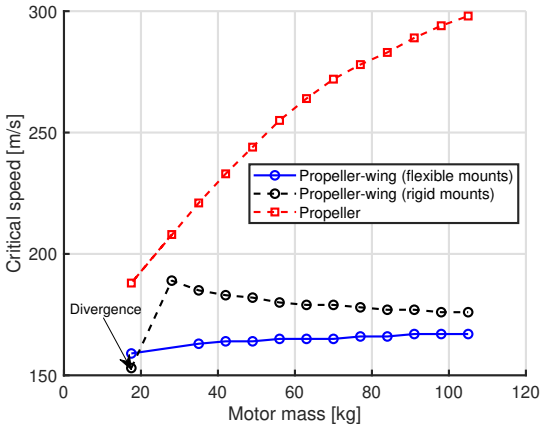

Figure 11.6: Effect of motor mass.

11.4. Propeller pivoting Length

The propeller pivoting length is the distance between the propeller pivot point and the rotor centre. Houbolt and Reed [45] states that a shorter pivot length requires higher nacelle stiffness — leads to lower whirl flutter speeds. This statement is based on the analysis of an isolated propeller with constant rotational speed. Present section analyses the effect of changing the propeller pivoting length in the wingtip-mounted propeller-wing model with a fixed-pitch propeller (non-constant rotational speed but constant pitch angle). Equal pivoting length in pitch and yaw is assumed $e_\theta = e_\psi$ and $l_\theta = l_\psi$.

Changes in the pivoting length also changes the propeller-wing inertia parameters ($I_{\theta,P}$, $I_{\psi,P}$, $S_{\theta,P}$, $I_{\alpha,P}$, $S_{\alpha,P}$, and $I_{\theta\alpha,P}$). The propeller pivoting length may be changed by:

- Moving the rotor CG and the motor-nacelle CG: the distance between the two remains constant, so does the location of the pivot point. It changes the values of $I_{\theta,P}$, $I_{\psi,P}$, $S_{\theta,P}$, $I_{\alpha,P}$, $S_{\alpha,P}$, and $I_{\theta\alpha,P}$.
- Moving the propeller pivot point: the location of the propeller CG remain constant. It changes the values of $I_{\theta,P}$, $I_{\psi,P}$, $S_{\theta,P}$, and $I_{\theta\alpha,P}$.
- Moving the propeller CG and the pivot point whilst maintaining the distance between them constant: this does not change the propeller pivoting length, but as the propeller is mounted on the wing, some of the inertial parameters (i.e. $I_{\alpha,P}$, $S_{\alpha,P}$, and $I_{\theta\alpha,P}$) are changed by this modification as the distance between the pivot point and the wing midchord-axis, $(l_\theta - a_P b_P)$, is varied (see Equation (8.5) and Equation (8.6)).

Figure 11.7 illustrates the position of the propeller CG and pivot point in the wingtip-mounted propeller-wing configuration.

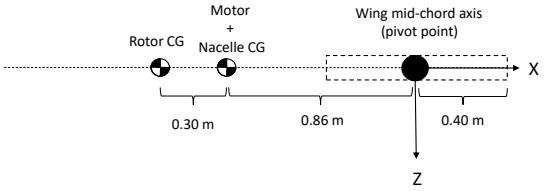

Figure 11.7: Diagram of the propeller CG and pivot point in the wingtip-mounted propeller-wing configuration.

11.4.1. Moving the Propeller CG

The shift in propeller CG is as shown in Figure 11.8.

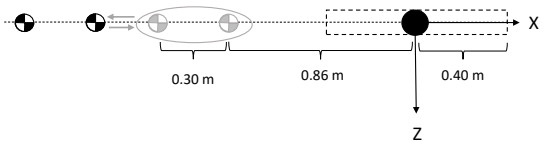

Figure 11.8: Diagram of moving the propeller CG.

Three cases are analysed, the value of the propeller CG and the corresponding inertia parameters are tabulated in Table 11.1. Case (1) moves the propeller CG forward the wing's leading edge. Case (2) moves the propeller's CG towards the wing's leading edge. Case (3) only moves the motor-nacelle CG to the wing's leading edge. This does not change the propeller pivoting length with respect to the baseline configuration, but it changes the inertia parameters.

Case ID	**Rotor CG** [m]	**Motor-Nacelle CG** [m]	$e_\theta = e_\psi$ [m]	$I_{\theta,P} = I_{\psi,P}$ [kg·m^2]	$S_{\theta,P}$ [kg·m]	$I_{\theta\alpha,P}$ [kg·m^2]	$I_{\alpha,P}$ [kg·m^2]	$S_{\alpha,P}$ [kg·m]
Baseline	-1.16	-0.86	-1.16	36.65	-39.38	36.65	36.65	-39.38
1	-1.56	-1.26	-1.56	75.03	-56.58	75.03	75.03	-56.58
2	-0.70	-0.40	-0.70	9.52	-19.60	9.52	9.52	-19.60
3	-1.16	-0.40	-1.16	12.16	-16.28	12.16	12.16	-16.28

Table 11.1: Moving the propeller CG: description of the cases analysed.

Table 11.2 tabulates the results of the aeroelastic analyses of the proposed cases. Figure 11.9, Figure 11.10, and Figure 11.11 show the V-g-f plots.

(1) Moving the propeller CG forward the wing's leading edge increases the pivoting length and the inertia parameters, the effect is stabilising. (2) On the contrary, moving the propeller's CG closer to the wing's leading edge decreases the pivoting length and the inertia parameters, the effect is destabilising; as it can be seen in Figure 11.10, the second wing mode goes unstable, followed by the backward whirl mode and the first wing mode. (3) Finally, maintaining the pivoting length but moving the motor-nacelle CG towards the wing's leading edge also decreases the inertia parameters; the effect is destabilising. Figure 11.11 shows that forward whirl mode still determines the critical speed but other coupled modes also become unstable with higher airspeeds.

Case ID	**Critical speed** [m/s]	**Critical frequency** [Hz]	**Instability type**	**Critical mode**
Baseline	163	11.49	Flutter	Forward whirl mode
1	183	10.95	Flutter	Forward whirl mode
2	125	13.62	Flutter	Second wing mode
3	146	11.73	Flutter	Forward whirl mode

Table 11.2: Moving propeller CG: Aeroelastic results

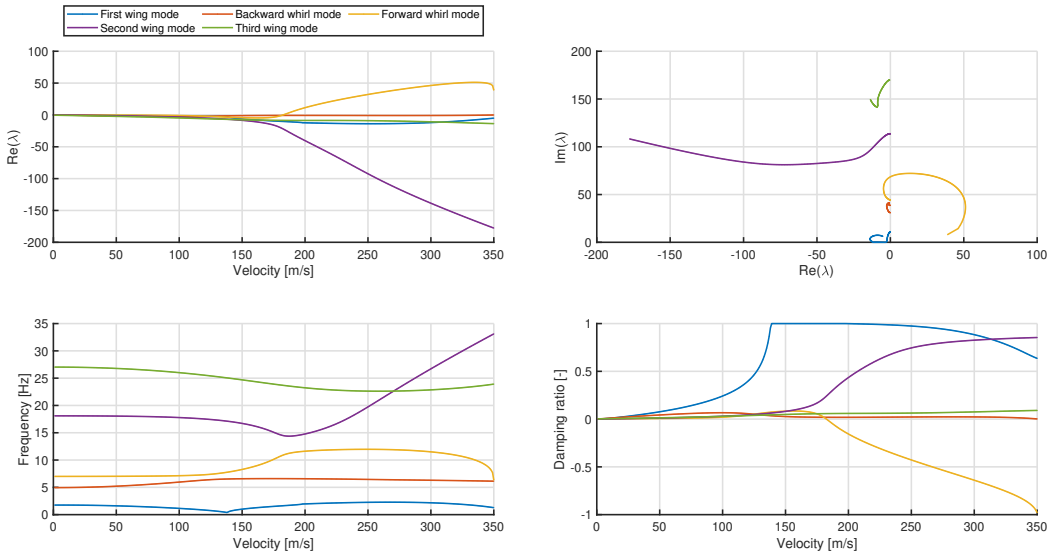

Figure 11.9: Case (1): V-g-f plots.

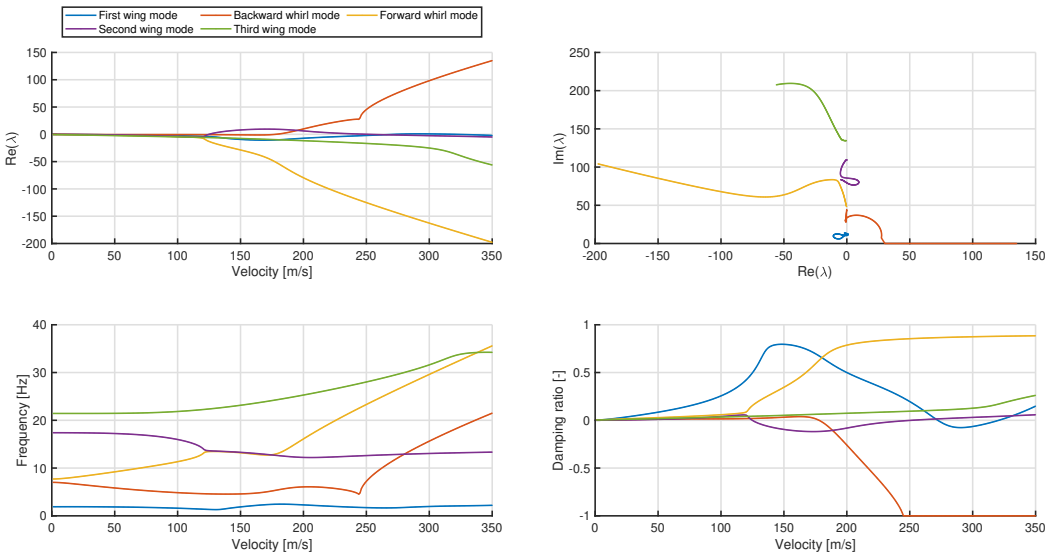

Figure 11.10: Case (2): V-g-f plots.

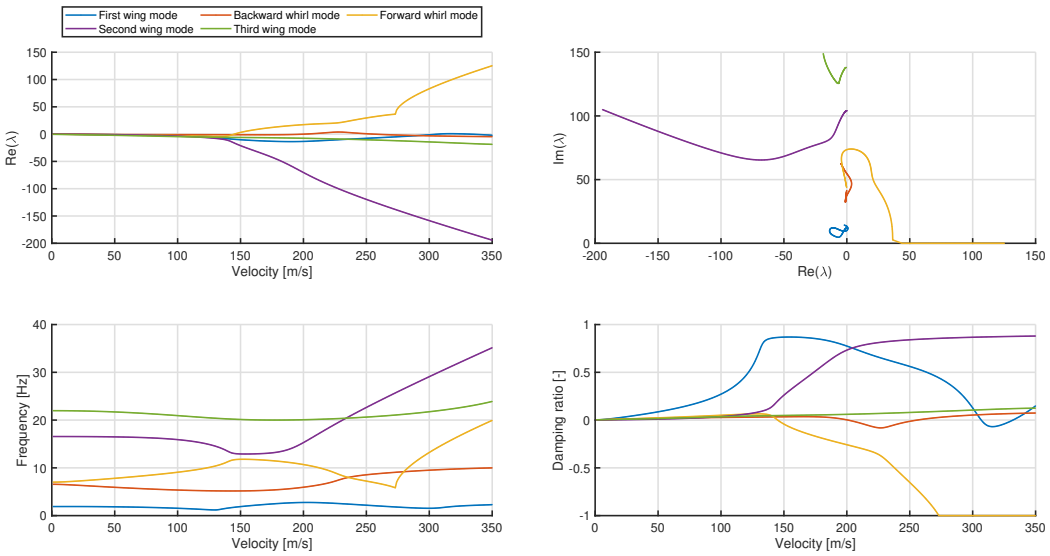

Figure 11.11: Case (3): V-g-f plots.

11.4.2. Moving the Propeller pivot Point

The shift in the propeller pivot point is as shown in Figure 11.12.

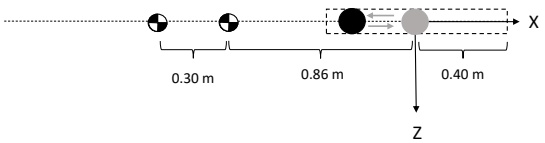

Figure 11.12: Diagram of moving the propeller pivot point.

The pivoting length is shortened as the pivot point is moved forward, towards the rotor. Consequently, the inertia parameters, $I_{\theta,P}$, $I_{\psi,P}$, $S_{\theta,P}$, and $I_{\theta\alpha,P}$, are decreased. Table 11.3 tabulates the values of the concerning parameters that are changed due to the shift of the pivot point. Aeroelastic results are shown in Table 11.4.

As suspected, moving the pivot point forward (shorter pivoting length) has a destabilising effect. Flutter speeds are lowered, although not significantly. Moreover, as the pivot point is moved forward, the backward whirl mode is destabilised; in fact, it goes unstable prior the forward whirl mode in case (4).

Case ID	$l_\theta = l_\psi$ [m]	$e_\theta = e_\psi$ [m]	$I_{\theta,P} = I_{\psi,P}$ [kg·m^2]	$S_{\theta,P}$ [kg·m]	$I_{\theta\alpha,P}$ [kg·m^2]	$I_{\alpha,P}$ [kg·m^2]	$S_{\alpha,P}$ [kg·m]
Baseline	0.00	-1.16	36.65	-39.38	36.65	36.65	-39.38
1	0.20	-1.36	54.12	-47.98	44.53	36.65	-39.39
2	-0.20	-0.96	22.62	-30.78	28.77	36.65	-39.38
3	-0.40	-0.76	12.03	-22.18	20.90	36.65	-39.38
4	-0.60	-0.56	4.87	-13.58	13.02	36.65	-39.38

Table 11.3: Moving the pivot point: description of the cases analysed.

Case ID	**Critical speed** [m/s]	**Critical frequency** [Hz]	**Instability type**	**Critical mode**
Baseline	163	11.49	Flutter	Forward whirl mode
1	163	11.24	Flutter	Forward whirl mode
2	161	11.9	Flutter	Forward whirl mode
3	158	12.67	Flutter	Forward whirl mode
4	149	2.63	Flutter	Backward whirl mode

Table 11.4: Moving the pivot point: aeroelastic results.

11.4.3. Moving Propeller CG and pivot Point

The shift in propeller CG and the pivot point is as shown in Figure 11.13.

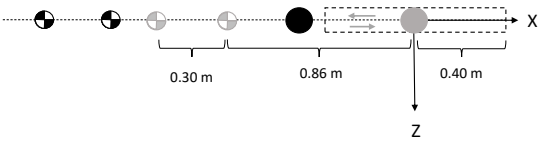

Figure 11.13: Diagram of moving propeller CG and the pivot point.

In this section, the propeller CG and the pivot points are shifted whilst maintaining constant their relative distance. This does not change the propeller pivoting length, but as the propeller is mounted on the wing, the inertia parameters $I_{\alpha,P}$, $S_{\alpha,P}$, and $I_{\theta\alpha,P}$ are changed.

Table 11.5 tabulates the values of the parameters changed due to the shift of the propeller CG and the pivot point. It can be observed that moving them forward (to the left) increases the inertia parameters $I_{\alpha,P}$, $S_{\alpha,P}$, and $I_{\theta\alpha,P}$. As a result, the critical speed is increased. Table 11.6 shows the aeroelastic results.

Case ID	$l_\theta = l_\psi$ [m]	$e_\theta = e_\psi$ [m]	$I_{\theta,P} = I_{\psi,P}$ [kg·m^2]	$S_{\theta,P}$ [kg·m]	$I_{\theta\alpha,P}$ [kg·m^2]	$I_{\alpha,P}$ [kg·m^2]	$S_{\alpha,P}$ [kg·m]
Baseline	0.00	-1.16	36.65	-39.38	36.65	36.65	-39.38
1.00	0.20	-1.16	36.65	-39.38	28.77	22.62	-30.78
2.00	-0.20	-1.16	36.65	-39.38	44.53	54.12	-47.98
3.00	-0.40	-1.16	36.65	-39.38	52.40	75.03	-56.58
4.00	-0.60	-1.16	36.65	-39.38	60.28	99.39	-65.18

Table 11.5: Moving propeller CG and pivot point: description of the cases analysed.

Case ID	Critical speed [m/s]	Critical frequency [Hz]	Instability type	Critical mode
Baseline	163	11.49	Flutter	Forward whirl mode
1	151	11.60	Flutter	Forward whirl mode
2	173	11.34	Flutter	Forward whirl mode
3	182	11.21	Flutter	Forward whirl mode
4	190	11.10	Flutter	Forward whirl mode

Table 11.6: Moving propeller CG and pivot point: aeroelastic results.

11.5. Propeller Mass Moment of Inertia about the axis of Rotation

The propeller mass moment of inertia about the axis of rotation I_Ω depends on the rotating masses that compose the propeller about the axis of rotation. Present work simplifies the calculation of this inertia parameter by applying Equation (9.2). The value of I_Ω depends on the rotor mass and the rotor radius, the contribution of the motor rotor is ignored. To analyse the impact of I_Ω on the aeroelastic stability of the wingtip-mounted propeller-wing model, the rotor mass is changed whilst maintaining constant the rotor radius. Such modification may be introduced when changing the material type of the rotor blades.

Increasing the value of I_Ω leads to higher gyroscopic coupling. This is represented by the terms containing I_Ω in Equation (8.13). Because of the increment of the rotor mass, the other inertia parameters (i.e. $I_{\theta,P}$, $I_{\psi,P}$, $S_{\theta,P}$, $I_{\alpha,P}$, $S_{\alpha,P}$, and $I_{\theta\alpha,P}$) are increased; as observed, this stabilises the propeller against whirl flutter.

Figure 11.14 shows the flutter speeds of the isolated propeller against the flutter speeds of the wingtip-mounted propeller wing model. The isolated propeller flutters in the backward whirl mode; flutter speed decreases with increasing I_Ω until it is counteracted by the increase of the other inertia parameters. The propeller-wing model experiences both backward whirl and forward whirl, with the latter defining the critical speed. Increasing I_Ω destabilises the backward whirl mode; it approximates to the backward whirl speed of the isolated propeller. Nevertheless, forward whirl mode is slightly stabilised, possibly because of the effects of increasing the other inertia parameters.

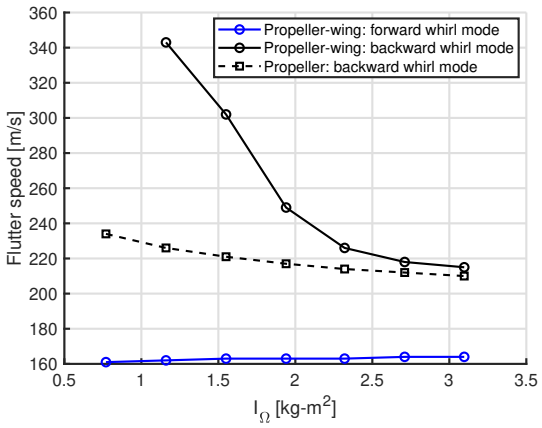

Figure 11.14: Effect of mass moment of inertia about the axis of rotation I_Ω (equivalent to effect of rotor mass).

11.6. Propeller Advance Ratio

Present work deals with fixed-pitch propellers, meaning that in windmilling conditions, the propeller rotational speed varies with the incoming airspeed so as to maintain the advance ratio set by the collective pitch angle, here defined by the blade angle at the three-quarter radius $\beta_{0.75R}$. The relationship between $\beta_{0.75R}$ and the advance ratio is determined by Equation (9.1).

Figure 11.15 plots critical speed against advance ratio ($\beta_{0.75R}$) for the wingtip-mounted propeller-wing model and the isolated propeller.

For a fixed-pitch isolated propeller, Reed III and Bland [88] show in their results that higher advance ratios requires less nacelle structural damping, in other words, higher advance ratios lead to higher flutter speeds in the backward whirl mode — increasing the advance ratio is stabilising. Such a trend is be observed in

Figure 11.15 for the isolated propeller. For a constant speed isolated propeller, windmilling conditions is achieved by allowing the propeller blades to pitch freely; the advance ratio is determined by the incoming airspeed and the propeller rotational speed. In this case, the effect of increasing advance ratio is destabilising; higher advance ratios requires higher nacelle stiffness [45] (this is not treated in present work). Note that at much higher $\beta_{0.75R}$ values, the critical speed becomes supersonic, hence, these analytical results lose their physical meaning. What's more, the curve reaches a maximum because the propeller aerodynamic derivatives are limited by compressibility effects in Houbolt-Reed's method: when the propeller blade tip speed becomes supersonic, a cut-off-value of compressible lift-curve slope is applied in the compressibility effect correction (Equation (4.24)).

On the other hand, for the wingtip-mounted propeller-wing model, increasing the pitch angle barely changes the resulting critical speed. Changing the advance ratio mainly changes propeller aerodynamics and the gyroscopic coupling; as the forward whirl mode is mainly driven by wing aerodynamics, changes of advance ratio are barely noticeable. However, as $\beta_{0.75R}$ reaches 74°, the forward whirl mode stabilizes and the backward whirl mode becomes unstable. This switch in critical mode is observed when analysing the V-g-f plots shown in Figure 11.16 and Figure 11.17. With $\beta_{0.75R} > 73°$ the backward whirl mode determines the critical speed.

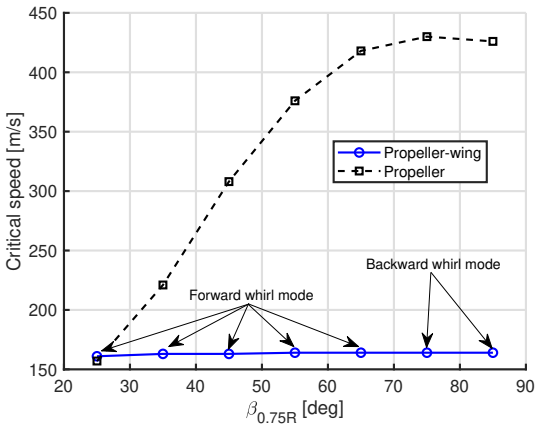

Figure 11.15: Effect of collective pitch angle $\beta_{0.75R}$.

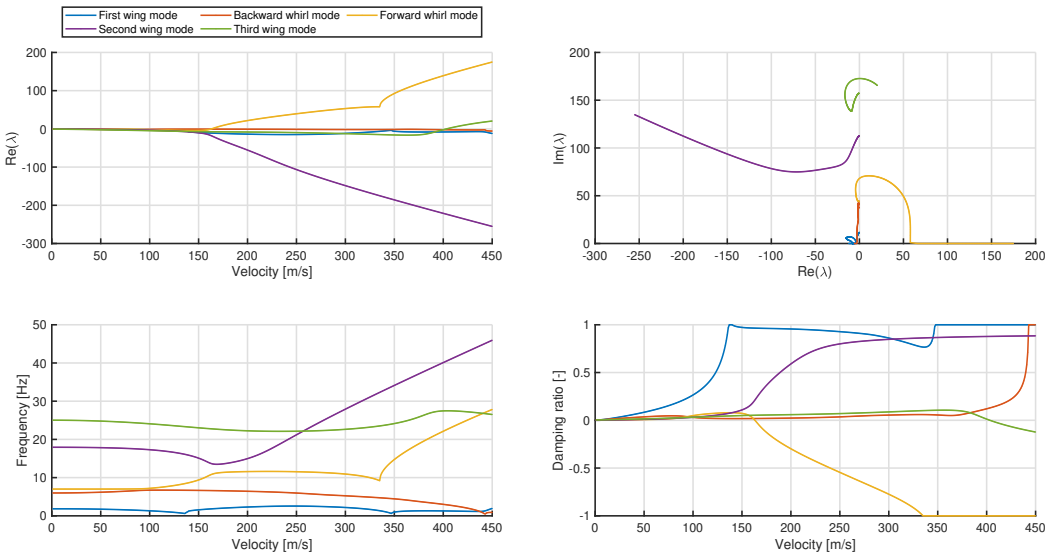

Figure 11.16: Wingtip-mounted propeller-wing with $\beta_{0.75R} = 73°$: V-g-f plots.

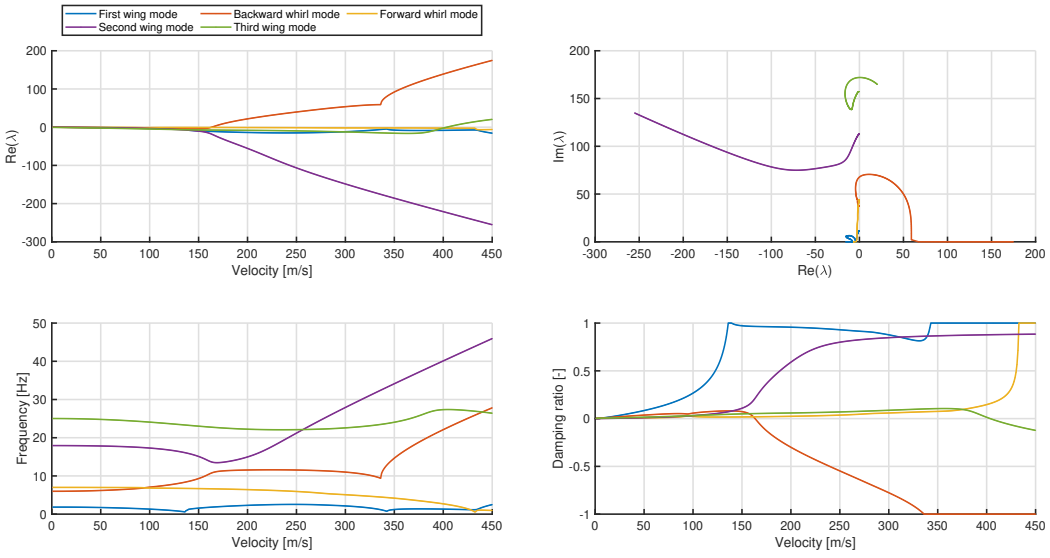

Figure 11.17: Wingtip-mounted propeller-wing with $\beta_{0.75R} = 74°$: V-g-f plots.

12

Conclusions and Recommendations

Conclusions are given in Section 12.1 and recommendations for future work in Section 12.2.

12.1. Conclusions

The project goal to develop an analytical model to be used to predict the onset of wing/whirl flutter in wingtip-mounted propeller and distributed-propeller wing configurations has been successfully achieved. Nevertheless, further quantitative validation/verification of wing flutter predictions using the propeller-wing model is still necessary to gain higher confidence in the predicted results.

The research objective is to improve the understanding of the aeroelastic behaviour of a cantilever wing with flexibly attached tractor propeller/s by predicting wing/whirl flutter behaviours using an analytical method.

For this purpose, three analytical aeroelastic models have been developed and then applied onto several case studies and parametric studies. The main findings are summarised below by answering the proposed research questions and sub-questions from Chapter 3.

1. What are the aeroelastic effects of propeller/s on a catilever wing? If a propeller is flexibly attached to the wing, two extra degrees of freedom are to be added in the aeroelastic analyses, namely propeller pitch and propeller yaw. These degrees of freedom are translated into a backward whirl mode and a forward whirl mode if the propeller is set to rotate. The propeller whirl modes also couple with the wing modes resulting in coupled propeller-wing modes.

The influence of installing a propeller on the wing is threefold: first, the added propeller mass changes the wing mass and inertial properties; second, a rotating propeller induces gyroscopic effects that change the wing natural vibration frequencies; and third, propeller aerodynamic forces and moments are additional sources of excitation loads on the flexible wing.

(a) **How does propeller gyroscopic effects influence the aeroelastic behaviour of the wing?** Gyroscopic effects exist because the propeller pivots due to low nacelle stiffness and the propeller CG is positioned in front of the pitch/yaw pivot point (towards the wing's leading edge). The influence of gyroscopic effects on the wing are twofold:

- First, gyroscopic effects further couple the propeller whirl modes with the wing modes: propeller yaw is not only coupled with propeller pitch but also with wing twist. When the propeller is set to rotate, increasing the propeller rotational speed increases the forward whirl mode frequency and decreases the backward whirl mode frequency. In turn, the natural vibrations of the wing are altered so as to avoid crossing with the whirl mode frequencies. If the whirl mode frequencies are close to the frequencies of the wing modes that go unstable, the instability of the propeller-wing system may be altered.

  In the models analysed in present work, the forward whirl mode interacts with the wing modes and the (coupled) forward whirl mode goes unstable; the instability is driven by wing aerodynamics alone. On the other hand, the backward whirl mode also interacts with the wing modes and

the (coupled) backward whirl mode goes unstable; the instability is driven unstable by both wing and propeller aerodynamics.

- Second, gyroscopic motions immerse the propeller blades in a non-uniform flow field. As a result, propeller in-plane forces and moments develop.

(b) **What is the influence of propeller aerodynamics?** Ignoring the propeller-wing aerodynamic interference effects, propeller aerodynamics may be represented by a vertical and a horizontal force acting on the propeller hub, a moment about the propeller pitch axis and a moment about the propeller yaw axis.

In the propeller-wing models analysed in present work, propeller aerodynamics is partially responsible for driving the backward whirl mode unstable. If propeller aerodynamics is excluded from the aeroelastic calculations, less conservative backward whirl flutter speeds are predicted. Since the critical speeds of present propeller-wing models are driven by either wing modes or forward whirl modes, propeller aerodynamics barely influence the critical speeds. In general, propeller aerodynamics has a stabilising effect on the whirl modes when wing aerodynamics is also included in the calculations. In some cases, it may drive the whirl modes divergent after flutter onset.

2. What are the effects of a cantilever flexible wing on propeller whirl flutter?

(a) **How does wing flexibility influence propeller whirl flutter?** As the wing undergoes heaving and pitching motions, it carries the propeller with it. Consequently, the propeller experiences additional inertial and gyroscopic effects. Moreover, the blades perceive modified effective pitch and yaw angles — this alters the propeller aerodynamic forces and moments.

In the propeller-wing models analysed, wing flexibility stabilises the backward whirl mode. However, forward whirl mode is triggered and dominates the critical speed. This contrasts with the isolated propeller (propeller flexibly attached to a rigid wing) where the forward whirl mode is always stable.

Wing flexibility introduces structural asymmetric characteristics on the propeller whirl mode behaviour; the coupled pitch mode (backward whirl) has lower stiffness than the coupled yaw mode (forward whirl). Hence, the mode shapes of the whirl modes describe an elliptical path despite the propeller having symmetric structural characteristics; changing nacelle stiffness/structural damping in pitch has different effects than changing nacelle stiffness/structural damping in yaw.

(b) **What is the influence of wing aerodynamics?** Wing aerodynamics is responsible for wing flutter. In the propeller-wing models analysed, wing aerodynamics also drives the forward whirl mode unstable and stabilises the backward whirl mode.

3. What are the aeroelastic effects of placing a propeller on the wing tip?

(a) **How does the spanwise location of the propeller influence wing/whirl flutter?** As the propeller is moved from an inboard position to the wing tip, there is further coupling between the propeller whirl modes and the wing modes.

In the wingtip-mounted propeller wing model, the wing modes no longer go unstable within the velocity interval analysed (0-350 m/s). The critical speed is determined by the forward whirl mode. The critical speed of the baseline propeller-wing model is lower than that of the wingtip-mounted propeller wing model; in the former case, the critical speed is driven by a wing aerodynamic lag state.

(b) **What are the effects of the main propeller-wing structural design parameters on wing/whirl flutter stability?** The propeller-wing design parameters analysed are:

- Nacelle stiffness: changing nacelle stiffness in pitch has different effects than changing nacelle stiffness in yaw. If the average nacelle stiffness is increased/decreased, having higher stiffness in pitch than in yaw is more stabilising until certain limiting conditions determined the stability of other propeller-wing modes. When the nacelle is very stiff in pitch and yaw, there is less interaction between the propeller whirl modes and the lower wing modes. Therefore, the mode that goes unstable becomes the wing mode that also goes unstable when the propeller is non-rotating and rigidly attached to the wing.
- Nacelle structural damping: small changes in the nacelle structural damping barely influences the critical speed. For very large values of average structural damping, higher structural damping in pitch is the most stabilizing. With very high structural damping in yaw, the forward whirl mode is damped and the backward whirl mode goes unstable.

- Propeller mass: higher propeller mass, namely, higher motor-nacelle mass results in higher propeller-wing inertia parameters. Hence, the system goes unstable at higher airspeeds. The affected inertia parameters do not include the propeller mass moment of inertia about the axis of rotation, I_Ω, which in present work, only depends on the rotor mass and the rotor radius.
- Propeller pivoting length: changes in the pivoting length may be achieved by shifting the propeller CG or/and the propeller pivot point. These changes result in changes in the propeller-wing inertia parameters (except I_Ω). Higher inertia parameter values lead to higher critical speeds, whilst lower inertia parameters lead to lower critical speeds.
- Propeller mass moment of inertia about the axis of rotation, I_Ω: an increase in the rotor mass increases I_Ω; it also increases the rest of the propeller-wing inertia parameters because the overall propeller mass is increased. Increasing I_Ω is destabilising due to higher gyroscopic couplings, but increasing the rest of the inertia parameters is stabilising. Increasing I_Ω, the critical mode (forward whirl mode) is slightly stabilised because of the effects of increasing the other inertia parameters are higher.
- Propeller advance ratio: in a fixed-pitch windmilling propeller, the propeller advance ratio is determined by the collective pitch angle, here, represented by the blade angle at the three-quarter-radius $\beta_{0.75R}$. The advance ratio increases with $\beta_{0.75R}$. Increasing $\beta_{0.75R}$ barely changes the critical speed. At $\beta_{0.75R} > 73°$ the critical mode switches from the forward whirl mode to the backward whirl mode.

The aeroelastic behaviour of a wing with flexibly mounted propeller/s may be very different from that of a wing with rigidly mounted propeller/s. Reasons lie in the interaction between the additional whirl modes and the wing modes due to gyroscopic coupling. Whereas propeller and wing aerodynamics may drive the backward whirl mode unstable, wing aerodynamics alone may drive the forward whirl mode unstable.

12.2. Recommendations for Future Work

As mentioned, further quantitative validation/verification of wing flutter predictions using the propeller-wing model developed in present work is still necessary to gain higher confidence in the predicted results.

Present work may be extended by relaxing some of the assumptions taken when deriving the aeroelastic models. These are:

- Present analyses have focused on fixed-pitch propellers. Constant speed propellers are also commonly used in propeller driven aircraft and should be further addressed in future analyses.
- Present results are restricted to propellers operating in windmilling conditions. It is recommended to investigate propeller whirl flutter in thrusting conditions. As first approach, thrust effects may be included by employing the aerodynamic derivatives of a thrusting propeller.
- The propeller model may be modified to include blade flexibility and blade inertia effects.
- The wing model may be extended to account for wing sweep, compressibility effects, and wing in-plane motions.
- In the case of wingtip-mounted propeller-wing configurations, the interaction with wing tip vortices is non-negligible. Future work should explore the relevance of the aerodynamic interference effects on propeller whirl flutter.

Other recommendations for future work are:

- Present work deals with stability of propeller-wing systems. Future work may explore the response of propeller-wing systems to random turbulence.
- Explore other analytical and numerical methods to predict propeller aerodynamic derivatives in thrusting conditions.
- Carry out experimental campaigns for verification of the theoretical methods.
- Investigate whirl flutter on propeller-wing models in pusher configurations.
- Analyse the influence of some structural and aerodynamic nonlinear effects on propeller-wing whirl flutter.

IV

APPENDICES

A

Gyroscopic Motion

The nature of gyroscopic motion is explained in Butikov [13] and MIT-OpenCourseWare [66].

Consider a pivoted rod with a solid disk attached to its free end as illustrated in Figure A.1. The rod is assumed to be rigid and massless so the centre of gravity of the system is located away from the pivot point. When released from a horizontal position parallel to the ground, the rod will fall and turn about the pivot point because of the action of gravity. Now, if the same rod is released again but with the disk rotating about its horizontal axis, the rod-disk system will remain in its horizontal position and the centre of mass of the system will follow a circular motion about the vertical axis that passes through the pivot point. This motion is called precession and the system that is carrying out this motion is called gyroscope.

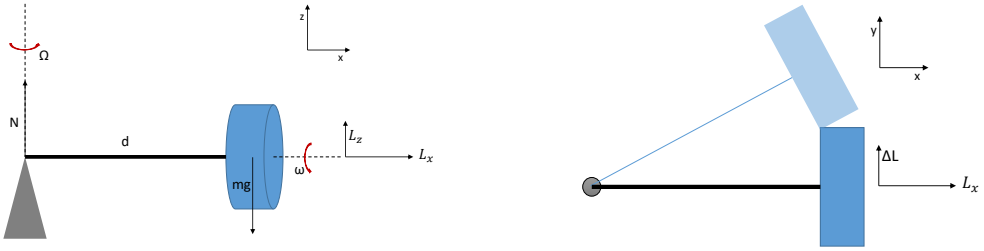

(a) Side view

(b) Top view

Figure A.1: Schematics of the gyroscope

The total angular momentum of the system is given by the spinning motion of the disk, $\mathbf{L}_{\text{spin}}$, and the translational motion of the centre of gravity about the vertical axis through the pivot point, $\mathbf{L}_{\text{trans}}$.

$$\begin{aligned} \mathbf{L}_{\text{spin}} &= I_1\omega\hat{i} + I_2\Omega\hat{k} \\ \mathbf{L}_{\text{trans}} &= m\Omega d^2\hat{k} \\ \mathbf{L} &= \mathbf{L}_{\text{spin}} + \mathbf{L}_{\text{trans}} \\ &= I_1\omega\hat{i} + (I_2\Omega + m\Omega d^2)\hat{k} \\ &= L_x\hat{i} + L_z\hat{k} \end{aligned} \tag{A.1}$$

where I_1 and I_2 are the moment of inertia about the axis perpendicular and parallel to the disk plane, respectively; ω is the spinning angular velocity, Ω is the precessional angular velocity, m is the mass of the disk, and d is the length of the rod.

In the presence of gravity the weight of the disk, mg, induces a reaction force, N, at the pivot point. This pair of forces creates a torque whose magnitude and direction is:

$$\tau = mgd\,\hat{j} \tag{A.2}$$

Assuming that the total angular momentum is much bigger than the torque (also $\omega >> \Omega$), the torque only changes the direction of the total angular momentum but not its magnitude. This means that the $\hat{k}$-component of the total angular momentum is constant and the $\hat{i}$-component of the total angular momentum rotates about the pivot point in circular motion.

$$\Delta\mathbf{L} = \tau\Delta t \tag{A.3}$$

From kinematics (see Figure A.2):

$$\|\frac{d\mathbf{L}_x}{dt}\| = L_x \cdot \frac{d\theta}{dt} = L_x\Omega \tag{A.4}$$

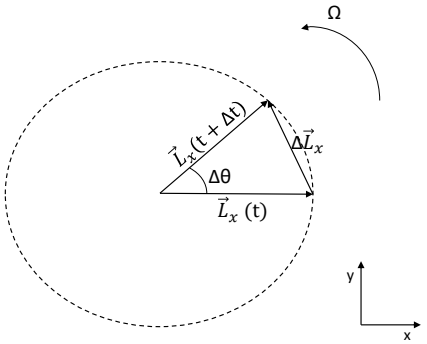

Figure A.2: Rotation of the L_x vector

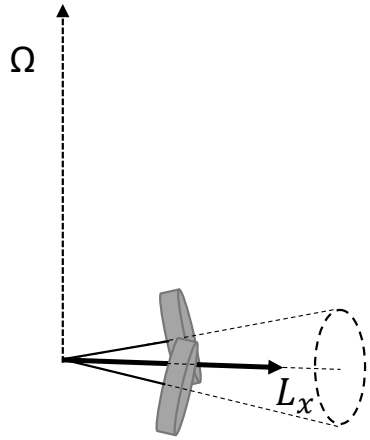

Figure A.3: Nutation of the gyroscope when $\Omega = 0$

From Equation A.1-Equation A.4, the precessional angular velocity Ω is:

$$\Omega = \frac{mgd}{I_1\omega} \tag{A.5}$$

In practice, when the gyroscope is released with a spinning disk the spin axis bounces up and down as it precesses. This motion is called nutation and it is caused by the deviation of the total angular momentum vector from the spin axis. Friction causes these bouncing movements to decrease in amplitude until steady uniform precession is achieved. Ignoring precessional motions, nutation would consist on a circular motion of the spin axis about the $\mathbf{L}_x$ direction as illustrated in Figure A.3.

B

Propeller Aerodynamic Derivatives

For a thrusting propeller with pitching and yawing motions the total forces and moments acting on the propeller are: thrust F_X, torque M_X, vertical side force F_Z, horizontal side force F_Y, pitching moment M_Y, and yawing moment M_Z.

The side forces and moments can be represented by sixteen propeller aerodynamic derivatives as given by the expressions in Equation (4.25). Considering the kinematic schematic of Figure 6.1 the following relations are found:

$$\begin{aligned} C_{Z_\psi} &= C_{Y_\theta} & C_{Z_r} &= C_{Y_q} \\ C_{m_\psi} &= -C_{n_\theta} & C_{m_r} &= -C_{n_q} \\ C_{Y_\psi} &= -C_{Z_\theta} & C_{Y_r} &= -C_{Z_q} \\ C_{n_\psi} &= C_{m_\theta} & C_{n_r} &= C_{m_q} \end{aligned} \tag{4.27}$$

Such relations are only valid when assuming no aerodynamic interference between the propeller and adjacent surfaces [7].

The change in signs of the derivatives can be reasoned by the illustrations in Figure B.1-Figure B.4. By definition, pitch and yaw angles rotate in the opposite direction. Therefore, when two analogous propeller aerodynamic derivatives follow the opposite direction, they must have equal signs (Figure B.1 and Figure B.3); whereas when two analogous propeller aerodynamic derivatives follow the same direction, they must have opposite signs (Figure B.2 and Figure B.4).

" $\odot$ " represents a vector that goes out of the plane of the page and " $\otimes$ " represents a vector that goes into the plane of the page.

Figure B.1: $C_{m_\theta} = C_{n_\psi}$ and $C_{m_q} = C_{n_r}$.

Figure B.2: $C_{m_\psi} = -C_{n_\theta}$ and $C_{m_r} = -C_{n_q}$.

Figure B.3: $C_{Z_\psi} = C_{Y_\theta}$ and $C_{Z_r} = C_{Y_q}$.

Figure B.4: $C_{Y_\psi} = -C_{Z_\theta}$ and $C_{Y_r} = -C_{Z_q}$.

C

Propeller-wing Aeroelastic State-Space System: with Wagner's Method

This section presents the derivation of the aeroelastic equations of motion of the propeller-flexible-wing system in a state-space form. The wing structural model will have two beam elements and the propeller is located on the second node. Extrapolation to more than two beam elements and the addition of more propellers follows systematically from the procedure explained below. Also, this example implements the aerodynamic model of the wing using Wagner's method. Implementation with the Leishman-Nguyen's method is analogous and it is described in Appendix D.

The unknowns of the system are grouped into the vectors $\mathbf{q_W}$, $\mathbf{q_P}$, and $\mathbf{w}$.

The global displacement vector for a wing composed of two beam elements is expressed as

$$\mathbf{q_W} = \begin{bmatrix} h_1 & \phi_1 & \alpha_1 & h_2 & \phi_2 & \alpha_2 & h_3 & \phi_3 & \alpha_3 \end{bmatrix}^T \tag{C.1}$$

where the subscript is the node number to which the variable is associated with.

The degrees of freedom of the propeller are grouped in

$$\mathbf{q_P} = \begin{bmatrix} \theta & \psi \end{bmatrix}^T \tag{C.2}$$

And the global vector of aerodynamic states from Wagner's method are represented by

$$\mathbf{w_g} = \begin{bmatrix} w_1^{(1)} & w_2^{(1)} & w_3^{(1)} & w_4^{(1)} & w_1^{(2)} & w_2^{(2)} & w_3^{(2)} & w_4^{(2)} & w_1^{(3)} & w_2^{(3)} & w_3^{(3)} & w_4^{(3)} \end{bmatrix}^T \tag{C.3}$$

where the superscript within parenthesis is the node number to which the variable is associated with. Note that there are four aerodynamic states per node.

C.1. Propeller aeroelastic Equations

The structural matrices are as given in Equation (8.14) with the difference that the vector $\mathbf{q_{WP}}$ is substituted by $\mathbf{q_W}$. Because of this, the matrices $\mathbf{B_s}$ and $\mathbf{D_s}$ need to be restructured accordingly depending on which node the propeller is located. In this example, the propeller is located on the second node of the beam model. The matrices $\mathbf{A_s}$, $\mathbf{C_s}$, and $\mathbf{E_s}$ are as defined in Equation (8.15), Equation (8.17), and Equation (8.19), respectively.

$$\mathbf{A_s}\ddot{\mathbf{q}}_\mathbf{P} + \mathbf{B_{s,g}}\ddot{\mathbf{q}}_\mathbf{W} + \mathbf{C_s}\dot{\mathbf{q}}_\mathbf{P} + \mathbf{D_{s,g}}\dot{\mathbf{q}}_\mathbf{W} + \mathbf{E_s}\mathbf{q_P} = \begin{bmatrix} Q_\theta \\ Q_\psi \end{bmatrix} \tag{C.4}$$

$$\mathbf{B_{s,g}} = \begin{bmatrix} \mathbf{0_{2x3}} & \mathbf{B_{s,e}} & \mathbf{0_{2x3}} \end{bmatrix} \tag{C.5}$$

$$\mathbf{B_{s,e}} = \begin{bmatrix} S_{\theta,P} & 0 & I_{\theta\alpha,P} \\ 0 & 0 & 0 \end{bmatrix} \tag{C.6}$$

$$\mathbf{D_{s,g}} = \begin{bmatrix} \mathbf{0_{2x3}} & \mathbf{D_{s,e}} & \mathbf{0_{2x3}} \end{bmatrix} \tag{C.7}$$

$$\mathbf{D_{s,e}} = \begin{bmatrix} 0 & 0 & 0 \\ 0 & 0 & -I_\Omega \Omega \end{bmatrix} \tag{C.8}$$

Similarly, the aerodynamic matrices are as given in Equation (8.27) with the difference that the vector $\mathbf{q_{WP}}$ is substituted by $\mathbf{q_W}$. Because of this, the matrices $\mathbf{B_a}$, $\mathbf{D_a}$, and $\mathbf{F_a}$ need to be restructured accordingly depending on which node the propeller is located. In this example, the propeller is located on the second node of the beam model. The matrices $\mathbf{A_a}$, $\mathbf{C_a}$, and $\mathbf{E_a}$ are as defined in Equation (8.28), Equation (8.30), and Equation (8.32), respectively.

$$\begin{bmatrix} Q_{\theta,P} \\ Q_{\psi,P} \end{bmatrix} = \mathbf{A_a}\ddot{\mathbf{q}}_\mathbf{P} + \mathbf{B_{ag}}\ddot{\mathbf{q}}_\mathbf{W} + \mathbf{C_a}\dot{\mathbf{q}}_\mathbf{P} + \mathbf{D_{ag}}\dot{\mathbf{q}}_\mathbf{W} + \mathbf{E_a}\mathbf{q_P} + \mathbf{F_{ag}}\mathbf{q_W} \tag{C.9}$$

$$\mathbf{B_{a,g}} = \begin{bmatrix} \mathbf{0_{2x3}} & \mathbf{B_{a,e}} & \mathbf{0_{2x3}} \end{bmatrix} \tag{C.10}$$

$$\mathbf{B_{a,e}} = \begin{bmatrix} k_2 C_{mq} \frac{R}{V} \frac{1}{V} + e_\theta k_1 C_{Zq} \frac{R}{V} \frac{1}{V} & 0 & k_2 C_{mq} \frac{R}{V} \frac{e_\alpha}{V} + e_\theta k_1 C_{Zq} \frac{R}{V} \frac{e_\alpha}{V} \\ k_2 C_{nq} \frac{R}{V} \frac{1}{V} - e_\psi k_1 C_{Yq} \frac{R}{V} \frac{1}{V} & 0 & k_2 C_{nq} \frac{R}{V} \frac{e_\alpha}{V} - e_\psi k_1 C_{Yq} \frac{R}{V} \frac{e_\alpha}{V} \end{bmatrix} \tag{C.11}$$

$$\mathbf{D_{a,g}} = \begin{bmatrix} \mathbf{0_{2x3}} & \mathbf{D_{a,e}} & \mathbf{0_{2x3}} \end{bmatrix} \tag{C.12}$$

$$\mathbf{D_{a,e}} = \begin{bmatrix} k_2 C_{m\theta} \frac{1}{V} + e_\theta k_1 C_{Z\theta} \frac{1}{V} & 0 & k_2 C_{m\theta} \frac{e_\alpha}{V} + k_2 C_{mq} \frac{R}{V} + e_\theta k_1 C_{Z\theta} \frac{e_\alpha}{V} + e_\theta k_1 C_{Zq} \frac{R}{V} \\ k_2 C_{n\theta} \frac{1}{V} - e_\psi k_1 C_{Y\theta} \frac{1}{V} & 0 & k_2 C_{n\theta} \frac{e_\alpha}{V} + k_2 C_{nq} \frac{R}{V} - e_\psi k_1 C_{Y\theta} \frac{e_\alpha}{V} - e_\psi k_1 C_{Yq} \frac{R}{V} \end{bmatrix} \tag{C.13}$$

$$\mathbf{F_{a,g}} = \begin{bmatrix} \mathbf{0_{2x3}} & \mathbf{F_{ae}} & \mathbf{0_{2x3}} \end{bmatrix} \tag{C.14}$$

$$\mathbf{F_{ae}} = \begin{bmatrix} 0 & 0 & k_2 C_{m\theta} + e_\theta k_1 C_{Z\theta} \\ 0 & 0 & k_2 C_{n\theta} - e_\psi k_1 C_{Y\theta} \end{bmatrix} \tag{C.15}$$

Final expression

The final expression in matrix form can be expressed as

$$\Big(\mathbf{A_s} - \mathbf{A_a}\Big)\ddot{\mathbf{q}}_\mathbf{P} + \Big(\mathbf{B_{sg}} - \mathbf{B_{ag}}\Big)\ddot{\mathbf{q}}_\mathbf{W} + \Big(\mathbf{C_s} - \mathbf{C_a}\Big)\dot{\mathbf{q}}_\mathbf{P} + \Big(\mathbf{D_{sg}} - \mathbf{D_{ag}}\Big)\dot{\mathbf{q}}_\mathbf{W} + \Big(\mathbf{E_s} - \mathbf{E_a}\Big)\mathbf{q_P} + \Big(-\mathbf{F_{ag}}\Big)\mathbf{q_W} = \mathbf{0} \tag{C.16}$$

C.2. Wing aeroelastic Equations

This section shows the assembly of the global equations of motion of the wing structural model employing two beam elements (three nodes) with one propeller mounted on the second node. The equations of motion are given by Equation (8.46). To solve this set of equations, the vector $\mathbf{q_{WP}}$ is substituted by $\mathbf{q_W}$ and the matrices $\mathbf{F_s}$, $\mathbf{G_s}$, and $\mathbf{H_s}$ need to be restructured into their global counterparts.

$$\mathbf{M_{s,g}}\ddot{\mathbf{q}}_\mathbf{W} + \mathbf{C_{s,g}}\dot{\mathbf{q}}_\mathbf{W} + \mathbf{K_{s,g}}\mathbf{q_W} + \mathbf{F_s}\ddot{\mathbf{q}}_\mathbf{P} + \mathbf{G_s}\ddot{\mathbf{q}}_\mathbf{WP} + \mathbf{H_s}\dot{\mathbf{q}}_\mathbf{P} = \mathbf{Q_W} + \mathbf{Q_P} \tag{8.46}$$

C.2.1. Structural matrices of the beam model

The global stiffness $\mathbf{K_{s,g}}$ and mass matrix $\mathbf{M_{s,g}}$ for a wing composed of two beam elements have the form

$$\mathbf{K_{s,g}} = \begin{bmatrix} \frac{12EI_1}{l_1^3} & \frac{6EI_1}{l_1^2} & 0 & -\frac{12EI_1}{l_1^3} & \frac{6EI_1}{l_1^2} & 0 & 0 & 0 & 0 \\ \frac{6EI_1}{l_1^2} & \frac{4EI_1}{l_1} & 0 & -\frac{6EI_1}{l_1^2} & \frac{2EI_1}{l_1} & 0 & 0 & 0 & 0 \\ 0 & 0 & \frac{GJ_1}{l_1} & 0 & 0 & -\frac{GJ_1}{l_1} & 0 & 0 & 0 \\ -\frac{12EI_1}{l_1^3} & -\frac{6EI_1}{l_1^2} & 0 & \frac{12EI_1}{l_1^3}+\frac{12EI_2}{l_2^3} & -\frac{6EI_1}{l_1^2}+\frac{6EI_2}{l_2^2} & 0 & -\frac{12EI_2}{l_2^3} & \frac{6EI_2}{l_2^2} & 0 \\ \frac{6EI_1}{l_1^2} & \frac{2EI_1}{l_1} & 0 & -\frac{6EI_1}{l_1^2}+\frac{6EI_2}{l_2^2} & \frac{4EI_1}{l_1}+\frac{4EI_2}{l_2} & 0 & -\frac{6EI_2}{l_2^2} & \frac{2EI_2}{l_2} & 0 \\ 0 & 0 & -\frac{GJ_1}{l_1} & 0 & 0 & \frac{GJ_1}{l_1}+\frac{GJ_2}{l_2} & 0 & 0 & -\frac{GJ_2}{l_2} \\ 0 & 0 & 0 & -\frac{12EI_2}{l_2^3} & -\frac{6EI_2}{l_2^2} & 0 & \frac{12EI_2}{l_2^3} & -\frac{6EI_2}{l_2^2} & 0 \\ 0 & 0 & 0 & \frac{6EI_2}{l_2^2} & \frac{2EI_2}{l_2} & 0 & -\frac{6EI_2}{l_2^2} & \frac{4EI_2}{l_2} & 0 \\ 0 & 0 & 0 & 0 & 0 & -\frac{GJ_2}{l_2} & 0 & 0 & \frac{GJ_2}{l_2} \end{bmatrix} \tag{C.17}$$

$$
\mathbf{M_{s,g}} = \left[\begin{array}{cccccc|cccccc}
\frac{13}{35} l_1 m_1 & \frac{11}{210} l_1^2 m_1 & \frac{7}{20} l_1 m_1 x_{a_1} b_1 & \frac{9}{70} l_1 m_1 & -\frac{13}{420} l_1^2 m_1 & \frac{3}{20} l_1 m_1 x_{a_1} b_1 & 0 & 0 & 0 & 0 & 0 & 0 \\
\frac{11}{210} l_1^2 m_1 & \frac{1}{105} l_1^3 m_1 & \frac{1}{20} l_1^2 m_1 x_{a_1} b_1 & \frac{13}{420} l_1^2 m_1 & -\frac{1}{140} l_1^3 m_1 & \frac{1}{30} l_1^2 m_1 x_{a_1} b_1 & 0 & 0 & 0 & 0 & 0 & 0 \\
\frac{7}{20} l_1 m_1 x_{a_1} b_1 & \frac{1}{20} l_1^2 m_1 x_{a_1} b_1 & \frac{\rho I_{p_1} l_1}{3} & \frac{3}{20} l_1 m_1 x_{a_1} b_1 & -\frac{1}{30} l_1^2 m_1 x_{a_1} b_1 & \frac{\rho I_{p_1} l_1}{6} & 0 & 0 & 0 & 0 & 0 & 0 \\
\frac{9}{70} l_1 m_1 & \frac{13}{420} l_1^2 m_1 & \frac{3}{20} l_1 m_1 x_{a_1} b_1 & \frac{13}{35} l_1 m_1 + \frac{13}{35} l_2 m_2 & -\frac{11}{210} l_1^2 m_1 + \frac{11}{210} l_2^2 m_2 & \frac{7}{20} l_1 m_1 x_{a_1} b_1 + \frac{7}{20} l_2 m_2 x_{a_2} b_2 & \frac{9}{70} l_2 m_2 & -\frac{13}{420} l_2^2 m_2 & \frac{3}{20} l_2 m_2 x_{a_2} b_2 \\
-\frac{13}{420} l_1^2 m_1 & -\frac{1}{140} l_1^3 m_1 & -\frac{1}{30} l_1^2 m_1 x_{a_1} b_1 & -\frac{11}{210} l_1^2 m_1 + \frac{11}{210} l_2^2 m_2 & \frac{1}{105} l_1^3 m_1 + \frac{1}{105} l_2^3 m_2 & -\frac{1}{20} l_1^2 m_1 x_{a_1} b_1 + \frac{1}{20} l_2^2 m_2 x_{a_2} b_2 & \frac{13}{420} l_1^2 m_1 & -\frac{1}{140} l_2^3 m_2 & \frac{1}{30} l_2^2 m_2 x_{a_2} b_2 \\
\frac{3}{20} l_1 m_1 x_{a_1} b_1 & \frac{1}{30} l_1^2 m_1 x_{a_1} b_1 & \frac{\rho I_{p_1} l_1}{6} & \frac{7}{20} l_1 m_1 x_{a_1} b_1 + \frac{7}{20} l_2 m_2 x_{a_2} b_2 & -\frac{1}{20} l_1^2 m_1 x_{a_1} b_1 + \frac{1}{20} l_2^2 m_2 x_{a_2} b_2 & \frac{\rho I_{p_1} l_1}{3} + \frac{\rho I_{p_2} l_2}{3} & \frac{3}{20} l_2 m_2 x_{a_2} b_2 & -\frac{1}{30} l_2^2 m_2 x_{a_2} b_2 & \frac{\rho I_{p_2} l_2}{6} \\
0 & 0 & 0 & \frac{9}{70} l_2 m_2 & \frac{13}{420} l_2^2 m_2 & \frac{3}{20} l_2 m_2 x_{a_2} b_2 & \frac{13}{35} l_2 m_2 & -\frac{11}{210} l_2^2 m_2 & \frac{7}{20} l_2 m_2 x_{a_2} b_2 \\
0 & 0 & 0 & -\frac{13}{420} l_2^2 m_2 & -\frac{1}{140} l_2^3 m_2 & -\frac{1}{30} l_2^2 m_2 x_{a_2} b_2 & -\frac{11}{210} l_2^2 m_2 & \frac{1}{105} l_2^3 m_2 & -\frac{1}{20} l_2^2 m_2 x_{a_2} b_2 \\
0 & 0 & 0 & \frac{3}{20} l_2 m_2 x_{a_2} b_2 & \frac{1}{30} l_2^2 m_2 x_{a_2} b_2 & \frac{\rho I_{p_2} l_2}{6} & \frac{7}{20} l_2 m_2 x_{a_2} b_2 & -\frac{1}{20} l_2^2 m_2 x_{a_2} b_2 & \frac{\rho I_{p_2} l_2}{3}
\end{array}\right] \tag{C.18}
$$

C.2.2. Coupling structural Wing Matrices

The matrices $\mathbf{F_{s,g}}$, $\mathbf{G_{s,g}}$, and $\mathbf{H_{s,g}}$ are introduced due to the presence of a rotating propeller.

$$\mathbf{F_{s,g}} = \begin{bmatrix} \mathbf{0_{3x2}} \\ \mathbf{F_{s,e}} \\ \mathbf{0_{3x2}} \end{bmatrix} \tag{C.19}$$

$$\mathbf{F_{s,e}} = \begin{bmatrix} S_{\theta,P} & 0 \\ 0 & 0 \\ I_{\theta\alpha,P} & 0 \end{bmatrix} \tag{C.20}$$

$$\mathbf{G_{s,g}} = \begin{bmatrix} \mathbf{0_{3x3}} & \mathbf{0_{3x3}} & \mathbf{0_{3x3}} \\ \mathbf{0_{3x3}} & \mathbf{G_{s,e}} & \mathbf{0_{3x3}} \\ \mathbf{0_{3x3}} & \mathbf{0_{3x3}} & \mathbf{0_{3x3}} \end{bmatrix} \tag{C.21}$$

$$\mathbf{G_{s,e}} = \begin{bmatrix} m_P & 0 & S_{\alpha,P} \\ 0 & 0 & 0 \\ S_{\alpha,P} & 0 & I_{\alpha,P} \end{bmatrix} \tag{C.22}$$

$$\mathbf{H_{s,g}} = \begin{bmatrix} \mathbf{0_{3x2}} \\ \mathbf{H_{s,e}} \\ \mathbf{0_{3x2}} \end{bmatrix} \tag{C.23}$$

$$\mathbf{H_{s,e}} = \begin{bmatrix} 0 & 0 \\ 0 & 0 \\ 0 & I_\Omega\Omega \end{bmatrix} \tag{C.24}$$

C.2.3. Propeller Effects on the Wing in global Matrix Form

The propeller effects on the wing are accounted for by the propeller aerodynamic loads acting on the direction of wing vertical displacement and wing twist. These effects are represented by $\mathbf{Q_P}$.

$$\mathbf{Q_P} = \begin{bmatrix} 0 \\ 0 \\ 0 \\ Q_{h,P} \\ 0 \\ Q_{\alpha,P} \\ 0 \\ 0 \\ 0 \end{bmatrix} = \mathbf{P_{1,g}}\ddot{\mathbf{q}}_\mathbf{P} + \mathbf{P_{2,g}}\ddot{\mathbf{q}}_\mathbf{W} + \mathbf{P_{3,g}}\dot{\mathbf{q}}_\mathbf{P} + \mathbf{P_{4,g}}\dot{\mathbf{q}}_\mathbf{W} + \mathbf{P_{5,g}}\mathbf{q_P} + \mathbf{P_{6,g}}\mathbf{q_W} \tag{C.25}$$

where the matrices $\mathbf{P_{1,g}}$, $\mathbf{P_{2,g}}$, $\mathbf{P_{3,g}}$, $\mathbf{P_{4,g}}$, $\mathbf{P_{5,g}}$, and $\mathbf{P_{6,g}}$ are restructured from the matrices $\mathbf{P_1}$, $\mathbf{P_2}$, $\mathbf{P_3}$, $\mathbf{P_4}$, $\mathbf{P_5}$, and $\mathbf{P_6}$ to account for the change from the vector $\mathbf{q_{WP}}$ into $\mathbf{q_W}$ and the addition of the force that act on the bending rotation of the beam node, which is null in this case. If the propeller imposed a torque on the wing, the value of this torque should be introduced here.

$$\mathbf{P_{1,g}} = \begin{bmatrix} \mathbf{0_{3x2}} \\ \mathbf{P_{1,e}} \\ \mathbf{0_{3x2}} \end{bmatrix} \tag{C.26}$$

$$\mathbf{P_{1,e}} = \begin{bmatrix} k_1 C_{Zq}\frac{R}{V}\frac{e_\theta}{V} & k_1 C_{Zr}\frac{R}{V}\frac{e_\psi}{V} \\ 0 & 0 \\ k_2 C_{mq}\frac{R}{V}\frac{e_\theta}{V} + e_\alpha k_1 C_{Zq}\frac{R}{V}\frac{e_\theta}{V} & k_2 C_{mr}\frac{R}{V}\frac{e_\psi}{V} + e_\alpha k_1 C_{Zr}\frac{R}{V}\frac{e_\psi}{V} \end{bmatrix} \tag{C.27}$$

$$\mathbf{P_{2,g}} = \begin{bmatrix} \mathbf{0_{3x3}} & \mathbf{0_{3x3}} & \mathbf{0_{3x3}} \\ \mathbf{0_{3x3}} & \mathbf{P_{1,e}} & \mathbf{0_{3x3}} \\ \mathbf{0_{3x3}} & \mathbf{0_{3x3}} & \mathbf{0_{3x3}} \end{bmatrix} \tag{C.28}$$

$$\mathbf{P_{2,e}} = \begin{bmatrix} k_1 C_{Zq} \frac{R}{V} \frac{1}{V} & 0 & k_1 C_{Zq} \frac{R}{V} \frac{e_\alpha}{V} \\ 0 & 0 & 0 \\ k_2 C_{mq} \frac{R}{V} \frac{1}{V} + e_\alpha k_1 C_{Zq} \frac{R}{V} \frac{1}{V} & 0 & k_2 C_{mq} \frac{R}{V} \frac{e_\alpha}{V} + e_\alpha k_1 C_{Zq} \frac{R}{V} \frac{e_\alpha}{V} \end{bmatrix} \tag{C.29}$$

$$\mathbf{P_{3,g}} = \begin{bmatrix} \mathbf{0_{3x2}} \\ \mathbf{P_{3,e}} \\ \mathbf{0_{3x2}} \end{bmatrix} \tag{C.30}$$

$$\mathbf{P_{3,e}} = \begin{bmatrix} k_1 C_{Z\theta} \frac{e_\theta}{V} + k_1 C_{Zq} \frac{R}{V} & k_1 C_{Z\psi} \frac{e_\psi}{V} + k_1 C_{Zr} \frac{R}{V} \\ 0 & 0 \\ k_2 C_{m\theta} \frac{e_\theta}{V} + k_2 C_{mq} \frac{R}{V} + e_\alpha k_1 C_{Z\theta} \frac{e_\theta}{V} + e_\alpha k_1 C_{Zq} \frac{R}{V} & k_2 C_{m\psi} \frac{e_\psi}{V} + k_2 C_{mr} \frac{R}{V} + e_\alpha k_1 C_{Z\psi} \frac{e_\psi}{V} + e_\alpha k_1 C_{Zr} \frac{R}{V} \end{bmatrix} \tag{C.31}$$

$$\mathbf{P_{4,g}} = \begin{bmatrix} \mathbf{0_{3x3}} & \mathbf{0_{3x3}} & \mathbf{0_{3x3}} \\ \mathbf{0_{3x3}} & \mathbf{P_{4,e}} & \mathbf{0_{3x3}} \\ \mathbf{0_{3x3}} & \mathbf{0_{3x3}} & \mathbf{0_{3x3}} \end{bmatrix} \tag{C.32}$$

$$\mathbf{P_{4,e}} = \begin{bmatrix} k_1 C_{Z\theta} \frac{1}{V} & 0 & k_1 C_{Z\theta} \frac{e_\alpha}{V} + k_1 C_{Zq} \frac{R}{V} \\ 0 & 0 & 0 \\ k_2 C_{m\theta} \frac{1}{V} + e_\alpha k_1 C_{Z\theta} \frac{1}{V} & 0 & k_2 C_{m\theta} \frac{e_\alpha}{V} + k_2 C_{mq} \frac{R}{V} + e_\alpha k_1 C_{Z\theta} \frac{e_\alpha}{V} + e_\alpha k_1 C_{Zq} \frac{R}{V} \end{bmatrix} \tag{C.33}$$

$$\mathbf{P_{5,g}} = \begin{bmatrix} \mathbf{0_{3x2}} \\ \mathbf{P_{5,e}} \\ \mathbf{0_{3x2}} \end{bmatrix} \tag{C.34}$$

$$\mathbf{P_{5,e}} = \begin{bmatrix} k_1 C_{Z\theta} & k_1 C_{Z\psi} \\ 0 & 0 \\ k_2 C_{m\theta} + e_\alpha k_1 C_{Z\theta} & k_2 C_{m\psi} + e_\alpha k_1 C_{Z\psi} \end{bmatrix} \tag{C.35}$$

$$\mathbf{P_{6,g}} = \begin{bmatrix} \mathbf{0_{3x3}} & \mathbf{0_{3x3}} & \mathbf{0_{3x3}} \\ \mathbf{0_{3x3}} & \mathbf{P_{6,e}} & \mathbf{0_{3x3}} \\ \mathbf{0_{3x3}} & \mathbf{0_{3x3}} & \mathbf{0_{3x3}} \end{bmatrix} \tag{C.36}$$

$$\mathbf{P_{6,e}} = \begin{bmatrix} 0 & 0 & k_1 C_{Z\theta} \\ 0 & 0 & 0 \\ 0 & 0 & k_2 C_{m\theta} + e_\alpha k_1 C_{Z\theta} \end{bmatrix} \tag{C.37}$$

where $k_1 = \frac{1}{2}\rho V^2 S'$, $k_2 = \rho V^2 S' R$, $S' = \pi R^2$ is the area swept by the propeller blades and R is the propeller radius.

C.2.4. Wing Aerodynamics in global Matrix Form

Wing aerodynamics are composed of lift and pitching moment acting on each node. These terms are represented by $\mathbf{Q_W}$.

$$\mathbf{Q_W} = \begin{bmatrix} Q^{(1)}_{h,P} \\ 0 \\ Q^{(1)}_{\alpha,P} \\ Q^{(2)}_{h,P} \\ 0 \\ Q^{(2)}_{\alpha,P} \\ Q^{(3)}_{h,P} \\ 0 \\ Q^{(3)}_{\alpha,P} \end{bmatrix} = \begin{bmatrix} -L^{(1)} \\ 0 \\ M^{(1)} \\ -L^{(2)} \\ 0 \\ M^{(2)} \\ -L^{(3)} \\ 0 \\ M^{(3)} \end{bmatrix} = \mathbf{M_{a,g}}\ddot{\mathbf{q}}_\mathbf{W} + \mathbf{C_{a,g}}\dot{\mathbf{q}}_\mathbf{W} + \mathbf{K_{a,g}}\mathbf{q_W} + \mathbf{W_{0,g}}\mathbf{w_g} + \mathbf{g_g}\dot{\phi}(t) \tag{C.38}$$

$$\dot{\mathbf{w}}_\mathbf{g} = \mathbf{W_{1,g}}\mathbf{q_W} + \mathbf{W_{2,g}}\mathbf{w_g}$$

The wing aerodynamic mass matrix is given by

$$\mathbf{M_{a,e}} = \begin{bmatrix} -\pi\rho b^2 & 0 & \pi\rho b^3 a \\ 0 & 0 & 0 \\ \pi\rho b^3 a & 0 & -\pi\rho b^4\left(\frac{1}{8} + a^2\right) \end{bmatrix} \tag{C.39}$$

$$\mathbf{M_{a,g}} = \begin{bmatrix} \mathbf{M^{(1)}_{a,e}} & \mathbf{0_{3x3}} & \mathbf{0_{3x3}} \\ \mathbf{0_{3x3}} & \mathbf{M^{(2)}_{a,e}} & \mathbf{0_{3x3}} \\ \mathbf{0_{3x3}} & \mathbf{0_{3x3}} & \mathbf{M^{(3)}_{a,e}} \end{bmatrix} \tag{C.40}$$

The wing aerodynamic damping matrix is given by

$$\mathbf{C_{a,e}} = \begin{bmatrix} -2\pi\rho bV\Phi(0) & 0 & -\pi\rho b^2 V - 2\pi\rho b^2 V\left(\frac{1}{2} - a\right)\Phi(0) \\ 0 & 0 & 0 \\ 2\pi\rho bV\Phi(0)b\left(a + \frac{1}{2}\right) & 0 & -\pi\rho b^3 V\left(\frac{1}{2} - a\right) + 2\pi\rho b^2 V\left(\frac{1}{2} - a\right)\Phi(0)b\left(a + \frac{1}{2}\right) \end{bmatrix} \tag{C.41}$$

$$\mathbf{C_{a,g}} = \begin{bmatrix} \mathbf{C^{(1)}_{a,e}} & \mathbf{0_{3x3}} & \mathbf{0_{3x3}} \\ \mathbf{0_{3x3}} & \mathbf{C^{(2)}_{a,e}} & \mathbf{0_{3x3}} \\ \mathbf{0_{3x3}} & \mathbf{0_{3x3}} & \mathbf{C^{(3)}_{a,e}} \end{bmatrix} \tag{C.42}$$

The wing aerodynamic stiffness matrix is given by

$$\mathbf{K_{a,e}} = \begin{bmatrix} -2\pi\rho bV\dot{\Phi}(0) & 0 & -2\pi\rho bV^2\Phi(0) - 2\pi\rho b^2 V\left(\frac{1}{2} - a\right)\dot{\Phi}(0) \\ 0 & 0 & 0 \\ 2\pi\rho bV\dot{\Phi}(0)b\left(a + \frac{1}{2}\right) & 0 & 2\pi\rho bV^2\Phi(0)b\left(a + \frac{1}{2}\right) + 2\pi\rho b^2 V\left(\frac{1}{2} - a\right)\dot{\Phi}(0)b\left(a + \frac{1}{2}\right) \end{bmatrix} \tag{C.43}$$

$$\mathbf{K_{a,g}} = \begin{bmatrix} \mathbf{K^{(1)}_{a,e}} & \mathbf{0_{3x3}} & \mathbf{0_{3x3}} \\ \mathbf{0_{3x3}} & \mathbf{K^{(2)}_{a,e}} & \mathbf{0_{3x3}} \\ \mathbf{0_{3x3}} & \mathbf{0_{3x3}} & \mathbf{K^{(3)}_{a,e}} \end{bmatrix} \tag{C.44}$$

The wing aerodynamic state influence matrix is given by $\mathbf{W_{0,e}} = 2\pi\rho bV\mathbf{W'_{0,e}}$, where $\mathbf{W'_{0,e}}$ is

$$\mathbf{W'_{0,e}} = \begin{bmatrix} \Psi_1\left(\epsilon_1\frac{V}{b}\right)^2 & \Psi_2\left(\epsilon_2\frac{V}{b}\right)^2 & -\Psi_1\epsilon_1\frac{V^2}{b}\left(1 - \epsilon_1\left(\frac{1}{2} - a\right)\right) & -\Psi_2\epsilon_2\frac{V^2}{b}\left(1 - \epsilon_2\left(\frac{1}{2} - a\right)\right) \\ 0 & 0 & 0 & 0 \\ -\Psi_1\left(\epsilon_1\frac{V}{b}\right)^2 b\left(a + \frac{1}{2}\right) & -\Psi_2\left(\epsilon_2\frac{V}{b}\right)^2 b\left(a + \frac{1}{2}\right) & \Psi_1\epsilon_1\frac{V^2}{b}\left(1 - \epsilon_1\left(\frac{1}{2} - a\right)\right)b\left(a + \frac{1}{2}\right) & \Psi_2\epsilon_2\frac{V^2}{b}\left(1 - \epsilon_2\left(\frac{1}{2} - a\right)\right)b\left(a + \frac{1}{2}\right) \end{bmatrix} \tag{C.45}$$

$$\mathbf{W_{0,g}} = \begin{bmatrix} \mathbf{W_{0,e}^{(1)}} & \mathbf{0_{3x4}} & \mathbf{0_{3x4}} \\ \mathbf{0_{3x4}} & \mathbf{W_{0,e}^{(2)}} & \mathbf{0_{3x4}} \\ \mathbf{0_{3x4}} & \mathbf{0_{3x4}} & \mathbf{W_{0,e}^{(3)}} \end{bmatrix} \tag{C.46}$$

The initial condition excitation vector is given by

$$\mathbf{g_e} = 2\pi\rho bV \left[h(0) + b\left(\frac{1}{2} - a\right)\alpha(0) \right] \begin{bmatrix} 1 \\ 0 \\ -b\left(a + \frac{1}{2}\right) \end{bmatrix} \tag{C.47}$$

$$\mathbf{g_g} = \begin{bmatrix} \mathbf{g_e}^{(1)} \\ \mathbf{g_e}^{(2)} \\ \mathbf{g_e}^{(3)} \end{bmatrix} \tag{C.48}$$

Finally, the aerodynamic state equation matrices are given by

$$\mathbf{W_{1,e}} = \begin{bmatrix} 1 & 0 & 0 \\ 1 & 0 & 0 \\ 0 & 0 & 1 \\ 0 & 0 & 1 \end{bmatrix} \tag{C.49}$$

$$\mathbf{W_{1,g}} = \begin{bmatrix} \mathbf{W_{1,e}^{(1)}} & \mathbf{0_{4x3}} & \mathbf{0_{4x3}} \\ \mathbf{0_{4x3}} & \mathbf{W_{1,e}^{(2)}} & \mathbf{0_{4x3}} \\ \mathbf{0_{4x3}} & \mathbf{0_{4x3}} & \mathbf{W_{1,e}^{(3)}} \end{bmatrix} \tag{C.50}$$

$$\mathbf{W_{2,e}} = \begin{bmatrix} -\frac{\epsilon_1 V}{b} & 0 & 0 & 0 \\ 0 & -\frac{\epsilon_2 V}{b} & 0 & 0 \\ 0 & 0 & -\frac{\epsilon_1 V}{b} & 0 \\ 0 & 0 & 0 & -\frac{\epsilon_2 V}{b} \end{bmatrix} \tag{C.51}$$

$$\mathbf{W_{2,g}} = \begin{bmatrix} \mathbf{W_{2,e}^{(1)}} & \mathbf{0_{4x4}} & \mathbf{0_{4x4}} \\ \mathbf{0_{4x4}} & \mathbf{W_{2,e}^{(2)}} & \mathbf{0_{4x4}} \\ \mathbf{0_{4x4}} & \mathbf{0_{4x4}} & \mathbf{W_{2,e}^{(3)}} \end{bmatrix} \tag{C.52}$$

Final expression

The final expression in matrix form can be expressed as

$$\begin{aligned} \mathbf{M_{s,g}}\ddot{\mathbf{q}}_\mathbf{W} + \mathbf{C_{s,g}}\dot{\mathbf{q}}_\mathbf{W} + \mathbf{K_{s,g}}\mathbf{q_W} + \mathbf{F_{s,g}}\ddot{\mathbf{q}}_\mathbf{P} + \mathbf{G_{s,g}}\ddot{\mathbf{q}}_\mathbf{W} + \mathbf{H_{s,g}}\dot{\mathbf{q}}_\mathbf{P} &= \mathbf{M_{a,g}}\ddot{\mathbf{q}}_\mathbf{W} + \mathbf{C_{a,g}}\dot{\mathbf{q}}_\mathbf{W} + \mathbf{K_{a,g}}\mathbf{q_W} + \mathbf{W_{0,g}}\mathbf{w_g} + \mathbf{g_g}\dot{\phi}(t) + \dots \\ &\quad + \mathbf{P_{1,g}}\ddot{\mathbf{q}}_\mathbf{P} + \mathbf{P_{2,g}}\ddot{\mathbf{q}}_\mathbf{W} + \mathbf{P_{3,g}}\dot{\mathbf{q}}_\mathbf{P} + \mathbf{P_{4,g}}\dot{\mathbf{q}}_\mathbf{W} + \mathbf{P_{5,g}}\mathbf{q_P} + \mathbf{P_{6,g}}\mathbf{q_W} \\ \dot{\mathbf{w}}_\mathbf{g} &= \mathbf{W_{1,g}}\mathbf{q_W} + \mathbf{W_{2,g}}\mathbf{w_g} \end{aligned} \tag{C.53}$$

C.3. Propeller-Wing aeroelastic Equations

Combining Equation (C.16) with Equation (C.53), the following expression is obtained

$$\begin{bmatrix} \mathbf{M_{s,g}} + \mathbf{G_{s,g}} - \mathbf{M_{a,g}} - \mathbf{P_{2,g}} & \mathbf{F_{s,g}} - \mathbf{P_{1,g}} \\ \mathbf{B_{s,g}} - \mathbf{B_{a,g}} & \mathbf{A_s} - \mathbf{A_a} \end{bmatrix} \begin{bmatrix} \ddot{\mathbf{q}}_\mathbf{W} \\ \ddot{\mathbf{q}}_\mathbf{P} \end{bmatrix} + \begin{bmatrix} \mathbf{C_{s,g}} - \mathbf{C_{a,g}} - \mathbf{P_{4,g}} & \mathbf{H_{s,g}} - \mathbf{P_{3,g}} \\ \mathbf{D_{s,g}} - \mathbf{D_{a,g}} & \mathbf{C_s} - \mathbf{C_a} \end{bmatrix} \begin{bmatrix} \dot{\mathbf{q}}_\mathbf{W} \\ \dot{\mathbf{q}}_\mathbf{P} \end{bmatrix} +$$
$$+ \begin{bmatrix} \mathbf{K_{s,g}} - \mathbf{K_{a,g}} - \mathbf{P_{6,g}} & -\mathbf{P_{5,g}} \\ -\mathbf{F_{a,g}} & \mathbf{E_s} - \mathbf{E_a} \end{bmatrix} \begin{bmatrix} \mathbf{q}_\mathbf{W} \\ \mathbf{q}_\mathbf{P} \end{bmatrix} = \begin{bmatrix} \mathbf{W_{0,g}} \\ \mathbf{0_{2x12}} \end{bmatrix} \mathbf{w_g} + \begin{bmatrix} \mathbf{g_g} \\ \mathbf{0_{2x1}} \end{bmatrix} \dot{\phi}(t) \tag{C.54}$$

$$\dot{\mathbf{w}}_\mathbf{g} = \begin{bmatrix} \mathbf{W_{1,g}} & \mathbf{0_{12x2}} \end{bmatrix} \begin{bmatrix} \mathbf{q}_\mathbf{W} \\ \mathbf{q}_\mathbf{P} \end{bmatrix} + \mathbf{W_{2,g}} \mathbf{w_g}$$

Defining $\mathbf{q} = \begin{bmatrix} \mathbf{q}_\mathbf{W} \\ \mathbf{q}_\mathbf{P} \end{bmatrix}$, Equation (C.54) becomes

$$\begin{aligned} \mathbf{S_1}\ddot{\mathbf{q}} + \mathbf{S_2}\dot{\mathbf{q}} + \mathbf{S_3}\mathbf{q} &= \mathbf{S_4}\mathbf{w_g} + \mathbf{S_5}\dot{\phi}(t) \\ \dot{\mathbf{w}}_\mathbf{g} &= \mathbf{S_6}\mathbf{q} + \mathbf{W_{2g}}\mathbf{w_g} \end{aligned} \tag{C.55}$$

where

$$\mathbf{S_1} = \begin{bmatrix} \mathbf{M_{s,g}} + \mathbf{G_{s,g}} - \mathbf{M_{a,g}} - \mathbf{P_{2,g}} & \mathbf{F_{s,g}} - \mathbf{P_{1,g}} \\ \mathbf{B_{s,g}} - \mathbf{B_{a,g}} & \mathbf{A_s} - \mathbf{A_a} \end{bmatrix} \tag{C.56}$$

$$\mathbf{S_2} = \begin{bmatrix} \mathbf{C_{s,g}} - \mathbf{C_{a,g}} - \mathbf{P_{4,g}} & \mathbf{H_{s,g}} - \mathbf{P_{3,g}} \\ \mathbf{D_{s,g}} - \mathbf{D_{a,g}} & \mathbf{C_s} - \mathbf{C_a} \end{bmatrix} \tag{C.57}$$

$$\mathbf{S_3} = \begin{bmatrix} \mathbf{K_{s,g}} - \mathbf{K_{a,g}} - \mathbf{P_{6,g}} & -\mathbf{P_{5,g}} \\ -\mathbf{F_{a,g}} & \mathbf{E_s} - \mathbf{E_a} \end{bmatrix} \tag{C.58}$$

$$\mathbf{S_4} = \begin{bmatrix} \mathbf{W_{0,g}} \\ \mathbf{0_{2x12}} \end{bmatrix} \tag{C.59}$$

$$\mathbf{S_5} = \begin{bmatrix} \mathbf{g_g} \\ \mathbf{0_{2x1}} \end{bmatrix} \tag{C.60}$$

$$\mathbf{S_6} = \begin{bmatrix} \mathbf{W_{1g}} & \mathbf{0_{12x2}} \end{bmatrix} \tag{C.61}$$

In state-space form

$$\begin{aligned} \ddot{\mathbf{q}} &= -\mathbf{S_1}^{-1}\mathbf{S_2}\dot{\mathbf{q}} - \mathbf{S_1}^{-1}\mathbf{S_3}\mathbf{q} + \mathbf{S_1}^{-1}\mathbf{S_4}\mathbf{w_g} + \mathbf{S_1}^{-1}\mathbf{S_5}\dot{\phi}(t) \\ \dot{\mathbf{w}}_\mathbf{g} &= \mathbf{S_6}\mathbf{q} + \mathbf{W_{2,g}}\mathbf{w_g} \end{aligned} \tag{C.62}$$

$$\begin{bmatrix} \dot{\mathbf{q}} \\ \ddot{\mathbf{q}} \\ \dot{\mathbf{w}}_\mathbf{g} \end{bmatrix} = \underbrace{\begin{bmatrix} \mathbf{0_{11x11}} & \mathbf{I_{11x11}} & \mathbf{0_{11x12}} \\ -\mathbf{S_1}^{-1}\mathbf{S_3} & -\mathbf{S_1}^{-1}\mathbf{S_2} & \mathbf{S_1}^{-1}\mathbf{S_4} \\ \mathbf{S_6} & \mathbf{0_{12x11}} & \mathbf{W_{2,g}} \end{bmatrix}}_{\mathbf{Z}} \begin{bmatrix} \mathbf{q} \\ \dot{\mathbf{q}} \\ \mathbf{w_g} \end{bmatrix} + \begin{bmatrix} \mathbf{0_{11x1}} \\ \mathbf{S_1}^{-1}\mathbf{S_5} \\ \mathbf{0_{12x1}} \end{bmatrix} \dot{\phi}(t) \tag{C.63}$$

Note that the degrees of freedom at wing root are always null since the wing is cantilevered at its root. Matrix $\mathbf{Z}$ must be reduced, meaning that the rows and columns associated with the degrees of freedom at the wing root are crossed out; these degrees of freedom are h_1, ϕ_1, α_1, $\dot{h}_1$, $\dot{\phi}_1$, $\dot{\alpha}_1$, $w_1^{(1)}$, $w_2^{(1)}$, $w_3^{(1)}$, and $w_4^{(1)}$. Therefore, the stability of the propeller-flexible-wing aeroelastic system is assessed by analysing the eigenvalues and eigenvectors of the reduced state matrix. Four types of instability can occur in this aeroelastic system: whirl flutter, whirl divergence, wing flutter, and wing divergence.

D

Prop.-Wing Aeroelastic State-Space System: with Leishman-Nguyen's Method and Multiple propellers

This section implements the aerodynamic model of the wing using Leishman-Nguyen's method. Moreover, the methodology for including multiple propellers is described.

D.1. Wing Aerodynamics in global Matrix Form

Wing aerodynamics are composed of lift and pitching moment acting on each node. These terms are represented by $\mathbf{Q_W}$.

$$\mathbf{Q_W} = \begin{bmatrix} Q_{h,P}^{(1)} \\ 0 \\ Q_{\alpha,P}^{(1)} \\ Q_{h,P}^{(2)} \\ 0 \\ Q_{\alpha,P}^{(2)} \\ Q_{h,P}^{(3)} \\ 0 \\ Q_{\alpha,P}^{(3)} \end{bmatrix} = \begin{bmatrix} -L^{(1)} \\ 0 \\ M^{(1)} \\ -L^{(2)} \\ 0 \\ M^{(2)} \\ -L^{(3)} \\ 0 \\ M^{(3)} \end{bmatrix} = \mathbf{M_{a,g}}\ddot{\mathbf{q}}_\mathbf{W} + \mathbf{C_{a,g}}\dot{\mathbf{q}}_\mathbf{W} + \mathbf{K_{a,g}}\mathbf{q_W} + \mathbf{W_{0,g}}\mathbf{w_g} \tag{D.1}$$

$$\dot{\mathbf{w}}_\mathbf{g} = \mathbf{W_{1,g}}\mathbf{w_g} + \mathbf{W_{2,g}}\dot{\mathbf{q}}_\mathbf{W} + \mathbf{W_{3,g}}\mathbf{q_W}$$

The vector of aerodynamic states is

$$\mathbf{w_g} = \begin{bmatrix} w_1^{(1)} & w_2^{(1)} & w_1^{(2)} & w_2^{(2)} & w_1^{(3)} & w_2^{(3)} \end{bmatrix}^T \tag{D.2}$$

The wing aerodynamic mass matrix is given by

$$\mathbf{M_{a,e}} = \begin{bmatrix} -\pi\rho b^2 & 0 & \pi\rho b^3 a \\ 0 & 0 & 0 \\ \pi\rho b^3 a & 0 & -\pi\rho b^4\left(\frac{1}{8} + a^2\right) \end{bmatrix} \tag{D.3}$$

$$\mathbf{M_{a,g}} = \begin{bmatrix} \mathbf{M_{a,e}^{(1)}} & \mathbf{0_{3x3}} & \mathbf{0_{3x3}} \\ \mathbf{0_{3x3}} & \mathbf{M_{a,e}^{(2)}} & \mathbf{0_{3x3}} \\ \mathbf{0_{3x3}} & \mathbf{0_{3x3}} & \mathbf{M_{a,e}^{(3)}} \end{bmatrix} \tag{D.4}$$

The wing aerodynamic damping matrix is given by

$$\mathbf{C_{a,e}} = \begin{bmatrix} -\pi\rho bV & 0 & -\pi\rho b^2V - \pi\rho b^2V\left(\frac{1}{2}-a\right) \\ 0 & 0 & 0 \\ \pi\rho bVb\left(a+\frac{1}{2}\right) & 0 & -\pi\rho b^3V\left(\frac{1}{2}-a\right) + \pi\rho b^2V\left(\frac{1}{2}-a\right)b\left(a+\frac{1}{2}\right) \end{bmatrix} \tag{D.5}$$

$$\mathbf{C_{a,g}} = \begin{bmatrix} \mathbf{C_{a,e}^{(1)}} & \mathbf{0_{3x3}} & \mathbf{0_{3x3}} \\ \mathbf{0_{3x3}} & \mathbf{C_{a,e}^{(2)}} & \mathbf{0_{3x3}} \\ \mathbf{0_{3x3}} & \mathbf{0_{3x3}} & \mathbf{C_{a,e}^{(3)}} \end{bmatrix} \tag{D.6}$$

The wing aerodynamic stiffness matrix is given by

$$\mathbf{K_{a,e}} = \begin{bmatrix} 0 & 0 & -\pi\rho bV^2 \\ 0 & 0 & 0 \\ 0 & 0 & \pi\rho bV^2b^2\left(a+\frac{1}{2}\right) \end{bmatrix} \tag{D.7}$$

$$\mathbf{K_{a,g}} = \begin{bmatrix} \mathbf{K_{a,e}^{(1)}} & \mathbf{0_{3x3}} & \mathbf{0_{3x3}} \\ \mathbf{0_{3x3}} & \mathbf{K_{a,e}^{(2)}} & \mathbf{0_{3x3}} \\ \mathbf{0_{3x3}} & \mathbf{0_{3x3}} & \mathbf{K_{a,e}^{(3)}} \end{bmatrix} \tag{D.8}$$

The wing aerodynamic state influence matrix is given by $\mathbf{W_{0,e}} = 2\pi\rho bV^2\mathbf{W'_{0,e}}$, where $\mathbf{W'_{0,e}}$ is

$$\mathbf{W'_{0,e}} = \begin{bmatrix} -\left(\Psi_1+\Psi_2\right)\epsilon_1\epsilon_2\left(\frac{V}{b}\right)^2 & -\left(\Psi_1\epsilon_1+\Psi_2\epsilon_2\right)\left(\frac{V}{b}\right) \\ 0 & 0 \\ \left(\Psi_1+\Psi_2\right)\epsilon_1\epsilon_2\left(\frac{V}{b}\right)^2 b\left(a+\frac{1}{2}\right) & \left(\Psi_1\epsilon_1+\Psi_2\epsilon_2\right)\left(\frac{V}{b}\right)b\left(a+\frac{1}{2}\right) \end{bmatrix} \tag{D.9}$$

$$\mathbf{W_{0,g}} = \begin{bmatrix} \mathbf{W_{0,e}^{(1)}} & \mathbf{0_{3x2}} & \mathbf{0_{3x2}} \\ \mathbf{0_{3x2}} & \mathbf{W_{0,e}^{(2)}} & \mathbf{0_{3x2}} \\ \mathbf{0_{3x2}} & \mathbf{0_{3x2}} & \mathbf{W_{0,e}^{(3)}} \end{bmatrix} \tag{D.10}$$

Finally, the aerodynamic state equation matrices are given by

$$\mathbf{W_{1,e}} = \begin{bmatrix} 0 & 1 \\ -\epsilon_1\epsilon_2\left(\frac{V}{b}\right)^2 & -(\epsilon_1+\epsilon_2)\left(\frac{V}{b}\right) \end{bmatrix} \tag{D.11}$$

$$\mathbf{W_{1,g}} = \begin{bmatrix} \mathbf{W_{1,e}^{(1)}} & \mathbf{0_{2x2}} & \mathbf{0_{2x2}} \\ \mathbf{0_{2x2}} & \mathbf{W_{1,e}^{(2)}} & \mathbf{0_{2x2}} \\ \mathbf{0_{2x2}} & \mathbf{0_{2x2}} & \mathbf{W_{1,e}^{(3)}} \end{bmatrix} \tag{D.12}$$

$$\mathbf{W_{2,e}} = \begin{bmatrix} 0 & 0 & 0 \\ \frac{1}{V} & 0 & \frac{b}{V}\left(\frac{1}{2}-a\right) \end{bmatrix} \tag{D.13}$$

$$\mathbf{W_{2,g}} = \begin{bmatrix} \mathbf{W_{2,e}^{(1)}} & \mathbf{0_{2x3}} & \mathbf{0_{2x3}} \\ \mathbf{0_{2x3}} & \mathbf{W_{2,e}^{(2)}} & \mathbf{0_{2x3}} \\ \mathbf{0_{2x3}} & \mathbf{0_{2x3}} & \mathbf{W_{2,e}^{(3)}} \end{bmatrix} \tag{D.14}$$

$$\mathbf{W_{3,e}} = \begin{bmatrix} 0 & 0 & 0 \\ 0 & 0 & 1 \end{bmatrix} \tag{D.15}$$

$$\mathbf{W_{3,g}} = \begin{bmatrix} \mathbf{W_{3,e}^{(1)}} & \mathbf{0_{2x3}} & \mathbf{0_{2x3}} \\ \mathbf{0_{2x3}} & \mathbf{W_{3,e}^{(2)}} & \mathbf{0_{2x3}} \\ \mathbf{0_{2x3}} & \mathbf{0_{2x3}} & \mathbf{W_{3,e}^{(3)}} \end{bmatrix} \tag{D.16}$$

Final expression

The final expression for the wing aeroelastic equation in matrix form can be expressed as

$$\begin{aligned}\mathbf{M_{s,g}}\ddot{\mathbf{q}}_\mathbf{W} + \mathbf{C_{s,g}}\dot{\mathbf{q}}_\mathbf{W} + \mathbf{K_{s,g}}\mathbf{q}_\mathbf{W} + \mathbf{F_{s,g}}\ddot{\mathbf{q}}_\mathbf{P} + \mathbf{G_{s,g}}\ddot{\mathbf{q}}_\mathbf{W} + \mathbf{H_{s,g}}\dot{\mathbf{q}}_\mathbf{P} &= \mathbf{M_{a,g}}\ddot{\mathbf{q}}_\mathbf{W} + \mathbf{C_{a,g}}\dot{\mathbf{q}}_\mathbf{W} + \mathbf{K_{a,g}}\mathbf{q}_\mathbf{W} + \mathbf{W_{0,g}}\mathbf{w_g} + \dots \\ &\quad + \mathbf{P_{1,g}}\ddot{\mathbf{q}}_\mathbf{P} + \mathbf{P_{2,g}}\ddot{\mathbf{q}}_\mathbf{W} + \mathbf{P_{3,g}}\dot{\mathbf{q}}_\mathbf{P} + \mathbf{P_{4,g}}\dot{\mathbf{q}}_\mathbf{W} + \mathbf{P_{5,g}}\mathbf{q}_\mathbf{P} + \mathbf{P_{6,g}}\mathbf{q}_\mathbf{W} \\ \dot{\mathbf{w}}_\mathbf{g} &= \mathbf{W_{1,g}}\mathbf{w_g} + \mathbf{W_{2,g}}\dot{\mathbf{q}}_\mathbf{W} + \mathbf{W_{3,g}}\mathbf{q}_\mathbf{W}\end{aligned} \tag{D.17}$$

D.2. Propeller-Wing aeroelastic Equations

Combining Equation (C.16) with Equation (D.17), the following expression is obtained

$$\begin{bmatrix} \mathbf{M_{s,g}} + \mathbf{G_{s,g}} - \mathbf{M_{a,g}} - \mathbf{P_{2,g}} & \mathbf{F_{s,g}} - \mathbf{P_{1,g}} \\ \mathbf{B_{s,g}} - \mathbf{B_{a,g}} & \mathbf{A_s} - \mathbf{A_a} \end{bmatrix} \begin{bmatrix} \ddot{\mathbf{q}}_\mathbf{W} \\ \ddot{\mathbf{q}}_\mathbf{P} \end{bmatrix} + \begin{bmatrix} \mathbf{C_{s,g}} - \mathbf{C_{a,g}} - \mathbf{P_{4,g}} & \mathbf{H_{s,g}} - \mathbf{P_{3,g}} \\ \mathbf{D_{s,g}} - \mathbf{D_{a,g}} & \mathbf{C_s} - \mathbf{C_a} \end{bmatrix} \begin{bmatrix} \dot{\mathbf{q}}_\mathbf{W} \\ \dot{\mathbf{q}}_\mathbf{P} \end{bmatrix} +$$
$$+ \begin{bmatrix} \mathbf{K_{s,g}} - \mathbf{K_{a,g}} - \mathbf{P_{6,g}} & -\mathbf{P_{5,g}} \\ -\mathbf{F_{a,g}} & \mathbf{E_s} - \mathbf{E_a} \end{bmatrix} \begin{bmatrix} \mathbf{q}_\mathbf{W} \\ \mathbf{q}_\mathbf{P} \end{bmatrix} = \begin{bmatrix} \mathbf{W_{0,g}} \\ \mathbf{0_{2x6}} \end{bmatrix} \mathbf{w_g} \tag{D.18}$$

$$\dot{\mathbf{w}}_\mathbf{g} = \mathbf{W_{1,g}}\mathbf{w_g} + \begin{bmatrix} \mathbf{W_{2,g}} & \mathbf{0_{6x2}} \end{bmatrix} \begin{bmatrix} \dot{\mathbf{q}}_\mathbf{W} \\ \dot{\mathbf{q}}_\mathbf{P} \end{bmatrix} + \begin{bmatrix} \mathbf{W_{3,g}} & \mathbf{0_{6x2}} \end{bmatrix} \begin{bmatrix} \mathbf{q}_\mathbf{W} \\ \mathbf{q}_\mathbf{P} \end{bmatrix}$$

Defining $\mathbf{q} = \begin{bmatrix} \mathbf{q}_\mathbf{W} \\ \mathbf{q}_\mathbf{P} \end{bmatrix}$, Equation (C.54) becomes

$$\begin{aligned}\mathbf{S_1}\ddot{\mathbf{q}} + \mathbf{S_2}\dot{\mathbf{q}} + \mathbf{S_3}\mathbf{q} &= \mathbf{S_4}\mathbf{w_g} \\ \dot{\mathbf{w}}_\mathbf{g} &= \mathbf{W_{1,g}}\mathbf{w_g} + \mathbf{S_5}\dot{\mathbf{q}} + \mathbf{S_6}\mathbf{q}\end{aligned} \tag{D.19}$$

where

$$\mathbf{S_1} = \begin{bmatrix} \mathbf{M_{s,g}} + \mathbf{G_{s,g}} - \mathbf{M_{a,g}} - \mathbf{P_{2,g}} & \mathbf{F_{s,g}} - \mathbf{P_{1,g}} \\ \mathbf{B_{s,g}} - \mathbf{B_{a,g}} & \mathbf{A_s} - \mathbf{A_a} \end{bmatrix} \tag{D.20}$$

$$\mathbf{S_2} = \begin{bmatrix} \mathbf{C_{s,g}} - \mathbf{C_{a,g}} - \mathbf{P_{4,g}} & \mathbf{H_{s,g}} - \mathbf{P_{3,g}} \\ \mathbf{D_{s,g}} - \mathbf{D_{a,g}} & \mathbf{C_s} - \mathbf{C_a} \end{bmatrix} \tag{D.21}$$

$$\mathbf{S_3} = \begin{bmatrix} \mathbf{K_{s,g}} - \mathbf{K_{a,g}} - \mathbf{P_{6,g}} & -\mathbf{P_{5,g}} \\ -\mathbf{F_{a,g}} & \mathbf{E_s} - \mathbf{E_a} \end{bmatrix} \tag{D.22}$$

$$\mathbf{S_4} = \begin{bmatrix} \mathbf{W_{0,g}} \\ \mathbf{0_{2x6}} \end{bmatrix} \tag{D.23}$$

$$\mathbf{S_5} = \begin{bmatrix} \mathbf{W_{2,g}} & \mathbf{0_{6x2}} \end{bmatrix} \tag{D.24}$$

$$\mathbf{S_6} = \begin{bmatrix} \mathbf{W_{3,g}} & \mathbf{0_{6x2}} \end{bmatrix} \tag{D.25}$$

In state-space form

$$\begin{aligned}\ddot{\mathbf{q}} &= -\mathbf{S_1}^{-1}\mathbf{S_2}\dot{\mathbf{q}} - \mathbf{S_1}^{-1}\mathbf{S_3}\mathbf{q} + \mathbf{S_1}^{-1}\mathbf{S_4}\mathbf{w_g} \\ \dot{\mathbf{w}}_\mathbf{g} &= \mathbf{W_{1,g}}\mathbf{w_g} + \mathbf{S_5}\dot{\mathbf{q}} + \mathbf{S_6}\mathbf{q}\end{aligned} \tag{D.26}$$

$$\begin{bmatrix} \dot{\mathbf{q}} \\ \ddot{\mathbf{q}} \\ \dot{\mathbf{w}}_\mathbf{g} \end{bmatrix} = \underbrace{\begin{bmatrix} \mathbf{0_{11x11}} & \mathbf{I_{11x11}} & \mathbf{0_{11x6}} \\ -\mathbf{S_1}^{-1}\mathbf{S_3} & -\mathbf{S_1}^{-1}\mathbf{S_2} & \mathbf{S_1}^{-1}\mathbf{S_4} \\ \mathbf{S_6} & \mathbf{S_5} & \mathbf{W_{1,g}} \end{bmatrix}}_{\mathbf{Z}} \begin{bmatrix} \mathbf{q} \\ \dot{\mathbf{q}} \\ \mathbf{w_g} \end{bmatrix} \tag{D.27}$$

Note that the degrees of freedom at wing root are always null since the wing is cantilevered at its root. Matrix **Z** must be reduced, meaning that the rows and columns associated with the degrees of freedom at the wing root are crossed out; these degrees of freedom are h_1, ϕ_1, α_1, $\dot{h}_1$, $\dot{\phi}_1$, $\dot{\alpha}_1$, $w_1^{(1)}$, and $w_2^{(1)}$. Therefore, the stability of the propeller-flexible-wing aeroelastic system is assessed by analysing the eigenvalues and eigenvectors of the reduced state matrix. Four types of instability can occur in this aeroelastic system: whirl flutter, whirl divergence, wing flutter, and wing divergence.

D.3. Inclusion of multiple Propellers

Let N be the number of propellers.

The degrees of freedom of the propellers are grouped in

$$\mathbf{q_P} = \begin{bmatrix} \theta_1 & \psi_1 & \cdots & \theta_N & \psi_N \end{bmatrix}^T \tag{D.28}$$

where the subscript is the propeller to which the variable is associated with.

Letting the superscripts "$(1)\cdots(N)$" reference the propeller to which the matrix is associated with and letting the superscript "$*$" reference the corresponding matrix accounting for all the propellers, the propeller-wing aeroelastic equations using Leishman-Nguyen's method for wing aerodynamics[1] are

$$\begin{bmatrix} \mathbf{M_{s,g}} + \mathbf{G^*_{s,g}} - \mathbf{M_{a,g}} - \mathbf{P^*_{2,g}} & \mathbf{F^*_{s,g}} - \mathbf{P^*_{1,g}} \\ \left(\mathbf{B_{s,g}} - \mathbf{B_{a,g}}\right)^* & \left(\mathbf{A_s} - \mathbf{A_a}\right)^* \end{bmatrix} \begin{bmatrix} \ddot{\mathbf{q}}_\mathbf{W} \\ \ddot{\mathbf{q}}_\mathbf{P} \end{bmatrix} + \begin{bmatrix} \mathbf{C_{s,g}} - \mathbf{C_{a,g}} - \mathbf{P^*_{4,g}} & \mathbf{H^*_{s,g}} - \mathbf{P^*_{3,g}} \\ \left(\mathbf{D_{s,g}} - \mathbf{D_{a,g}}\right)^* & \left(\mathbf{C_s} - \mathbf{C_a}\right)^* \end{bmatrix} \begin{bmatrix} \dot{\mathbf{q}}_\mathbf{W} \\ \dot{\mathbf{q}}_\mathbf{P} \end{bmatrix} +$$
$$+ \begin{bmatrix} \mathbf{K_{s,g}} - \mathbf{K_{a,g}} - \mathbf{P^*_{6,g}} & -\mathbf{P^*_{5,g}} \\ \left(-\mathbf{F_{a,g}}\right)^* & \left(\mathbf{E_s} - \mathbf{E_a}\right)^* \end{bmatrix} \begin{bmatrix} \mathbf{q}_\mathbf{W} \\ \mathbf{q}_\mathbf{P} \end{bmatrix} = \begin{bmatrix} \mathbf{W_{0,g}} \\ \mathbf{0_{2Nx6}} \end{bmatrix} \mathbf{w_g} \tag{D.29}$$

$$\dot{\mathbf{w}}_\mathbf{g} = \mathbf{W_{1,g}}\mathbf{w} + \begin{bmatrix} \mathbf{W_{2,g}} & \mathbf{0_{6x2N}} \end{bmatrix} \begin{bmatrix} \dot{\mathbf{q}}_\mathbf{W} \\ \dot{\mathbf{q}}_\mathbf{P} \end{bmatrix} + \begin{bmatrix} \mathbf{W_{3,g}} & \mathbf{0_{6x2N}} \end{bmatrix} \begin{bmatrix} \mathbf{q}_\mathbf{W} \\ \mathbf{q}_\mathbf{P} \end{bmatrix}$$

where

$$\mathbf{F^*_{s,g}} = \begin{bmatrix} \mathbf{F^{(1)}_{s,g}} & \cdots & \mathbf{F^{(N)}_{s,g}} \end{bmatrix} \tag{D.30}$$

$$\mathbf{H^*_{s,g}} = \begin{bmatrix} \mathbf{H^{(1)}_{s,g}} & \cdots & \mathbf{H^{(N)}_{s,g}} \end{bmatrix} \tag{D.31}$$

$$\mathbf{G^*_{s,g}} = \sum_{j=1}^{N} \mathbf{G^j_{s,g}} \tag{D.32}$$

$$\mathbf{P^*_{1,g}} = \begin{bmatrix} \mathbf{P^{(1)}_{1,g}} & \cdots & \mathbf{P^{(N)}_{1,g}} \end{bmatrix} \tag{D.33}$$

$$\mathbf{P^*_{3,g}} = \begin{bmatrix} \mathbf{P^{(1)}_{3,g}} & \cdots & \mathbf{P^{(N)}_{3,g}} \end{bmatrix} \tag{D.34}$$

$$\mathbf{P^*_{5,g}} = \begin{bmatrix} \mathbf{P^{(1)}_{5,g}} & \cdots & \mathbf{P^{(N)}_{5,g}} \end{bmatrix} \tag{D.35}$$

$$\mathbf{P^*_{2,g}} = \sum_{j=1}^{N} \mathbf{P^{(j)}_{2,g}} \tag{D.36}$$

[1] Implementation using Wagner's method for wing aerodynamics is analogous.

$$\mathbf{P}^{*}_{\mathbf{4,g}} = \sum_{j=1}^{N} \mathbf{P}^{(\mathbf{j})}_{\mathbf{4,g}} \tag{D.37}$$

$$\mathbf{P}^{*}_{\mathbf{6,g}} = \sum_{j=1}^{N} \mathbf{P}^{(\mathbf{j})}_{\mathbf{6,g}} \tag{D.38}$$

$$\left(\mathbf{A_{s,g}} - \mathbf{A_{a,g}}\right)^{*} = \begin{bmatrix} \mathbf{A}^{(1)}_{\mathbf{s,g}} - \mathbf{A}^{(1)}_{\mathbf{a,g}} & \cdots & \mathbf{0} \\ \vdots & \ddots & \vdots \\ \mathbf{0} & \cdots & \mathbf{A}^{(N)}_{\mathbf{s,g}} - \mathbf{A}^{(N)}_{\mathbf{a,g}} \end{bmatrix} \tag{D.39}$$

$$\left(\mathbf{C_{s,g}} - \mathbf{C_{a,g}}\right)^{*} = \begin{bmatrix} \mathbf{C}^{(1)}_{\mathbf{s,g}} - \mathbf{C}^{(1)}_{\mathbf{a,g}} & \cdots & \mathbf{0} \\ \vdots & \ddots & \vdots \\ \mathbf{0} & \cdots & \mathbf{C}^{(N)}_{\mathbf{s,g}} - \mathbf{C}^{(N)}_{\mathbf{a,g}} \end{bmatrix} \tag{D.40}$$

$$\left(\mathbf{E_{s,g}} - \mathbf{E_{a,g}}\right)^{*} = \begin{bmatrix} \mathbf{E}^{(1)}_{\mathbf{s,g}} - \mathbf{E}^{(1)}_{\mathbf{a,g}} & \cdots & \mathbf{0} \\ \vdots & \ddots & \vdots \\ \mathbf{0} & \cdots & \mathbf{E}^{(N)}_{\mathbf{s,g}} - \mathbf{E}^{(N)}_{\mathbf{a,g}} \end{bmatrix} \tag{D.41}$$

$$\left(\mathbf{B_{s,g}} - \mathbf{B_{a,g}}\right)^{*} = \begin{bmatrix} \mathbf{B}^{(1)}_{\mathbf{s,g}} - \mathbf{B}^{(1)}_{\mathbf{a,g}} \\ \vdots \\ \mathbf{B}^{(N)}_{\mathbf{s,g}} - \mathbf{B}^{(N)}_{\mathbf{a,g}} \end{bmatrix} \tag{D.42}$$

$$\left(\mathbf{D_{s,g}} - \mathbf{D_{a,g}}\right)^{*} = \begin{bmatrix} \mathbf{D}^{(1)}_{\mathbf{s,g}} - \mathbf{D}^{(1)}_{\mathbf{a,g}} \\ \vdots \\ \mathbf{D}^{(N)}_{\mathbf{s,g}} - \mathbf{D}^{(N)}_{\mathbf{a,g}} \end{bmatrix} \tag{D.43}$$

$$\left(-\mathbf{F_{a,g}}\right)^{*} = \begin{bmatrix} -\mathbf{F}^{(1)}_{\mathbf{a,g}} \\ \vdots \\ -\mathbf{F}^{(N)}_{\mathbf{a,g}} \end{bmatrix} \tag{D.44}$$

Equation (D.29) may be rearranged into a state-space form and solved using eigenvalue analysis.

E

Additional aeroelastic Results: Constant Speed Propeller

Propeller-wing models with constant speed propeller/s. Propeller rotational speed set at 2250 RPM.

E.1. Baseline Propeller-Wing Model

Critical instability	Value	Units
Wing divergence speed	153	[m/s]

Table E.1: Baseline wing (constant speed propeller): aeroelastic results.

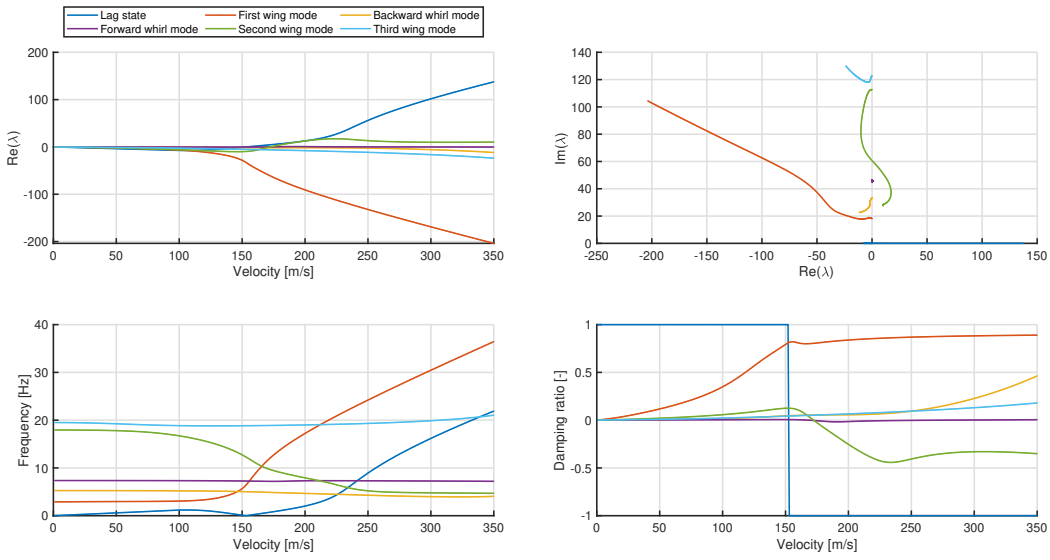

Figure E.1: Baseline propeller-wing (constant speed propeller): V-g-f plots.

E.2. Wingtip-mounted Propeller-Wing Model

Critical instability	Value	Units
Propeller whirl flutter speed (forward whirl mode)	163	[m/s]
Propeller whirl flutter frequency (forward whirl mode)	11.13	[Hz]

Table E.2: Wingtip-mounted propeller-wing (constant speed propeller): aeroelastic results.

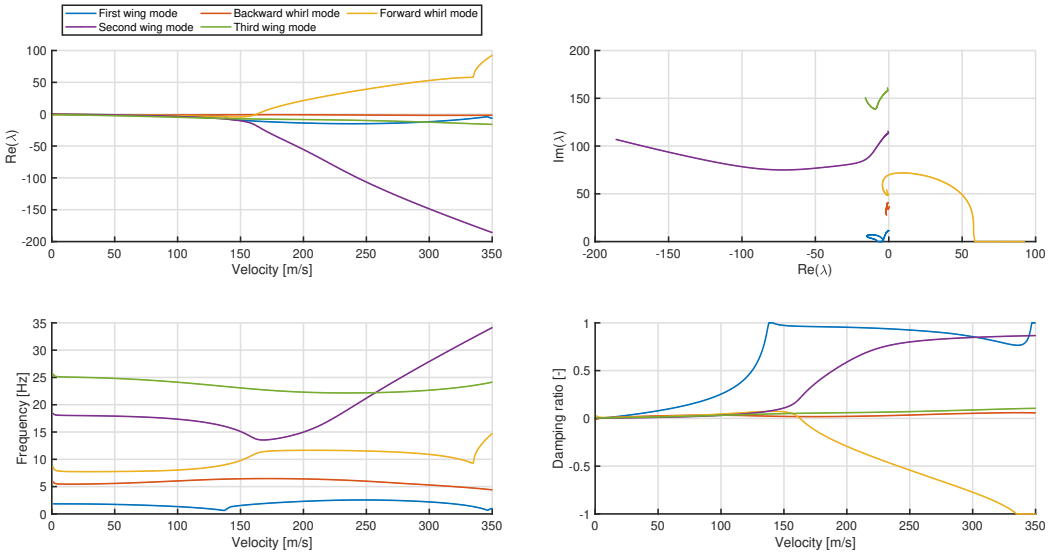

Figure E.2: Wingtip-mounted propeller-wing (constant speed propeller): V-g-f plots.

E.3. Two-Propeller-Wing Model

Critical instability	Value	Units
Propeller whirl flutter speed (second forward whirl mode)	186	[m/s]
Propeller whirl flutter frequency (second forward whirl mode)	12.51	[Hz]

Table E.3: Two-propeller-wing (constant speed propeller): aeroelastic results.

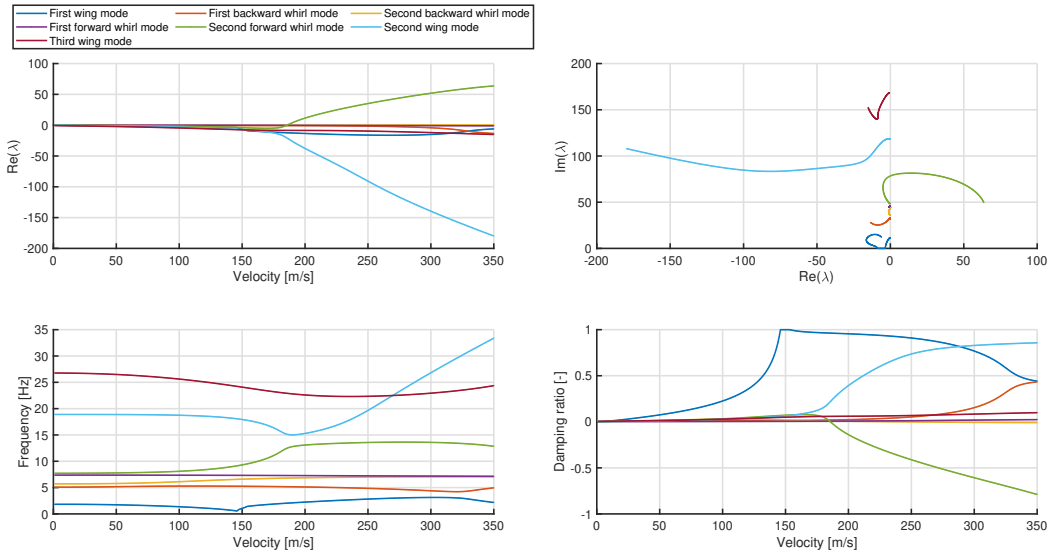

Figure E.3: Two-propeller-wing (constant speed propeller): V-g-f plots.

Comparing the critical speeds and frequencies of each model to those of their counterparts with fixed-pitch propeller/s (see Table 10.9), it can be observed that very approximate results are obtained. The critical speeds are determined by either wing modes and the forward whirl mode, whose behaviour are largely dominated by propeller-wing coupling and wing aerodynamics. Hence, the effect of changing the propeller to a constant speed propeller, barely changes the critical aeroelastic behaviour of the propeller-wing models. On the other hand, when comparing the V-g-f plots, it can be observed that the backward whirl mode does not go unstable in the velocity interval considered (0-350 m/s); as explained in Figure 9.13, the baseline propeller at constant speed conditions have much higher (backward) whirl flutter speeds.

Bibliography

[1] F.T. Abbott Jr., H. N. Kelley, and K.D. Hampton. Investigation of propeller-power-plant autoprecession boundaries for a dynamic-aeroelastic model of a four-engine turboprop transport airplane. NASA Technical Note D-1806, 1963.

[2] Airbus. https://www.airbus.com/, (accessed June 01, 2020).

[3] R.M. Ajaj, M.I. Friswell, D. Smith, and A.T. Isikveren. A conceptual wing-box weight estimation model for transport aircraft. *The Aeronautical Journal*, 117(1191):533–551, 2013.

[4] J.D. Anderson Jr. *Introduction to Flight*. McGraw-Hill, 1989.

[5] J.D. Anderson Jr. *Fundamentals of aerodynamics*. McGraw-Hill Education, 2017.

[6] R.M. Bennett and S.R. Bland. Wind-tunnel measurement of propeller whirl-flutter speeds and static-stability derivatives and comparison with theory. NASA Tecnical Note D-1807, 1963.

[7] R.M. Bennett and S.R. Bland. Experimental and analytical investigation of propeller whirl flutter of a power plant on a flexible wing. NASA Technical Note D-2399, 1964.

[8] R.L. Bielawa. *Rotary wing structural dynamics and aeroelasticity*. American Institute of Aeronautics and Astronautics, 2006.

[9] M.A. Biot and L. Arnold. Low-speed flutter and its physical interpretation. *Journal of the Aeronautical Sciences*, 15(4):232–236, 1948.

[10] R.L. Bisplinghoff, H. Ashley, and R.L. Halfman. *Aeroelasticity*. Courier Corporation, 2013.

[11] S.R. Bland and E.C. Yates Jr. Comparative evaluation of methods for predicting flutter and divergence of unswept wings of finite span. NASA Technical Note D-2051, 1963.

[12] N.K. Borer, M.D. Moore, and A. Turnbull. Tradespace exploration of distributed propulsors for advanced on-demand mobility concepts. In *14th AIAA Aviation Technology, Integration, and Operations Conference*, page 2850, 2014.

[13] E. Butikov. Precession and nutation of a gyroscope. *European journal of physics*, 27(5):1071, 2006.

[14] J. Cecrdle. Analysis of twin turboprop aircraft whirl-flutter stability boundaries. *Journal of Aircraft*, 49 (6):1718–1725, 2012.

[15] J. Cecrdle. Influence of propeller blade lift distribution on whirl flutter stability characteristics. *World Academy of Science, Engineering and Technology. International Journal of Aerospace and Mechanical Engineering*, 8(4), 2014.

[16] J. Cecrdle. *Whirl flutter of turboprop aircraft structures*. Woodhead Publishing, 2015.

[17] J. Cecrdle. Updating of dynamic model of aircraft structure with wing tip-tanks according to results of ground vibration test. In *AIAA Scitech 2019 Forum*, page 1529, 2019.

[18] W. Chajec, W.A. Krzymien, and A. Strohmayer. The effect of wing-tip propulsors on icaré 2 aeroelasticity. *Aircraft Engineering and Aerospace Technology*, 91(3):509–524, 2019.

[19] A. Cravana, G. Manfreda, E. Cestino, G. Frulla, R. Carrese, and P. Marzocca. Aeroelastic behaviour of flexible wings carrying distributed electric propulsion systems. Technical report, SAE Technical Paper, 2017.

[20] R. De Vries. Unsteady pylon loading for pylon-mounted tractor propellers. Master's thesis, Delft University of Technology, 2016.

[21] G. Dimitriadis. *Introduction to nonlinear aeroelasticity*. John Wiley & Sons, 2017.

[22] R.E. Donham and D.J. Osterholt. Utilizing test results to show adding flexibility of propeller blades is more representative than the classical rigid blade propeller whirl flutter analysis. In *Proceedings of International Forum on Aeroelasticity and Structural Dynamics (IFASD), Stockholm, Sweden*, pages 18–20, 2007.

[23] E.H. Dowell. *A modern course in aeroelasticity*. Springer, 2015.

[24] FAA. https://lessonslearned.faa.gov/ll_main.cfm?TabID=2&LLID=7&LLTypeID=2, (accessed June 1, 2020).

[25] J. Fischer. Simulation and analysis of the aerodynamic interactions between distributed propellers and wings. Master's thesis, Delft University of Technology, 2017.

[26] H.W. Försching. *Grundlagen der aeroelastik*. Springer-Verlag, 2013.

[27] Y.C. Fung. *An introduction to the theory of aeroelasticity*. Courier Dover Publications, 2008.

[28] I.E. Garrick and W. H. Reed III. Historical development of aircraft flutter. *Journal of Aircraft*, 18(11): 897–912, 1981.

[29] M. Gennaretti and L. Greco. Whirl flutter analysis of prop-rotors using unsteady aerodynamics reduced-order models. *The Aeronautical Journal*, 112(1131):261–270, 2008.

[30] I. Gonzalez-Martino, M. Costes, B. Rodriguez, and P. Devinant. Application of an unsteady curved lifting-line theory to propeller simulations. In *30th AIAA Applied Aerodynamics Conference*, page 2917, 2012.

[31] J.M. Greenberg. Airfoil in sinusoidal motion in a pulsating stream. NACA Technical Note 1326, 1947.

[32] S. Gudmundsson. *General aviation aircraft design: Applied Methods and Procedures*. Butterworth-Heinemann, 2013.

[33] G.P. Guruswamy. Dynamic aeroelasticity of wings with tip propeller by using navier–stokes equations. *AIAA Journal*, 57(8):3200–3205, 2019.

[34] G.P. Guruswamy, P. M. Goorjian, and U.L. Tu. Transonic aeroelasticity of wings with tip stores. *Journal of aircraft*, 24(10):688–695, 1987.

[35] C. Hammond, H. Runyan, and J. Mason. Application of unsteady lifting surface theory to propellers in forward flight. In *15th Structural Dynamics and Materials Conference*, page 419, 1974.

[36] D.H. Hodges and G.A. Pierce. *Introduction to structural dynamics and aeroelasticity (2nd)*. Cambridge University Press, 2003.

[37] D.H. Hodges, M.J. Patil, and S. Chae. Effect of thrust on bending-torsion flutter of wings. *Journal of Aircraft*, 39(2):371–376, 2002.

[38] C.B. Hoover. *Propeller whirl flutter analysis of the NASA all-electric X-57 through multibody dynamics simulations*. PhD thesis, The University of Alabama, 2018.

[39] C.B. Hoover and J. Shen. Parametric study of propeller whirl flutter stability with full-span model of x-57 maxwell aircraft. *Journal of Aircraft*, 55(6):2530–2537, 2018.

[40] C.B. Hoover and J. Shen. Whirl flutter analysis of a free-flying electric driven propeller aircraft. In *2018 Aviation Technology, Integration, and Operations Conference*, page 3210, 2018.

[41] C.B. Hoover and J. Shen. Fundamental understanding of propeller whirl flutter through multibody dynamics. In *AIAA Scitech 2019 Forum*, page 1864, 2019.

[42] C.B. Hoover and J. Shen. Whirl flutter analysis of a free-flying electric-driven propeller aircraft. *Journal of Aircraft*, 56(2):831–836, 2019.

[43] C.B. Hoover, J. Shen, A.R. Kreshock, B. Stanford, D.J. Piatak, and J. Heeg. Whirl flutter stability and its influence on the design of the distributed electric propeller aircraft x-57. In *17th AIAA Aviation Technology, Integration, and Operations Conference*, page 3785, 2017.

[44] C.B. Hoover, J. Shen, and A.R. Kreshock. Propeller whirl flutter stability and its influence on x-57 aircraft design. *Journal of Aircraft*, 55(5):2169–2175, 2018.

[45] J.C. Houbolt and W.H. Reed. Propeller-nacelle whirl flutter. *Journal of the Aerospace Sciences*, 29(3): 333–346, 1962.

[46] J.T. Hwang and A. Ning. Large-scale multidisciplinary optimization of an electric aircraft for on-demand mobility. In *2018 AIAA/ASCE/AHS/ASC Structures, Structural Dynamics, and Materials Conference*, page 1384, 2018.

[47] D.J. Inman. *Engineering vibration (4th.)*. Pearson Education, Inc, 2014.

[48] D.C. Janetzke and K.R.V. Kaza. Whirl flutter analysis of a horizontal-axis wind turbine with a two-bladed teetering rotor. *Solar Energy*, 31(2):173–182, 1983.

[49] J.M. Janus, A. Chatterjee, and C. Cave. Computational analysis of a wingtip-mounted pusher turboprop. *Journal of aircraft*, 33(2):441–444, 1996.

[50] R. Johnson and J. Sullivan. Propeller tip vortex interactions. In *28th Aerospace Sciences Meeting*, page 437, 1990.

[51] R.T. Johnson, D.P. Witkowski, and J.P. Sullivan. Experimental results of a propeller/wing interaction study. *SAE transactions*, pages 121–130, 1991.

[52] W. Johnson. Dynamics of tilting proprotor aircraft in cruise flight. NASA Technical Note D-7677, 1974.

[53] W. Johnson. Theory and comparison with tests of two full-scale proprotors. NASA Ames Research Center Conference paper, 1974.

[54] W. Johnson. *Rotorcraft aeromechanics*, volume 36, chapter 20. Cambridge University Press, 2013.

[55] R.T. Johnston and J.P. Sullivan. Unsteady wing surface pressures in the wake of a propeller. *Journal of aircraft*, 30(5):644–651, 1993.

[56] R.T. Jones. The unsteady lift of a finite wing. NACA Technical Note 682, 1939.

[57] E. Jonsson, C. Riso, C.A. Lupp, C.E.S. Cesnik, J.R.R.A. Martins, and B.I. Epureanu. Flutter and post-flutter constraints in aircraft design optimization. *Progress in Aerospace Sciences*, 2019.

[58] M.W. Kehoe. A historical overview of flight flutter testing. NASA Technical Memorandum 4720, 1995.

[59] T. Kim, S. Shin, and T. Kim. Analysis of tiltrotor whirl flutter in time and frequency domain. *Journal of mechanical science and technology*, 23(12):3281–3291, 2009.

[60] D.L. Kunz. Analysis of proprotor whirl flutter: review and update. *Journal of aircraft*, 42(1):172–178, 2005.

[61] R.G. Kvaternik. *Studies in tilt-rotor VTOL aircraft aeroelasticity, Volume 1*. PhD thesis, Case Western Reserve University, 1973.

[62] R.G. Kvaternik and J.S. Kohn. An experimental and analytical investigation of proprotor whirl flutter. NASA Technical Paper 1047, 1977.

[63] J.G. Leishman and K.Q. Nguyen. State-space representation of unsteady airfoil behavior. *AIAA journal*, 28(5):836–844, 1990.

[64] R.G. Loewy. A two-dimensional approximation to the unsteady aerodynamics of rotary wings. *Journal of the Aeronautical Sciences*, 24(2):81–92, 1957.

[65] C. Mair, D. Rezgui, and B. Titurus. Nonlinear stability analysis of whirl flutter in a rotor-nacelle system. *Nonlinear dynamics*, 94(3):2013–2032, 2018.

[66] MIT-OpenCourseWare. Classical Mechanics: gyroscopes. https://ocw.mit.edu/, (accessed November 06, 2019).

[67] NASA. https://sacd.larc.nasa.gov/x57maxwell/, (accessed June 1, 2020).

[68] NASA. X-57 Technical Document Portal. https://nasa.gov/x57/technical, (accessed May 11, 2020).

[69] K.J. Nelson and J. Shen. Multibody dynamics simulations of distributed electric propellers of x-57 aircraft. In *AIAA Scitech 2020 Forum*, page 1680, 2020.

[70] S. Neumark. *Concept of complex stiffness applied to problems of oscillations with viscous and hysteretic damping*. HM Stationery Office, 1962.

[71] N.T. Nguyen, K.W. Reynolds, and E. Ting. Wing shaping concept for distributed propulsion aircraft to improve aerodynamic efficiency. In *34th AIAA Applied Aerodynamics Conference*, 2016.

[72] F. Nicolosi, A. De Marco, and P. Della Vecchia. Stability, flying qualities and longitudinal parameter estimation of a twin-engine cs-23 certified light aircraft. *Aerospace Science and Technology*, 24(1):226–240, 2013.

[73] F. Nitzsche. Whirl-flutter investigation on an advanced turboprop configuration. *Journal of Aircraft*, 26 (10):939–946, 1989.

[74] F. Nitzsche. Insights on the whirl-flutter phenomena of advanced turboprops and propfans. *Journal of Aircraft*, 28(7):463–470, 1991.

[75] F. Nitzsche. Whirl-flutter suppression in advanced turboprops and propfans by active control techniques. *Journal of Aircraft*, 31(3):713–719, 1994.

[76] F. Nitzsche and E. Rodrigues. Whirl flutter stability of a pusher configuration subject to a nonuniform flow. In *31st Structures, Structural Dynamics and Materials Conference*, page 1162, 1990.

[77] OpenVSP. http://www.openvsp.org/, (accessed May 11, 2020).

[78] B. Ortun, R. Boisard, and I. Gonzalez-Martino. Assessment of propeller 1p loads predictions. *International Journal of Engineering Systems Modelling and Simulation 46*, 4(1-2):36–46, 2012.

[79] B. Ortun, R. Boisard, and I. Gonzalez-Martino. In-plane airloads of a propeller with inflow angle: prediction vs. experiment. In *30th AIAA Applied Aerodynamics Conference*, page 2778, 2012.

[80] M. Patil. Aeroelastic tailoring of composite box beams. In *35th Aerospace Sciences Meeting and Exhibit*, page 15, 1997.

[81] M.J. Patil, D.H. Hodges, and C.E.S. Cesnik. Nonlinear aeroelasticity and flight dynamics of high-altitude long-endurance aircraft. *Journal of Aircraft*, 38(1):88–94, 2001.

[82] M.D. Patterson and B.J. German. Conceptual design of electric aircraft with distributed propellers: multidisciplinary analysis needs and aerodynamic modeling development. In *52nd Aerospace Sciences Meeting*, page 0534, 2014.

[83] M.D. Patterson, B.J. German, and M.D. Moore. Performance analysis and design of on-demand electric aircraft concepts. In *12th AIAA Aviation Technology, Integration, and Operations (ATIO) Conference and 14th AIAA/ISSMO Multidisciplinary Analysis and Optimization Conference*, 2012.

[84] J.C. Patterson Jr. and G.R. Bartlett. Evaluation of installed performance of a wing-tip-mounted pusher turboprop on a semispan wing. NASA Technical Paper 2739, 1987.

[85] W.H. Reed and R.M. Bennett. Propeller whirl flutter considerations for v/stol aircraft. In *Proceedings of the CAL/TRECOM Symposium on Dynamic Loads Problems Associated with Helicopters, Buffalo, USA, Cornell Aeronautical Laboratory*, pages 1–42, 1963.

[86] W.H. Reed III. Propeller-rotor whirl flutter: A state-of-the-art review. *Journal of Sound and Vibration*, 4 (3):526–544, 1966.

[87] W.H. Reed III. Review of propeller-rotor whirl flutter. NASA Technical Report R-264, 1967.

[88] W.H. Reed III and S.R. Bland. An analytical treatment of aircraft propeller precession instability. NASA Technical Note D-659, 1961.

[89] N. Reveles, J. Schoneman, C. Rupp, and E. Blades. Utilizing analytic and direct methods for the verification and validation of whirl flutter analyses. In *AIAA Scitech 2019 Forum*, page 1865, 2019.

[90] A. Rezaeian. *Dynamic stability analysis of a propeller-wing wind tunnel model*. Deutsche Gesellschaft für Luft-und Raumfahrt-Lilienthal-Oberth eV, 2012.

[91] H.S. Ribner. Propellers in yaw. NACA Technical Report 820, 1943.

[92] H.S. Ribner. Formulas for propellers in yaw and charts of the side-force derivative. NACA Technical Report 819, 1945.

[93] W.P. Rodden and T.L. Rose. Propeller/nacelle whirl flutter addition to msc/nastran. In *Proceedings of the 1989 MSC World User's Conference*, 1989.

[94] H.L. Runyan. *Unsteady lifting surface theory applied to a propeller and helicopter rotor*. PhD thesis, © Harry Laird Runyan, 1973.

[95] H.L. Runyan and H. Tai. *Compressible, Unsteady Lifting-surface Theory for a Helicopter Rotor in Forward Flight*, volume 2503. National Aeronautics and Space Administration, Scientific and Technical . . . , 1985.

[96] R.H. Scanlan and J.C. Truman. The gyroscopic effect of a rigid rotating propeller on engine and wing vibration modes. *Journal of the Aeronautical Sciences*, 17(10):653–659, 1950.

[97] J.L. Sewall. An analytical trend study of propeller whirl instability. Technical report, NATIONAL AERONAUTICS AND SPACE ADMINISTRATION WASHINGTON DC, 1962.

[98] B. Singh and I. Chopra. Elastic-blade whirl flutter stability analysis of two-bladed proprotor/pylon systems. *Journal of aircraft*, 42(2):519–527, 2005.

[99] T. Sinnige. *Aerodynamic and Aeroacoustic Interaction Effects for Tip-Mounted Propellers: An Experimental Study*. PhD thesis, Delft University of Technology, 2018.

[100] T. Sinnige, N. van Arnhem, T.C.A. Stokkermans, G. Eitelberg, and L.L.M. Veldhuis. Wingtip-mounted propellers: Aerodynamic analysis of interaction effects and comparison with conventional layout. *Journal of Aircraft*, 56(1):295–312, 2018.

[101] G.E. Smith. Whirl of an aircraft power-plant installation and its interaction with the flutter motion of a flexible wing. ARM-RM-3536, 1968.

[102] M.H. Snyder Jr. and G.W. Zumwalt. Effects of wingtip-mounted propellers on wing lift and induced drag. *Journal of Aircraft*, 6(5):392–397, 1969.

[103] A.M. Stoll, J.B. Bevirt, M.D. Moore, W.J. Fredericks, and N.K. Borer. Drag reduction through distributed electric propulsion. In *14th AIAA aviation technology, integration, and operations conference*, page 2851, 2014.

[104] E.S. Taylor and K.A. Browne. Vibration isolation of aircraft power plants. *Journal of the Aeronautical Sciences*, 6(2):43–49, 1938.

[105] P. Teixeira and C.E. Cesnik. Propeller effects on the dynamic response of hale aircraft. In *2018 AIAA/ASCE/AHS/ASC Structures, Structural Dynamics, and Materials Conference*, page 1202, 2018.

[106] T. Theodorsen. General theory of aerodynamic instability and the mechanism of flutter. NACA Technical Report 496, 1949.

[107] L.L.M. Veldhuis. *Propeller wing aerodynamic interference*. PhD thesis, Delft University of Technology, 2005.

[108] H. Wagner. Über die entstehung des dynamischen auftriebes von tragflügeln. *ZAMM-Journal of Applied Mathematics and Mechanics/Zeitschrift für Angewandte Mathematik und Mechanik*, 5(1):17–35, 1925.

[109] Z. Wang and P. Chen. Whirl flutter analysis with propeller aerodynamic derivatives computed by unsteady vortex lattice method. In *56th AIAA/ASCE/AHS/ASC Structures, Structural Dynamics, and Materials Conference*, page 1419, 2015.

[110] M.H. Williams. An unsteady lifting surface method for single rotation propellers. NASA Contractor Report 4302, 1990.

[111] Y. Yang, G. Huang, D. Zhao, and C. Tang. A new whirl flutter analysis method. In *33rd AIAA Applied Aerodynamics Conference*, page 2887, 2015.

[112] E.C. Yates Jr. Calculation of flutter characteristics for finite-span swept or unswept wings at subsonic and supersonic speeds by a modified strip analysis. NACA Research Memorandum L57L10, 1958.

[113] M.I. Young and R.T. Lytwyn. The influence of blade flapping restraint on the dynamic stability of low disk loading propeller-rotors. *Journal of the American Helicopter Society*, 12(4):38–54, 1967.

[114] X. Zhang, M. Zhao, H. Liang, and M. Zhu. Structural and aeroelastic analyses of a wing with tip rotor. *Journal of Fluids and Structures*, 86:44–69, 2019.